Interaction region optics design of a monochromatization scheme for direct *s*-channel Higgs production at FCC-ee

Conception optique de la région d'interaction pour un schéma de monochromatisation en vue de la production directe du boson de Higgs via le canal s au FCC-ee

Thèse de doctorat de l'Université Paris-Saclay et University of Chinese Academy of Sciences

École doctorale n° 576 : particules, hadrons, énergie et noyau : instrumentation, imagerie, cosmos et simulatiion (PHENIICS)
Spécialité de doctorat : Physique des accélérateurs
Graduate School : Physique. Référent : Faculté des sciences d'Orsay

Thèse préparée dans les unités de recherche **IJCLab (Université Paris-Saclay, CNRS)** et **IHEP (Chinese Academy of Sciences)**, sous la direction d'**Angeles FAUS-GOLFE**, Ingénieure de Recherche, IJCLab, la co-direction de **Yunlong CHI**, Professeur, IHEP, et le co-encadrement de **Frank ZIMMERMANN**, Ingénieur de Recherche, CERN

Thèse soutenue à Paris-Saclay, le 25 novembre 2024, par

Zhandong ZHANG

Composition du jury

Membres du jury avec voix délibérative

Jie GAO Professeur, IHEP	Président
Guy WILKINSON Professeur, University of Oxford	Rapporteur & Examinateur
Jingyu TANG Professeur, University of Science and Technology of China	Rapporteur & Examinateur
Catia MILARDI Directrice de Recherche, INFN	Examinatrice
Wenhui HUANG Professeur, Tsinghua University	Examinateur
Yukiyoshi OHNISHI Professeur, KEK	Examinateur

THESE DE DOCTORAT

NNT : 2024UPASP139

ÉCOLE DOCTORALE
Particules, hadrons, énergie et noyau : instrumentation, imagerie, cosmos et simulation (PHENIICS)

Titre : Conception optique de la région d'interaction pour un schéma de monochromatisation en vue de la production directe du boson de Higgs via le canal *s* au FCC-ee

Mots clés : FCC-ee, monochromatisation, conception optique, luminosité, dispersion de l'énergie dans le centre de masse, beamstrahlung

Résumé : Le FCC-ee offre la possibilité de mesurer le couplage de Yukawa de l'électron via la production directe du Higgs dans le canal *s* à une énergie au centre de masse (CM) d'environ 125 GeV. Cette mesure est grandement facilitée si la dispersion en énergie au centre de masse des collisions électron-positron peut être réduite à un niveau comparable à la largeur naturelle du boson de Higgs dans le Modèle Standard, qui est de 4,1 MeV, sans perte substantielle de luminosité. Cette réduction de la dispersion en énergie des collisions est possible grâce au concept de « monochromatisation ». L'idée de base consiste à créer des corrélations opposées entre la position spatiale et la déviation en énergie au sein des faisceaux en collision, ce qui peut être réalisé en termes d'optique des faisceaux en introduisant une fonction de dispersion non nulle avec des signes opposés pour les deux faisceaux au point d'interaction.

Depuis la première proposition en 2016, la mise en œuvre de la monochromatisation au FCC-ee a été continuellement améliorée, en commençant par des études paramétriques préliminaires. Dans cette thèse, une étude détaillée de la conception optique de la région d'interaction a été menée pour ce mode de collision nouvellement proposé, explorant différentes configurations potentielles et leur mise en œuvre dans le réseau global du FCC-ee, ainsi que des simulations de la dynamique des faisceaux et des évaluations de performance, incluant l'impact du « beamstrahlung ».

Title : Interaction region optics design of a monochromatization scheme for direct *s*-channel Higgs production at FCC-ee

Keywords : FCC-ee, monochromatization, optics design, luminosity, centre-of-mass energy spread, beamstrahlung

Abstract : The FCC-ee offers the potential to measure the electron Yukawa coupling via direct *s*-channel Higgs production at a centre-of-mass (CM) energy of about 125 GeV. This measurement is significantly facilitated if the CM energy spread of electron-positron collisions can be reduced to a level comparable to the Standard Model Higgs boson's natural width of 4.1 MeV without substantial loss in luminosity. Achieving this reduction in collision-energy spread is possible through the "monochromatization" concept. The basic idea consists of creating opposite correlations between spatial position and energy deviation within the colliding beams, which can be accomplished in beam-optics terms by introducing a nonzero dispersion function with opposite signs for the two beams at the interaction point.

Since the first proposal in 2016, the monochromatization implementation at the FCC-ee has been continuously improved, starting from preliminary parametric studies. In this thesis, a detailed study of the interaction region optics design has been conducted for this newly proposed collision mode, exploring different potential configurations and their implementation in the FCC-ee global lattice, along with beam dynamics simulations and performance evaluations including the "beamstrahlung" impact.

I would like to dedicate this thesis to my loving family ...

Declaration

I hereby declare that except where specific reference is made to the work of others, the contents of this dissertation are original and have not been submitted in whole or in part for consideration for any other degree or qualification in this, or any other university. This dissertation is my own work and contains nothing which is the outcome of work done in collaboration with others, except as specified in the text and Acknowledgements.

Zhandong ZHANG
December 2024

Acknowledgements

Throughout my PhD journey, I have been fortunate to receive guidance, support, and encouragement from many individuals. Although words may fall short in expressing my deepest gratitude, I would like to take this opportunity to sincerely thank all those who have been by my side and contributed to the completion of this thesis.

First and foremost, I extend my heartfelt thanks to the Institute of High Energy Physics, Chinese Academy of Sciences (IHEP)—University of Chinese Academy of Sciences (UCAS) and the Laboratoire de Physique des 2 Infinis Irène Joliot-Curie (IJCLab, formerly Laboratoire de l'Accélérateur Linéaire)—Centre national de la recherche scientifique (CNRS)/ Institut national de physique nucléaire et de physique des particules (IN2P3)—Université Paris-Saclay (UPSaclay), where I completed my PhD as an international cotutelle student. My deep gratitude goes to the UCAS and the China Scholarship Council (CSC), for their financial support of my studies in France and for facilitating international travel. Special thanks are also due to IHEP, CNRS, the European Physical Society (EPS), and the France China Particle Physics Laboratory (FCPPL) for supporting my participation in international conferences, mainly including the International Particle Accelerator Conference (IPAC), FCC Week, CEPC Workshop and FCPPL Workshop. I also appreciate the European Organization for Nuclear Research (CERN) for awarding me the student grant to attend the CERN accelerator school. Lastly, I am grateful to the dedicated staff at these institutions for their invaluable administrative assistance throughout my studies.

It has been a privilege to work under the supervision of Dr. Angeles Faus-Golfe (IJCLab), Dr. Frank Zimmermann (CERN), and Prof. Yunlong Chi (IHEP) throughout my three-year PhD journey in accelerator physics. This thesis would not have been possible without their dedicated guidance, support, and insightful suggestions. Their vast expertise not only provided me with a strong foundation for problem-solving but also expanded my understanding of the broader field of accelerator physics. Their passion and dedication to research have continuously inspired me to overcome challenges and pursue excellence. The opportunities they gave me to collaborate on both domestic and international projects, working alongside experts from various fields, have been instrumental in shaping my growth as a researcher. I am especially grateful to Angeles for her daily discussions, both academic and personal, which greatly aided my adjustment to life in Paris and enriched my overall experience.

I would like to extend my sincere thanks to the six members of my thesis committee: Prof. Jie Gao (IHEP), Prof. Guy Wilkinson (University of Oxford), Dr. Catia Milardi (INFN), Prof. Jingyu Tang (University of Science and Technology of China), Prof. Wenhui Huang (Tsinghua University) and Prof. Yukiyoshi Ohnishi (KEK), for their valuable feedback, constructive criticism, and for taking the time to review my work. I would also like to express my appreciation to the two members of my individual follow-up committee in UPSaclay: Dr. Iryna Chaikovska and Dr. Xavier Sarazin, for their attentive support and guidance during my PhD studies in France.

The projects I have been involved in, under the framework of FCC-ee and CEPC, provided me with the valuable opportunity to meet and collaborate with numerous colleagues and friends. I would like to extend my thanks to Prof. Alain Blondel, Prof. Patrick Janot, Dr. David d'Enterria, Prof. Dmitry Shatilov, Dr. Jacqueline Keintzel, Prof. Guy Wilkinson, and Dr. Jörg Wenninger for the fruitful discussions within the EPOL FCC-ee working group. Special thanks go to Prof. Katsunobu Oide, Prof. Pantaleo Raimondi, Dr. Michael Hofer, Dr. Kevin Daniel Joel André and Dr. Xavier Buffat for their private communications and discussions during the FCC-ee accelerator design meetings, which helped me gain a deeper understanding of the FCC-ee baseline optics and provided significant inspiration for my PhD research. Special thanks to Prof. Jie Gao for his recognition of my PhD work and for inviting me to present numerous reports at international conferences. I am equally grateful to Prof. Zusheng Zhou for his kind assistance during my time at IHEP and for his dedicated guidance on my master internship project, "Design study of S-band 80 MW high-efficiency klystron for CEPC LINAC", which helped shape me beyond just being a accelerator physics researcher. To all other colleagues and friends, I extend my heartfelt thanks for any assistance, large or small.

I must also acknowledge the members of the IJCLab BIMP group and the LINAC group of IHEP's Accelerator Division. Special thanks go to Dr. Luc Perrot for his kind assistance in helping me quickly adapt to the research life at IJCLab. I am deeply grateful to Dr. Hongping Jiang for laying the groundwork for my PhD project and giving me a strong starting point, as well as for helping me quickly integrate into life in France when I first arrived. Many thanks to Dr. Bowen Bai, who offered tremendous help in building the connection between Angeles and me. I also extend my gratitude to all my colleagues for the joyful relationships during my PhD journey. I will never forget the meaningful discussions we had during lunchtimes and coffee breaks. It has truly been a pleasure to learn from and collaborate with all of them. My heartfelt thanks go to my roommate, Dr. Shu Zhang, for his constant companionship and daily support throughout this journey. I would also like to thank all my dearest friends for their listening ears, conversations, and companionship during the stressful times throughout these years.

Lastly, I would like to express my deepest gratitude to my family, especially my parents, for their unwavering support, encouragement, and love throughout my academic journey. To my beloved girlfriend, Tianyue Wei, thank you for your patience, understanding, and constant encouragement, which have been a source of strength during both the highs and lows of this journey. I couldn't have made it this far without all of you by my side.

Résumé

L'une des mesures les plus fondamentales depuis la découverte du boson de Higgs est la détermination de ses couplages de Yukawa. Le seul moyen connu de mesurer le couplage de Yukawa du Higgs aux leptons de première génération consiste à mesurer le couplage de Yukawa de l'électron par la production directe de Higgs en canal s : $e^+e^- \to \mathrm{H}$ à une énergie de centre de masse (CM) d'environ 125 GeV. Une telle mesure est grandement facilitée si la dispersion de l'énergie CM des collisions e^+e^-, qui est d'environ 50 MeV en raison uniquement du rayonnement synchrotron dans un schéma de collision conventionnel, peut être réduite à un niveau comparable à la largeur naturelle du boson de Higgs du Modèle Standard $\Gamma_{\mathrm{H}} = 4.1\,\mathrm{MeV}$ dans un futur collisionneur circulaire à haute énergie tel que le FCC-ee proposé au CERN. Pour atteindre la dispersion énergétique souhaitée et améliorer la résolution en énergie CM dans les expériences à faisceaux en collision, le concept de « monochromatisation » a été proposé. L'idée de base consiste à créer des corrélations opposées entre la position spatiale et la déviation énergétique au sein des faisceaux en collision, ce qui peut être réalisé en termes d'optique de faisceau en introduisant une fonction de dispersion non nulle avec des signes opposés pour les deux faisceaux au point d'interaction (PI).

Les concepts essentiels et la théorie de base de la monochromatisation dans les collisionneurs circulaires e^+e^- ont été proposés pour la première fois en 1975 par A. Renieri pour améliorer la résolution en énergie d'ADONE. Depuis, une variété de schémas de monochromatisation utilisant différentes techniques pour générer la fonction de dispersion au PI, incluant des quadrupôles électrostatiques inclinés, des dispositifs magnétiques à radiofréquence, des aimants dipolaires avec des séparateurs électrostatiques, des cavités radiofréquences supraconductrices défléchissantes, ont été proposés dans de multiples collisionneurs circulaires e^+e^-, principalement à basses énergies et en configuration de collision frontale. Bien que le principe de monochromatisation soit théoriquement simple, il n'a jamais été étudié de manière approfondie jusqu'à sa mise en œuvre dans un collisionneur pour une validation expérimentale. Les obstacles à la mise en œuvre de diverses propositions incluaient : des études insuffisantes et l'incertitude des performances, le coût et les efforts de mise en œuvre matérielle, ainsi que l'évolution des intérêts physiques

qui a entraîné des améliorations significatives des performances des collisionneurs existants sans introduction de la monochromatisation.

Des études récentes ont revisité et étendu le concept de monochromatisation dans le contexte des collisionneurs circulaires e^+e^- à haute énergie et en configuration de collision avec angle de croisement. Deux nouveaux problèmes devaient être résolus dans cette condition. L'un est l'extension du concept de monochromatisation précédent, initialement conçu pour des collisions frontales, à la configuration impliquant un angle de croisement. L'autre est la prise en compte de l'impact du « beamstrahlung », qui devient de plus en plus significatif dans les collisionneurs circulaires e^+e^- à haute énergie.

Depuis la première proposition en 2016, la mise en œuvre de la monochromatisation au FCC-ee a été continuellement améliorée, en commençant par des études paramétriques préliminaires combinées à une évaluation des performances physiques. Dans cette thèse, en sélectionnant la Version 2022 des optiques FCC-ee GHC comme optiques de référence, une étude détaillée de la conception optique de la région d'interaction (RI) a été menée pour ce nouveau mode de collision proposé, explorant différentes configurations potentielles et leur mise en œuvre dans le lattice global du FCC-ee, ainsi que des simulations de dynamique de faisceau et des évaluations de performances prenant en compte l'impact du beamstrahlung.

La thèse commence par une introduction détaillée au concept de monochromatisation au Chapitre 1, débutant avec sa formulation originale pour les collisionneurs e^+e^- à basse énergie et en configuration de collision frontale, suivie de l'extension de ce concept pour son application dans des collisionneurs à haute énergie avec des configurations de collision avec angle croisé, incluant la prise en compte des effets d'horloge et du beamstrahlung. Nous discutons ensuite de l'application de la monochromatisation au FCC-ee, incluant ses motivations physiques et les études paramétriques préliminaires combinées à une évaluation des performances physiques, avant la conception optique.

Au Chapitre 2, nous fournissons un aperçu du projet FCC-ee, de ses motivations et de son potentiel en tant que plateforme de haute précision pour l'investigation du Modèle Standard et l'exploration de nouvelles physiques au-delà de celui-ci. Nous décrivons ensuite la disposition générale de l'accélérateur FCC-ee et deux types d'optiques standard de base du FCC-ee : les optiques GHC FCC-ee et les optiques LCC FCC, qui servent de point de départ pour les trois conceptions d'optique RI monochromatisantes distinctes du FCC-ee GHC, présentées dans les chapitres suivants de cette thèse.

Le Chapitre 3 explore le scénario de monochromatisation impliquant une dispersion horizontale non nulle au PI. Basée sur les paramètres cibles du PI dérivés de l'optimisation paramétrique auto-cohérente de la monochromatisation FCC-ee, avec $\beta^*_{x,y} = 90,1\,\mathrm{mm}$ et

$D_x^* = 0.105\,\mathrm{m}$, la conception de cette optique RI de monochromatisation a été développée en utilisant deux types d'optiques "FCC-ee GHC V22". La conception a été réalisée en intégrant quatre structures de chicane à orbite fermée "trois angles" progressives, optimisées pas à pas, en garantissant la compatibilité avec les modes d'opération standard et en maintenant une luminosité à un niveau idéal en minimisant l'augmentation de l'émittance horizontale. Après l'implémentation globale, nous avons observé que la dispersion de l'énergie CM a été réduite avec succès, en prenant en compte l'impact du beamstrahlung. Les évaluations des performances physiques démontrent que cette approche pourrait significativement améliorer le taux de production de bosons de Higgs par production directe en canal s. Sous la configuration frontale, l'optique "MonochroM TH2IP" (avec l'optique RI de monochromatisation intégrée uniquement dans deux RI), basée sur l'optique "FCC-ee GHC V22 $\mathrm{t\bar{t}}$", atteint le meilleur benchmark $\delta_{\sqrt{s}}$-$\mathcal{L}_{\mathrm{int}}$, avec $\sigma_W = 15.54\,\mathrm{MeV}$ et $\mathcal{L}_{\mathrm{int}} = 4.51\,\mathrm{ab}^{-1}$. Cela correspond à des limites supérieures $|y_e| < 2.7|y_e^{\mathrm{SM}}|$ dans les contours de niveau de confiance à 95% pour le couplage Higgs-électron. Sous la configuration à angle croisé, l'optique "MonochroM TH2IP" offre également le meilleur benchmark, avec $\sigma_W = 23.68\,\mathrm{MeV}$ et $\mathcal{L}_{\mathrm{int}} = 2.94\,\mathrm{ab}^{-1}$, indiquant des limites supérieures $|y_e| < 3.2|y_e^{\mathrm{SM}}|$. Bien que ce schéma de monochromatisation offre les meilleures performances physiques par rapport aux autres, sa conception optique complexe — où tous les dipôles horizontaux LCC du RI sont divisés en trois ensembles avec des quadrupôles fins insérés entre eux pour assurer la compatibilité avec le mode d'opération standard — nécessite une simplification supplémentaire.

Au Chapitre 4, nous examinons un deuxième schéma de monochromatisation, introduisant une dispersion verticale non nulle au PI. En raison de l'émittance verticale exceptionnellement faible du FCC-ee, une dispersion verticale de seulement 1 mm suffit pour obtenir l'effet de monochromatisation souhaité. Inspirée par le schéma de compensation du solénoïde du détecteur utilisé dans l'optique "FCC LCC V22", cette approche a été appliquée aux deux types d'optiques "FCC-ee GHC V22" en incorporant des quadrupôles déviés dans le RI. Pour atténuer l'augmentation de l'émittance verticale causée par le beamstrahlung avec une dispersion verticale non nulle au PI, la fonction bêta horizontale au PI a été augmentée. La conception résultante s'est avérée efficace pour réduire la dispersion de l'énergie CM. Les meilleures performances physiques ont été obtenues avec l'optique "MonochroM TV0.5" (avec une dispersion verticale de 0.5 mm dans quatre PI), fournissant des limites supérieures $|y_e| < 4.9|y_e^{\mathrm{SM}}|$ pour les collisions frontales et $|y_e| < 5.1|y_e^{\mathrm{SM}}|$ pour les collisions à angle croisé. Bien que les performances physiques soient moins favorables que celles du schéma avec dispersion horizontale non nulle au PI, cette approche est plus facile à mettre en œuvre sans modifier l'orbite du RI, ce qui la rend faisable pour les collisionneurs existants à plus basse énergie. Sans l'augmentation de l'émittance verticale causée par le beamstrahlung, ce schéma pourrait potentiellement offrir de meilleures performances dans de tels environnements.

Le chapitre 5 combine les deux approches précédentes en introduisant à la fois une dispersion horizontale et verticale au PI. Ce schéma hybride a été mis en œuvre en intégrant des quadrupôles inclinés dans les optiques de la RI, qui incluaient déjà une dispersion horizontale non nulle au PI. Lorsqu'il a été évalué par rapport aux schémas de dispersion horizontale et verticale individuels, il a été constaté que, bien que le schéma hybride entraîne une réduction de la dispersion de l'énergie CM, ses performances physiques ne s'améliorent pas comme prévu en raison de la perte de luminosité accrue. De plus, cette conception pourrait rencontrer des défis potentiels liés au couplage de betatron.

En conclusion, bien que la monochromatisation soit une idée conceptuelle simple, sa mise en œuvre pratique dans un collisionneur est complexe, notamment si elle n'est pas intégrée dès le départ dans la conception des optiques de la RI en tant que mode opérationnel dédié. Les recherches sur la monochromatisation n'ont pas encore atteint un niveau de maturité permettant sa mise en œuvre complète et sa validation expérimentale. Pour y remédier, une conception de réseau flexible qui permette les deux modes opérationnels — avec et sans monochromatisation — est essentielle. Cette thèse a démontré que la monochromatisation est une approche prometteuse pour améliorer la résolution en énergie CM dans les futurs collisionneurs e^+e^- à haute énergie, en particulier pour les mesures précises du boson de Higgs au FCC-ee. En explorant divers schémas de monochromatisation et en optimisant les optiques de la RI pour chaque scénario, nous avons posé les bases pour une future mise en œuvre expérimentale et validation. Les résultats indiquent que les schémas de dispersion horizontale et verticale sont des options viables, avec le potentiel de réduire considérablement la dispersion de l'énergie CM et d'améliorer la portée physique du FCC-ee. De plus, il est évident que l'implémentation des cavités "crab" améliore les performances physiques des réglages de monochromatisation.

Plusieurs pistes de recherche future ont été identifiées à travers cette thèse. Premièrement, les optiques de la RI de monochromatisation du FCC-ee GHC seront mises à jour vers la dernière version des optiques en évolution continue du FCC-ee GHC, la version 2024 étant la plus actuelle. Les paramètres optiques pour le mode de monochromatisation, tels que la fonction de betatron au PI, la dispersion au PI, la population des paquets, le réglage du synchrotron, et le facteur de compression du moment, continueront à être optimisés pour de meilleures performances. Deuxièmement, l'optimisation de l'aperture dynamique pour ces nouveaux types d'optique de monochromatisation sera réalisée étape par étape en ajustant les familles de sextupôles dans l'arc, en se basant sur les résultats de suivi des particules. Cela permettra de réaliser des simulations de faisceau-faisceau avec dispersion non nulle au PI dans Xsuite, en tenant compte des effets en forme de sablier et de beamstrahlung, plutôt que de se limiter aux évaluations analytiques. Troisièmement, des comparaisons supplémentaires et des implémentations de la monochromatisation dans des RI plus symétriques, telles que celles dans les optiques LCC du FCC-ee et les optiques du CEPC, seront explorées. Quatrièmement, deux schémas novateurs de monochromatisation — cavités radiofréquences supraconductrices défléchissantes et chromaticité verticale locale résiduelle non nulle — seront étudiés pour en évaluer la faisabilité. Enfin, la validation expérimentale du concept de monochromatisation dans des collisionneurs à basse énergie existants, tels que BEPC II, DAΦNE, et SuperKEKB, est en cours d'étude. Ces efforts futurs seront essentiels pour réaliser le plein potentiel de la monochromatisation dans les futurs projets de collisionneurs.

Mots-clés : FCC-ee, monochromatisation, conception optique, luminosité, dispersion de l'énergie dans le centre de masse, beamstrahlung

Abstract

One of the most fundamental measurements since the Higgs boson discovery, is determining its Yukawa couplings. The only known path to measure the Higgs Yukawa coupling to first-generation leptons involves measuring the electron Yukawa coupling through direct s-channel Higgs production: $e^+e^- \to \mathrm{H}$ at a centre-of-mass (CM) energy of about 125 GeV. Such a measurement is significantly facilitated if the CM energy spread of e^+e^- collisions, which is approximately 50 MeV due only to synchrotron radiation in a conventional collision scheme, can be reduced to a level comparable to the natural width of the Standard Model Higgs boson $\Gamma_{\mathrm{H}} = 4.1\,\mathrm{MeV}$ at a future high-energy circular collider such as the proposed FCC-ee at CERN. To reach the desired collision-energy spread and enhance the CM energy resolution in colliding-beam experiments, the concept of "monochromatization" has been proposed. The basic idea consists in creating opposite correlations between spatial position and energy deviation within the colliding beams, which can be accomplished in beam-optics terms by introducing a nonzero dispersion function with opposite signs for the two beams at the interaction point (IP).

The essential concepts and the basic theory of monochromatization in e^+e^- circular colliders were first proposed in 1975 by A. Renieri to improve the energy resolution of ADONE. Since then, a variety of monochromatization schemes using different techniques for the generation of the dispersion function in the IP, including electrostatic skew quadrupoles, Radio Frequency (RF) magnetic devices, dipole magnets with electrostatic separators or superconducting RF deflecting cavities, have been proposed in multiple e^+e^- circular colliders, mostly at low-energies and in head-on collision configuration. Despite its theoretical simplicity, the monochromatization principle has never been thoroughly investigated to the point of implementation in a collider for experimental validation. Impediments to implementation of various proposals included: insufficient studies and uncertainty of performance; the cost and effort of hardware implementation; shifting perceptions of the physics interest, which resulted in significant performance improvements at the operating colliders without the introduction of monochromatization.

Recent studies have revisited and extended the concept of monochromatization in the context of e^+e^- circular colliders high energies and in crossing-angle collision configuration.

Two new issues needed to be addressed under this condition. One is the extension of the previous monochromatization concept, originally designed for head-on collisions, to the configuration involving a crossing angle. The other is the consideration of the impact of "beamstrahlung," which becomes increasingly significant in high-energy e^+e^- circular colliders.

Since the first proposal in 2016, the monochromatization implementation at the FCC-ee has been continuously improved, starting from preliminary parametric studies combined with physics performance evaluation. In this thesis, selecting Version 2022 of the FCC-ee GHC optics as a baseline standard optics, a detailed study of the interaction region (IR) optics design has been conducted for this newly proposed collision mode, exploring three different potential configurations:

- **Nonzero horizontal dispersion at the IP** generated by several sets of different configurations of dipole magnets in the local chromaticity correction system.
- **Nonzero vertical dispersion at the IP** generated by implementing skew quadrupoles at the location of sextupole pairs in the IR.
- **Nonzero combined horizontal/vertical dispersion at the IP** generated by integrating skew quadrupoles into the designed monochromatization IR, already featuring nonzero horizontal dispersion at the IP.

After completing the IR optic designs for each monochromatization scheme, the respective IR lattices were individually integrated into the global lattice. Subsequently, local and global chromaticity corrections, tune corrections, and synchrotron radiation energy loss compensation were performed. Taking into account the beamstrahlung impact, the feasibility of each design was then analyzed, including global optical performance calculations, dynamic aperture studies, and physics performance evaluations. Finally, the feasibility, advantages, and disadvantages of the different monochromatization schemes were compared and assessed.

Keywords: FCC-ee, monochromatization, optics design, luminosity, centre-of-mass energy spread, beamstrahlung

Table of contents

List of figures

List of tables

Nomenclature

Symbols

α	fine structure constant
α_{C}	momentum compaction factor
$\beta_{x,y}$	betatron function
$\beta^*_{x,y}$	betatron function at the interaction point
c	speed of light
C	circumference
δ	relative energy deviation
$D_{x,y}$	dispersion
$D^*_{x,y}$	dispersion at the interaction point
e	elementary charge
E_0	beam energy
$\varepsilon_{x,y}$	emittance
f_r	revolution frequency
γ	relativistic Lorentz factor
Γ_{H}	Higgs boson width
h	harmonic number
$\hbar$	Planck constant

I	beam current
$J_{x,y,z}$	damping partition number
κ	coupling ratio
$\mathcal{L}$	luminosity per interaction point
Λ	differential luminosity
λ	monochromatization factor
m_e	electron rest mass
m_{H}	Higgs boson mass
N_b	bunch population
n_b	bunches per beam
n_{IP}	the number of interaction points
φ	Piwinski angle
Q_s	synchrotron tune
$Q_{x,y}$	transverse tune
r_e	classical electron radius
ρ	bending radius
σ_δ	relative beam energy spread
$\delta_{\sqrt{s}}$	centre-of-mass energy spread (physics expression)
σ_W	centre-of-mass energy spread
$\sigma_{x,y}$	transverse beam size
$\sigma^*_{x\beta,y\beta}$	betatron contribution to transverse beam size at the interaction point
$\sigma^*_{x,y}$	transverse beam size at the interaction point
σ_z	bunch length
$\tau_{x,y,E}$	radiation damping time

θ_c	full crossing angle
$T_{\rm rev}$	revolution period
W	centre-of-mass energy
$\sqrt{s}$	centre-of-mass energy (physics expression)
$\xi_{x,y}$	beam-beam tune shift
y_e	electron Yukawa

Acronyms / Abbreviations

BS	beamstrahlung
CC	Crab Crossing
CDR	Conceptual Design Report
CEPC	Circular Electron Positron Collider
CERN	Conseil Européen pour la Recherche Nucléaire (European Organization for Nuclear Research)
CL	confidence level
CLIC	Compact Linear Collider
CM	centre-of-mass
CNRS	Centre National de la Recherche Scientifique
CSC	China Scholarship Council
CS	crab sextupole
DA	dynamic aperture
EPS	European Physical Society
ES	energy-scaled
ESQ	electrostatic skew quadrupole
EW	electroweak

FCC	Future Circular Collider
FCC-ee	Future Circular electron positron Collider
FCC-hh	Future Circular hadron hadron Collider
FCC FS	Future Circular Collider Feasibility Study
FCPPL	France China Particle Physics Laboratory
FFS	final focus system
FODO	Focus-Drift-Defocus-Drift
GHC	global hybrid correction
Guinea-Pig	Generator of Unwanted Interactions for Numerical Experiment Analysis Program Interfaced to GEANT
HEB	High Energy Booster
HL-LHC	High Luminosity Large Hadron Collider
IHEP	Institute of High Energy Physics, Chinese Academy of Sciences
IJCLab	Laboratoire de Physique des 2 Infinis Irène Joliot-Curie
ILC	International Linear Collider
IN2P3	Institut national de physique nucléaire et de physique des particules
INFN	Istituto Nazionale di Fisica Nucleare (National Institute for Nuclear Physics)
IPAC	International Particle Accelerator Conference
IP	interaction point
IR	interaction region
IRS	Integrated Resonances Scan
KEK	High Energy Accelerator Research Organization
LCC	local chromaticity correction

LEP	Large Electron Positron
LHC	Large Hadron Collider
MAD-X	Methodical Accelerator Design - X
MonochroM	monochromatization
RF	radio frequency
SAD	Strategic Accelerator Design
SR	synchrotron radiation
SM	Standard Model
UCAS	University of Chinese Academy of Sciences
UPSaclay	Université Paris-Saclay
V22	Version 2022

Chapter 1

Introduction to monochromatization concept and its application at FCC-ee

The Future Circular electron positron Collider (FCC-ee) [1] offers the potential to measure the electron Yukawa coupling through direct s-channel Higgs production: $e^+e^- \to \mathrm{H}$ at about 125 GeV centre-of-mass (CM) energy. This measurement is significantly facilitated if the CM energy spread of e^+e^- collisions can be reduced from about 50 MeV in a conventional setup, to a level comparable to the natural width of the Standard Model (SM) Higgs boson $\Gamma_{\mathrm{H}} = 4.1\,\mathrm{MeV}$ [2–4]. Achieving this reduction is possible through "monochromatization," which was initially proposed in the 1970s for improving the energy resolution of a low-energy e^+e^- collider [5].

In this chapter, we begin by introducing the basic concept of monochromatization in e^+e^- circular colliders, initially focusing on its application to low-energy e^+e^- circular colliders with head-on collisions. We then explore the recent studies that extend this concept to collision configurations involving a crossing angle. Finally, we delve into the ongoing efforts to implement monochromatization in the FCC-ee, starting with preliminary parametric studies and incorporating evaluations of physics performance, with consideration of the significant impact of "beamstrahlung."

1.1 Monochromatization in e^+e^- circular colliders

Collider experiments represent a joint venture between accelerator experts and particle/detector physicists. The former are responsible for delivering the luminosity and ensuring other required beam parameters, while the latter focus on the detection and analysis of the products of the particle collision. Enhancement in the quality of the physics measurements could be pursued on either side. The possibilities for improving accelerators performance are vast and not limited to luminosity production. One possible way to extend the physics reach of a colliding-beam experiment through an accelerator technique is to apply "monochromatization" of the collision energy. Initially proposed for low-energy e^+e^- circular colliders with head-on collisions, this concept consists in reducing the spread of the centre-of mass (CM) energies, without necessarily reducing the inherent energy spread of the two individual beams, which is of particular interest when operating on a narrow resonance or at the threshold of its pair production.

1.1.1 Basic formulas for head-on collisions

For a head-on collision in an e^+e^- collider, the relative spread of CM energy is $\sqrt{2}$ times lower than the relative beam energy spread σ_δ, namely:

$$\frac{\sigma_W}{W} = \frac{\sigma_\delta}{\sqrt{2}} , \tag{1.1}$$

with the CM energy W equals to 2 times of beam energy E_0, so the CM energy spread σ_W is defined as:

$$\sigma_W = \sqrt{2} E_0 \sigma_\delta . \tag{1.2}$$

The σ_δ is mainly due to synchrotron radiation (SR) emitted when an ultra-relativistic particle passes through a bending magnet [6]:

$$\sigma_\delta^2 = C_q \gamma^2 \frac{I_3}{J_z I_2} . \tag{1.3}$$

C_q is a constant given by:

$$C_q = \frac{55}{32\sqrt{3}} \frac{\hbar}{m_e c} , \tag{1.4}$$

where $\hbar$ is the Planck constant [7], c is the speed of light and m_e is the electron rest mass [7], J_z is the longitudinal damping partition number (Eq. A.13) and γ is the relativistic Lorentz factor, which approximately equals to the ratio of E_0 and the electron rest mass energy $m_e c^2$. All the bending magnets (dipoles) in a circular accelerator share the same bending radius of the dipoles ρ, so the ratio of second and third synchrotron radiation integrals (Eq. A.4 and Eq. A.5) becomes:

$$\frac{I_3}{I_2} \simeq \frac{1}{\rho} , \tag{1.5}$$

so:

$$\sigma_W \propto \frac{1}{\sqrt{\rho J_z}} \, . \tag{1.6}$$

In view of this formula we can conceive of usual ways to enhance the energy resolution of the interacting beams either by increasing the ρ and J_z [8]. Increasing ρ leads to an increase in the circumference of the machine; moreover, for reasons of beam stability, the variation of the parameter J_z, which we can envisage, is relatively modest:

$$0.5 \leq J_z = 3 - J_x \leq 2.5 \, , \tag{1.7}$$

where J_x is the horizontal damping partition number (Eq. A.13). Such variation requires particular magnetic elements ("wigglers") and leads to practical limitations [9, 10].

Another alternative scheme is "monochromatization," which involves reducing the spread of CM energy without necessarily reducing the inherent energy spread of the two individual beams. In terms of beam optics, this configuration can be achieved by generating a non-zero horizontal or vertical interaction point (IP) dispersion $D^*_{x,y}$. In this case, each particle in a beam has a transverse position displacement of $D^*_{x,y}\delta$, according its relative energy deviation:

$$\delta = \frac{E - E_0}{E_0} = \frac{\Delta E}{E} \, . \tag{1.8}$$

If the two head-on colliding beams have the same $D^*_{x,y}$, thus featuring the same correlation between transverse spatial position and energy deviation, the positrons of energy $E_0 + \Delta E$ will encounter the electrons of the same energy as schematically depicted in Fig. 1.1. The CM energy W will be:

$$W = 2\,(E_0 + \Delta E) \, . \tag{1.9}$$

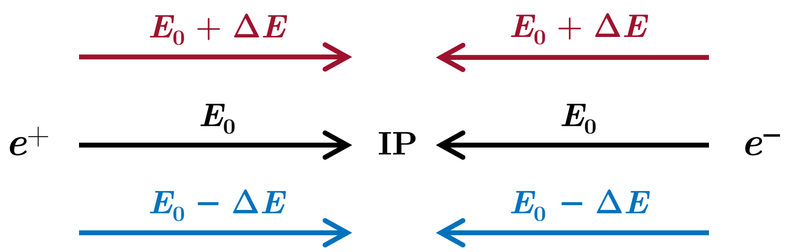

Fig. 1.1 Head-on collision scheme with equal-sign nonzero IP dispersion and no monochromatization.

If we introduce a non-zero $D^*_{x,y}$ with equal magnitudes but opposite signs at either sides of the IP, there will be inverse correlations between transverse spatial position and

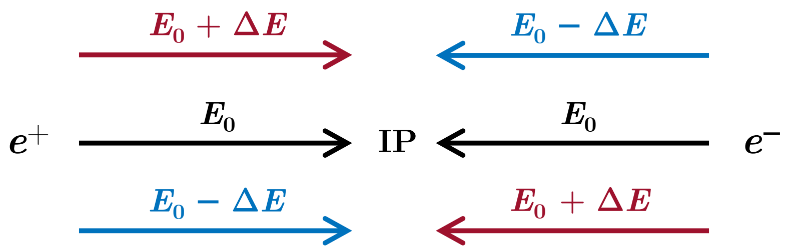

Fig. 1.2 Head-on collision scheme with monochromatization.

energy deviation in the colliding beams. The positrons of energy $E_0 + \Delta E$ will encounter the electrons of energy $E_0 - \Delta E$ as schematically depicted in Fig. 1.2. The CM energy W now becomes:

$$W = 2E_0 + \mathcal{O}\left(\Delta E^2\right) , \tag{1.10}$$

independent of ΔE at first order. So it is evident that the CM energy spread reduces with such kind of configuration at the IP.

1.1.2 Trade-off between luminosity and CM energy spread

While lowering the CM energy spread by monochromatization, the IP dispersion will blow up the IP transverse beam size, thus causing the luminosity loss. The quantitative description of this CM energy spread reduction and luminosity loss in a monochromatization scheme necessitates the introduction of the concepts of luminosity and differential luminosity [11].

Luminosity and differential luminosity

The total luminosity per IP, distributed over all CM energies, is given by a four-fold integral:

$$\mathcal{L} = n_b f_r \int f_+ \left(x, y, \delta_+\right) f_- \left(x, y, \delta_-\right) \, dx \, dy \, d\delta_+ \, d\delta_- \, , \tag{1.11}$$

where n_b is the number of bunches per beam, f_r is revolution frequency. f_+ and f_- are the density functions of colliding positron and electron bunches associated to the two transverse spatial coordinates x, y and relative energy deviation (Eq. 1.8), which is independent of Gaussian distribution. If denoting N_b as the number of particles in each interacting bunch (bunch population), we can write $f_\pm$ as:

$$f_\pm(x,y,\delta_\pm) = \frac{N_{b\pm}}{(2\pi)^{3/2}\sigma^*_{x\beta}\sigma^*_{y\beta}\sigma_\delta}\exp\left(-\frac{\left(x+D^*_{x\pm}\delta_\pm\right)^2}{2\sigma^{*2}_{x\beta}} - \frac{\left(y+D^*_{y\pm}\delta_\pm\right)^2}{2\sigma^{*2}_{y\beta}} - \frac{\delta^2_\pm}{2\sigma^2_\delta}\right) . \tag{1.12}$$

The $\sigma^*_{x\beta}$ and $\sigma^*_{y\beta}$ are the betatron contribution to the horizontal and vertical beam size at the IP, respectively:

$$\sigma^*_{x\beta} = \sqrt{\beta^*_x\varepsilon_x}\,, \quad \sigma^*_{y\beta} = \sqrt{\beta^*_y\varepsilon_y}\,, \tag{1.13}$$

where $\beta^*_{x,y}$ are the IP betatron functions and $\varepsilon_{x,y}$ are the emittances (Eq. A.14). Note that the two colliding beams share the same $\sigma^*_{x\beta,y\beta}$ and $\beta^*_{x,y}$, which is the symmetric-collider case often used in e^+e^- circular colliders.

To describe the distribution of luminosity over different energy ranges within the CM frame of the colliding particles, we will introduce the differential luminosity $\Lambda(W)$ as a function of CM energy W. Then the total luminosity $\mathcal{L}_{[W_1,W_2]}$ over an energy interval $[w_1, w_2]$ can be calculated by integrating $\Lambda(W)$ over the interval:

$$\mathcal{L}_{[W_1,W_2]} = \int_{W_1}^{W_2} \Lambda(W)\,dw\,. \tag{1.14}$$

with

$$\begin{aligned}\Lambda(W) = n_b f_r \int & f_+(x,y,\delta_+)f_-(x,y,\delta_-)\\ &\delta\left(W - 2E_0\sqrt{(1+\delta_+)}\sqrt{(1+\delta_-)}\right)dx\,dy\,d\delta_+\,d\delta_-\,.\end{aligned} \tag{1.15}$$

The argument of the function δ takes into account the energy in the CM during the collision between particles with different energies. This expression can be simplified by approximating the argument of the function δ as:

$$W - 2E_0 - E_0\delta_+ - E_0\delta_- = E_0\left(2\Delta - \delta_+ - \delta_-\right)\,, \tag{1.16}$$

where Δ is is the relative deviation of W with respect to its average value $2E_0$:

$$\Delta = \frac{W}{2E_0} - 1\,. \tag{1.17}$$

It should be noted that $\Lambda(W)$ is defined as function of W, not of Δ, as was done in Ref. [5, 12], so that the differential luminosity differs by a factor $(2E_0)^{-1}$ from that of these authors. The present definition ought to be more directly relevant for experimental purposes since it is the luminosity per unit CM energy.

Quantitative description

With the definition of luminosity and differential luminosity, the trade-off between CM energy spread and luminosity of monochromatization scheme can be described quantitatively as following.

For comparison, we start with the condition without $D^*_{x,y}$:

$$D^*_{x+} = -D^*_{x-} = 0\,, \quad D^*_{y+} = -D^*_{y-} = 0\,, \tag{1.18}$$

which corresponds to the optics usually achieved for a collider, so called standard mode. In this case, the luminosity (Eq. 1.11) can be written in the well-known form:

$$\mathcal{L}_0 = \frac{n_b f_r N_{b+} N_{b-}}{4\pi \sigma^*_{x\beta} \sigma^*_{y\beta}} \tag{1.19}$$

and the differential luminosity (Eq. 1.15) will be:

$$\Lambda_0(W) = \frac{\mathcal{L}_0}{\sqrt{2\pi}\sigma_W} \exp\left(-\frac{(W-2E_0)^2}{2\sigma_W^2}\right)\,, \tag{1.20}$$

with the CM energy spread σ_W already defined in Eq. 1.2.

In terms of monochromatization mode with a non-zero $D^*_{x,y}$ achieved for each of the two colliding beams, equal in amplitude and of opposite sign, we have:

$$D^*_{x+} = -D^*_{x-} = D^*_x\,, \quad D^*_{y+} = -D^*_{y-} = D^*_y\,. \tag{1.21}$$

If extending Eq. 1.19 to a general form:

$$\mathcal{L} = \frac{n_b f_r N_{b+} N_{b-}}{4\pi \sigma^*_x \sigma^*_y}\,, \tag{1.22}$$

with the increased transverse horizontal and vertical beam size at the IP:

$$\sigma^*_x = \sqrt{\beta^*_x \varepsilon_x + D^{*2}_x \sigma^2_\delta}\,, \quad \sigma^*_y = \sqrt{\beta^*_y \varepsilon_y + D^{*2}_y \sigma^2_\delta}\,, \tag{1.23}$$

the Eq. 1.11 and Eq. 1.15 become:

$$\mathcal{L} = \frac{\mathcal{L}_0}{\sqrt{1 + \sigma^2_\delta \left(\frac{D^{*2}_x}{\sigma^{*2}_{x\beta}} + \frac{D^{*2}_y}{\sigma^{*2}_{y\beta}}\right)}}\,, \tag{1.24}$$

and

$$\Lambda(W) = \Lambda_0(2E_0)\exp\left(-\frac{1}{2}\left(\frac{D_x^{*2}}{\sigma_{x\beta}^{*2}} + \frac{D_y^{*2}}{\sigma_{y\beta}^{*2}} + \frac{1}{\sigma_\delta^2}\right)\frac{(W-2E_0)^2}{(\sqrt{2}E_0)^2}\right) , \tag{1.25}$$

with $\mathcal{L}_0$ and Λ_0 corresponding to the Eq. 1.19 and Eq. 1.20. Evaluating Eq. 1.25 at the center of the distribution in CM energy $2E_0$, we have:

$$\Lambda(2E_0) = \Lambda_0(2E_0) , \tag{1.26}$$

with the CM energy spread of the monochromatization mode:

$$\sigma_W = \frac{\sqrt{2}E_0\sigma_\delta}{\sqrt{1+\sigma_\delta^2\left(\frac{D_x^{*2}}{\sigma_{x\beta}^{*2}} + \frac{D_y^{*2}}{\sigma_{y\beta}^{*2}}\right)}} . \tag{1.27}$$

Comparing Eq. 1.27 with its value Eq. 1.2 in the absence of horizontal or vertical dispersion at the IP, leads us to define the enhancement factor for the energy resolution:

$$\lambda = \frac{[\sigma_W]_{D_{x,y}^*=0}}{[\sigma_W]_{D_{x,y}^*\neq 0}} = \sqrt{1+\sigma_\delta^2\left(\frac{D_x^{*2}}{\sigma_{x\beta}^{*2}} + \frac{D_y^{*2}}{\sigma_{y\beta}^{*2}}\right)} , \tag{1.28}$$

so called "monochromatization factor." The luminosity loss is also determined by this factor λ according to Eq. 1.24.

In conclusion, the CM energy spread and luminosity of this monochromatization mode are both reduced by the monochromatization factor λ compared with the standard mode:

$$\sigma_W = \frac{\sqrt{2}E_0\sigma_\delta}{\lambda} , \quad \mathcal{L} = \frac{\mathcal{L}_0}{\lambda} . \tag{1.29}$$

This trade-off means that the development of a monochromatization scheme must consider the optimization of other collider parameters to mitigate the luminosity loss while introducing non-zero dispersion at the IP.

1.1.3 Application in low-energy e^+e^- circular colliders

The essential ideas and the basic theory of the monochromatization concept in e^+e^- circular colliders were proposed in 1975 by A. Renieri, aimed at improving the energy resolution of ADONE [5, 13]. Since then, a variety of monochromatization schemes using different techniques for generating the dispersion function at the IP, including electrostatic skew quadrupoles, Radio Frequency (RF) magnetic devices, dipole magnets with electrostatic separators, Superconducting RF Deflecting (SCRF-D) cavities, have been proposed in multiple e^+e^- circular colliders, mostly at low energies and in head-on collision configuration: VEPP-4 [12, 14], SPEAR [15], LEP [16–18], B-factory [19, 20] or Tau-Charm factories [21–26].

Electrostatic skew quadrupole

Monochromatization scheme was firstly applied for ADONE [5, 13], with two beams in a single ring. The D_y^* is generated by a tilted electrostatic skew quadrupole (ESQ) placed at a location where the D_x is not zero. Its sign depends on the electric charge of the deflected particle. The complete scheme uses two tilted electrostatic skew quadrupoles, placed symmetrically with respect to the IP, with a phase advance adapted to avoid the coupling of dispersion into the rest of the ring.

More details of this technique, an electric field is applied at a point where the vertical betatron phase advance relative to the IP $\psi_y = (2n+1)\pi/2$ (n is an integer), and where $D_x \neq 0$. The quadrupole electric field is given by:

$$E_y = G_x \; , \quad K = \frac{G}{B\rho} \; , \tag{1.30}$$

where K is the normalized strength and $B\rho$ is the magnetic rigidity of the particles. With the non-zero D_x at this point, particles with different energies will have a vertical deflection proportional to their energy deviation.

For implementing monochromatization in this scheme, we need the vertical betatron dimension and the vertical dispersion at the IP. The vertical dispersion at the IP can be calculated by considering that a tilted electrostatic skew quadrupole generates a vertical dispersion that begins with a slope:

$$D'_y = (Kl)D_x \; , \tag{1.31}$$

where (Kl) is the integrated normalized gradient of the tilted electrostatic skew quadrupole, l is the length of the quadrupole, and D_x^* is the horizontal dispersion at the quadrupole location.

The vertical dispersion at the IP is then:

$$D_y^* = D'_y \sqrt{\beta_y^* \beta_y} \sin \psi_y \; , \tag{1.32}$$

with β and β^* are the betatron functions in the quadrupole and at the IP, respectively. With $\psi_y = (2n+1)\pi/2$ this gives:

$$D_y^* = \pm D_y' \sqrt{\beta_y^* \beta_y} \, . \tag{1.33}$$

That is to say:

$$D_y^* = \pm \sqrt{\beta_y^* \beta_y} (Kl) D_x \, , \tag{1.34}$$

which corresponds to a coupling of the horizontal dispersion into the vertical plane.

In the same way, the coupling effect will influence the betatron motion around the chromatic orbit and will consequently result in a new distribution of horizontal and vertical emittances. An intuitive formulation has been proposed [9] for the new vertical betatron dimension thus created, which combines statistically at the IP the natural vertical betatron dimension with a term originating from the horizontal dimension at the location of the tilted electrostatic skew quadrupole and transferred into the vertical plane, just like the dispersion:

$$\sigma_{y\beta}^* = \sqrt{\sigma_{y\beta 0}^{*2} + \beta_y^* \beta_y (Kl)^2 \sigma_{x\beta}^2} \, , \tag{1.35}$$

where $\sigma_{y\beta 0}^*$ is the vertical betatron size at the IP in the absence of the tilted electrostatic skew quadrupole and $\sigma_{x\beta}$ is the horizontal betatron size at the point where the electrostatic skew quadrupole is placed. By introducing the previous formulas into the definition of the λ (Eq. 1.28), we obtain:

$$\lambda = \sqrt{1 + \frac{\sigma_\delta^2 D_x^2}{\sigma_{x\beta}^2} \left(\frac{1}{1 + \kappa/B} \right)} \, , \tag{1.36}$$

where $B = \beta_x \beta_y (Kl)^2$ and $\kappa = \varepsilon_x / \varepsilon_y$ is the coupling factor. If in Eq. 1.35 we consider that the natural vertical betatron beam size at the IP $\sigma_{y\beta 0}^{*2}$ is small compared to that induced by the coupling, we conclude that $\kappa/B \simeq 1$. Considering a ring with a betatron approximation, we have an extremely low λ of 1.22. It can be hoped to improve it by studying a particular insertion where the values of the functions β_x, β_y, D_x and β_x^* (β_x^* being imposed by other considerations) would be chosen to minimize the term κ/B and maximum the ratio $D_x/\sigma_{x\beta}$.

Further studies have been done at VEPP-4 [12, 14], also in the case of a single ring, to try to improve this type of monochromatization scheme. They use four judiciously positioned electrostatic skew quadrupoles relative to the IP, and two dipoles as shown in Fig. 1.3. The first turned electrostatic skew quadrupoles ESQ1 has a vertical betatron phase advance of $\pi/2$ relative to the IP and is placed in a location where $D_x = 0$. The second quadrupoles ESQ2 is at a point where $D_x \neq 0$. The phase advance between the two quadrupoles is π in both plane. The ESQ2 is used to couple horizontal dispersion into the vertical plane therefore generating the necessary vertical dispersion at the IP. The vertical dispersion thus introduced by ESQ2 on the axis is not affected by ESQ1. The role of ESQ1 is precisely to cancel the betatron coupling introduced by ESQ2 provided the condition:

$$(K_1 l_1) = -(K_2 l_2)\sqrt{\frac{\beta_{x1}\beta_{y1}}{\beta_{x2}\beta_{y2}}} \tag{1.37}$$

is satisfied, where index 1 and index 2 refers to ESQ1 and ESQ2, respectively.

In Fig. 1.3, one can also see that a dipole has been placed between ESQ1 and ESQ2 to ensure that $D_x = D'_x = 0$ at ESQ1, thus avoiding any new influence of D_x and D_y. The bottom of this figure also shows the vertical betatron oscillation induced by ESQ2 and compensated by ESQ1. This allows to keep $\sigma_{x\beta}$ small and allows for the possibility of a significant increase in λ.

To calculate the D^*_y, the same procedure is used as before. The turned electrostatic quadrupole ESQ2 generates D^*_y:

$$D^*_y = D'_y\sqrt{\beta^*_y\beta_y}\sin\psi_y \, . \tag{1.38}$$

The other important parameter for the calculation of λ is the vertical emittance ε_y, which defines the $\sigma^*_{y\beta}$ according to Eq. 1.13. If considering that the coupling is compensated, this emittance is entirely determined by the quantum excitation due to synchrotron radiation in the dipoles where $D_y \neq 0$. Assuming all the dipole featuring a bending radius ρ, the ε_y is approximately given by:

$$\varepsilon_y = \frac{aE_0^2 D_y^{*2}}{\rho\beta^*_y}\frac{l_n}{l_b} \, , \tag{1.39}$$

with $a = 1.4675 \times 10^{-6}\,\mathrm{m\,GeV^{-2}}$. l_b is the total orbit length of all dipoles in the ring and l_n is the the orbit length of dipoles with $D_y = 0$. Finally, the λ (Eq. 1.28) will be:

$$\lambda = \sqrt{1 + \frac{\rho\sigma_\delta^2}{aE_0^2}\frac{l_n}{l_b}} \, . \tag{1.40}$$

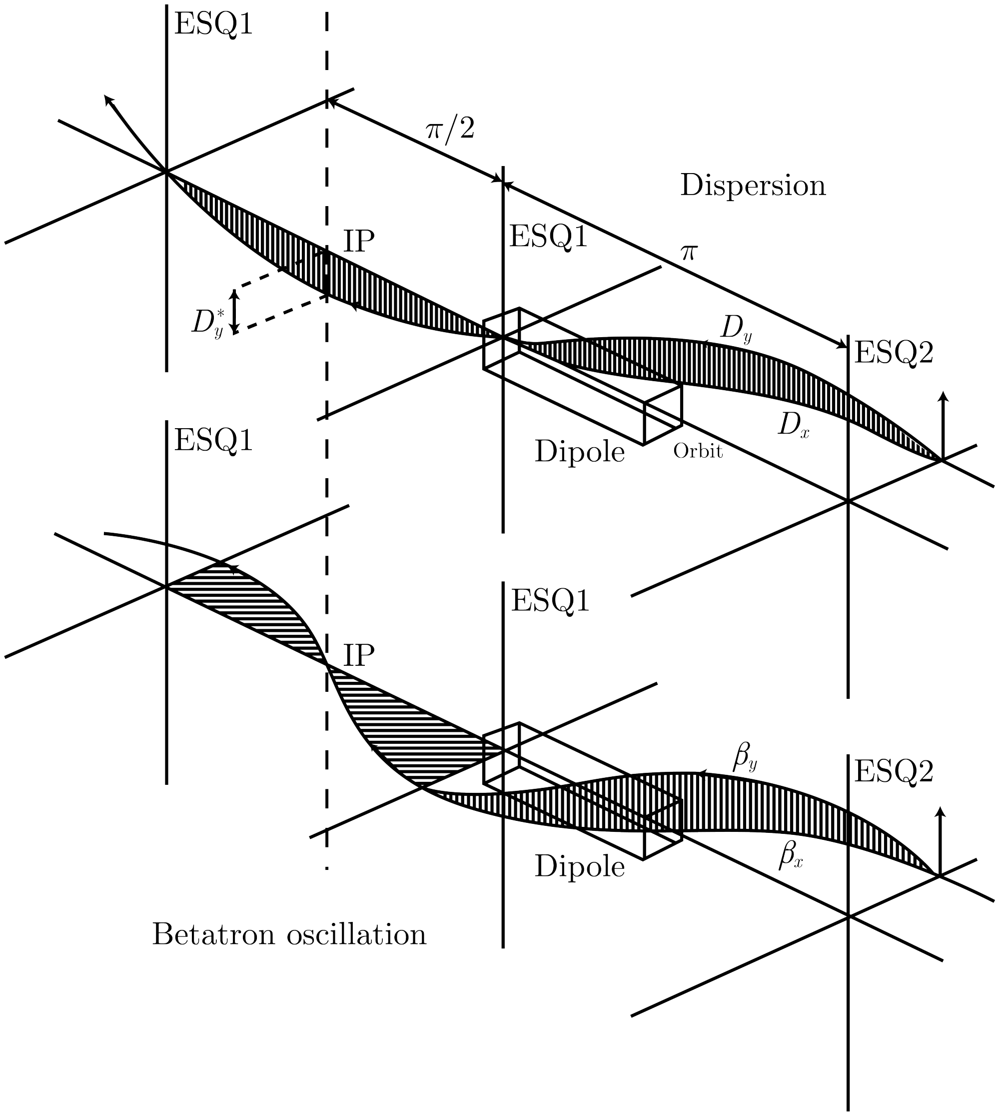

Fig. 1.3 Monochromatization optics scheme with ESQ.

Note that λ is independent of the beam energy, since $\sigma_\delta \propto E_0$ (Eq. 1.3), and independent of D_y and β_y^*. However, the turned electrostatic quadrupole must provide enough force so that $D_y^*\sigma_\delta$ is larger than the vertical betatron size due to residual coupling.

Taking these considerations into account, another two feasibility studies were carried for two different colliders. In the case of the SPEAR ring, Stanford [15], a detailed study of the most favorable optics led to a theoretical expectation of $\lambda \sim 8$. The implementation of such a scheme, rather difficult, has never been realized.

The case of the LEP at CERN presents better flexibility from the optical point of view. A modest $\lambda \sim 2-3$ has been calculated [16]. This work has been improved by using more precise calculations of the vertical emittance [17]. However, practical implementation was not been undertaken.

RF magnetic skew quadrupole

It is well known that the force of an electrostatic quadrupole is weaker than that of a magnetic quadrupole of the same length. A similar focusing effect can be produced by shorter magnetic quadrupoles, but the sign of the fields must change when particles of different charges pass through them.

To achieve this condition, it is preferable to have a large circumference machine, like LEP. One can then choose the frequency so that the fields oscillate in such a way as to have different signs during the passage of bunches. The choice of frequency f_1, for ESQ1 is made by considering the distance d_1, between the ESQ1s on each side of IP, knowing that during this distance the field must change sign and that the betatron phase advance between these two quadrupoles must be π. It is also necessary to take into account the number of equidistant bunches n_b, in each beam. The frequency f_1, and the distance d_1 must also satisfy:

$$f_1 = \frac{c}{2d_1} = n f_r n_b \,, \tag{1.41}$$

where c is the speed of light, n is an integer. A similar reasoning is valid for ESQ2.

The RF phases are such that all fields are null at the moment of collision and have their maximum when a bunch passes through the center of the quadrupole.

In the case of LEP, the RF frequencies for the magnetic quadrupoles would be of the order of 360 kHz and 180 kHz for ESQ1 and ESQ2, respectively. The possible magnetic field at these frequencies is around 500 Gs, for a pole face radius of 0.05 m, at an energy of 2.0 GeV, the normalized gradient K is $0.15\,\mathrm{m}^{-2}$, which is four times stronger that what can be hoped for with electrostatic quadrupoles. This feasibility study for LEP was not extended by a technical study of the components involved. It is recalled that the expected $\lambda \sim 3$ would lead to a total luminosity loss by the same factor [16, 17].

Vertical dipole magnets with electrostatic separators

In the 1980s, a type of e^+e^- collider known as particle factories, which operate at medium energy within the high-precision frontier, began to be studied and constructed. One can distinguish three very interesting energy ranges of these factories: $E_0 \simeq 1$ GeV (Φ-factory), $E_0 \simeq 3-5$ GeV (tau-charm factory [27, 28]) and $E_0 \simeq 10-13$ GeV (B-factory [29, 30]).

The implementation of monochromatization in these factories includes a double ring with head-on collisions and vertical separation scheme. In the case of tau-charm factories [21–23, 25, 26], the orbits of the electrons and positrons get some pre-separation in the horizontal plane. The electrostatic separator placed mirror symmetrically on each side of the IP are used for this purpose. This horizontal separation of the orbit makes it sufficient for the installation of two vertical bending magnets, which create horizontal magnetic field of opposite signs and tilt electrons and positrons in the vertical plane in opposite directions. As for the B-factory, it features two rings with different beam energies, thus inherently two different orbits. Therefore, the beams can be vertically separated owing to the different trajectories of the beams with different energies directly with separating magnets field without electrostatic separator [19, 20].The necessary D_y^*, required for the monochromatization scheme of these two kinds of factories, can be generated by a mismatch of the vertical dipole magnets. With this opposite signed non-zero D_y^* and zero D_x^*, the λ (Eq. 1.28) will be:

$$\lambda = \sqrt{1 + \frac{\sigma_\delta^2 D_y^{*2}}{\sigma_{y\beta}^{*2}}} \, . \tag{1.42}$$

The reduced CM energy spread and luminosity are already defined in Eq. 1.29.

To restore the luminosity loss, an essential horizontal compression is necessary, which mainly can be achieved by lowering the ε_x. However, the limitation of the beam-beam tune shift (impact of space charge) $\xi_{x,y}$ should be taken into account. For equal beam intensities (N_{b+}=N_{b-}=N_b), it will be described as:

$$\xi_{x,y} = \frac{N_b r_e}{2\pi\gamma(\sigma_x^* + \sigma_y^*)} \frac{\beta_{x,y}^*}{\sigma_{x,y}^*} \leq 0.04 \, , \tag{1.43}$$

where the r_e is the classical electron radius [7]. According to Eq. 1.22 and Eq. 1.43, the luminosity (Eq. 1.22) can be written as a function of beam-beam parameters (Eq. 1.43):

$$\mathcal{L} = \frac{I\gamma}{2er_e} \left(\frac{\xi_x}{\beta_x^*} + \frac{\xi_y}{\beta_y^*} \right) \, , \tag{1.44}$$

with the beam current I defined as $I = en_b f_r N_b$ and e is the elementary charge [31]. As the D_y^* increase the σ_y^* dominated by the relative beam energy spread (Eq. 1.23) and $D_y^* \sigma_\delta \gg \sqrt{\beta_y^* \varepsilon_y}$ due to the low β_y^*, we have:

$$\sigma_y^* = \sqrt{\beta_y^* \varepsilon_y + (D_y^* \sigma_\delta)^2} \simeq D_y^* \sigma_\delta \, . \tag{1.45}$$

Then, we can deduce from Eq. 1.43 that the second term ξ_y/β_y^* will not be predominant any more, that leads to the reduction in the luminosity. This reduction can be compensated by increasing the first term ξ_x/β_x^*. The increase can be implemented through the reduction of β_x^*. For practical reasons, a small β_x^* implies a larger β_y^*, which can be only implemented for round beams. From Ref. [32] we know that a flat beam case is more relaxed since the gradients of low-β quadrupoles are smaller; the limiting acceptance, much higher than the case of a round beam, will occur in the vertical plane but it will lead to a stored current well beyond realistic ones. This inversion is only valid if we keep $\xi_x = \xi_{max} \simeq 0.04$, and that implies a drastic reduction of the ε_x ($\sigma_x^* \ll \sigma_y^*$). Under these conditions the luminosity will be given by:

$$\mathcal{L} \simeq \frac{I\gamma}{2er_e}\frac{\xi_x}{\beta_x^*} , \tag{1.46}$$

and the luminosity will be constant while introducing the non-zero λ. According to the beam-beam studies using finite dispersion at the IP [33], we have a condition on the vertical beam-beam parameter $\xi_y \leq 0.04$, which implies $\xi_y \leq \xi_x$. As we have:

$$\frac{\xi_y}{\xi_x} = \frac{2\pi\gamma}{N_b r_e}\varepsilon_x\xi_x\frac{\beta_y^*}{\beta_x^*}\left(1+\frac{\sigma_x^*}{\sigma_y^*}\right) \tag{1.47}$$

according to Eq. 1.43, the limitation of the necessary ε_x will be determined by:

$$\frac{2\pi\gamma}{N_b r_e}\varepsilon_x\xi_x\frac{\beta_y^*}{\beta_x^*} \leq 1 , \tag{1.48}$$

which can be achieved by designing a low-emittance arc [23, 25].

Superconducting RF deflecting cavity

We have seen in the previous schemes that good monochromatization is possible but at the expense of luminosity. In 1986, a new monochromatization scheme appeared [34, 35] with RF deflecting cavities that theoretically increase luminosity while reducing energy deviation. The principle of RF monochromatization consists of installing an accelerating RF cavity in a straight section on each side of the IP, as shown in Fig. 1.4.

The distance between the centers of these cavities is taken equal to $(n + 1/2)\lambda_0$, where n is an integer and λ_0 is the RF wavelength. At the intervals occupied by the resonators, a large horizontal decomposition of the beam, relative to its energy, is created due to a special lattice. It is required here that the synchrotron beam size $\sigma_{x\delta}$ should be significantly larger than the betatron beam size $\sigma_{x\beta}$. Then, the non-equilibrium particles with relative energy deviation δ (Eq. 1.8), will have an orbit deviation in the

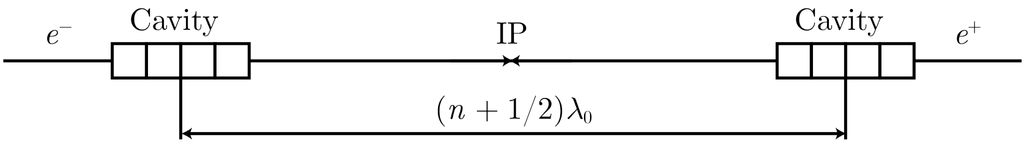

Fig. 1.4 Schematic view of the two RF deflecting cavities.

accelerating cavity given by $x = D_x\delta$, where D_x is the horizontal dispersion function. If the mode of the electromagnetic field excited in the cavity is such that the longitudinal component of the electric field E_s is proportional to x, one can get a situation when the energy gain of the particles in the superconducting accelerating RF structure, is exactly opposite to their energy deviation from the equilibrium one. In this case, the necessary conditions for monochromatization are met. After passing through the first cavity, either e^- or e^+, compensated in energy, when passing through the second cavity after the collision, the energies are brought back to their initial values. This latter condition is met if the distance between the cavities is an integer number of horizontal betatron wavelengths. This scheme also plans that the relative blowup of the transverse horizontal beam size, due to the dispersion in the cavities, is transferred to the IP. This allows considering an increase of the beam current and hence in the luminosity. The functioning of the entire system requires relatively significant field values, thus the interest in using superconducting cavities to limit the corresponding RF power.

Residual local chromaticity

Another interesting alternative approach to monochromatization is operating with a residual nonzero local vertical chromaticity (RLC) [36, 37]. This enables the focal length of the final quadrupoles to change with the momentum deviation of a beam particle and establishes a dependence between the vertical beam size waist and momentum offset, as illustrated in Fig. 1.5. In this way, waist location for beam 1 particles with a momentum offset δ, can be made to coincide with the waist location for beam 2 particles with a momentum offset $-\delta$, leading to an effective monochromatization, without adding any new hardware. The resulting monochromatization factor will be enhanced for smaller β_y^*. The latter is more easily reached with a larger β_x^*, that would also help suppress beamstrahlung and increase the longitudinal overlap region of the two colliding beams (limited by the crossing angle).

In summary of this part, while monochromatization is conceptually straightforward, it has never been thoroughly investigated to the point of implementation in a e^+e^-

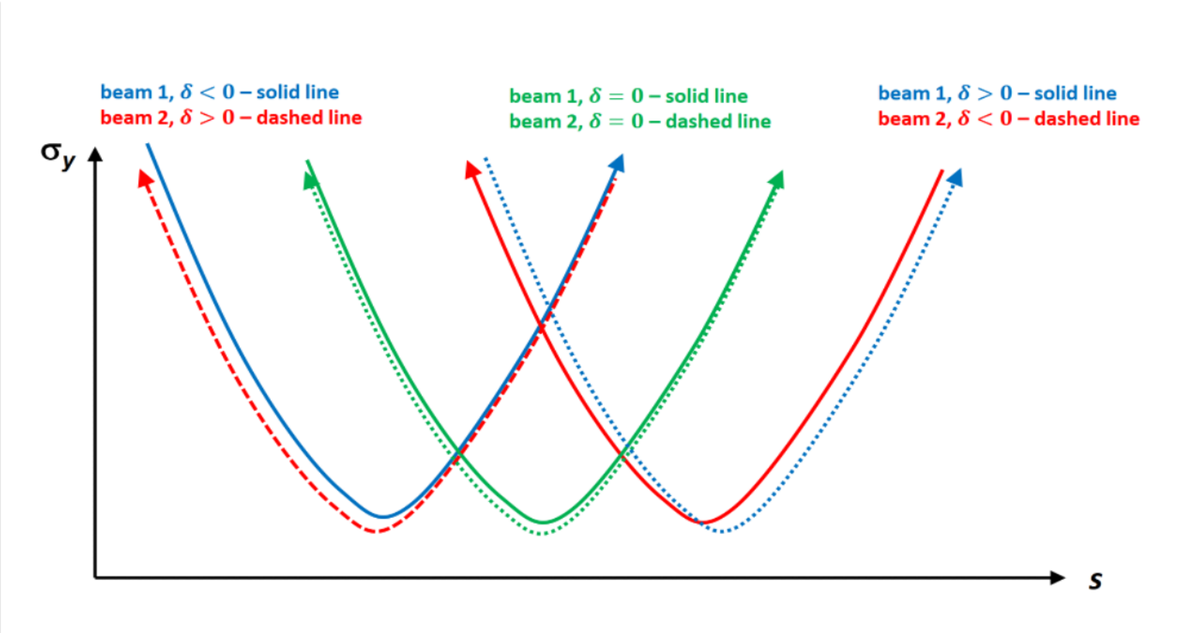

Fig. 1.5 Monochromatization with residual non-zero local chromaticity (RLC) at the IP [36].

collider for experimental validation. Impediments to implementation of various proposals included: insufficient studies and uncertainty of performance; the cost and effort of hardware implementation; shifting perceptions of the physics interest that resulted in gains at the operating energies of previous colliders.

1.1.4 Extended formulas for crossing-angle collisions

The new generation of e^+e^- circular colliders (DAΦNE [38–40], SuperKEKB [38, 41], c-τ [42], FCC-ee [1], CEPC [43]) utilize the so-called "crab-waist" collision scheme [39, 44]. In this scheme, the beams collide at a horizontal crossing angle $\theta_c \gg \sigma_x^*/\sigma_z$, where σ_z is the bunch length (Eq. A.17). When the luminosity is limited by the tune shift, characterized by ξ_y, the crab-waist collision scheme allows much higher luminosity to be reached compared to head-on collisions. For the same beam current, the maximum luminosity for head-on collisions $\mathcal{L} \propto 1/\sigma_z$, while for collisions with a angle $\mathcal{L} \propto 1/\beta_y^*$, where the β_y^* can be $20-30$ times smaller that σ_z. As a result, the luminosity can be higher by the same beam parameters.

Recent studies have revisited and extended the concept of monochromatization in the context of e^+e^- circular colliders in crossing-angle collision configuration [45–55]. The implementation of monochromatization in head-on collisions, as discussed in Subsec. 1.1.1, can be achieved by introducing non-zero horizontal or vertical IP dispersion

$D^*_{x,y}$. This approach can be extended to cases with a crossing angle θ_c. Compared to the head-on collision scenario shown in Fig. 1.2, a non-zero θ_c decreases efficiency of monochromatization due to the correlation between the collision energy and longitudinal position, as schematically depicted in Fig. 1.6, but it remains feasible since particles with energy deviations still encounter a higher density of the particles with opposite energy deviations.

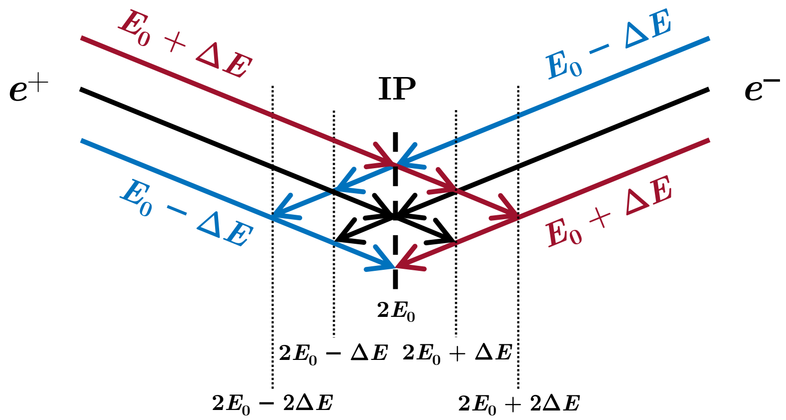

Fig. 1.6 Crossing-angle collision scheme with monochromatization.

In such a collision configuration, the CM energy W depends on both the energy of the colliding beams E_0 and their full crossing angle θ_c (depicted in Fig. 1.7). The W of head-on collisions without monochromatization (Eq. 1.9) and with monochromatization (Eq. 1.10) are respectively extended to the case of crossing-angle collisions as:

$$W = \sqrt{2}\,(E_0 + \Delta E)\,\sqrt{1+\cos\theta_c} \tag{1.49}$$

and

$$W = \sqrt{2}\left(E_0 + \mathcal{O}\left(\Delta E^2\right)\right)\sqrt{1+\cos\theta_c}\,. \tag{1.50}$$

To quantitatively describe the luminosity and CM energy under this new condition, it is necessary to revisit and extend the definition of luminosity (Eq. 1.11) and differential luminosity (Eq. 1.15) by incorporating two additional integrals in longitudinal plane, the longitudinal spatial coordinate s and the time t:

$$\mathcal{L} = n_b f_r \int f_+\left(x_+, y_+, s_+, t, \delta_+\right) f_-\left(x_-, y_-, s_-, t, \delta_-\right)\, dx\, dy\, ds\, dct\, d\delta_+\, d\delta_- \tag{1.51}$$

and

$$\begin{aligned}\Lambda(W) = n_b f_r \int & f_+(x_+, y_+, s_+, t, \delta_-) f_-(x_-, y_-, s_-, t, \delta_+) \\ & \delta\left(W - \sqrt{2}E_0\sqrt{1+\cos\theta_c}\sqrt{(1+\delta_+)}\sqrt{(1+\delta_-)}\right) dx\, dy\, ds\, dct\, d\delta_+\, d\delta_- \ ,\end{aligned} \tag{1.52}$$

where c is the speed of light and the density functions of the positrons and electrons $f_\pm$ (Eq. 1.12) are extended to:

$$\begin{aligned}f_\pm(x_\pm, y_\pm, s_\pm, t, \delta_\pm) = & \frac{N_{b\pm}}{(2\pi)^{4/2}\sigma^*_{x\beta}\sigma^*_{y\beta}\sigma_\delta} \exp\left[-\frac{\left(x_\pm \pm D^*_{x\pm}\delta_\pm\right)^2}{2\sigma^{*2}_{x\beta}}\right. \\ & \left. -\frac{\left(y_\pm + D^*_{y\pm}\delta_\pm\right)^2}{2\sigma^{*2}_{y\beta}} - \frac{(s_\pm - ct)^2}{2\sigma_z^2} - \frac{\delta_\pm^2}{2\sigma_\delta^2}\right] \ .\end{aligned} \tag{1.53}$$

Assuming that the positrons move along the positive s direction and the electrons in the opposite direction as depicted in Fig. 1.7, the coordinates $x_\pm$, $y_\pm$, and $s_\pm$ in the two beam frames are transformed from coordinates x, y, and s in the laboratory frame with the following expressions [56, 57]:

$$\begin{aligned}x_\pm &= \pm x\cos(\theta_c/2) - s\sin(\theta_c/2) \\ y_\pm &= y \\ s_\pm &= \pm s\cos(\theta_c/2) + x\sin(\theta_c/2) \ .\end{aligned} \tag{1.54}$$

Neglecting the hourglass effect (described in Subsec. 1.1.5), the luminosity and CM energy spread in absence of IP dispersion ($D_{x,y} = 0$) are then given by [48, 56–58]:

$$\mathcal{L}_0 = \frac{n_b f_r N_{b+} N_{b-}}{4\pi\sigma^*_{x\beta}\sigma^*_{y\beta}\sqrt{1+\varphi^2}} \tag{1.55}$$

and

$$\sigma_W = \sqrt{2}E_0\sqrt{\left(\sigma_\delta\cos(\theta_c/2)\right)^2 + \left(\sigma^*_{x'}\sin(\theta_c/2)\right)^2} \tag{1.56}$$

with φ the Piwinski angle [59]:

$$\varphi = \frac{\sigma_z}{\sigma^*_x}\tan(\theta_c/2) \tag{1.57}$$

and $\sigma^*_{x'} = \sqrt{\varepsilon_x/\beta^*_x}$ the beam angular spread at the IP in horizontal plane.

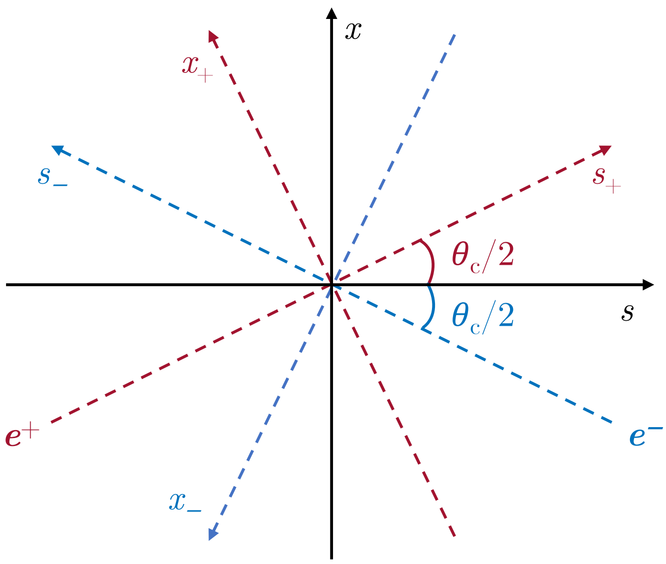

Fig. 1.7 Coordinate transformation under crossing-angle collision configuration [56].

With non-zero $D^*_{x,y}$, the luminosity (Eq. 1.22) is extended to:

$$\mathcal{L} = \frac{n_b f_r N_{b+} N_{b-}}{4\pi\sigma_x^*\sigma_y^*\sqrt{1+\varphi^2}}\,, \tag{1.58}$$

whose loss still follows the previous established relationship described in Eq. 1.29 with the extended λ defined as [48]:

$$\lambda = \sqrt{1+\sigma_\delta^2\left(\frac{D_x^{*2}}{\sigma_{x\beta}^{*2}(1+\varphi^2)}+\frac{D_y^{*2}}{\sigma_{y\beta}^{*2}}\right)}\,, \tag{1.59}$$

and the reduced CM energy spread is defined as:

$$\sigma_W = \sqrt{2}E_0\sqrt{\left(\frac{\sigma_\delta\cos(\theta_c/2)}{\lambda}\right)^2+(\sigma_{x'}^*\sin(\theta_c/2))^2}\,. \tag{1.60}$$

The beam-beam parameters $\xi_{x,y}$ (Eq. 1.43) are also supposed to be corrected by replacing the transverse IP beam size σ_x^* in the crossing plane with the effective beam size $\sqrt{\sigma_x^{*2} + \sigma_z^2(\tan(\theta_c/2))^2}$ [57, 58]:

$$\begin{aligned}\xi_x &= \frac{N_b r_e}{2\pi\gamma(\sigma_x^*\sqrt{1+\varphi^2}+\sigma_y^*)}\frac{\beta_x^*}{\sigma_x^*\sqrt{1+\varphi^2}}\\ \xi_y &= \frac{N_b r_e}{2\pi\gamma(\sigma_x^*\sqrt{1+\varphi^2}+\sigma_y^*)}\frac{\beta_y^*}{\sigma_y^*}\ .\end{aligned} \tag{1.61}$$

Combined with Eq. 1.55, we note that the collisions with a crossing angle allows more bunch population N_b thus higher luminosity under the limitation of the beam-beam tune shift, compared to head-on collisions.

1.1.5 Hourglass effect

The hourglass effect is a phenomenon in colliders where the luminosity is reduced due to a mismatch between the bunch length σ_z and the focal region near the IP. This effect occurs because only a portion of the particles within the bunch can be focused to the minimum transverse beam size at the IP, while others experience an increase in transverse beam size due to their position along the bunch.

In a collider, the betatron function $\beta_{x,y}(s)$ from the IP to the first final focus quadrupole varies with the distance s along the beam's trajectory and can be expressed as [8]:

$$\beta_{x,y}(s) = \beta_{x,y}^* + \frac{s^2}{\beta_{x,y}^*}\ , \tag{1.62}$$

where $\beta_{x,y}^*$ is the betatron function at the IP. The betatron transverse beam size $\sigma_{x\beta,y\beta}(s)$ at the position s is then given by:

$$\sigma_{x\beta,y\beta}(s) = \sqrt{\varepsilon_{x,y}\beta_{x,y}(s)} = \sigma_{x\beta,y\beta}^*\sqrt{1+\frac{s^2}{\beta_{x,y}^{*2}}} \tag{1.63}$$

with $\varepsilon_{x,y}$ the emittance. As s increases, $\sigma_{x\beta,y\beta}(s)$ grows rapidly, indicating that particles further from the IP cannot maintain the minimum transverse beam size. A smaller $\beta_{x,y}^*$ results in a more rapid increase in $\sigma_{x\beta,y\beta}(s)$, causing particles along the bunch to experience a greater increase in transverse beam size. Additionally, a larger σ_z implies that more particles are distributed over a longer longitudinal range, leading to a significant portion of the bunch experiencing this increase in transverse beam size. Therefore, the significance of the hourglass effect in a collider can be assessed by the ratio of $\beta_{x,y}^*$ to σ_z. The effect becomes more severe when this ratio is too small, indicating that $\beta_{x,y}^*$ is too short compared to σ_z.

A quantitative description of the hourglass effect has been explored in the context of the monochromatization scheme ($D_{x,y} \neq 0$) and crossing-angle collision configuration [48]. When defining the bunch density (Eq. 1.53) in Subsec. 1.1.4, we neglect the dependence of the betatron functions on the longitudinal position s (Eq. 1.62). This approximation is valid for the horizontal plane under the assumption of a vertical flat beam ($\sigma^*_{y\beta} \ll \sigma^*_{x\beta}$, $\varepsilon_y \ll \varepsilon_x$, and $\beta^*_y \ll \beta^*_x$), as $\beta_x(s)$ changes little along s within the bunch. However, for the vertical plane, it is necessary to extend the $\sigma^*_{y\beta}$ term in Eq. 1.53 to account for its s-dependence:

$$\sigma_{y\beta\pm}(s) = \sigma^*_{y\beta}\sqrt{1 + \frac{[\pm s\cos(\theta_c/2) + x\sin(\theta_c/2)]^2}{\beta^{*2}_y}} \tag{1.64}$$

by transforming the beam frame coordinate s in Eq. 1.63 to the laboratory frame using Eq. 1.54. Assuming that $\sigma_z\cos(\theta_c/2) \gg \sigma_x\sin(\theta_c/2)$ around the IP ($\theta_c \sim$ mrad), we can neglect the $x\sin(\theta_c/2)$ term in Eq. 1.64, and extend the luminosity (Eq. 1.58) to:

$$\begin{aligned}\mathcal{L}_{\text{hg}} = n_b f_r \frac{N_{b+}N_{b-}}{4\pi\sigma^*_{x\beta}\sigma^*_{y\beta}}\frac{1}{\sqrt{\pi}} \times \int \frac{dr}{\sqrt{\left(1 + r^2\frac{\sigma_z^2}{\beta^{*2}_y}\right)\left(1 + \frac{D^{*2}_x\sigma_\delta^2}{\sigma^{*2}_{x\beta}}\right) + \frac{D^{*2}_y\sigma_\delta^2}{\sigma^{*2}_{y\beta}}}} \\ \times \exp\left\{-r^2\left[(1 + \varphi^2 - \frac{D^{*2}_x\sigma_\delta^2\varphi^2(1 + r^2\frac{\sigma_z^2}{\beta^{*2}_y})}{\sigma^{*2}_{x\beta}\left[\left(1 + r^2\frac{\sigma_z^2}{\beta^{*2}_y}\right)\left(1 + \frac{D^{*2}_x\sigma_\delta^2}{\sigma^{*2}_{x\beta}}\right) + \frac{D^{*2}_y\sigma_\delta^2}{\sigma^{*2}_{y\beta}}\right]}\right]\right\}\end{aligned} \tag{1.65}$$

with $r = (s/\sigma_z)\cos(\theta_c/2)$ and φ the Piwinski angle (Eq. 1.57).

The obtained expression could be further calculated analytically for particular cases. In the case of $D^*_x \neq 0$ and $D^*_y = 0$, the luminosity is given by:

$$\begin{aligned}\mathcal{L}_{\text{hg1}} = n_b f_r \frac{N_{b+}N_{b-}}{4\pi\sigma^*_{x\beta}\sigma^*_{y\beta}}\frac{\beta^*_y}{\sqrt{\pi}\sigma_z} \times \frac{1}{\sqrt{1 + \frac{D^{*2}_x\sigma_\delta^2}{\sigma^{*2}_{x\beta}}}} \times \exp\left[\frac{\beta^{*2}_y}{2\sigma_z^2}\left(1 + \frac{\sigma^{*2}_{x\beta}\varphi^2}{\sigma^{*2}_{x\beta} + D^{*2}_x\sigma_\delta^2}\right)\right] \\ \times K_0\left[\frac{\beta^{*2}_y}{2\sigma_z^2}\left(1 + \frac{\sigma^{*2}_{x\beta}\varphi^2}{\sigma^{*2}_{x\beta} + D^{*2}_x\sigma_\delta^2}\right)\right],\end{aligned} \tag{1.66}$$

where $K_0(x)$ is modified Bessel function of the second kind or Macdonald function.

In the case of $D_x^* = 0$ and $D_y^* \neq 0$, the luminosity is given by:

$$\begin{aligned}\mathcal{L}_{\rm hg2} = n_b f_r \frac{N_{b+}N_{b-}}{4\pi\sigma_{x\beta}^*\sigma_{y\beta}^*}\frac{\beta_y^*}{\sqrt{\pi}\sigma_z} \times \exp\left[\frac{\beta_y^{*2}}{2\sigma_z^2}(1+\varphi^2)\left(1+\frac{D_y^{*2}\sigma_\delta^2}{\sigma_{y\beta}^{*2}}\right)\right] \\ \times K_0\left[\frac{\beta_y^{*2}}{2\sigma_z^2}(1+\varphi^2)\left(1+\frac{D_y^{*2}\sigma_\delta^2}{\sigma_{y\beta}^{*2}}\right)\right] .\end{aligned} \tag{1.67}$$

We introduce the hourglass reduction factor $R_{\rm hg}$ as shown in Fig. 1.8:

$$R_{\rm hg}(t_i) = \frac{\mathcal{L}_{{\rm hg}i}}{\mathcal{L}} , \tag{1.68}$$

where $\mathcal{L}_{{\rm hg}i}$ is luminosity for cases Eq. 1.66 and Eq. 1.67, and $\mathcal{L}$ is luminosity without hourglass effect (Eq. 1.58), and the corresponding t_i is defined as:

$$t_1 = \frac{\beta_y^{*2}}{2\sigma_z^2}\left(1+\frac{\sigma_{x\beta}^{*2}\varphi^2}{\sigma_{x\beta}^{*2}+D_x^{*2}\sigma_\delta^2}\right) , \tag{1.69}$$

$$t_2 = \frac{\beta_y^{*2}}{2\sigma_z^2}(1+\varphi^2)\left(1+\frac{D_y^{*2}\sigma_\delta^2}{\sigma_{y\beta}^{*2}}\right) . \tag{1.70}$$

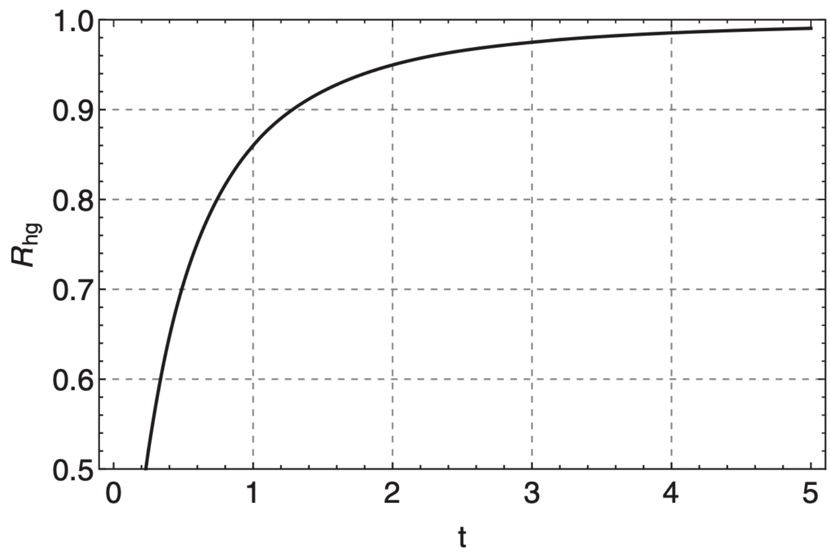

Fig. 1.8 Hourglass reduction factor [48].

1.1.6 Beamstrahlung in high-energy e^+e^- circular colliders

In existing low-energy e^+e^- circular colliders, the energy spread of the beams is mainly due to synchrotron radiation emitted when a charged ultra-relativistic particle passes through accelerator bending magnets (rings). In collider physics, the SR emitted due to the electromagnetic field of the opposing beam during collision, is known as "beamstrahlung" (BS). This beamstrahlung effect is negligible in the currently existing low-energy e^+e^- circular colliders. On the contrary, in future high-energy e^+e^- circular colliders, said effect will become of significant magnitude for the first time, contributing to the increase of relative beam energy spread σ_δ and impacting also emittances [53, 55]. Studies on the impact of beamstrahlung have recently been conducted under the conditions of FCC-ee, characterized by a vertical flat beam ($\sigma^*_{y\beta} \ll \sigma^*_{x\beta}$) [46, 47, 49–53].

The strength of beamstrahlung is characterized by the parameter Υ, defined as [60]:

$$\Upsilon = \frac{\gamma\left(|B| + |E|/c\right)}{B_c} = \frac{2}{3}\frac{\hbar\omega_c}{E_e} \tag{1.71}$$

with $B_c = m_e^2 c^2/(e\hbar) \approx 4.4\,\mathrm{GT}$ the Schwinger critical field, $\hbar\omega_c = (3/2)\hbar c\gamma^3/\rho$ the critical photon energy [61], E_e the electron (or positron) energy before radiation, $B(E)$ the local magnetic (electric) field of the opposing bunch, $\rho = e/(pB)$ the local bending radius, γ the relativistic Lorentz factor corresponding to E_e, $p \approx E_e/c$ the particle momentum. The higher the Υ, the more beamstrahlung photons with higher energies will be emitted. The average Υ during the collision is [61]:

$$\langle\Upsilon\rangle = \frac{r_e\gamma^2}{\alpha}\left\langle\frac{1}{\rho}\right\rangle_{x,y,z,s}, \tag{1.72}$$

where α represents the fine structure constant [7], and the average $\langle\rangle$ is taken over the transverse coordinates (x, y), longitudinal coordinate s (along the beam line), and $z = (s - ct)$ with t denoting the time. It should be noted that the local bending radius ρ depends on the transverse and longitudinal positions of the colliding particle, as well as on the time during the collision, or equivalently, with the coordinate z.

In context of the proposed high energy e^+e^- circular colliders like FCC-ee [1] and CEPC [43], $\langle\Upsilon\rangle \ll 1$. In this case, the average number of photons per collision n_γ can be approximated as:

$$n_\gamma \approx \frac{5}{2\sqrt{3}}\alpha\gamma\int ds\left\langle\frac{1}{\rho}\right\rangle_{x,y,z}, \tag{1.73}$$

where the integral over s extends through the collision region. The mean emission rate is given by n_γ divided by the average time interval between collisions. The average relative energy loss due to beamstrahlung (subscript "BS") is [61]:

$$\delta_{\mathrm{BS}} \approx \frac{2}{3} r_e \gamma^3 \int ds \left\langle \frac{1}{\rho^2} \right\rangle_{x,y,z} . \tag{1.74}$$

The average photon energy normalized to the beam energy $\langle u \rangle$, is obtained as the ratio $\delta_{\mathrm{BS}}/n_\gamma$. Therefore, the quantum excitation [61] from beamstrahlung emitted in a single collision is proportional to the average of the inverse third power of the local bending radius ρ, written as:

$$\{n_\gamma \langle u^2 \rangle\}_{\mathrm{BS}} \approx \frac{55}{24\sqrt{3}} \frac{r_e^2 \gamma^5}{\alpha} \int ds \left\langle \frac{1}{\rho^3} \right\rangle_{x,y,z} . \tag{1.75}$$

Balancing the sum of the excitation due to beamstrahlung and due to arc synchrotron radiation against the radiation damping from the arcs alone (the average energy loss and, hence, the damping effect due to beamstrahlung is negligible [46]) yields the total equilibrium emittances $\varepsilon_{x,y,\mathrm{tot}}$ as:

$$\varepsilon_{x,y,\mathrm{tot}} = \varepsilon_{x,y,\mathrm{SR}} + \frac{n_{\mathrm{IP}} \tau_{x,y,\mathrm{SR}}}{4T_{\mathrm{rev}}} \{n_\gamma \langle u^2 \rangle\}_{\mathrm{BS}} \mathcal{H}^*_{x,y} , \tag{1.76}$$

and the total relative beam energy spread $\sigma_{\delta,\mathrm{tot}}$ as:

$$\sigma^2_{\delta,\mathrm{tot}} = \sigma^2_{\delta,\mathrm{SR}} + \frac{n_{\mathrm{IP}} \tau_{E,\mathrm{SR}}}{4T_{\mathrm{rev}}} \{n_\gamma \langle u^2 \rangle\}_{\mathrm{BS}} , \tag{1.77}$$

where τ_x, τ_y, and τ_E denote the usual horizontal, vertical, and longitudinal radiation damping times [61], respectively, T_{rev} the revolution period (Eq. A.12) and n_{IP} the number of IP. The terms with subindex "SR" refer to the standard equilibrium parameters without beamstrahlung. The IP dispersion invariant $\mathcal{H}^*_{x,y}$ is defined as [61]:

$$\mathcal{H}^*_{x,y} = \frac{\left(\beta^*_{x,y} D'^*_{x,y} + \alpha^*_{x,y} D^*_{x,y}\right)^2 + \left(D^*_{x,y}\right)^2}{\beta^*_{x,y}} , \tag{1.78}$$

where $\beta^*_{x,y}$, $\alpha^*_{x,y}$, $D^*_{x,y}$, and $D'^*_{x,y}$ are optical beta and alpha function (Twiss parameters), the dispersion, and slope of the dispersion at the IP, respectively. In Eq. 1.76 and Eq. 1.77, possible correlations between a particle's transverse or longitudinal amplitudes is ignored and the field it experiences in successive collisions during τ_{SR}.

With the approximation of vertical flat beam ($\sigma^*_{y\beta} \ll \sigma^*_{x\beta}$) and negligible hourglass effect (described in Sucsec. 1.1.5) in the expression of $1/\rho$, the integrals in Eq. 1.75 for head-on collisions without a crossing angle is approximated as [52, 53]:

$$\int ds \left\langle \frac{1}{\rho^3} \right\rangle_{x,y,z} \approx \frac{1}{\sqrt{2\pi}^3} \frac{1}{\sigma^2_{z,\mathrm{tot}}} \left(\frac{2N_b r_e}{\gamma \sigma^*_{x,\mathrm{tot}}} \sqrt{\frac{2}{\pi}} \right)^3 \times 0.7183 \,. \tag{1.79}$$

In presence of crossing-angle collisions, the Piwinski angle φ (Eq. 1.57) is introduced to the approximation [52, 53]:

$$\int ds \left\langle \frac{1}{\rho^3} \right\rangle_{x,y,z} \approx \frac{1}{\sqrt{2\pi}^3} \frac{1}{\sigma^2_{z,\mathrm{tot}}} \left(\frac{2N_b r_e}{\gamma \sigma^*_{x,\mathrm{tot}}} \sqrt{\frac{2}{\pi}} \right)^3 \times \frac{0.77562}{\varphi} \,. \tag{1.80}$$

The total horizontal beam size $\sigma^*_{x,\mathrm{tot}}$ is determined by the $\varepsilon_{x,\mathrm{tot}}$ and $\sigma_{\delta,\mathrm{tot}}$:

$$\sigma^*_{x,\mathrm{tot}} = \sqrt{\beta^*_x \varepsilon_{x,\mathrm{tot}} + D^{*2}_x \sigma^2_{\delta,\mathrm{tot}}} \,, \tag{1.81}$$

and the total bunch length $\sigma_{z,\mathrm{tot}}$ is related to the $\sigma_{\delta,\mathrm{tot}}$ through the classical relation [61]:

$$\sigma_{z,\mathrm{tot}} = \frac{\alpha_{\mathrm{C}} C}{2\pi Q_s} \sigma_{\delta,\mathrm{tot}} \tag{1.82}$$

with α_{C} the momentum compaction factor (Eq. A.18) [8], C the collider circumference and Q_s the synchrotron tune (Eq. A.19) [8].

Introducing a coefficient V as:

$$V = \frac{n_{\mathrm{IP}} \tau_{E,\mathrm{SR}}}{4 T_{\mathrm{rev}}} \{ n_\gamma \langle u^2 \rangle \}_{\mathrm{BS}} \sigma^2_{\delta,\mathrm{tot}} \sigma^{*3}_{x,\mathrm{tot}} \,, \tag{1.83}$$

and assuming a planar designed orbit ($\tau_{x,y} = 2\tau_E$), the Eq. 1.76 and Eq. 1.77 can be respectively re-written in self-consistency condition [53]:

$$\varepsilon_{x,y,\mathrm{tot}} = \varepsilon_{x,y,\mathrm{SR}} + \frac{2V\mathcal{H}^*_{x,y}}{\sigma^2_{\delta,\mathrm{tot}} \sigma^{*3}_{x,\mathrm{tot}}} \tag{1.84}$$

and

$$\sigma^2_{\delta,\mathrm{tot}} = \sigma^2_{\delta,\mathrm{SR}} + \frac{V}{\sigma^2_{\delta,\mathrm{tot}} \sigma^{*3}_{x,\mathrm{tot}}} \,. \tag{1.85}$$

Inserting the expression $\{n_\gamma\langle u^2\rangle\}_{\mathrm{BS}}$ from Eq. 1.75, we obtain:

$$V = \frac{55}{24\sqrt{3}} \frac{r_e^2\gamma^5}{\alpha} \frac{n_{\mathrm{IP}}\tau_{E,\mathrm{SR}}}{4T_{\mathrm{rev}}} \sigma_{\delta,\mathrm{tot}}^2 \sigma_{x,\mathrm{tot}}^{*3} \int ds \left\langle \frac{1}{\rho^3} \right\rangle_{x,y,z} . \tag{1.86}$$

Using the approximation of Eq. 1.79 for head-on collisions and Eq. 1.80 for crossing-angle collisions, the coefficient V for these two conditions are respectively approximated to:

$$V \approx \frac{55\pi^2}{3\sqrt{3}} \left(\sqrt{\frac{2}{\pi}}\right)^3 \frac{n_{\mathrm{IP}}\tau_{E,\mathrm{SR}} Q_s^2 r_e^5 \gamma^2 N_b^3}{T_{\mathrm{rev}}\alpha_{\mathrm{C}}^2 C^2 \alpha} \times 0.7183 \tag{1.87}$$

and

$$V \approx \frac{55\pi^2}{3\sqrt{3}} \left(\sqrt{\frac{2}{\pi}}\right)^3 \frac{n_{\mathrm{IP}}\tau_{E,\mathrm{SR}} Q_s^2 r_e^5 \gamma^2 N_b^3}{T_{\mathrm{rev}}\alpha_{\mathrm{C}}^2 C^2 \alpha} \times \frac{0.77562}{\varphi} . \tag{1.88}$$

Note that $\sigma_{\delta,\mathrm{tot}}$ and $\varepsilon_{x,y,\mathrm{tot}}$ are in self-consistency condition and are coupled. Thus, Eq. 1.85 and Eq. 1.84 should be solved together for the $\sigma_{\delta,\mathrm{tot}}$ and $\varepsilon_{x,y,\mathrm{tot}}$. Then the $\sigma_{z,\mathrm{tot}}$ follows from Eq. 1.82.

To preliminary evaluate the beamstrahlung impact on the FCC-ee, the provided equations are solved using the FCC-ee CDR parameters [52, 53]. For the standard modes without monochromatization ($D^*_{x,y} = 0$), the $\mathcal{H}^*_{x,y}$ in Eq. 1.84 equals to zero with zero $D'^*_{x,y}$ and $\alpha^*_{x,y}$ in FCC-ee lattice design. So the beamstrahlung effect excites the beam particles only longitudinally (no impact on emittance), and the indicated values of $\sigma_{\delta,\mathrm{tot}}$ are derived from Eq. 1.85 at a beam energy of 62.5 GeV. In scaled monochromatization scenarios with $D^*_x \neq 0$, the $\sigma_{\delta,\mathrm{tot}}$ and $\varepsilon_{x,\mathrm{tot}}$ are calculated using Eq. 1.85 and Eq. 1.84 together with $\mathcal{H}^*_x = D^{*2}_x/\beta^*_x$. The $\sigma_{z,\mathrm{tot}}$ for all cases is determined by Eq. 1.82. The results clearly demonstrate that beamstrahlung significantly impacts such a high-energy e^+e^- collider. It's worth mentioning that, while a non-zero D^*_x increases the emittance to some extent, it mitigates the blow-up of $\sigma_{\delta,\mathrm{tot}}$. This observation motivates the introduction of dispersion in horizontal plane when implementing monochromatization in FCC-ee.

Additionally, the impact of beamstrahlung is primarily defined by parameters in the horizontal plane, under the condition that $\sigma^*_{y\beta} \ll \sigma^*_{x\beta}$. This scenario remains valid even when a small D^*_y is introduced, as will be discussed in Chapter 4 and Chapter 5. Therefore, the same equation can be used to preliminary estimate the beamstrahlung impact in presence of a non-zero D^*_y. With $\mathcal{H}^*_y = D^{*2}_y/\beta^*_y$, the vertical emittance blow-up will be defined by Eq. 1.84.

1.2 Monochromatization at FCC-ee

With a target of measuring the electron Yukawa coupling via direct s-channel Higgs production at 125 GeV CM energy, the monochromatization technique was proposed to be implemented at FCC-ee [45]. Preliminary parametric studies and physics performance evaluations have been made under the framework of the Future Circular Collider Feasibility Study (FCC FS) before the monochromatization optics design [47, 49, 51, 53, 55].

1.2.1 Direct s-channel Higgs production at FCC-ee

After the discovery of the Higgs boson [62, 63], specific questions about its nature remain unresolved. For instance, researchers are still debating whether the Higgs boson is an elementary particle or a composite state made up of confined unknown particles. Additionally, there is ongoing discussion about whether the mass of the Higgs boson can be calculated within a theoretical framework or if it is merely an arbitrary parameter within the model. Another significant question pertains to the early Universe: "what was the nature of the phase transition that led to the electroweak symmetry breaking?" Precision measurements of the Higgs boson's properties and electroweak interactions above the weak scale are required for addressing these questions.

The FCC-ee will collide e^+e^- pairs at several CM energies $\sqrt{s}$. A large number of Z^0 bosons, $\mathrm{W}^\pm$ pairs, and top quarks t would be produced, whose clean environment would allow a high-precision measurement. Higgs bosons (through *Higgsstrahlung* [64]) would be produced (at least) involving two processes: decay through Z bosons as $e^+e^- \to \mathrm{Z}^0\mathrm{H}$ (at $\sqrt{s} = 240\,\mathrm{GeV}$) and through W-boson fusion as $e^+e^- \to \mathrm{H}\nu\bar{\nu}$ (at $\sqrt{s} = 365\,\mathrm{GeV}$).

A third possible production mode of Higgs bosons at FCC-ee is direct s-channel Higgs production. This proposed collision mode offers a unique opportunity to measure the electron Yukawa coupling, by directly producing the Higgs boson resonantly at the s-channel as $e^+e^- \to \mathrm{H}$ at CM energy $\sqrt{s} = m_\mathrm{H}$ ($\sim 125\,\mathrm{GeV}$). This is the only known path to measure the Higgs Yukawa coupling to first generation leptons (u and d quarks, and electron), which presents significant experimental challenges due to their low masses and consequently small Yukawa couplings to the Higgs field.

The Yukawa coupling of the electron, $y_e = \sqrt{2}m_e/v$ (with the electron rest mass energy $m_e = 0.511 \times 10^{-3}\,\mathrm{GeV}$ and the Higgs field vacuum expectation value $v = (\sqrt{2}G_F)^{-1/2} = 246.22\,\mathrm{GeV}$), is virtually impossible to measure at hadron colliders because the $\mathrm{H} \to e^+e^-$ decay has a tiny branching fraction of $\mathcal{B}\,(\mathrm{H} \to e^+e^-) = 5.22 \times 10^{-9}$ and it is completely swamped by the Drell-Yan dielectron continuum with many orders of magnitude larger cross section. The possibility of studying resonant Higgs production at leptons colliders has been explored in the literature [65], particularly for $\mu^+\mu^-$ annihilation at a CM energy $\sqrt{s} = m_{\rm H}$, notably as a promising method to directly and precisely measure Higgs boson mass $m_{\rm H}$, width $\Gamma_{\rm H}$, and the muon Yukawa coupling, by exploiting a large peak production cross section of $\sigma_{\mu\mu\to{\rm H}} = 70\,\text{pb}$. The same measurement at an e^+e^- collider had never been seriously considered given the sub-femtobarn cross section for the $e^+e^- \to {\rm H}$ process, suppressed by at least a factor m_e^2/m_μ^2 compared to the muon collider case. Notwithstanding this difficulty, when the FCC-ee was first proposed [66], it was noticed that an unparalleled integrated luminosity $\mathcal{L}_{\rm int}$ of about $10\,\text{ab}^{-1}$ per year, available at $\sqrt{s} = 125\,\text{GeV}$, could enable an attempt to observe the resonant s-channel production of the scalar boson, namely the reaction $e^+e^- \to {\rm H}$ at the Higgs pole [67–69]. This motivation led to subsequent theoretical [2, 70–72] and accelerator [45–55] studies of the $e^+e^- \to {\rm H}$ process.

From the accelerator perspective, such a measurement is more easily feasible if the CM energy spread $\delta_{\sqrt{s}}$ of e^+e^- collisions, can be reduced to a level comparable to the natural width of the SM Higgs boson $\Gamma_{\rm H} = 4.1\,\text{MeV}$ [1–4]. However, in a conventional collision scheme, the natural CM energy spread at 125 GeV, due only to synchrotron radiation, is about 50 MeV. Its reduction to the desired level could be achieved by exploiting the monochromatization concept, as described in Sec. 1.1.

1.2.2 Preliminary parametric studies

Since the first proposal of monochromatization for FCC-ee in 2016 [45], preliminary parametric studies have been made at ∼125 GeV CM energy, taken into account the impact of beamstrahlung (Subsec. 1.1.6) [47, 49, 51, 53, 55]. As previously mentioned, at this high-energy the natural collision energy spread due to synchrotron radiation, is around 50 MeV. In standard FCC-ee running conditions ($D^*_{x,y} = 0$), this spread increases to around 70 MeV due to the CM energy spread blow-up caused by beamstrahlung, as described by Eq. 1.85. Reducing the CM energy spread to the desired level can be achieved, by up to one order of magnitude (monochromatization factor (Eq. 1.28) $\lambda = 10$), by means of monochromatization concept in e^+e^- circular colliders (Sec. 1.1). If we suppose a nonzero horizontal dispersion of opposite sign for the two colliding beams at the IP ($D^*_{x+} = D^*_{x-} = D^*_x$), such non-zero D^*_x leads to a significant increase in the horizontal emittance due to beamstrahlung from Eq. 1.84. This emittance blow-up combined with IP dispersion leads to a much-increased horizontal beam size, so that the relative beam energy spread and bunch length return to their natural values attained without collision. This effect alone already decreases the collision energy spread if considering the effect of beamstrahlung. An additional reduction is caused by colliding particles with exactly opposite energy deviations, thanks to the opposite sign of D_x^*.

The baseline layout of FCC-ee was optimized for operation at the Z-pole resonance, for WW pair production, for ZH running, and at the top quark threshold. It features a large crossing angle of 30 mrad [73]. A large crossing angle is also required in the possible additional run for s-channel Higgs production, to separate the two beams and feed them into their respective beam pipe, corresponding to the right aperture in the next arc, and to avoid any harmful effects of parasitic collisions.

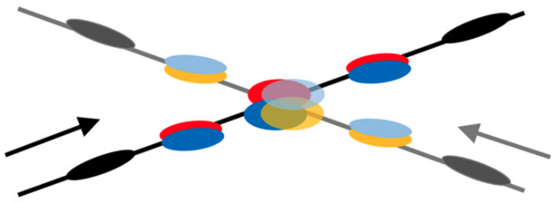

(a) CC scheme with crab cavities (head-on collision configuration).

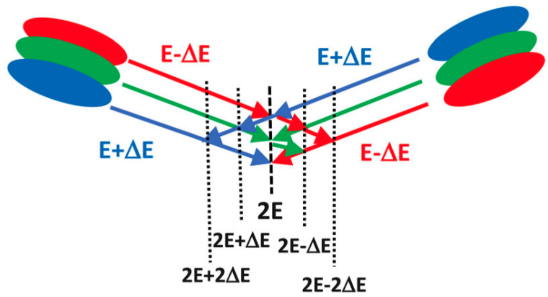

(b) IRS scheme without crab cavities (crossing-angle collision configuration).

Fig. 1.9 Two kinds of FCC-ee monochromatization schemes featuring IP horizontal dispersion of opposite sign for the the two colliding beams. Different colors schematically indicate bunch portions with sightly different energies [55].

There have been illustrated in Fig. 1.9, two monochromatization schemes compatible with the above assumptions [74]. In Fig. 1.9a, crab cavities are added for both beams on either side of each IP, so called Crab Crossing (CC) scheme. With an average betatron function at the crab cavities $\beta_{\rm crab}$ of about 2300 m and an IP betatron function β_x^* of 0.1 m, a crab RF frequency $f_{\rm RF}$ of 400 MHz and at a full crossing angle θ_c of 30 mrad, the required crab-cavity voltage is:

$$V_{\rm crab} = \frac{cE_0 \tan(\theta_c/2)}{2\pi f_{\rm RF} e\sqrt{\beta_{\rm crab}\beta_x^*}} \approx 2\,\mathrm{MV} \tag{1.89}$$

per side of the IP and per beam, to be compared with an HL-LHC crab-cavity voltage of 6 MV [75]. These crab cavities will render the collision effectively head-on, and yield the “optimum” monochromatization, i.e., the smallest possible CM energy spread, for a given value of D_x^*. In Fig. 1.9b, the crab cavities are omitted, namely Integrated Resonances Scan (IRS) scheme [76]. The combination of large crossing angle and non-zero D_x^* then leads to a correlation between collision energy and longitudinal position, thus lowering the efficiency of the CM energy spread reduction. The two schemes are both considered and compared with each other under the FCC-ee monochromatization implementation.

The non-zero dispersion at the IP, D_x^*, as required for monochromatization, can be generated by a set of (additional or stronger) dipole magnets in the final focus system (FFS) [53, 55]. Prior to the monochromatization optics design for FCC-ee, a preliminary parameters optimization of crab-crossing monochromatization (head-on collision configuration) for FCC-ee based on its CDR design [1, 73], featuring a total of two IPs, was proceeded at ~125 GeV CM energy to maximum the luminosity while introducing non-zero D_x^*, aimed at a higher rate of Higgs bosons in s-channel production [47, 49, 51, 53, 55].

Table 1.1 Optimized FCC-ee monochromatization self-consistent parameters with an overall CM energy spread of 13 MeV (with crab cavities) and 25 MeV (without crab cavities) [53, 55].

Parameter	**Symbol**	**Unit**	**Value**
CM energy	W	GeV	125
# of IPs	n_{IP}		2
Full crossing angle	θ_c	mrad	30
Beam current	I	mA	395
Bunch population	N_b	10^{10}	6.0
Bunches per beam	n_b		13420
Horizontal, vertical emittance with (without) BS	$\varepsilon_{x,y}$	nm	2.5 (0.51), 0.002
Relative beam energy spread	σ_δ	%	0.052
Bunch length	σ_z	mm	3.3
Horizontal dispersion at the IP	D_x^*	m	0.105
IP betatron function	$\beta_{x,y}^*$	mm	90, 1
Beam size at the IP	$\sigma_{x,y}^*$	µm	55, 0.045
Vertical beam-beam tune shift	ξ_y		0.106
Hourglass reduction factor	R_{hg}		~ 0.3
Luminosity per IP with (without) crab cavities	$\mathcal{L}$	$\mathrm{cm}^{-2}\,\mathrm{s}^{-1}$	2.6×10^{35} (2.3×10^{35})
CM energy spread with (without) crab cavities	σ_W	MeV	13 (25)

Table 1.1 summarizes the optimized FCC-ee monochromatization self-consistent parameters [53, 55] and the expected effective CM energy spread and luminosity performance obtained from a simulation of a single collision using the simulation tool Guinea-Pig [24]. For the Guinea-Pig simulation, the equilibrium beam parameters are assumed including the effect of beamstrahlung, which were obtained from the analytical description in Subsec. 1.1.6. Fig. 1.10 compares the CM energy spread with and without crab cavities. The correlation between collision energy and longitudinal position for the second scenario is evidenced in the bottom picture. The effective CM energy spread over 100 µm around $z \approx 0$ is the same as for the scenario with crab cavities.

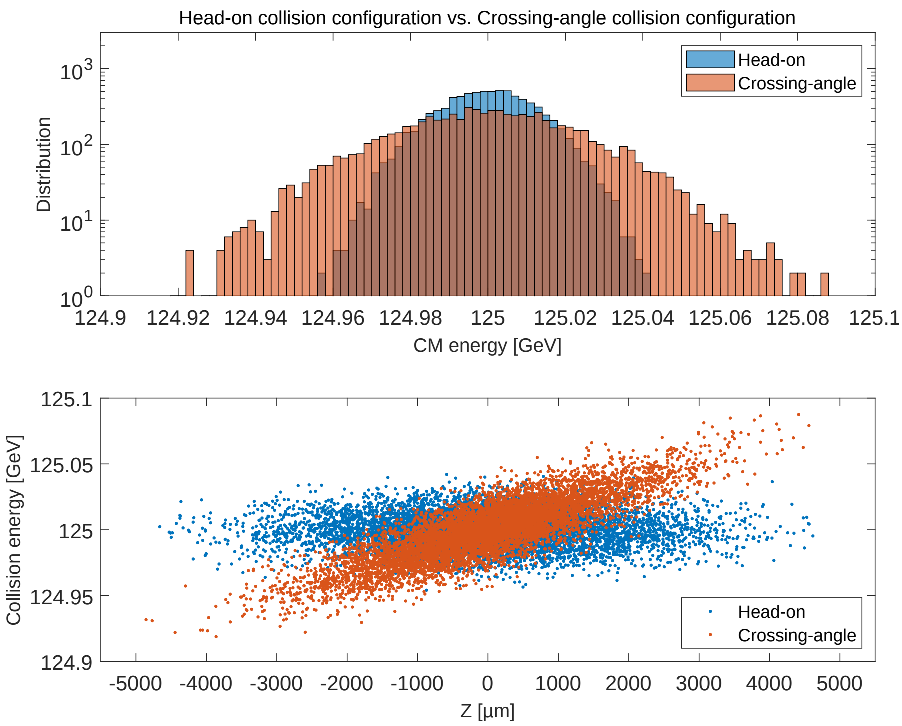

Fig. 1.10 CM energy distribution with and without crab cavities (top) and correlation between collision energy and longitudinal position (bottom), obtained from the simulation of a beam-beam collision using the code Guinea-Pig.

Regarding the impact of the hourglass effect on luminosity, as discussed in Subsec.1.1.5, the calculated t_1 (Eq. 1.1.5) based on the FCC-ee monochromatization self-consistent parameters (Table 1.1) is 0.05, indicating an hourglass reduction factor R_{hg} of ~ 0.3, as estimated from Fig. 1.8. This can be optimized by shaping the vertical IP betatron function β_y^*. For instance, setting the β_y^* to 4 mm could increase the R_{hg} to ~ 0.8. In this study, we did not account for this effect, but its feasibility for optimization remains if necessary.

Concerning the integrated luminosity, following the assumptions laid out in the FCC-ee CDR [1] of 185 physics days per year, with a physics efficiency of 75%, an instantaneous luminosity of $10^{35}\,\mathrm{cm}^{-2}\,\mathrm{s}^{-1}$ would result in $1.2\,\mathrm{ab}^{-1}$ per IP and year, while $7.6 \times 10^{35}\,\mathrm{cm}^{-2}\,\mathrm{s}^{-1}$ would deliver $9.1\,\mathrm{ab}^{-1}$ per IP and year.

Finally, at FCC-ee the monochromatized s-channel Higgs production can be accomplished by operating at a beam energy of 62.5 GeV and introducing a non-zero horizontal dispersion at the IP. A luminosity of about $2.5 \times 10^{35}\,\mathrm{cm}^{-2}\,\mathrm{s}^{-1}$ is expected for an effective CM energy spread σ_W of 13 MeV, compared with close to $8 \times 10^{35}\,\mathrm{cm}^{-2}\,\mathrm{s}^{-1}$ at $\sigma_W \approx 115\,\mathrm{MeV}$ without monochromatization [53].

1.2.3 Physics performance evaluations

The signature for direct Higgs production is a small rise in the cross sections for final states, consistent with Higgs decays, over the expectations for their occurrence due to other SM processes shown in Fig. 1.11 (left). Performing such a measurement is

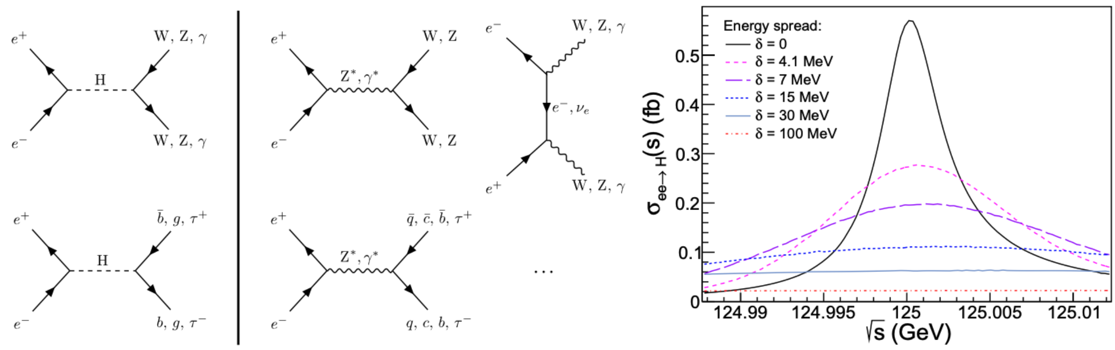

Fig. 1.11 Typical diagrams for the direct Higgs channel production (left) decaying into electroweak bosons (top) and fermions or gluons (bottom) and associated backgrounds (center), considered in this study. Notice that the Higgs is shown decaying directly into $\gamma\gamma$ and gg in the left-most diagram, but in reality this process occurs through higher-order diagrams. Resonant Higgs production cross section (right), including ISR effect, for several values of the e^+e^- CM energy spread $\delta_{\sqrt{s}} = 0$, 4.1, 7, 15, 30, and 100 MeV [2].

remarkably challenging for four reasons. First, the low value of the electron mass leads to a tiny electron Yukawa (y_e) coupling, and correspondingly small cross section at the Higgs pole: $\sigma_{ee\to\mathrm{H}} \propto m_e^2 = 0.57\,\mathrm{fb}$ [2, 68, 70], also accounting for initial-state γ radiation (ISR) that reduces the cross section and generates an asymmetry of the Higgs lineshape. Fig. 1.11 (right) shows the Higgs lineshape for various values of CM energy spread $\delta_{\sqrt{s}}$. The combination of ISR plus $\delta_{\sqrt{s}} = \Gamma_\mathrm{H} = 4.1\,\mathrm{MeV}$ reduces the peak Higgs cross section down to $\sigma_{ee\to\mathrm{H}} = 0.28\,\mathrm{fb}$. Second, the narrow width of the SM Higgs boson, $\Gamma_\mathrm{H} = 4.1\,\mathrm{eV}$

in comparison to the natural relative beam energy spread due to SR of about 50 MeV. Third, the Higgs mass must also be known beforehand with a few-MeV accuracy in order to operate the collider at the resonant peak, $\sqrt{s} = m_{\mathrm{H}}$. Finally, the cross sections of the background process (center of Fig. 1.11) are many orders-of-magnitude larger than those of the Higgs decay signals. Given these facts, the only known way to successfully realize this measurement is to implement a monochromatization scheme to reduce the CM energy spread at the level of the Higgs boson width while keeping ideal beam luminosity.

To evaluate physics performance of the scaled FCC-ee monochromatization parameters, large samples of simulated signal ($e^+e^- \to \mathrm{H} \to \mathrm{XX}$) and associated background ($e^+e^- \to \mathrm{Z}^* \to \mathrm{XX}$) events have been generated with the Pythia 8 Monte Carlo code [77]. This was done for 11 Higgs decay channels, employing a multivariate analysis that utilizes Boosted Decision Trees to discriminate between signal and background events. This analysis leads to the identification of two promising final states in terms of statistical significance (in units of std. deviations σ): $\mathrm{H} \to gg$ and $\mathrm{H} \to \mathrm{WW}^* \to \ell\nu 2j$. Taking a monochromatization benchmark providing an ideal CM energy spread of 4.1 MeV (leading to $\sigma_{ee\to\mathrm{H}} = 0.28$ fb) and an integrated luminosity of 10 ab^{-1}, a 1.3 σ signal significance can be reached. This corresponds to an upper limit on the y_e coupling at 1.6 times of the

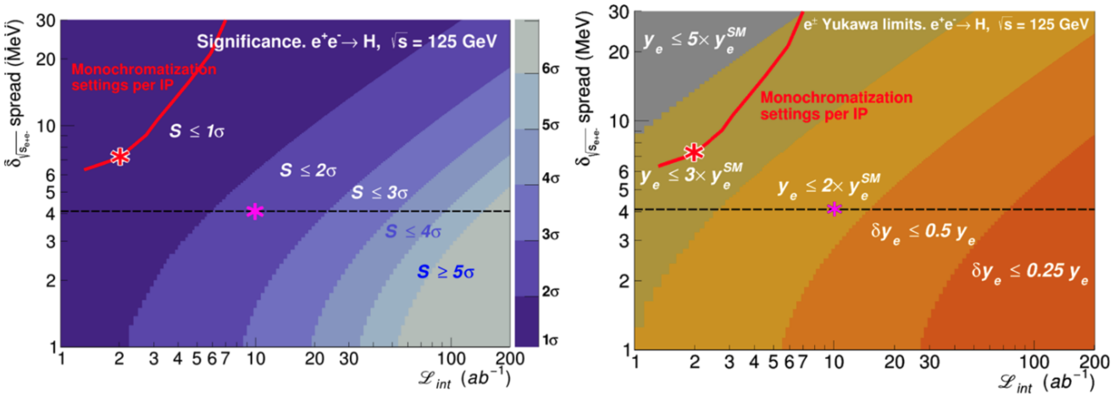

Fig. 1.12 Left: Significance contours (in std. dev. units σ) in the CM energy spread vs. integrated luminosity plane for the resonant $\sigma_{ee\to\mathrm{H}}$ cross section at $\sqrt{s} = m_{\mathrm{H}}$. Right: Associated upper limits contours (95% CL) on the y_e. The red curves show the range of parameters presently reached in preliminary FCC-ee monochromatization studies [49, 51]. The red star indicates the best signal strength monochromatization point in the plane (the pink star over the $\delta_{\sqrt{s}} = \Gamma_{\mathrm{H}} = 4.1$ MeV dashed line, indicates the ideal baseline point assumed in default analysis). All results are given per IP and year [69].

SM Higgs s-channel cross section: $|y_e| < 1.6\,|y_e^{SM}|$ at 95% confidence level (CL) per IP per year, depicted as the pink stars in Fig. 1.12. The preliminary settings of the FCC-ee monochromatization parameters [49, 51] gives a Higgs signal strength corresponding to 7 MeV CM energy spread and $2\,\mathrm{ab}^{-1}$ integrated luminosity. This translates into a significance of $0.4\,\sigma$ on the Higgs cross section, or corresponding to an upper bound on the y_e coupling of $|y_e| < 2.6\,|y_e^{SM}|$ (95% CL) per IP per year (red stars in Fig. 1.12).

Forthcoming extension and consolidation of FCC-ee monochromatization implementation, requires, among others, to continue and to extend the accelerator monochromatization studies in order to improve the current best working point. This aims at further reducing the collision energy spread while increasing the luminosity and developing the corresponding optical lattices and devices to make monochromatization a reality.

Chapter 2

FCC-ee project and its baseline standard optics

Since the Higgs boson was firstly discovered at the Large Hadron Collider (LHC) [78, 79] in 2012 [62, 63], there has been a worldwide interest towards precision measurements in electroweak (EW) physics, specifically concerning the properties of the Higgs boson, which has spurred the development of advanced high-energy, high-luminosity, and high-precision e^+e^- collider studies. As the initial stage of the Future Circular Collider (FCC) initiative [80], spearheaded by European Organization for Nuclear Research (CERN), the FCC-ee is designed as a high-luminosity circular e^+e^- collider. Building on the successes of LHC, the FCC-ee aspires to become a pivotal platform for precision studies of the Standard Model (SM) [81] and potential new phenomena beyond it.

In this chapter, we begin with a general introduction to the FCC-ee, covering its motivation, the physics opportunity it offers, and the key technologies involved in its accelerator design. Following this, we present the placement and general layout of the FCC-ee accelerator, along with the detailed descriptions of two kinds of baseline standard optics designs, that has been taken as initial step of the monochromatization optics design.

2.1 General introduction to FCC-ee

Over the past decade, the field of particle physics has experienced a significant and transformative phase in its development. The SM, the core theory behind the known set of elementary particles and three of four fundamental interactions, was completed with the discovery of the 125 GeV Higgs boson at LHC [78, 79] in 2012 [62, 63]. This monumental observation confirmed the existence of the Higgs boson, a critical component of the SM, and provided significant insights into the mechanism of mass generation for elementary particles.

However, several experimental facts require the extension of the SM and explanations are needed for observations such as the domination of matter over antimatter, the evidence for dark matter and the non-zero neutrino masses [80]. Additionally, some theoretical issues that need to be addressed include the hierarchy problem, the neutrality of the Universe, the stability of the Higgs boson mass upon quantum corrections and the strong Charge-Parity (CP) problem. The exploration of these open questions of physics beyond the SM, necessitates the development of a new generation of high-energy, high-luminosity, and high-precision colliders.

"*There is a strong scientific case for an electron-positron collider, complementary to the LHC, that can study the properties of the Higgs boson and other particles with unprecedented precision and whose energy can be upgraded.*" [82]

This strategic guideline from the 2013 update of the European Strategy for Particle Physics (ESPP 2013) unambiguously defines the high standards to be met by the future e^+e^- collider, quite possibly the next high-energy collider to be built. As a result of this renewed interest for e^+e^- physics, four leading proposals for future e^+e^- colliders are contemplated to study the properties of the Higgs boson and other SM particles with an unprecedented precision:

- **ILC** (International Linear Collider [83]), for which the above guideline was originally tailored, now focuses on studying the Higgs boson with a CM energy of 250 GeV [84];
- **CLIC** (Compact Linear Collider [85]), whose lowest centre-of-mass energy point was reduced from 500 to 380 GeV [86], in order to better study the Higgs boson and the top quark;
- **CEPC** (Circular Electron Positron Collider [43, 87]), in a 100 km tunnel in China, able to study the Z, the W, and the Higgs boson, with CM energies from 90 to 250 GeV;
- **FCC-ee** (Future Circular electron positron Collider [1]), in a new ∼90 km tunnel at CERN, which can study the EW sector (Z and W bosons, Higgs boson, top quark) with CM energies between 90 and 365 GeV.

The baseline luminosities and CM energies expected to be delivered at the ILC, CLIC, CEPC, and FCC-ee are illustrated in Fig. 2.1.

Built on the experience of previous colliders, the Large Electron-Positron (LEP) [88] and LHC, the FCC-ee will be the most powerful of all proposed e^+e^- colliders at the EW scale, thus proposing a broad multifaceted exploration to [1]:

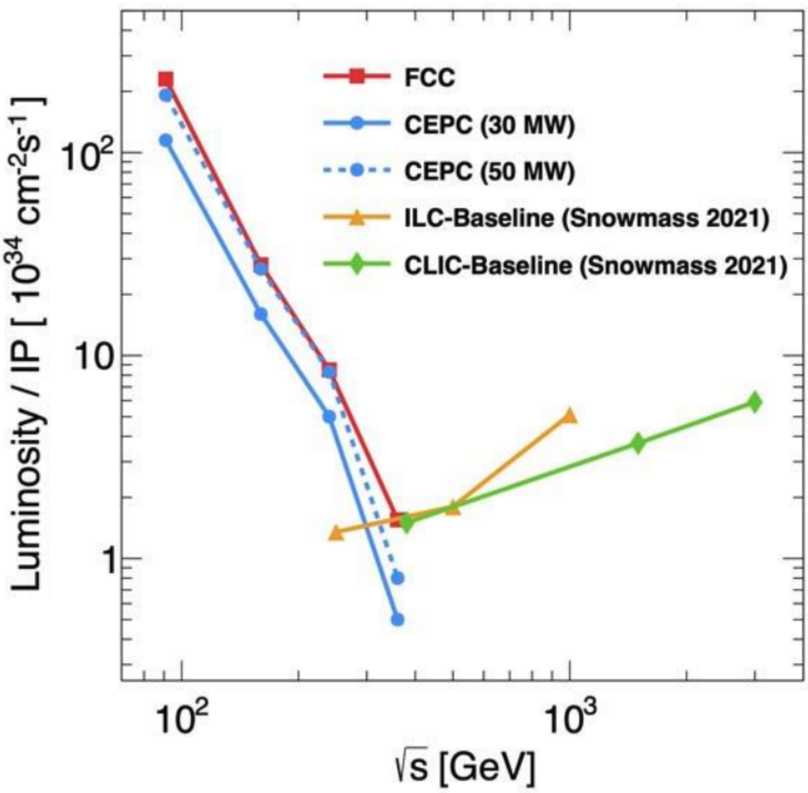

Fig. 2.1 Baseline luminosities expected to be delivered as a function of the CM energy $\sqrt{s}$, at each of the four leading worldwide projects for future e^+e^- collider [87].

- **Precision measurements**:
  - **Z and W bosons**: The FCC-ee will allow for high-precision measurements of the Z and W bosons' properties, such as their masses, widths, and couplings. These measurements are critical for testing the consistency of the Standard Model.
  - **Higgs boson**: By operating at energies around the Higgs boson mass, the FCC-ee will provide detailed studies of the Higgs boson's properties, including its mass, total decay width, and couplings to other particles. These measurements will help clarify the mechanism of electroweak symmetry breaking.
  - **Top quark**: The FCC-ee will also explore the top quark with high precision, focusing on its mass, width, and couplings, which are essential for understanding the top quark's role in the Standard Model and beyond.
- **New physics searches**:
  - **Rare decays and anomalies**: The high luminosity of the FCC-ee will enable the search for rare decays and potential anomalies that could indicate new

physics. These include potential new particles or forces that are not explained by the Standard Model.

- **EW sector**: The collider will provide unprecedented sensitivity to electroweak observables, allowing for stringent tests of the Standard Model and the exploration of possible extensions.

- **Beyond the SM**
  - **Dark matter and dark energy**: The FCC-ee's precision measurements may shed light on the nature of dark matter and dark energy, addressing some of the most profound mysteries in cosmology.
  - **Lepton flavor violation**: The collider will explore processes that could indicate lepton flavor violation, a phenomenon not predicted by the Standard Model but suggested by some extensions.

Therefore, it maximize opportunities for major fundamental discoveries.

The accelerator design of the FCC-ee features the following key technologies [1]:

- **High luminosity**: The FCC-ee's design incorporates advanced accelerator technology to achieve extremely high luminosity, enabling the collection of vast amounts of data for precision measurements;
- **Energy flexibility**: The collider will operate at multiple energy levels, allowing for a wide range of experimental studies from the Z pole to the top quark threshold;
- **Precision instrumentation**: The FCC-ee will be equipped with state-of-the-art detectors and instrumentation to accurately measure particle interactions and properties;
- **Environmental and economic sustainability**: The design includes measures for energy efficiency and aims to minimize environmental impact, reflecting CERN's commitment to sustainable research practices.

The overall layout of FCC-ee and the details of its lattice design will be presented in the next section.

2.2 FCC-ee baseline standard optics

The FCC-ee [1], is the first part of the so-called integrated FCC program [80], which foresees, first, the construction of an almost 90 km long tunnel infrastructure and the integration and commissioning of the FCC-ee. After completion of its physics program, it is then envisaged to decommission the FCC-ee, followed by integration of the Future Circular hadron hadron Collider [89], FCC-hh, into the same tunnel infrastructure. Within the framework of the FCC FS, launched in 2021, the design of the electron-positron collider FCC-ee is being optimized, as a double collider ring, currently foreseen to start operation during the 2040s [90]. Such a flexible high energy electron-positron collider offers the potential for high precision physics experiments at various particle physics resonances. In case of the FCC-ee beam energies from 45.6 GeV, corresponding to Z-pole, and up to the top-pair-threshold with 182.5 GeV are foreseen. To limit the synchrotron radiation power to 50 MeV per turn the beam current decreases with increasing energy. Each energy stage leads, therefore, to unique beam dynamics challenges, and solutions need to be found in accordance with the general layout.

For the highest beam energy of 182.5 GeV, as required for the $t\bar{t}$ mode, the estimated circumference is about 100 km [91]. The tunnel infrastructure required to host the FCC-ee in the Geneva basin is assumed to be constructed approximately 100 m below ground, similar to the tunnel which presently hosts the LHC [79]. Tunnel construction is one of the main cost drivers, and depends on the tunnel dimensions, depth, and composition of the ground material. Additionally, shafts and surface sites around the circumference are required to host various infrastructures, demanding dedicated civil engineering solutions. Geographic constraints to integrate a circular collider into the Franco-Swiss-Basin are the various mountain ranges surrounding it, including the Jura-mountains in the north-west and the Plateau des Bornes in the southeast in addition to the Geneva lake in the north-east. Furthermore, a possible circular tunnel should surround the Salève-mountain and, hence, these constraints already limit the circumference to about 80 km to 100 km. Considering all the cost and geographic constraints, it has been found that a 90 km tunnel with a four-fold symmetry together with 8 surface sites and straight sections is the most suitable layout. Fig. 2.2 (left) compares the FCC and the LHC placement schematically. Compared to the FCC-ee CDR [1] version numerous changes have been made in the FCC-ee layout, including a shorter circumference and the possibility of integrating four instead of two experiments. The FCC-ee baseline lattice follows the new, so-called lowest risk tunnel scenario with approximately 91.1 km circumference, eight straight sections (PA, PB, PD, PF, PG, PH, PJ, and PL) and is shown in Fig. 2.2. It offers the possibility

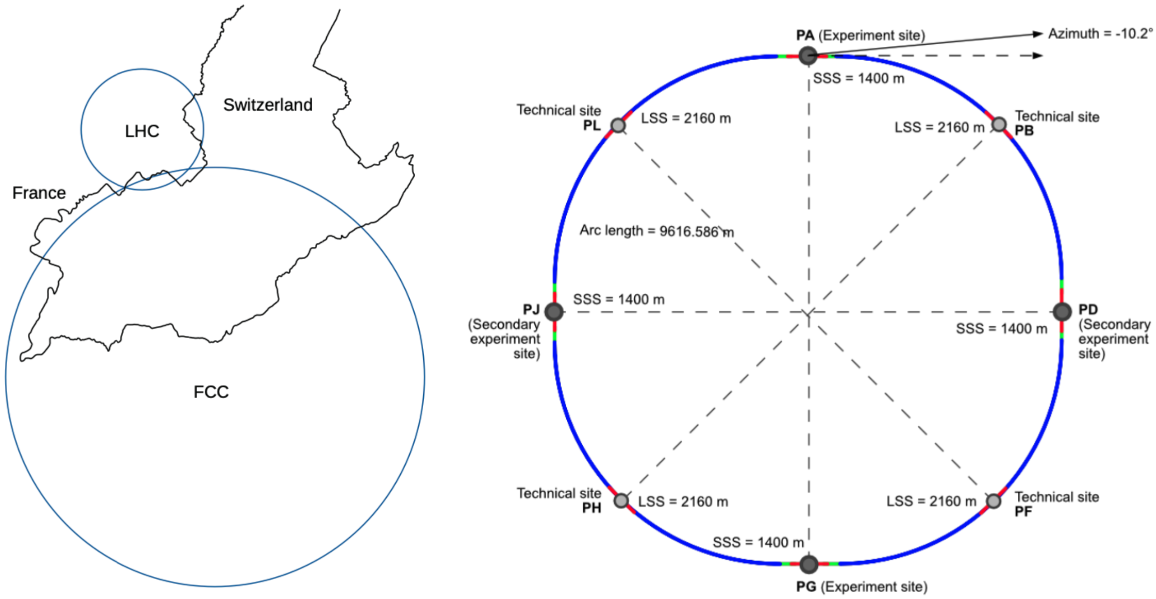

Fig. 2.2 Comparison between the LHC, the FCC, and the Franco-Swiss border (left) [92]. The baseline layout of FCC-ee following the lowest risk tunnel scenario (∼91.1 km) with eight straight sections (PA, PB, PD, PF, PG, PH, PJ, and PL) (right).

of up to four experimental interaction regions (IRs) in PA, PD, PG, and PL, where the beams are brought to collision from the inside outwards. Thus, beams are required to change from the inside to the outside aperture in all IRs. The other four straight sections (PB, PF, PH, and PL) are technical sections, with one or more of these sections integrated with RF cavities, which are also referred to as RF sections. Additionally, the beam collimation section is placed in PF. The electron and the positron beams are presumed to be injected continuously at nominal beam energy in PB (top-up injection) from the High Energy Booster (HEB). The HEB is designed to be installed in the same tunnel infrastructure and thus its lattice design must also be compatible with the one for the colliding rings. Thus, the lattice design of the FCC-ee must comply with all three rings hosted in the same tunnel, and thus two IRs are dedicated for the RF cavities of the three rings. Following this baseline layout, two different FCC-ee lattice designs are currently being investigated [93]: the so-called Global Hybrid Correction optics (GHC) [73] and the Local Chromaticity Correction (LCC) optics [94, 95] as presented in this section.

2.2.1 FCC-ee GHC optics

The lattice design used in FCC-ee CDR [1] was first proposed by K. Oide in 2016 [73] using the SAD program [96], so-called FCC-ee GHC optics [92, 93]. Designed at four different beam energies of 45.6, 80, 120, and 182.5 GeV, it allows for physics precision experiments at the Z-pole (Z mode), the W-pair-threshold (WW mode), the ZH-maximum (ZH mode), and above the top-pair-threshold ($t\bar{t}$ mode) [97]. It is presently presumed to operate the FCC-ee with increasing beam energy over years, which, among others, requires a flexible lattice and optics design, allowing for fast transitions including upgrades of the RF cavities to compensate increasing synchrotron radiation energy losses.

The monochromatization interaction region (IR) optics design presented in the following chapters are based on Version 2022 of the FCC-ee GHC optics, which has been translated to the MAD-X program [98], namely "FCC-ee GHC V22" optics [99]. The performance parameters of this "FCC-ee GHC V22" optics are summarized in Table 2.1, considering the beamstrahlung impact on the relative energy spread and bunch length [100]. There are two types of "FCC-ee GHC V22" lattice, specifically designed for Z mode and $t\bar{t}$ mode, respectively labeled as "FCC-ee GHC V22 Z" and "FCC-ee GHC V22 $t\bar{t}$." Apart of the beam energy and beam current, from the optics point of view the two lattice differ on the arc cell type, IR, and RF insertion.

Arc and emittances

The eight arcs between the straight sections are structured with FODO (Focus-Drift-Defocus-Drift) cell structures [8], incorporating horizontally focusing and defocusing quadrupoles (QF and QD in the lattice), with bending dipoles, featuring a bending radius of 9.937 km. Although these dipoles have a transverse phase advance of 90° at all energy stages, it is noteworthy that the FODO cell length of the four mode is different according to their beam energy. In an electron ring, the natural emittance $\varepsilon_{x,y}$ is given by

$$\varepsilon_{x,y} = C_q \gamma^2 \frac{I_{5x,y}}{J_{x,y} I_2} , \tag{2.1}$$

where C_q is the physical constant (Eq. 1.4), γ is the relativistic factor, $J_{x,y}$ are the damping partition numbers (Eq. A.13), I_2 and I_5 are the second and fifth synchrotron radiation integrals (Eq. A.4 and Eq. A.7). Note that $J_{x,y}$, I_2, and I_5 are all fixed by the layout of the lattice and the optics, and are independent of the beam energy.

Considering the case of a FODO cell structure lattice and making the approximation $J_x \approx 1$ (no quadrupole component in the dipole), the horizontal emittance ε_x of one

Table 2.1 Performance parameters of the Version 2022 of FCC-ee GHC optics [100].

Parameter	**[Unit]**	**Z**	**WW**	**ZH**	**$t\bar{t}$**
# of IPs n_{IP}		4			
Circumference C	[km]	91			
Full crossing angle θ_c	[mrad]	30			
Bending radius of arc dipole ρ	[km]	9.937			
SR power / beam P_{SR}	[MW]	50			
Beam energy E_0	[GeV]	45.6	80	120	182.5
Energy loss / turn U_0	[GeV]	0.0391	0.370	1.869	10.0
Beam current I	[mA]	1280	135	26.7	5.00
Bunches / beam n_b		10000	880	248	40
Bunch population N_b	[10^{11}]	2.43	2.91	2.04	2.37
Horizontal emittance ε_x	[nm]	0.71	2.16	0.64	1.49
Vertical emittance ε_y	[pm]	1.42	4.32	1.29	2.98
Arc cell phase advance	[°]	90 / 90			
Arc cell length	[m]	100		50	
Momentum compaction factor α_C	[10^{-6}]	28.5		7.33	
Arc sextupole families		75		146	
$\beta^*_{x/y}$	[mm]	100 / 0.8	200 / 1.0	300 / 1.0	1000 / 1.6
Transverse tunes / IP $Q_{x/y}$		53.563 / 53.600		100.565 / 98.595	
Relative energy spread (SR / BS) σ_δ	[%]	0.038 / 0.132	0.069 / 0.154	0.103 / 0.185	0.157 / 0.221
Bunch length (SR / BS) σ_z	[mm]	4.38 / 15.4	3.55 / 8.01	3.34 / 6.00	1.95 / 2.75
RF voltage 400/800 MHz V_{RF}	[GV]	0.120 / 0	1.0 / 0	2.08 / 0	2.5 / 8.8
Harmonic number for 400 MHz h		121648			
RF frequency (400 MHz) f_{RF}	[MHz]	399.994581		399.994627	
Synchrotron tune Q_s		0.0370	0.0801	0.0328	0.0826
Long. damping time τ_E/T_{rev}	[turns]	1168	217	64.5	18.5
RF acceptance	[%]	1.6	3.4	1.9	3.0
Energy acceptance (DA)	[%]	±1.3	±1.3	±1.7	$-2.8+2.5$
Beam-beam $\xi_{x/y}$		0.0023 / 0.135	0.011 / 0.125	0.014 / 0.131	0.091 / 0.140
Luminosity / IP $\mathcal{L}$	[10^{34} cm^{-2} s^{-1}]	182	19.4	7.26	1.25

FODO cell is approximated to [6]:

$$\varepsilon_x \approx C_q \gamma^2 \left(\frac{2f}{L}\right)^3 \theta^3 \,. \tag{2.2}$$

The ε_x is proportional to the square of the beam energy and to the cube of the bending angle θ. Increasing the number of cells in the arc lattice reduces the bending angle of each dipole, thus decreasing the ε_x. With f the focus length of quadrupoles and L the

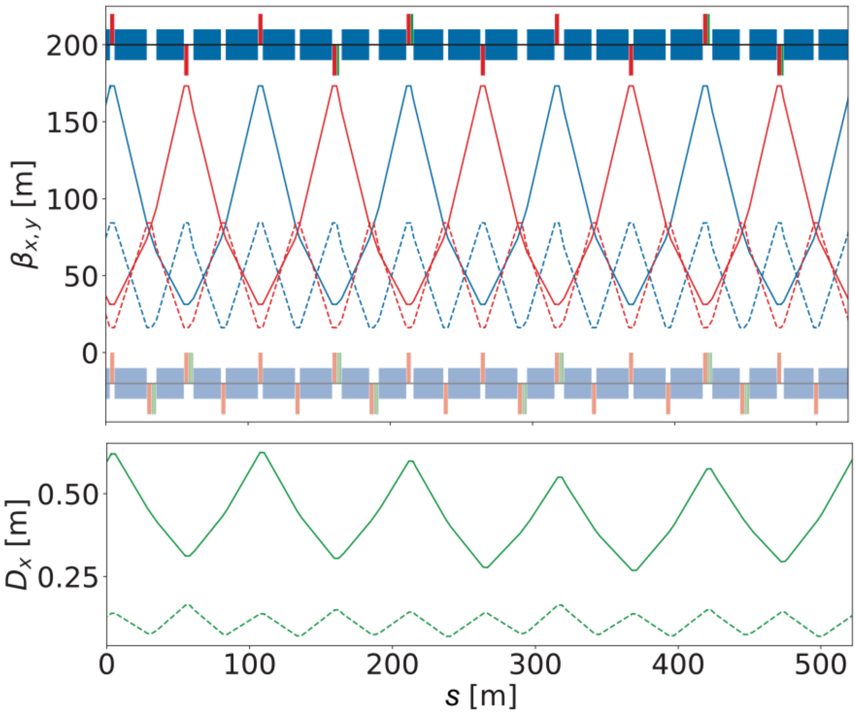

Fig. 2.3 "FCC-ee GHC V22" arc lattice and optics calculated using MAD-X for five FODO cells (equivalent to one super-cell) for the Z and WW mode (solid lines); and ten FODO cells (equivalent to two super-cells) for ZH and $t\bar{t}$ mode (dashed lines). In the lattice, dipoles, quadrupoles, and sextupoles are shown in blue, red, and green, respectively, while focusing and defocusing elements are positioned above and below the orbit. In the optics, horizontal and vertical betatron functions are shown in blue and red, respectively, while horizontal dispersion function is shown in green [92].

length of the bending dipoles, the ε_x is also proportional to the cube of f: strong focusing results in lower emittance. Finally, the ε_x is inversely proportional to the cube of the arc cell length. Therefore, to maintain the ε_x of the four energy stages in a same level, the arc cell length of Z mode and WW mode is 100 m, so-called long 90/90 arc cell, while at ZH mode and $t\bar{t}$ mode it is reduced to about 50 m by inserting additional quadrupoles, so-called 90/90 arc cell, as summarized in Table 2.1 [100]. With no vertical bendings in the ideal ring optics, the vertical emittance is given by assumed FCC-ee coupling ratio (full current) of motion between the horizontal and vertical planes:

$$\kappa = \frac{\varepsilon_y}{\varepsilon_x} = 0.2\% \,, \tag{2.3}$$

which can be matched by installing wigglers in the arcs.

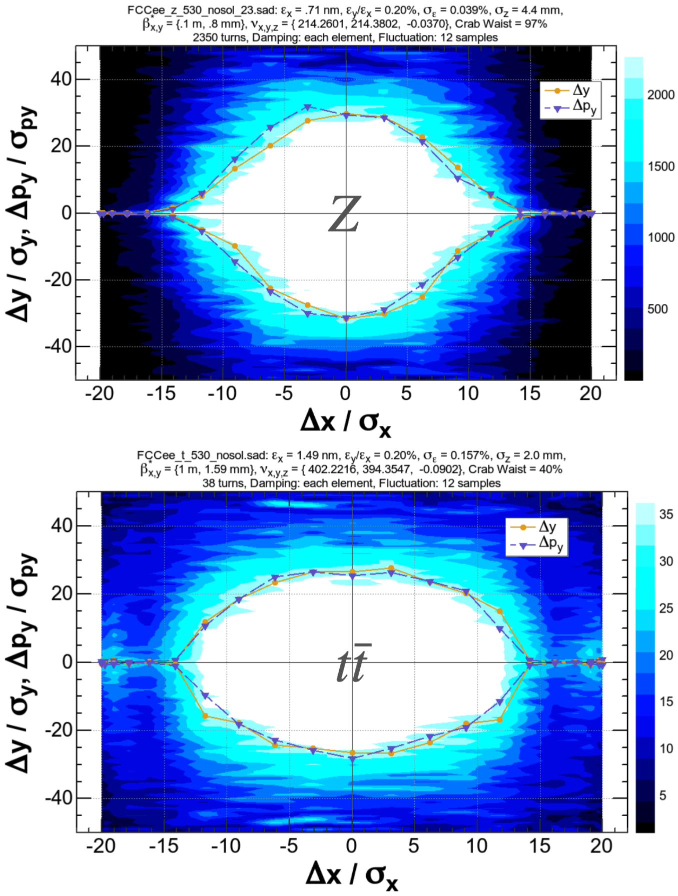

Fig. 2.4 Dynamic aperture after optimization of arc sextupole family simulated in SAD. Assuming a zero momentum deviation ($\delta = 0$), the stable horizontal amplitude ($\Delta x/\sigma_x$, with particle motion phase $\phi = 0$) as a function of the stable vertical amplitude, averaged over all particle motion phases ϕ (from 0 to $\pi/2$), is calculated for the "FCC-ee GHC V22 Z" optics (top) and "FCC-ee GHC V22 t$\bar{\text{t}}$" optics (bottom), respectively. The purple curve represents the stable vertical amplitude $\Delta y/\sigma_y$ when $\phi = 0$, while the orange curve corresponds to the stable vertical amplitude $\Delta py/\sigma_{py}$ when $\phi = \pi/2$. The number of turns was selected to approximate twice the longitudinal damping time (τ_E/T_{rev}) [100]. The varying shades of blue indicate the number of particle surviving turns, while the white regions denote the stable amplitude areas.

Non-interleaved individually powered 76 or 146 sextupole pairs, respectively for the two lower or higher beam energy modes, are installed with a $-I$ transformation between them. The periodic structure within the arc, named super-cell, consists of five FODO cells and contains one focusing and one defocusing sextupole pair. Therefore also additional sextupole magnets are required to be installed when switching to the shorter FODO cells arc lattice for the higher beam energies. Due to fewer quadruple magnets in the arc optics for the lower beam energies at the Z mode and WW mode, the arc betatron function are roughly a factor 2 larger and the horizontal dispersion by almost a factor 4. The lattice and optics calculated using MAD-X of one or two super-cells, respectively, for the lower and higher beam energy arc design is shown in Fig. 2.3.

The sextupole families are optimized to maximize the momentum acceptance up to about 2.8% at 182.5 GeV, since beamstrahlung and synchrotron radiation lead to a wide momentum spread. Additionally, horizontal on-momentum dynamic aperture of about $15\,\sigma$ is achieved in SAD, as depicted in Fig. 2.4. The possibility of using 75 and 146 sextupole pairs, respectively, for the lower energy and higher energy operation modes, while reaching the required momentum aperture, is envisaged to be explored.

Interaction region

All four experimental IRs (PA, PD, PG, and PJ) feature the same lattice, where the electron and positron beams are brought to collision from the inside outwards with a crossing angle of 30 mrad in horizontal plane.

Figure 2.5 shows the “FCC-ee GHC V22 Z” IR lattice and optics calculated using MAD-X. In both upstream and downstream of the IR, there are six horizontal dipoles signaled in blue. The horizontal and vertical betatron functions (blue and red) at the IP with $\beta^*_{x,y} = 100, 0.8\,\mathrm{mm}$. The dispersion function (green) equals to zero around the IP and there are two dispersion-free regions before the arcs. The “FCC-ee GHC V22 $\mathrm{t\bar{t}}$” IR lattice and optics is depicted in Fig. 2.6, with the horizontal and vertical betatron functions at the IP with $\beta^*_{x,y} = 1000, 1.6\,\mathrm{mm}$. Although β^*_y is about 3 times larger than the SuperKEKB design [41], the generated chromaticity around the IP is of the same order of magnitude for both colliders. It has to noted, that the minimum β^*_y achieved in SuperKEKB is 0.8 mm and thus approximately a factor 3 larger than its design.

To control the chromaticity generated in the IR, a local chromaticity correction (LCC) system consisting of non-interleaved sextupole pairs, for only the vertical plane is integrated on both IP sides. In this context, the IR horizontal chromaticity is corrected globally using arc sextupoles, while the vertical IR chromaticity is compensate by the inner sextupole pairs positioned at the locations with nonzero dispersion, whose geometric

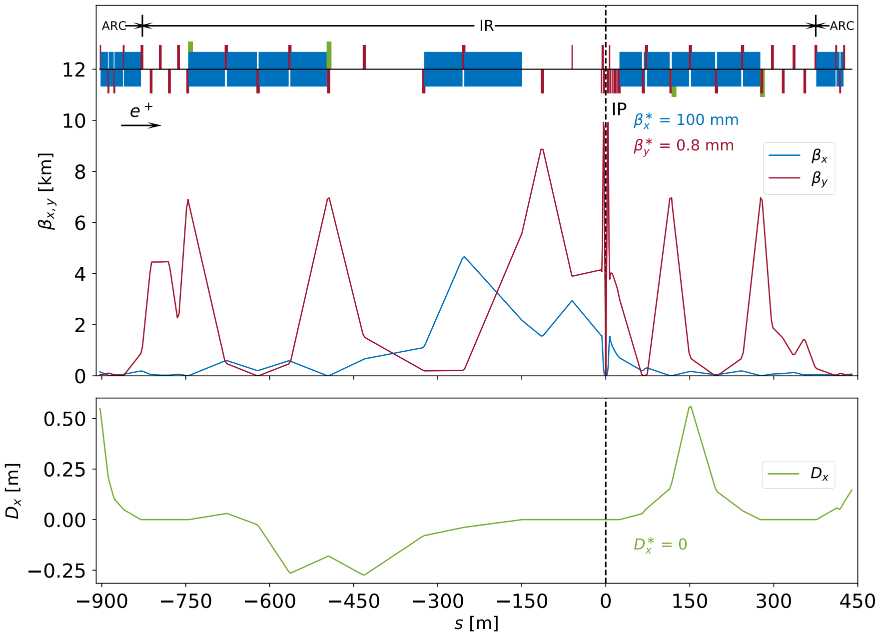

Fig. 2.5 "FCC-ee GHC V22 Z" IR lattice and optics calculated using MAD-X. The beam direction is from left to right; the dashed line $s = 0$ marks the location of IP. In the lattice, dipoles, quadrupoles, and sextupoles are shown in blue, red, and green, respectively, while focusing and defocusing elements are positioned above and below the orbit. In the optics, horizontal and vertical betatron functions are shown in blue and red, respectively, while horizontal dispersion function is shown in green.

aberrations are canceled by the outer sextupole pairs located within the dispersion-free regions. Additionally, these outer sextupole pairs of this LCC system are also utilized for the crab-waist transformation [38–40]. For the crab-waist collision scheme, vertical beam sizes in the order of a few nm are brought to collision with a large Piwinksi angle (Eq. 1.57) aligning the waist of the betatron functions on the axis of the other beam via adequate sextupole powering. The horizontal and vertical phase advances $\mu_{x,y}$ for each inner sextupole pair are π and 1.5π, respectively, with respect to the IP on both sides, while for each outer sextupole pair, the $\mu_{x,y}$ are 2π and 2.5π, respectively, as schematically illustrated in Fig. 2.7, along with the presently used terminology of the IR quadrupole types. This scheme has first been tested successfully at DAΦNE [38–40] with dedicated crab-sextupoles and is presently also used in SuperKEKB [38, 41] using the virtual crab-waist collision scheme which is also foreseen for the FCC-ee [73].

With the same angles of all the horizontal dipole in the IR, the "FCC-ee GHC V22 Z" and "FCC-ee GHC V22 $t\bar{t}$" lattice features the same IR orbit, where beams cross the inside to the outside aperture at the IP, as shown in Fig. 2.8. This asymmetric design

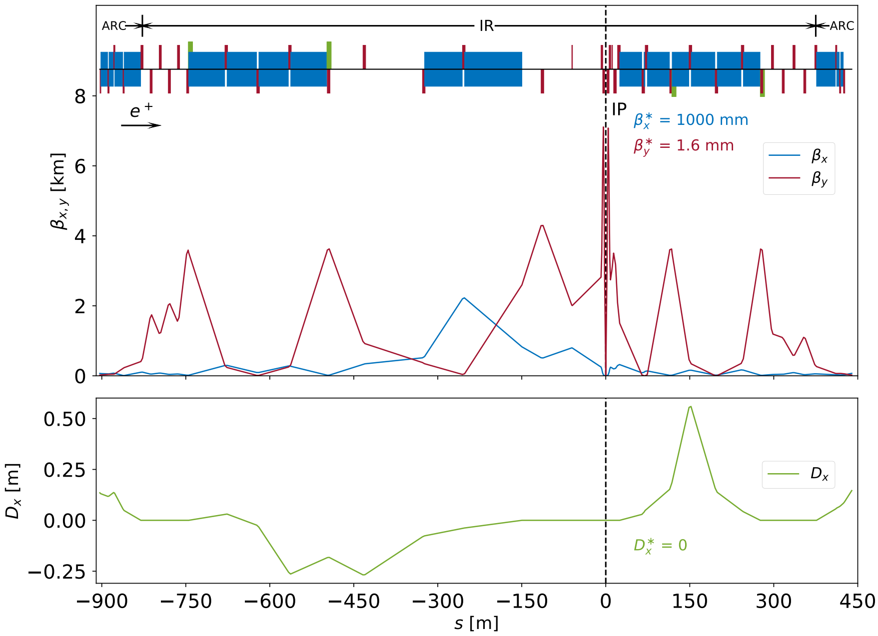

Fig. 2.6 "FCC-ee GHC V22 $t\bar{t}$" IR lattice and optics calculated using MAD-X. The beam direction is from left to right; the dashed line $s = 0$ marks the location of IP. In the lattice, dipoles, quadrupoles, and sextupoles are shown in blue, red, and green, respectively, while focusing and defocusing elements are positioned above and below the orbit. In the optics, horizontal and vertical betatron functions are shown in blue and red, respectively, while horizontal dispersion function is shown in green.

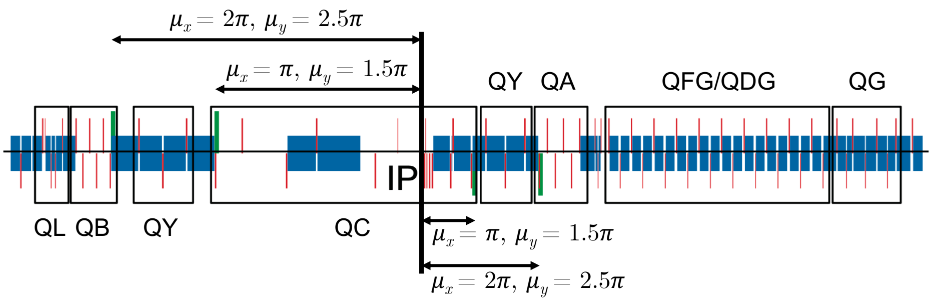

Fig. 2.7 Betatron phase advance between the IP and the LCC sextupoles and terminology of quadrupole types in the experimental IRs. Dipoles, quadrupoles, and sextupoles are shown in blue, red, and green, respectively, while focusing and defocusing elements are positioned above and below the horizontal axis.

mitigates the impact of synchrotron radiation at the detectors by having weaker dipole magnets upstream of the IP, and stronger ones downstream of it. Since the beams are crossing from the inside aperture at all experimental IRs (PA, PD, PG, and PJ), beam crossings from the outside towards the inside are required at all other straight sections (PB, PF, PH, and PL). In the experimental IRs no common magnets are foreseen for the electron and the positron beam [101].

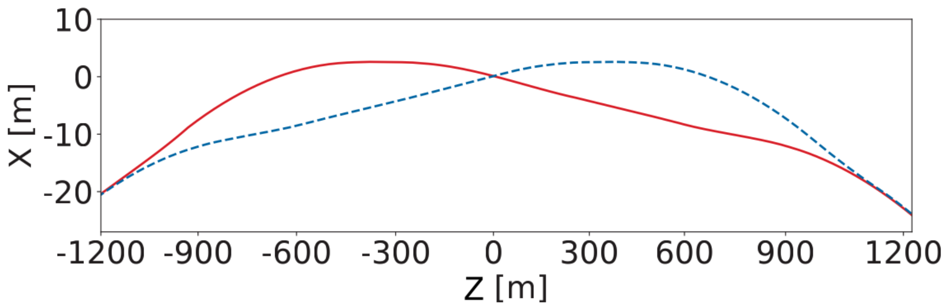

Fig. 2.8 Beam crossing at the IP from the inner towards the outer aperture. The point $X = 0, Z = 0$ marks the location of the IP [92].

Injection

The positron and the electron beams are injected continuously from the HEB in PB at nominal energy, known as top-up injection. One can distinguish in principle between on- and off-momentum injection, and using a conventional orbit bump or a multipole kicker injection (MKI), resulting in four possible scenarios presently investigated for the FCC-ee [102]. For multipole-kicker injection, a dedicated optics has been designed and the on-momentum one is shown in Fig. 2.9.

It features a large horizontal betatron function of about 2000 m at the injection point, centered between the MKI and a corrector magnet, MKIC. Previous tracking studies have shown that by integrating an additional MKIC beam size blow-up at the IP is successfully corrected [103]. We note that this optics is optimized for the 2-IP version and significant changes for the 4-IP lattice will need to be applied [104]. Furthermore, if the RF cavities are not located in the same IR for the HEB and the main rings, the energy saw tooth could lead to different local beam energies between the injector, the electron and the positron ring which must be considered [105]. Future studies will show the most suitable injection technique for the 4-IP FCC-ee lattice.

RF sections

Although beams are injected at the nominal energy into the main rings, energy is lost due to, for instance, synchrotron radiation, beamstrahlung or longitudinal impedance sources. The "FCC-ee GHC V22" optics foresees elliptical cavities with frequencies of

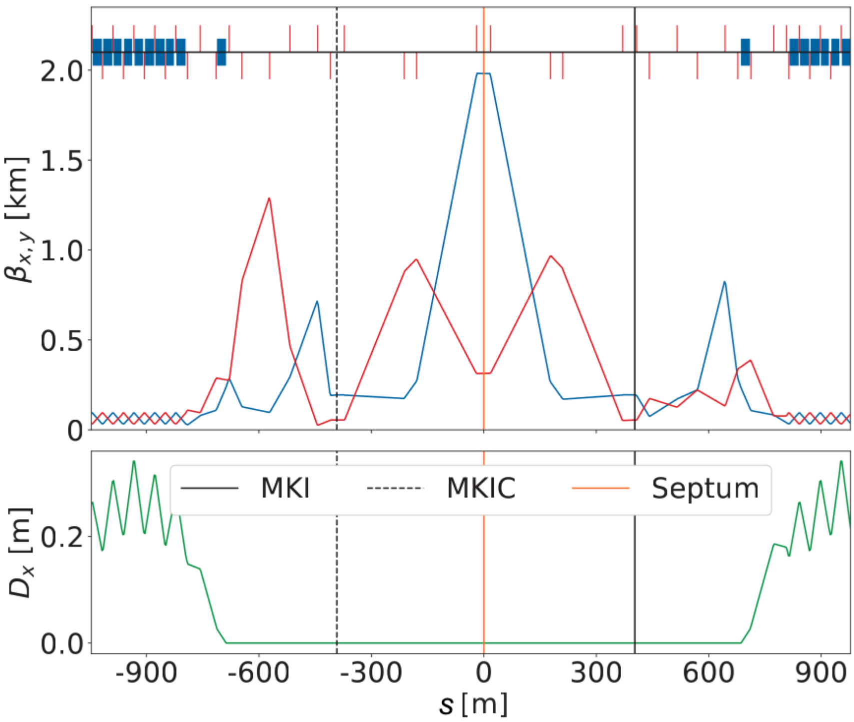

Fig. 2.9 Lattice and optics for on-momentum injection using a multipole kicker (MKI) and a correction magnet (MKIC) for a 2-IP lattice. The beam direction is from left to right. In the lattice, dipoles, quadrupoles, and sextupoles are shown in blue, red, and green, respectively, while focusing and defocusing elements are positioned above and below the orbit. In the optics, horizontal and vertical betatron functions are shown in blue and red, respectively, while horizontal dispersion function is shown in green [92].

400 MHz and 800 MHz, whereby novel studies investigate the so-called "slotted waveguide elliptical" cavities with 600 MHz [106].

In the "FCC-ee GHC V22" optics, the RF cavities are installed in all four technical sections (PB, PF, PH, and PL). At the Z and the WW operation mode, separate RF cavities are foreseen for the electron and the positron beam with a beam crossing in the center of the straight section. Contrarily, at the ZH and $t\bar{t}$ mode the present design has common RF cavities and thus beams must cross before or after being accelerated. To reduce synchrotron radiation power on the RF cavities only the outgoing beam is deflected [73]. The lattices and terminology of quadrupoles for the straight sections hosting the RF-system are illustrated schematically in Fig. 2.10 for "FCC-ee GHC V22 Z" (top) and "FCC-ee GHC V22 $t\bar{t}$" (bottom) optics. The corresponding optics are presented in Fig. 2.11.

It is worth noting that in the Version 2023 of the FCC-ee GHC optics, to control the range of CM energy fluctuations at all the IPs, RF cavities are no longer installed in all technical sections. Instead, two RF sections (PL and PH) are foreseen at the highest beam energy stage ($t\bar{t}$ mode) and only one (PH) for the other three lower operation energies (Z mode, WW mode, and ZH mode). Especially at the Z mode and the WW mode, placing the collider RF cavities in only one technical section is crucial for precision physics requirements [97], since this allows for keeping the CM energy constant within a difference of few keV at all the IPs when considering losses from synchrotron radiation and beamstrahlung [107].

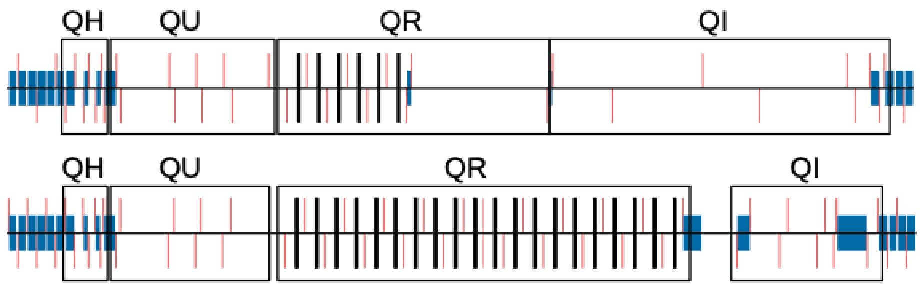

Fig. 2.10 Terminology of quadrupole types in the RF insertions of "FCC-ee GHC V22 Z" (top) and "FCC-ee GHC V22 $t\bar{t}$" (bottom) optics. Dipoles, quadrupoles, and RF cavities are shown in blue, red, and black, respectively, while focusing and defocusing elements are positioned above and below the horizontal axis [92].

2.2.2 FCC-ee LCC optics

Aligned with the four energy stages (Z mode, WW mode, ZH mode, and $t\bar{t}$ mode) of the FCC-ee GHC optics, the other alternative lattice design, known as the Local Chromaticity Correction (LCC) optics, was proposed by P. Raimondi in 2022 [94, 95]. This section presents the Version 2022 of this optics, referred to as "FCC-ee LCC V22" optics, also known as "FCC-ee HFD" optics [99]. There are also two specific variations of this optics tailored for different operational modes: the "FCC-ee LCC V22 Z" optics, designed for the Z mode, and the "FCC-ee LCC V22 $t\bar{t}$" optics, developed for the $t\bar{t}$ mode.

Arc and emittance

Based on a hybrid FODO lattice [108], a particular case of the multi-bend achromat (MBA) lattice [109], the design of the eight arcs in the "FCC-ee LCC V22" optics incorporates cells with a uniform length of approximately 65 m across all the energy stages. The periodic super-cell extends to around 300 m, containing 10 quadrupoles with symmetrically interleaved sextupoles. As depicted at the top of Fig. 2.12, the arc lattice

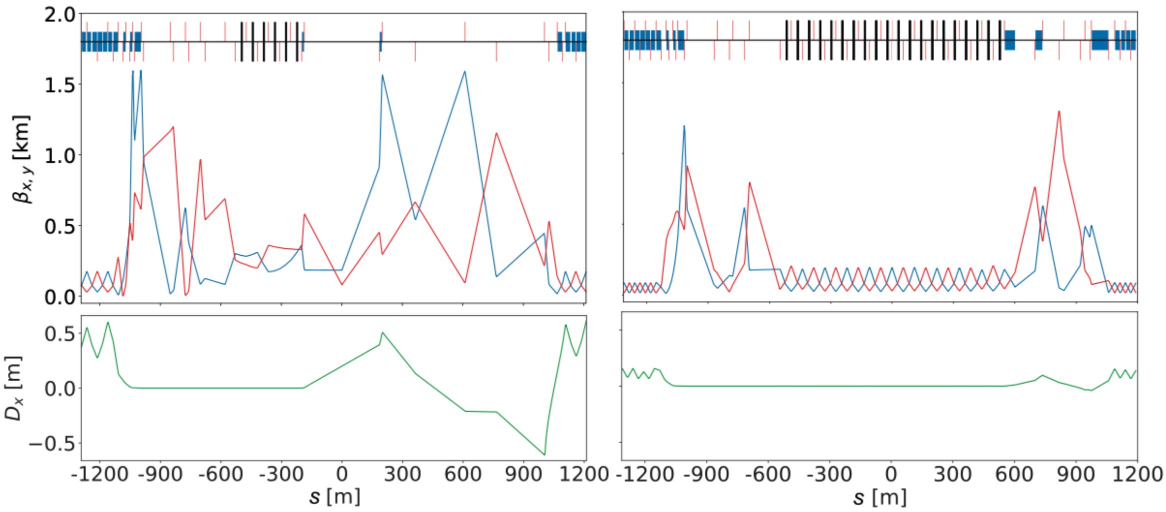

Fig. 2.11 Lattices and optics of the RF insertion of the “FCC-ee GHC V22 Z” (left) and “FCC-ee GHC V22 $\mathrm{t\bar{t}}$” (right) optics. The beam direction is from left to right. In the lattice, dipoles, quadrupoles, and RF cavities are shown in blue, red, and black, respectively, while focusing and defocusing elements are positioned above and below the orbit. In the optics, horizontal and vertical betatron functions are shown in blue and red, respectively, while horizontal dispersion function is shown in green [92].

and optics for the “FCC-ee LCC V22 Z” configuration achieve a horizontal emittance of roughly 0.51 nm calculated using MAD-X. In the “FCC-ee LCC V22 $\mathrm{t\bar{t}}$” optics, the quadrupole strength is increased in the arcs to lower the betatron and dispersion functions, and control the horizontal emittance at higher beam energies, resulting in a horizontal emittance of about 2 nm, as shown at the bottom Fig. 2.12.

Interaction region

In contrast to the asymmetric IR lattice in the FCC-ee GHC optics, the FCC-ee LCC IR design is more symmetric and streamlined, resembling the final focus design of the CEPC IR [43]. The top of Fig. 2.13 illustrates the IR of the “FCC-ee LCC V22 Z” optics with the horizontal and vertical betatron functions (blue and red) at the IP with $\beta_x^* = 200, 0.8$ mm, while the bottom shows the IR of the “FCC-ee LCC V22 $\mathrm{t\bar{t}}$” optics with the horizontal and vertical betatron functions (blue and red) at the IP with $\beta_x^* = 1000, 1.6$ mm.

The “FCC-ee LCC V22” IR incorporates local chromaticity correction in both the horizontal and vertical planes using sextupoles. In addition, it also employs a crab-waist collision scheme with a crossing angle of 30 mrad. Unlike the virtual crab-waist scheme [73], the “FCC-ee LCC V22” IR uses dedicated additional sextupoles for this purpose.

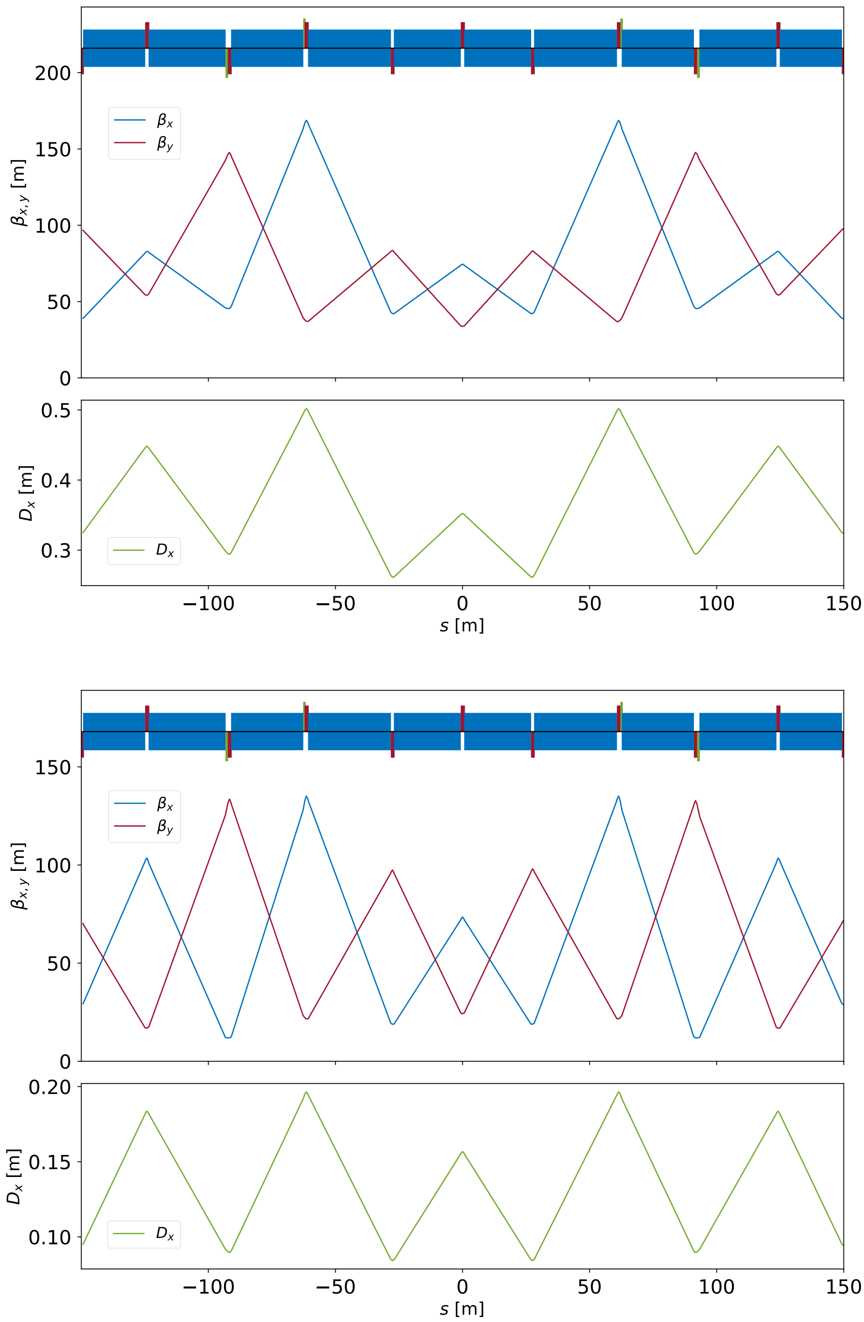

Fig. 2.12 Arc lattices and optics of the "FCC-ee LCC V22 Z" (top) and "FCC-ee LCC V22 $t\bar{t}$" (bottom) optics calculated using MAD-X for one periodic unit cell ($\sim$300 m), with $s = 0$ indicating the center of the super-cell. In the lattice, dipoles, quadrupoles, and sextupoles are shown in blue, red, and green, respectively, while focusing and defocusing elements are positioned above and below the orbit. In the optics, horizontal and vertical betatron functions are shown in blue and red, respectively, while horizontal dispersion function is shown in green.

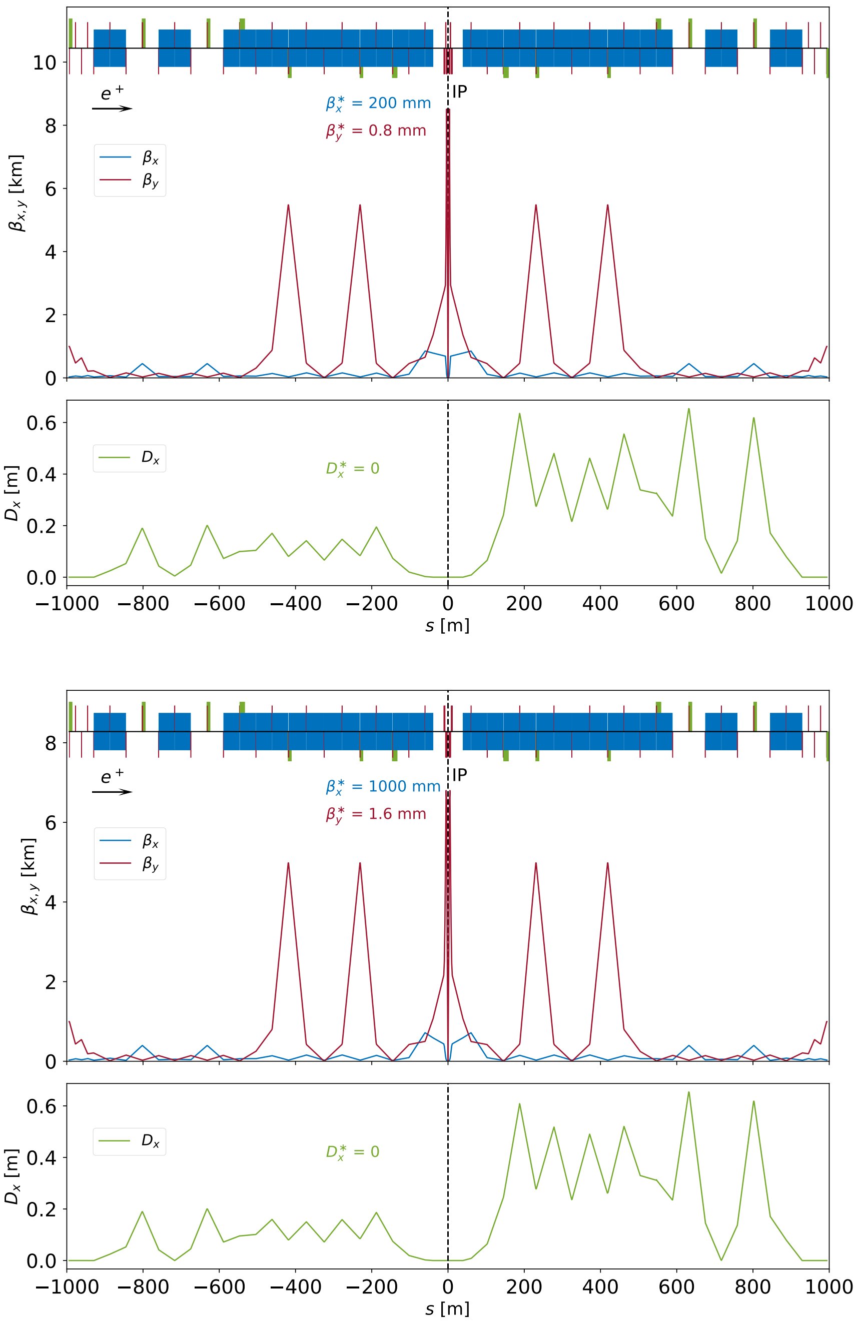

Fig. 2.13 IR lattices and optics of the “FCC-ee LCC V22 Z” (top) and “FCC-ee LCC V22 optics $t\bar{t}$” (bottom) calculated using MAD-X. The beam direction is from left to right; the dashed line $s = 0$ marks the location of IP. In the lattice, dipoles, quadrupoles, and sextupoles are shown in blue, red, and green, respectively, while focusing and defocusing elements are positioned above and below the orbit. In the optics, horizontal and vertical betatron functions are shown in blue and red, respectively, while horizontal dispersion function is shown in green.

Both the FCC-ee GHC and LCC optics are continuously optimized within the framework of FCC FS. The latest version, Version 2024 [99], has only minor changes in terms of the IR, compared to the Version 2022 optics detailed in this chapter. In this study, the monochromatization optics design is based on Version 2022 of these two standard baseline optics.

Chapter 3

FCC-ee GHC monochromatization IR optics design with horizontal IP dispersion

Based on the formula for the monochromatization factor λ (Eq. 1.28), it is possible to introduce nonzero horizontal or vertical dispersion at the IP to implement the monochromatization of the beams and hence to reduce the CM energy spread in a collider. Selecting the "FCC-ee GHC V22" optics (Subsec. 2.2.1) as the starting point, we explored three different monochromatization scenarios: horizontal only, vertical only, and combined horizontal/vertical dispersion at the IP. These scenarios were applied to both types of the "FCC-ee GHC V22" optics: the "FCC-ee GHC V22 Z" optics and the "FCC-ee GHC V22 $\mathrm{t\bar{t}}$" optics. Considering that monochromatization has not yet been experimentally tested, all newly proposed IR optics have been designed to remain compatible with a standard operation mode without dispersion at the IP, thereby minimizing potential risks.

Given that the horizontal bending magnets are already present in the IR of "FCC-ee GHC V22" standard optics for introducing the crossing-angle configuration and thus creating non-zero horizontal dispersion within the LCC system ($D_x \neq 0$ in LCC system and $D_x = 0$ close to the IP for high luminosity), the most straightforward approach to implementing the monochromatization in this FCC-ee lattice type is re-configuring these horizontal bending magnets to generate a nonzero horizontal dispersion at the IP ($D_x^* \neq 0$), while maintaining the same crossing angle. The nonzero D_x^* increases the IP beam size (Eq. 1.23) only in the horizontal plane. As indicated by from Eq. 1.85, a wide horizontal beam size σ_x^* helps to mitigate to impact of beamstrahlung on relative beam energy spread σ_δ, while preserving a small vertical beam size σ_y^* is crucial for maintaining a high luminosity. Taking into account the reference parameter table (Table 2.1) of the

"FCC-ee GHC V22" lattice, with a $\sigma^*_{x\beta}$ of the order of mm and a $\sigma_{\delta,\mathrm{SR}}$ of about 0.05 % at s-channel Higgs production energy ($\sim$125 GeV), a D^*_x of around 10 cm is required to achieve a λ of $5-8$ from Eq. 1.59.

In this chapter, such a monochromatization scenario with nonzero horizontal dispersion at the IP is presented. With the targeted IP parameters taken from the FCC-ee monochromatization self-consistent parameter optimization (Table 1.1): $\beta^*_{x,y} = 90, 1\,\mathrm{mm}$ with $D^*_x = 0.105\,\mathrm{m}$, the monochromatization IR optics design, based on each type of baseline standard optics ("FCC-ee GHC V22 Z" and "FCC-ee GHC V22 $\mathrm{t\bar{t}}$") was developed and optimized step by step [110–128] using MAD-X, followed by corresponding performance evaluations after integration into the FCC-ee global lattice.

3.1 Principle of horizontal IP dispersion generation

The IR of the "FCC-ee GHC V22" optics, as detailed in Subsec. 2.2.1, incorporates a large crossing angle of 30 mrad in the horizontal plane and a LCC system implemented only in the vertical plane, resulting in nonzero horizontal dispersion created by the weak horizontal dipole magnets at the two sides of the IP within the LCC system, namely "LCC horizontal dipole." Therefore, the nonzero horizontal dispersion at the IP, as required for monochromatization, can be generated by several sets of different configuration of these LCC horizontal dipoles.

3.1.1 "Three-angle" chicane structure

In the first FCC-ee monochromatization IR optics design presented in Ref. [110–114], all the IR LCC horizontal dipoles in the "FCC-ee GHC V22 Z" optics were split into three sets, with additional thin quadrupoles, each 1 m in length, inserted between these split sets, as shown in Fig. 3.1. This split was done to enhance the flexibility and optimize matching efficiency in MAD-X. By deliberately "mismatching" the horizontal dispersion in the LCC region, the required horizontal IP dispersion of $D^*_x = 0.105\,\mathrm{m}$ was achieved, in accordance with the FCC-ee monochromatization self-consistent parameters. The angles of two of the three split sets of the last LCC horizontal dipole farthest from the IP as marked in orange in Fig. 3.2, were then modified to restore the horizontal dispersion back to zero outside the LCC region, following a half chicane structure [116]. The IP betatron function were matched to be same with the FCC-ee monochromatization self-consistent parameters as: $\beta^*_{x,y} = 90, 1\,\mathrm{mm}$, while ensuring that the beam parameters at the entrance and exit of the IR remained consistent with the standard IR optics values in the absence of monochromatization.

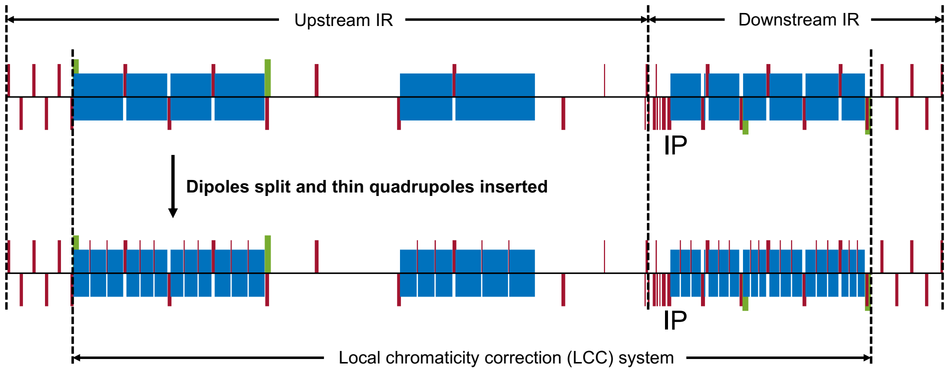

Fig. 3.1 Lattice of the “FCC-ee GHC V22 Z” optics (top) and the lattice after splitting the dipoles and inserting thin quadrupoles for its monochromatization implementation (bottom). Dipoles, quadrupoles, and sextupoles are shown in blue, red, and green, respectively, while focusing and defocusing elements are positioned above and below the orbit.

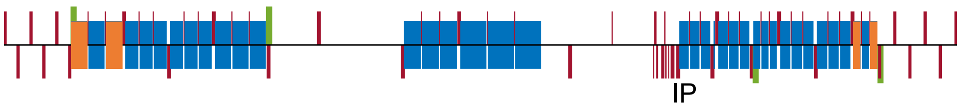

Fig. 3.2 Location of the half chicane structure (marked in orange) in the first FCC-ee monochromatization IR optics design based on the “FCC-ee GHC V22 Z” optics. Dipoles, quadrupoles, and sextupoles are shown in blue, red, and green, respectively, while focusing and defocusing elements are positioned above and below the orbit.

However, this half chicane structure significantly alters the IR orbit, resulting in differences in both the position and angle at the entrance and exit of the monochromatization IR orbit compared to the baseline orbit of the standard IR. This discrepancy makes it impossible to directly integrate the designed monochromatization IR back into the whole ring as a replacement for the standard IR. To address this issue, a new chicane structure with three angles, as schematically shown in Fig. 3.3, has been proposed in Ref. [115–128], so-called “three-angle” chicane structure. In this configuration, where L_{12} is the distance from Angle 1 to Angle 2 and L_{23} is the distance from Angle 2 to Angle 3, the ratio of the values of Angle 1 and Angle 3 exhibits an inverse proportionality with respect to the ratio of L_{12} and L_{23}:

$$\theta_1 = \frac{L_{23}}{L_{12}}\theta_3 \,. \tag{3.1}$$

The value of Angle 2 is opposite in sign and equal in magnitude to the sum of the θ_1 and θ_3:

$$\theta_2 = -(\theta_1 + \theta_3) . \tag{3.2}$$

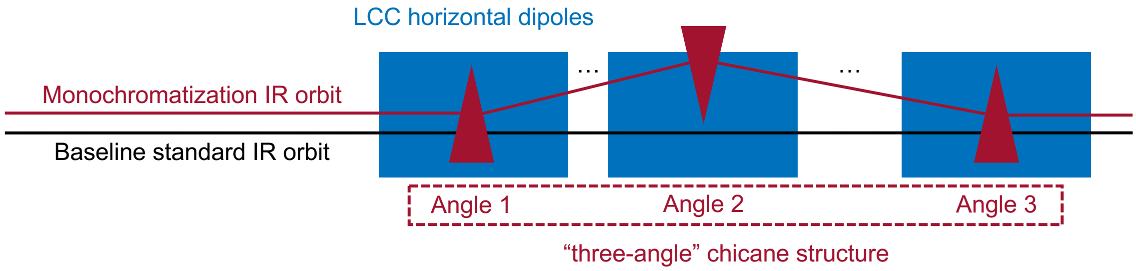

Fig. 3.3 Layout of the "three-angle" chicane structure. The IR LCC horizontal dipoles are depicted in blue, while the angles of the chicane structure are in red. The baseline standard orbit is shown in black, and the monochromatization orbit is in red.

The "three-angle" chicane structure was first implemented in the three split sets of the last upstream and downstream LCC horizontal dipoles farthest from the IP [115] (marked in orange at the top of Fig. 3.4) based on the "FCC-ee GHC V22 Z" optics, and later in one of three split sets of the last three upstream and downstream LCC horizontal dipoles [116–118] (marked in orange at the bottom of Fig. 3.4). The results

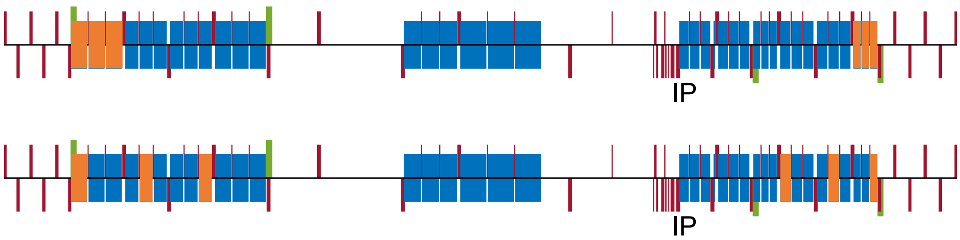

Fig. 3.4 Location of the "three-angle" chicane structure (marked in orange) in the preliminary FCC-ee monochromatization IR optics design based on the "FCC-ee GHC V22 Z" optics. The top one is the case in Ref. [115], while the bottom one is the case in Ref. [116–118]. Dipoles, quadrupoles, and sextupoles are shown in blue, red, and green, respectively, while focusing and defocusing elements are positioned above and below the orbit.

of the monochromatization IR optics design of the later case are depicted in Fig. 3.5. In this design, the phase advances between the IP and the LCC sextupole pairs were also matched to those values of the standard optics (Fig. 2.7) to facilitate further local chromaticity corrections.

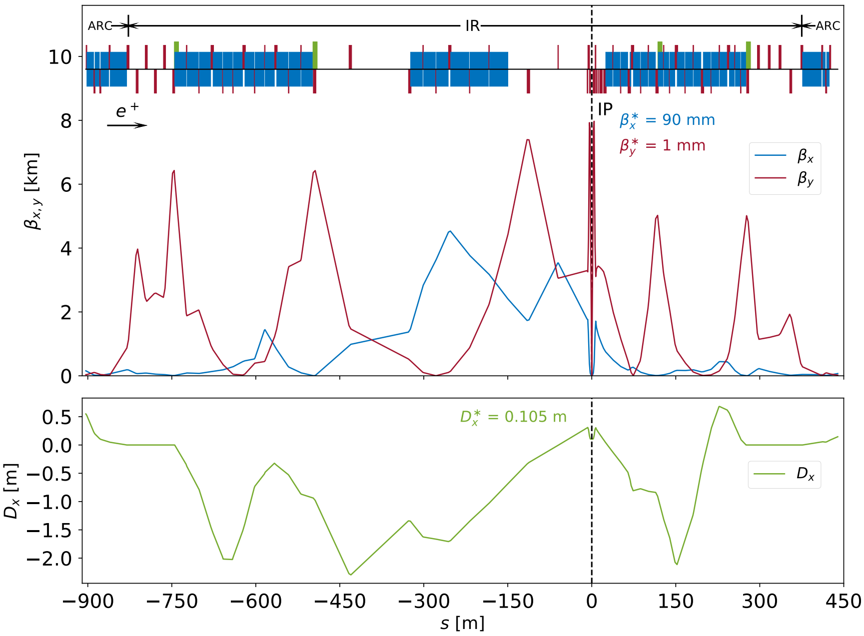

Fig. 3.5 First monochromatization IR optics design with "three-angle" chicane structure based on the "FCC-ee GHC V22 Z" optics [117] calculated using MAD-X. The beam direction is from left to right; the dashed line $s = 0$ marks the location of IP. In the lattice, dipoles, quadrupoles, and sextupoles are shown in blue, red, and green, respectively, while focusing and defocusing elements are positioned above and below the orbit. In the optics, horizontal and vertical betatron functions are shown in blue and red, respectively, while horizontal dispersion function is shown in green.

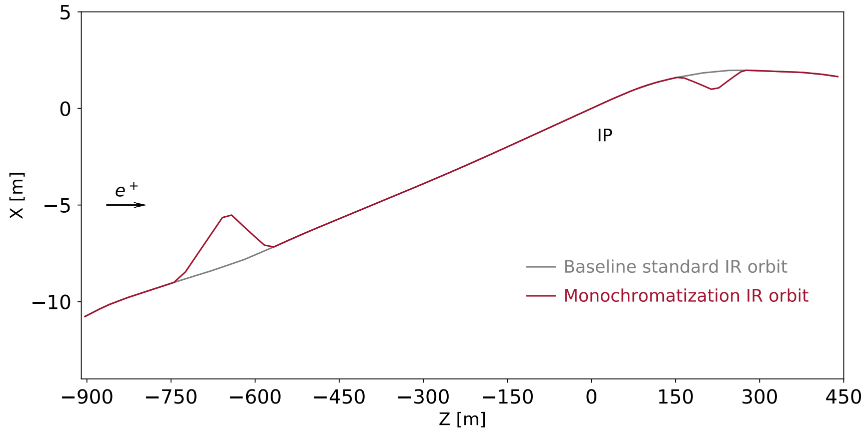

Fig. 3.6 Comparison between the "FCC-ee GHC V22 Z" IR orbit (grey) and the first designed monochromatization IR orbit (red) with "three-angle" chicane structures. The beam direction is from left to right; the point $\mathrm{X} = 0, \mathrm{Z} = 0$ marks the location of IP.

Compared to the baseline IR orbit of the "FCC-ee GHC V22" optics, the orbit of the designed monochromatization IR with the two "three-angle" chicane structures differs from the standard orbit only at the locations where these chicanes are implemented, as shown in Fig. 3.6. The positions and angles at the entrance and exit of the two orbits are identical, allowing for the global implementation of the designed monochromatization IR.

3.1.2 Smooth chicane structure for mitigating horizontal emittance blow-up

In Fig. 3.6, we observe that the angles of added chicane structures are significantly larger than those of the original LCC horizontal dipoles. This results in a high level of synchrotron radiation and a blow-up of the horizontal emittance. After the global implementation of this first monochromatization IR optics and completing all the corrections that described in Sec. 3.2.3, the horizontal emittance of the monochromatization ring optics with the "three-angle" chicane structure at all four IPs increased to 400 nm, which is two orders of magnitude higher than the that of the standard mode (~ 1 nm) [117]. This substantial increase in horizontal emittance leads to a larger IP betatron horizontal beam size $\sigma^*_{x\beta}$, thereby reducing the monochromatization factor λ to nearly 1, using Eq. 1.28. This implies that, according to Eq. 1.29, the CM energy spread will not decrease, even with the introduction of nonzero horizontal dispersion at the IP.

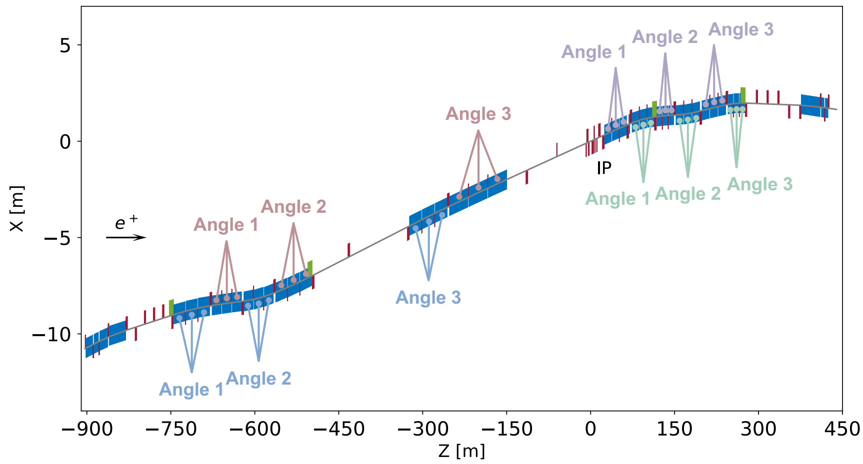

Fig. 3.7 Optimized monochromatization orbit with four sets of smooth close orbit "three-angle" chicane structure marked in different colors. The beam direction is from left to right; the point X = 0, Z = 0 marks the location of IP. Dipoles, quadrupoles, and sextupoles are represented in blue, red, and green, respectively, while focusing and defocusing elements are positioned above and below the orbit [119–128].

To mitigate the horizontal emittance blow-up, we implemented two longer "three-angle" chicane structures to both upstream and downstream IR, resulting in a total of four chicane structures added to the twelve LCC horizontal dipoles within the IR. Each chicane angle was equally distributed across the three split dipole sets. After performing step-by-step matching and optimization using MAD-X, we ultimately integrated four sets of smooth close orbit "three-angle" chicane structure into the LCC system. Fig. 3.7 shows this optimized monochromatization orbit based on the "FCC-ee GHC V22 Z" baseline standard optics. With this configuration, the horizontal emittance was successfully reduced to about 2 nm [119–128].

3.2 Application to FCC-ee GHC optics

In the following, we detail the implementation of monochromatization by introducing horizontal IP dispersion in the IR of the "FCC-ee GHC V22 Z" and "FCC-ee GHC V22 $\mathrm{t\bar{t}}$" optics, as explained in Sec. 3.1. This is followed by the design of the corresponding standard optics that align with the monochromatization orbit. Finally, the global integration of these optics within the framework of monochromatization is presented.

3.2.1 Monochromatization IR optics design

With the principle of horizontal IP dispersion generation, we performed first the monochromatization IR optics design using MAD-X based on the "FCC-ee GHC V22 Z" baseline standard optics using the following steps and constraints:

Design steps:

1. Switch off the RF cavities in standard optics and calculate the optics function in the whole ring without considering the synchrotron radiation energy loss.
2. Get the Twiss function ($\beta_{x,y}$ and $\alpha_{x,y}$), dispersion function ($D_{x,y}$) and its slope ($D'_{x,y}$) at the IR entrance, IR exit and IP.
3. Extract the IR from the global ring, for instance, we extracted the IR at the straight section labeled as "PG" in Fig. 2.2, from the marker "FF1.2" to "FG.5."
4. Separate the upstream IR (from "FF1.2" to "IP") and downstream IR (from "IP" to "Fg.5"), then reflect the lattice of upstream IR, as it is easier to match with a starting point that has simple optical functions, especially since the optical functions at the IP are characterized by: $\alpha_{x,y} = 0$, $D'_{x,y} = 0$.

5. For each LCC horizontal dipole with a length of L and an angle of θ, replace it with three identical horizontal dipoles, each with a length of $(L-2)/3$ and a angle of $\theta/3$, and insert two thin quadrupoles, each with a length of 1 m and a zero initial strength, between the three dipoles.

6. Add the angles with a zero initial angle for the each set of the "three-angle" chicane structures, following the layout depicted in Fig. 3.7. Note that we need to introduce the chicane angles for only the last and the second-to-last upstream and downstream LCC horizontal dipoles farthest from the IP as variables. The other two angles in each set of the "three-angle" chicane structures can be determined by these variable angles, in accordance with shown in Fig. 3.3. For instance, for the outer set of chicane structures in the downstream IR shown in Fig. 3.7, with Angle 3 defined as the variable θ_3, Angle 1 is determined by Eq. 3.1, and Angle 2 is given by Eq. 3.2.

7. Maintain the strength of the inserted thin quadrupoles and the additional chicane angles as zero. Calculate the optical functions for the downstream IR and the reflected upstream IR, respectively, using the initial optical functions at the IP from the global ring optical function. Ensure that the optical functions at the entrance and exit of the IR match those taken from the global ring.

8. Give a small IP horizontal dispersion of about 10 mm first. Vary the strength of all the quadrupoles and the additional chicane angles to match all constraints that will be discussed later. Note that it is important to find the chicane angles as low as possible for a smoother orbit.

9. Use the matched strength of each quadrupole and the angle of each chicane as a new initial condition. Increase the IP horizontal dispersion to 20 mm, and match all the constraints again. Repeat this step until the required IP horizontal dispersion for monochromatization is achieved.

10. Reflect the designed monochromatization upstream IR back to its normal orientation, and connect it with the designed monochromatization downstream IR.

Matching constraints:

1. The optical functions at the IP match the FCC-ee monochromatization self-consistent parameters (Table 1.1): $\beta^*_{x,y} = 90, 1\,\mathrm{mm}$, and $D^*_x = 0.105\,\mathrm{m}$, with all other optical functions maintained at zero.

2. The optical functions at the entrance and exit of the IR match those of the standard IR optics without monochromatization.

3. The dispersion-free region before the arc in either upstream or downstream IR should be restored.

4. As depicted in Fig. 2.7, the phase advance between the IP and the inner sextupole pairs should be $\mu_{x,y} = \pi, 1.5\pi$. The phase advance between the IP and the outer sextupole pairs should be $\mu_{x,y} = 2\pi, 2.5\pi$.

5. The four peak values of the vertical betatron function at the locations of the sextupole pairs should be the same.

6. The horizontal dispersion at the locations of the inner sextupole pairs should be nonzero to control the strength of the sextupoles for local chromaticity correction.

The top panel of Fig. 3.8 shows the monochromatization IR lattice and optics based on "FCC-ee GHC V22 Z" optics satisfied all the constraints mentioned above.

3.2.2 Orbit compatibility with standard operation mode

Fig. 3.10 compares the "FCC-ee GHC V22 Z" IR orbit and its corresponding monochromatization IR orbit. Although the orbit of the monochromatization IR with four sets of smooth close orbit "three-angle" chicane structure is slightly different from the standard baseline orbit, the positions and the angles at the entrance and exit of the two orbits are identical.

As the monochromatization IR orbit differs from the original IR orbit, it becomes necessary to rematch the standard optics without IP dispersion utilizing the monochromatization orbit (incorporating chicane structures) to enable further comparison and demonstrate the orbit compatibility with the standard operation mode. By fixing the angles of all horizontal dipoles within the IR, thus preserving the monochromatization orbit, we re-matched the beam parameters at the IP to be aligned with those of the original optics while maintaining all the other matching constraints. The results of this process are presented in the bottom panel of Fig. 3.8.

A similar approach was also applied to the "FCC-ee GHC V22 $t\bar{t}$" optics [123]. Fig. 3.11 compares the "FCC-ee GHC V22 $t\bar{t}$" IR orbit and its monochromatization orbit. Fig. 3.9 shows the monochromatization IR optics with an horizontal IP dispersion of 0.105 m at the top, and the corresponding standard mode IR optics with orbit compatibility at the bottom.

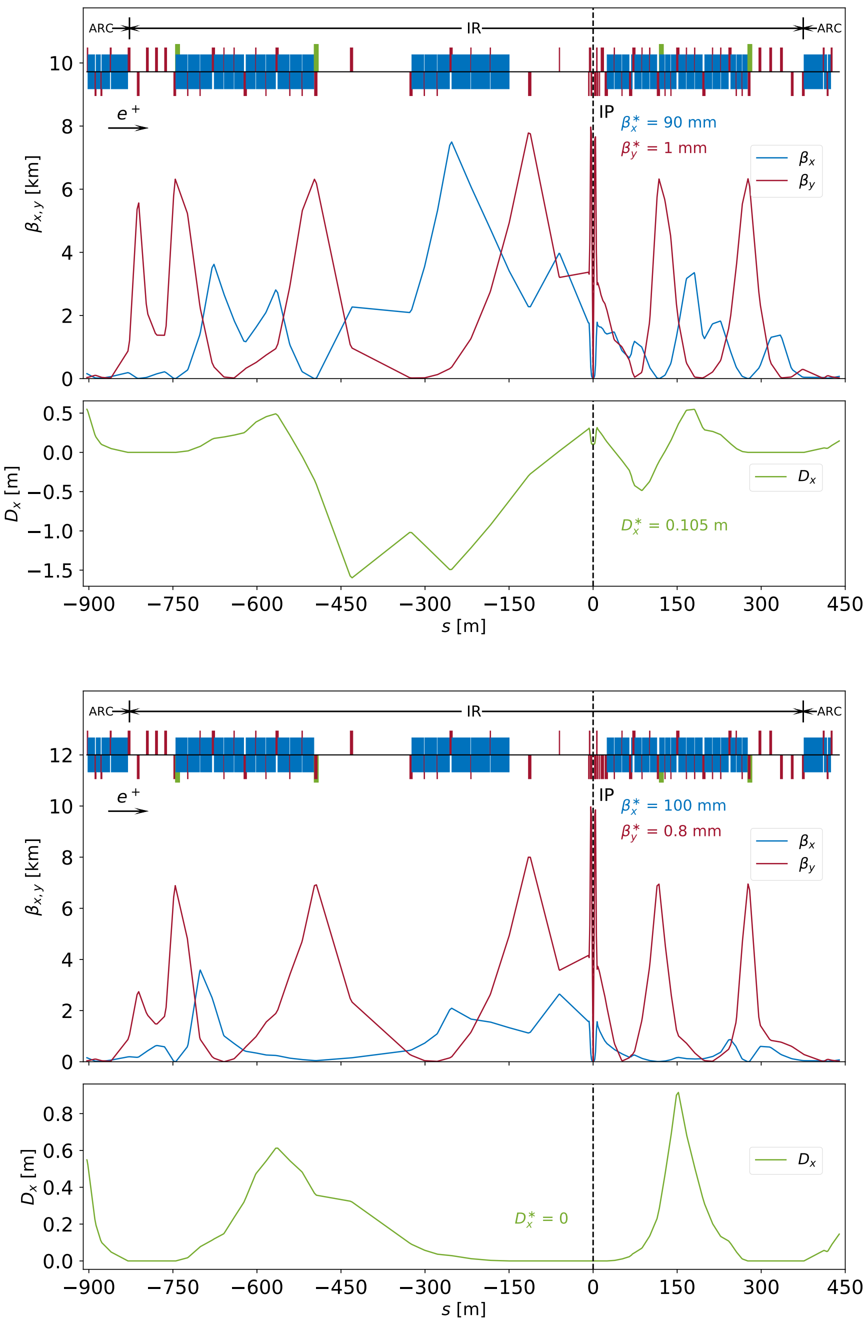

Fig. 3.8 Lattices and optics of monochromatization IR with nonzero horizontal IP dispersion of 0.105 m (top) and the corresponding standard mode IR with orbit compatibility (bottom) based on the "FCC-ee GHC V22 Z" optics calculated using MAD-X. The beam direction is from left to right; the dashed line $s = 0$ marks the location of IP. In the lattice, dipoles, quadrupoles, and sextupoles are shown in blue, red, and green, respectively, while focusing and defocusing elements are positioned above and below the orbit. In the optics, horizontal and vertical betatron functions are shown in blue and red, respectively, while horizontal dispersion function is shown in green.

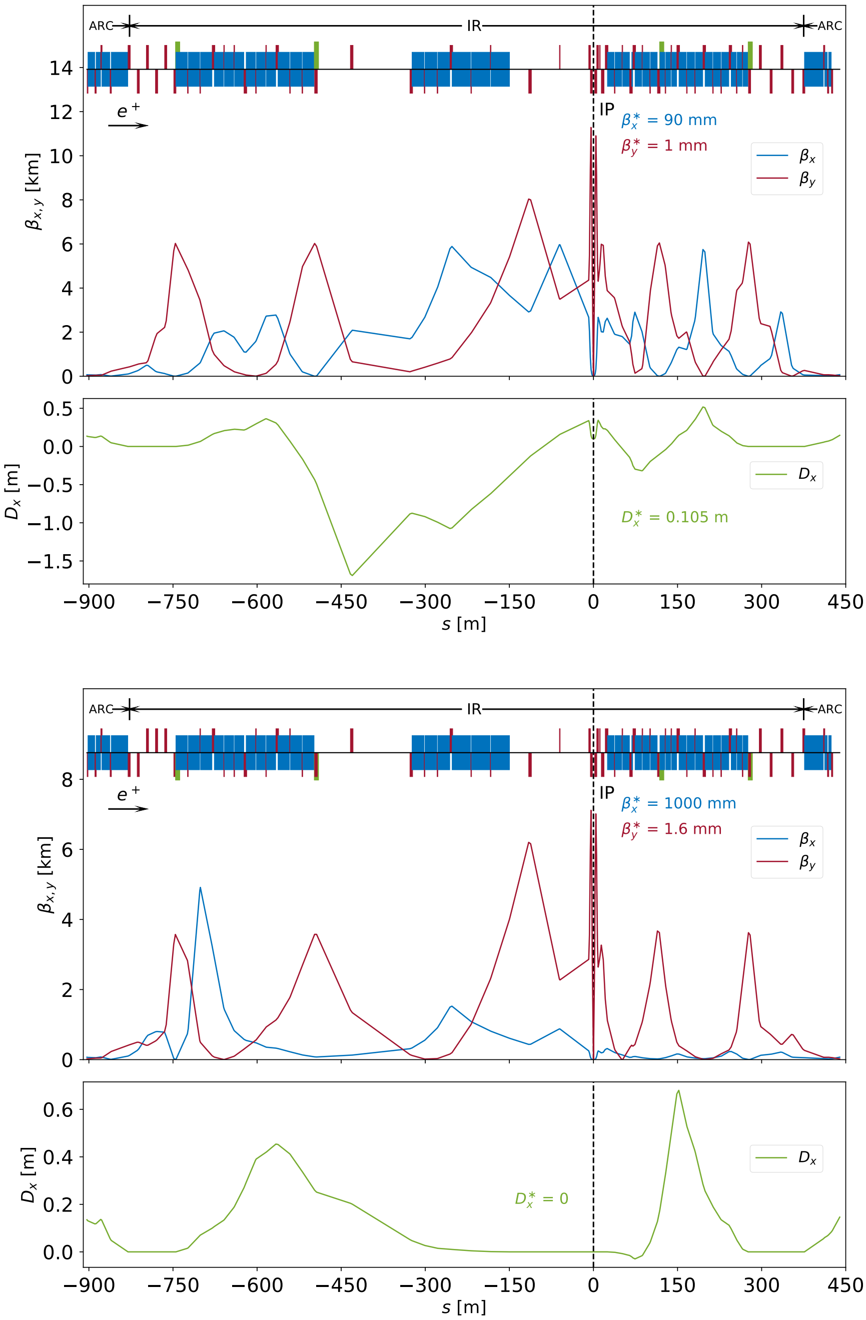

Fig. 3.9 Lattices and optics of monochromatization IR with nonzero horizontal IP dispersion of 0.105 m (top) and the corresponding standard mode IR with orbit compatibility (bottom) based on the “FCC-ee GHC V22 $t\bar{t}$” optics calculated using MAD-X. The beam direction is from left to right; the dashed line $s = 0$ marks the location of IP. In the lattice, dipoles, quadrupoles, and sextupoles are shown in blue, red, and green, respectively, while focusing and defocusing elements are positioned above and below the orbit. In the optics, horizontal and vertical betatron functions are shown in blue and red, respectively, while horizontal dispersion function is shown in green.

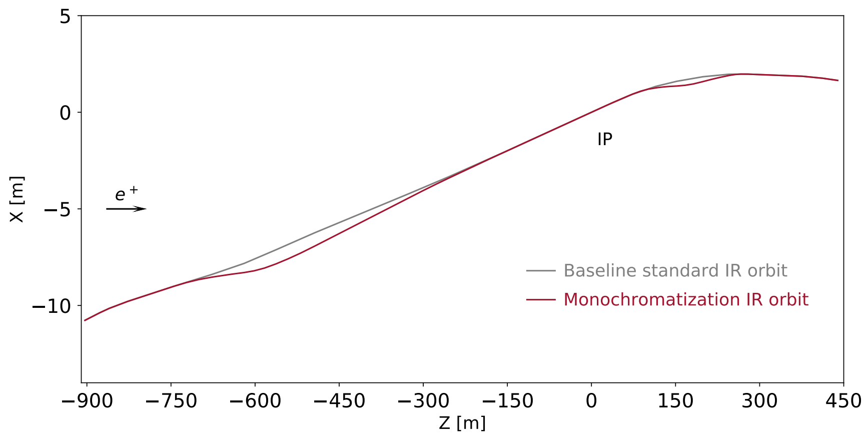

Fig. 3.10 Comparison between the “FCC-ee GHC V22 Z” IR orbit (grey) and its monochromatization IR orbit (red) with four sets of smooth close orbit “three-angle” chicane structure. The beam direction is from left to right; the point $X = 0, Z = 0$ marks the location of IP.

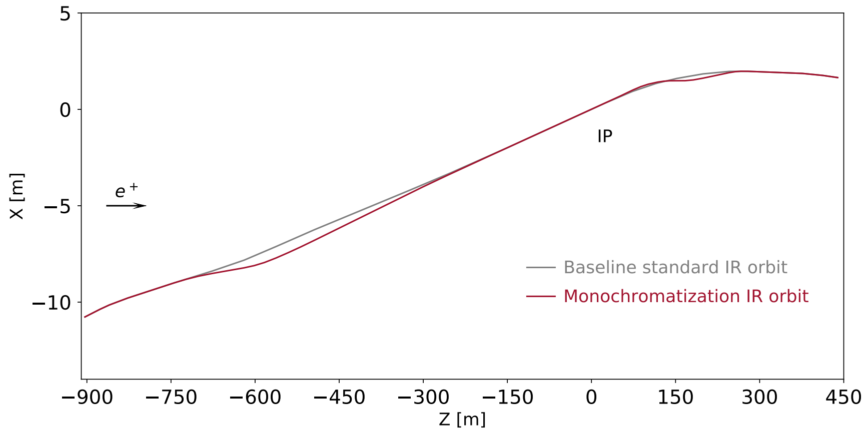

Fig. 3.11 Comparison between the “FCC-ee GHC V22 $t\bar{t}$” IR orbit (grey) and its monochromatization IR orbit (red) with four sets of smooth close orbit “three-angle” chicane structure. The beam direction is from left to right; the point $X = 0, Z = 0$ marks the location of IP.

3.2.3 Implementation in the global lattice

With the same beam parameters and orbit at the entrance and exit of the monochromatization IR as the standard one, it was successfully inserted into the entire ring as a replacement of the original standard IR for global performance evaluation. The following corrections were performed before the performance calculation [117–129].

Local chromaticity correction

As described in Sec. 2.2.1, the local vertical chromaticity is corrected by the inner sextupole pairs, positioned at locations with nonzero horizontal dispersion on both sides of the IP, referred to as “chromatic sextupoles.” The aberrations caused by these chromatic sextupoles are canceled by the outer sextupole pairs, which are located at dispersion-free points. These outer sextupoles also serve the purpose of crab-waist transformation [38–40], and are referred to as “crab sextupoles.”

For the local chromaticity correction of the monochromatization optics, we first matched the vertical chromaticity from the crab sextupoles to the IP to zero by adjusting the strength of the chromatic sextupoles, denoted by the subindex “chrom.” Then, we calculated the strength of the crab sextupoles, denoted by the subindex “CS,” for crab-waist collision scheme, using the following from [73]:

$$k_{2,\mathrm{CS}} = k_{2,\mathrm{chrom}} - \frac{F}{\theta_c \beta_y^* \beta_y} \sqrt{\frac{\beta_x^*}{\beta_x}} \tag{3.3}$$

with $\beta_{x,y}$ the betatron function at the locations of crab sextupole pairs. The crab factor F is determined from beam-beam studies, with values of 97% for the Z mode, and 87% for the WW mode [129]. We temporarily set it as 90% for our monochromatization optics, so that the nonlinearity introduced by crab sextupoles will be counteracted by the crab sextupoles located on the other side of the IP.

Global chromaticity correction

As the local chromaticity correction has only been completed in the vertical plane, the global chromaticity correction will use the arc sextupoles to correct both the horizontal and vertical chromaticities in the arc, as well as the horizontal chromaticity in the IR. There are two types of sextupoles in the arc: focusing and defocusing sextupoles. These sextupoles generate positive chromaticity, which can offset the negative chromaticity produced by the quadrupoles in the ring, resulting in a positive overall chromaticity.

Positive chromaticity is beneficial for beam stability as it provides damping effects. For the global chromaticity correction for the designed monochromatizaiton optics, the strength of all focusing and defocusing sextupoles was each multiplied by two respective coefficients. By varying these two coefficients, the global horizontal and vertical chromaticities were matched to a value of 5, consistent with the values in the original standard optics design.

Tune correction

By adjusting the strength of the quadrupoles in the RF insertions (Fig. 2.11), the horizontal and vertical tunes, $Q_{x,y}$, were matched to those of the standard mode. The slopes of the horizontal and vertical betatron functions, $\alpha_{x,y}$, at the center of the RF insertion were matched to zero, while maintaining the beam parameters at all four IPs. After this process, the lattices and optics of the RF insertion of the designed monochromatization optics based on the "FCC-ee GHC V22 Z" and "FCC-ee GHC V22 $\mathrm{t\bar{t}}$" optics are illustrated at the top and bottom of Fig. 3.12, respectively. All the RF cavities were kept in the dispersion-free region.

Synchrotron radiation energy loss compensation

For compensating the energy loss due to synchrotron radiation, we switched on the RF cavities and matched the value of the energy difference ΔE, divided by the reference momentum p times the velocity of light c:

$$t' = \frac{\Delta E}{pc} \tag{3.4}$$

to zero by varying the phase of the RF cavities. The voltage of the RF cavity V_{RF} affects the synchrotron tune Q_s according to the relation [130]:

$$Q_s^2 = \frac{\alpha_{\mathrm{C}} h}{2\pi E_0}\sqrt{e^2 V_{\mathrm{RF}}^2 - U_0^2} \tag{3.5}$$

with h the Harmonic number (Eq. A.22), e the elementary charge and U_0 the energy loss per turn (Eq. A.10). This, in turn, influences the bunch length σ_z as described in Eq. A.17. Therefore, an appropriate RF cavity voltage was selected to achieve a bunch length of about 4 mm, which falls between the bunch length of the Z mode and WW mode.

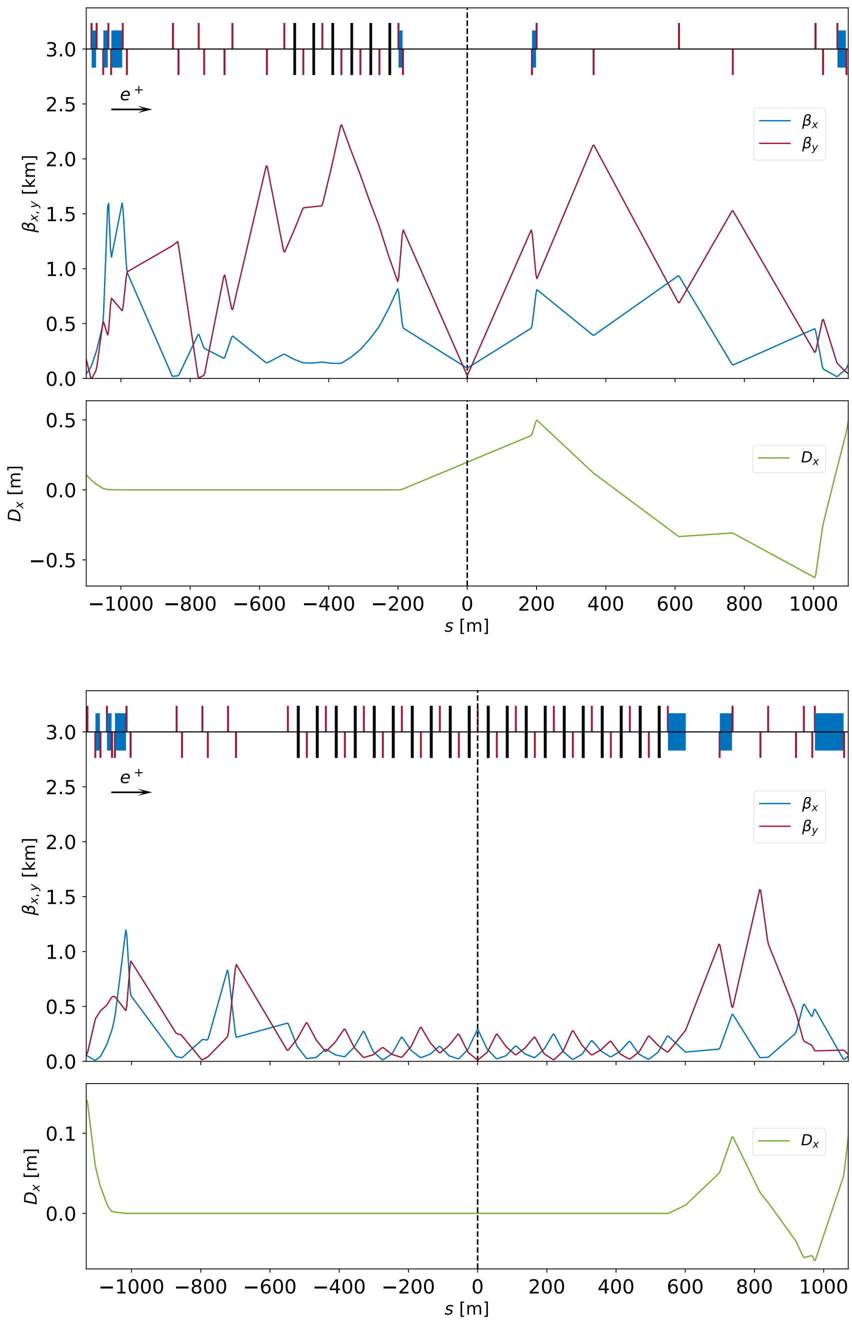

Fig. 3.12 Lattices and optics of the RF insertion after tune correction of the global implementation of monochromatization IR optics with nonzero horizontal IP dispersion based on the “FCC-ee GHC V22 Z” (top) and “FCC-ee GHC V22 $t\bar{t}$” (bottom) optics calculated using MAD-X. The beam direction is from left to right, with the dashed line $s = 0$ indicating the center of the RF insertion. In the lattice, dipoles, quadrupoles, and RF cavities are shown in blue, red, and black, respectively, while focusing and defocusing elements are positioned above and below the orbit. In the optics, horizontal and vertical betatron functions are shown in blue and red, respectively, while horizontal dispersion function is shown in green.

3.3 Performance evaluation

3.3.1 Global optical performance

After the global implementation of the designed monochromatization IR optics, its global performance, including the impact of beamstrahlung, was evaluated analytically. This evaluation considered the two proposed FCC-ee monochromatization collision schemes shown in Fig. 1.9: CC scheme with crab cavities (head-on collision configuration) and IRS scheme without crab cavities (crossing-angle collision configuration). It should be noted that the use of crab cavities is not part of the baseline collision scheme for FCC-ee, as the design assumes a large Piwinski angle, which does not need or even contradicts crab cavities [131]. Consequently, no dedicated studies on crab cavities for the FCC-ee have been conducted to date. This thesis retains an analysis of the performance of the monochromatization scheme under head-on collision mode, primarily to provide a comparison with the crossing-angle collision mode, thereby enabling a more comprehensive evaluation of the impact of the crossing angle on the performance of the monochromatization scheme.

The values of energy loss per turn U_0 (Eq. A.10), momentum compaction factor α_{C} (Eq. A.18), synchrotron tune Q_s (Eq. A.19), radiation longitudinal damping time τ_E (Eq. A.9), relative beam energy spread σ_δ (Eq. A.16), horizontal emittance ε_x (Eq. A.14), and bunch length σ_z (Eq. A.17) were calculated using MAD-X, considering only the effects of synchrotron radiation. The vertical emittance ε_y was calculated with the assumed 0.2% coupling ratio (Eq. 2.3) (full current) of motion between the horizontal and vertical planes. The beam current I (Eq. A.21) was maximized based on the maximum allowable total synchrotron radiation power loss P_{SR} of 50 MW, following the relation $P_{\mathrm{SR}} = U_0 I$ (Eq. A.20). The beam-beam tune-shift $\xi_{x,y}$ was calculated using Eq. 1.43 for the head-on collision configuration and Eq. 1.61 for the crossing-angle collision configuration. The CM energy spread σ_W was calculated using Eq. 1.29 for the head-on collision configuration and Eq. 1.60 for the crossing-angle collision configuration. Finally, the luminosity per IP $\mathcal{L}$ was calculated using Eq. 1.29 for the head-on collision configuration and Eq. 1.58 for the crossing-angle collision configuration.

The relative beam energy spread σ_δ, horizontal and vertical emittance $\varepsilon_{x,y}$ with the impact of beamstrahlung were calculated by solving Eq. 1.84 and Eq. 1.85 together. Different coefficients V were used for the two different collision schemes: Eq. 1.87 for the head-on collision configuration and Eq. 1.88 for the crossing-angle collision configuration. The bunch length σ_z with beamstrahlung impact was derived from Eq. 1.82. Then, the beam-beam tune-shift $\xi_{x,y}$, CM energy spread σ_W, and luminosity per IP $\mathcal{L}$ were recalculated, accounting for the impact of beamstrahlung.

The results of the analytical global performance evaluation for the monochromatization IR optics based on the "FCC-ee GHC V22 Z" optics are summarized in two tables: Table 3.1 for the head-on collision configuration and Table 3.2 for the crossing-angle configuration. Parameters due only to synchrotron radiation are marked with "SR," while those including the impact of beamstrahlung are marked with "BS." For comparison, the first column, labeled "Standard ZES," presents an energy-scaled (ES) optics configuration without realistic implementation. Its performance parameters were calculated after increasing the beam energy of the "FCC-ee GHC V22 Z" optics from 45.6 GeV to 62.5 GeV, followed by completing all corrections and synchrotron radiation power loss compensation. The optics labeled "MonochroM ZH4IP" integrates the IP horizontal dispersion generation monochromatization IR optics at all four IPs, while "MonochroM ZH2IP" does so at only two IPs. The designation "MonochroM ZHS" refers to the re-matched standard optics design that is orbit-compatible with the "MonochroM ZH4IP" optics. The number of bunches per beam n_b is constrained by two factors: its minimum is limited by the beam-beam tune shift limitation [132]:

$$\xi_y \leq 0.14 \,, \tag{3.6}$$

and its maximum is capped at a value of 12000 by the harmonic number h (Eq. A.22) and a minimum bunch spacing of 25 ns at FCC-ee. To select an appropriate n_b, we plotted the trade-off between the luminosity per IP $\mathcal{L}$ and the CM energy spread σ_W of the "MonochroM ZH4IP" optics, as a function of n_b, including the beamstrahlung impact under the crossing-angle collision configuration, as shown in Fig. 3.13. From this analysis, we determined that n_b should be larger than 1,500 due to the limitation of beam-beam tune shift (Eq. 3.6). The $\mathcal{L}$ remains relatively constant as the n_b increases, while the σ_W decreases. Therefore, we selected the maximum n_b of 12000 to achieve a minimum bunch population N_b, thereby minimizing the impact of beamstrahlung on the efficiency of monochromatization.

Under the head-on collision configuration, the relative beam energy spread σ_δ of the "Standard ZES" optics increases from 0.054% to 0.115%, resulting to a corresponding increase in the CM energy spread σ_W from 47.47 MeV to 101.89 MeV. This rise in σ_δ also causes the bunch length σ_z to grow from 4.09 mm to 8.61 mm. The beam-beam tune shift $\xi_{x,y}$ and luminosity per IP $\mathcal{L}$ are not affected by the beamstrahlung impact. However, ξ_y exceeds its limitation (Eq. 3.6). With nonzero horizontal dispersion at the IP ($D_x^* \neq 0$), the horizontal emittance ε_x of the "MonochroM ZH4IP" optics significantly

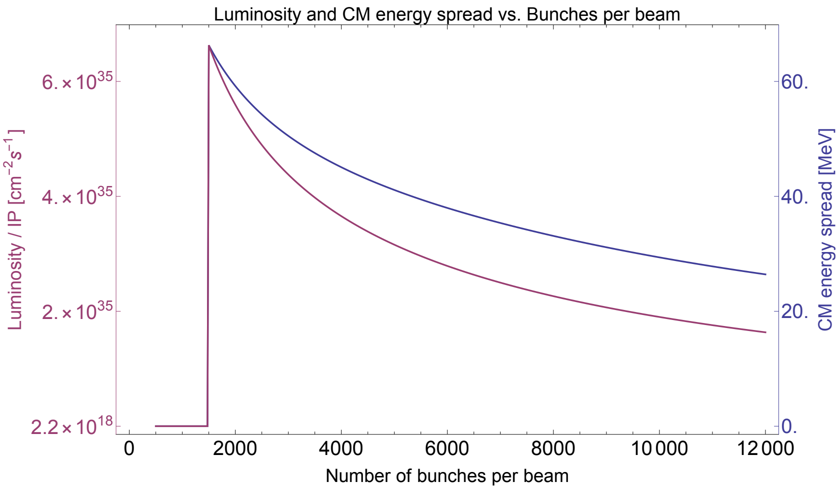

Fig. 3.13 Trade-off between luminosity per IP (red curve) and CM energy spread (blue curve) of the "MonochroM ZH4IP" optics, plotted as a function of bunches per beam, including the beamstrahlung impact under the crossing-angle collision configuration.

increases from 2.09 nm to 7.34 nm due to the impact of beamstrahlung, as per Eq. 1.84, which decreases the monochromatization factor λ according to Eq. 1.28. However, the σ_δ (Eq. 1.85) with the beamstrahlung impact, remains nearly the same as the σ_δ due only to synchrotron radiation, around 0.055%, resulting in a reduced CM energy spread of about 50 MeV without monochromatization effect. This reduction, combined with the inverse correlation between horizontal spatial position and energy deviation in monochromatization scheme, further decreases the CM energy spread to 19.87 MeV. The ξ_y satisfies its limitation (Eq. 3.6), proving the feasibility of the CC collision scheme for the FCC-ee GHC monochromatization mode with nonzero D_x^*. The decrease of $\mathcal{L}$, compared to that of the "Standard ZES" optics, is attributed to the increased horizontal beam size at the IP, which results from both the increased ε_x and the nonzero D_x^*. The "MonochroM ZH2IP" optics, with nonzero D_x at only two IPs, exhibits a smaller ε_x but a larger σ_δ with the beamstrahlung impact, compared to the "MonochroM ZH4IP" configuration. This results in improved σ_W and $\mathcal{L}$, measuring 11.60 MeV and $1.83 \times 10^{35}\,\mathrm{cm}^{-2}\,\mathrm{s}^{-1}$, respectively. Additionally, the comparison of ε_x between the "Standard ZES" optics and "MonochroM ZHS" optics indicates that the ε_x blow-up due to the chicane structure implementation is significantly mitigated with the four smooth close orbit "three-angle" chicane structures, as described in Subsec. 3.1.2.

Under the crossing-angle collision configuration, the σ_δ blow-up due to beamstrahlung in the "Standard ZES" optics is mitigated to 0.078%, because the introduced Piwinski angle (Eq. 1.57) in coefficient V (Eq. 1.88) in Eq. 1.85. This Piwinski angle reduces

$\xi_{x,y}$ to within its limitation and also reduces $\mathcal{L}$ to $2.51 \times 10^{35}\,\mathrm{cm^{-2}\,s^{-1}}$ including the beamstrahlung impact. With an enlarged horizontal beam size at the IP, the Piwinski angles of the "MonochroM ZH4IP" and "MonochroM ZH2IP" optics are much smaller than that of the "Standard ZES" optics, resulting in less luminosity loss due to the crossing angle. The CM energy spread is increased by the Piwinski angle compared to the head-on configuration, following the extended formulas for the monochromatization factor λ (Eq. 1.59) and CM energy spread (Eq. 1.60).

The same calculations and analyses were also performed for the monochromatization IR optics based on the "FCC-ee GHC V22 $t\bar{t}$" optics and are also summarized in two tables: Table 3.3 for the head-on collision configuration and Table 3.4 for the crossing-angle configuration. The similar corresponding optics designs are labeled as "Standard TES," "MonochroM TH4IP," "MonochroM TH2IP," and "MonochroM THS," respectively. Based on the trade-off between $\mathcal{L}$ and σ_W for the "MonochroM TH4IP" optics as a function of n_b, which accounts for the impact of beamstrahlung under the crossing-angle collision configuration (as illustrated in Fig. 3.14), we selected a maximum n_b of 12000, consistent with the value used in the monochromatization optics derived from the "FCC-ee GHC V22 Z" optics. Compared to the monochromatization IR optics with nonzero horizontal

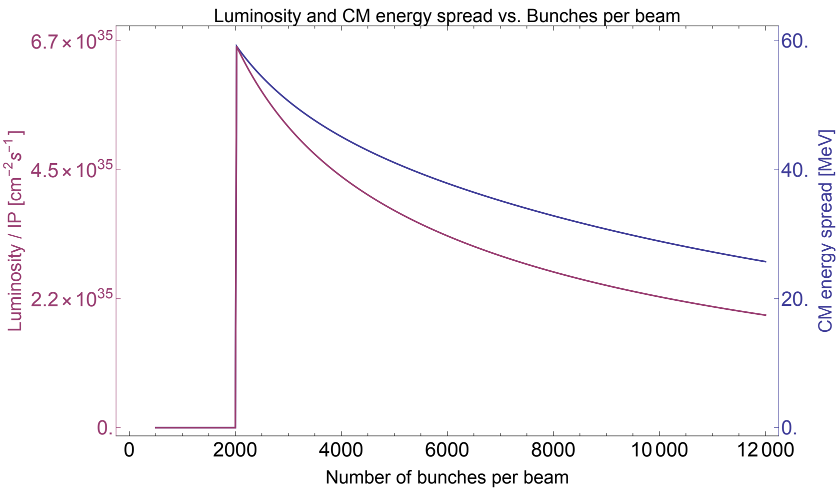

Fig. 3.14 Trade-off between luminosity per IP (red curve) and CM energy spread (blue curve) of the "MonochroM TH4IP" optics, plotted as a function of bunches per beam, including the beamstrahlung impact under the crossing-angle collision configuration.

IP dispersion based on the "FCC-ee GHC V22 Z" optics, those based on the "FCC-ee GHC V22 $t\bar{t}$" optics exhibit better CM energy spread and luminosity per IP due to the inherently lower horizontal emittance of the baseline standard optics.

Table 3.1 Global performance parameters of monochromatization IR optics with nonzero horizontal IP dispersion based on the "FCC-ee GHC V22 Z" optics under the head-on configuration.

Parameter	**[Unit]**	**Standard ZES**	**MonochroM ZH4IP**	**MonochroM ZH2IP**	**MonochroM ZHS**
# of IPs n_{IP}		4			
Circumference C	[km]	91			
Full crossing angle θ_c	[mrad]	30			
SR power / beam P_{SR}	[MW]	50	50.0	49	50.0
Beam energy E_0	[GeV]	62.5			
Energy loss / turn U_0	[GeV]	0.138	0.143	0.140	0.143
Beam current I	[mA]	360	350	350	350
Bunches / beam n_b		12000			
Bunch population N_b	$[10^{11}]$	0.57	0.55	0.55	0.55
Horizontal emittance (SR / BS) ε_x	[nm]	1.33 / 1.33	2.09 / 7.34	1.71 / 2.16	1.66 / 1.66
Vertical emittance (SR / BS) ε_y	[pm]	2.65 / 2.65	4.17 / 4.17	3.42 / 3.42	3.33 / 3.33
Momentum compaction factor α_{C}	$[10^{-6}]$	28.0	27.4	27.7	27.6
$\beta^*_{x/y}$	[mm]	100 / 0.8	90 / 1	90 / 1	100 / 0.8
$D^*_{x/y}$	[m]	0 / 0	0.105 / 0	0.105 / 0	0 / 0
Relative energy spread (SR / BS) σ_δ	[%]	0.054 / 0.115	0.055 / 0.057	0.054 / 0.085	0.055 / 0.105
Bunch length (SR / BS) σ_z	[mm]	4.09 / 8.61	4.15 / 4.22	4.13 / 6.32	4.17 / 7.82
RF voltage 400/800 MHz V_{RF}	[GV]	0.360 / 0			
RF frequency (400 MHz) f_{RF}	[MHz]	399.994581			
Synchrotron tune Q_s		0.054	0.053	0.054	0.054
Long. damping time τ_E/T_{rev}	[turns]	453	438	446	438
Horizontal beam-beam (SR / BS) ξ_x		0.16 / 0.16	0.0052 / 0.0043	0.0053 / 0.0022	0.12 / 0.12
Vertical beam-beam (SR / BS) ξ_y		0.31 / 0.31	0.053 / 0.048	0.059 / 0.039	0.24 / 0.24
CM energy spread (SR / BS) σ_W	[MeV]	47.47 / 101.89	11.22 / 19.87	10.21 / 11.60	48.46 / 92.61
Luminosity / IP (SR / BS) $\mathcal{L}$	$[10^{34}\ \mathrm{cm}^{-2}\,\mathrm{s}^{-1}]$	192 / 192	25.2 / 23.0	28.2 / 18.3	145 / 145

Table 3.2 Global performance parameters of monochromatization IR optics with nonzero horizontal IP dispersion based on the "FCC-ee GHC V22 Z" optics under the crossing-angle configuration.

Parameter	**[Unit]**	**Standard ZES**	**MonochroM ZH4IP**	**MonochroM ZH2IP**	**MonochroM ZHS**
# of IPs n_{IP}		4			
Circumference C	[km]	91			
Full crossing angle θ_c	[mrad]	30			
SR power / beam P_{SR}	[MW]	50	50	49	50
Beam energy E_0	[GeV]	62.5			
Energy loss / turn U_0	[GeV]	0.138	0.143	0.140	0.143
Beam current I	[mA]	360	350	350	350
Bunches / beam n_b		12000			
Bunch population N_b	[10^{11}]	0.57	0.55	0.55	0.55
Horizontal emittance (SR / BS) ε_x	[nm]	1.33 / 1.33	2.09 / 7.78	1.71 / 3.56	1.66 / 1.66
Vertical emittance (SR / BS) ε_y	[pm]	2.65 / 2.65	4.17 / 4.17	3.42 / 3.42	3.33 / 3.33
Momentum compaction factor α_{C}	[10^{-6}]	28.0	27.4	27.7	27.6
$\beta^*_{x/y}$	[mm]	100 / 0.8	90 / 1	90 / 1	100 / 0.8
$D^*_{x/y}$	[m]	0 / 0	0.105 / 0	0.105 / 0	0 / 0
Relative energy spread (SR / BS) σ_δ	[%]	0.054 / 0.078	0.055 / 0.057	0.054 / 0.064	0.055 / 0.075
Bunch length (SR / BS) σ_z	[mm]	4.09 / 5.82	4.15 / 4.23	4.13 / 4.74	4.17 / 5.59
RF voltage 400/800 MHz V_{RF}	[GV]	0.360 / 0			
RF frequency (400 MHz) f_{RF}	[MHz]	399.994581			
Synchrotron tune Q_s		0.054	0.053	0.054	0.054
Long. damping time τ_E/T_{rev}	[turns]	453	438	446	438
Horizontal beam-beam (SR / BS) ξ_x		0.0054 / 0.0027	0.0025 / 0.0022	0.0025 / 0.0019	0.0050 / 0.0028
Vertical beam-beam (SR / BS) ξ_y		0.058 / 0.041	0.037 / 0.034	0.041 / 0.035	0.049 / 0.037
CM energy spread (SR / BS) σ_W	[MeV]	47.47 / 68.78	15.83 / 26.42	14.52 / 20.19	48.46 / 66.15
Luminosity / IP (SR / BS) $\mathcal{L}$	[10^{34} cm^{-2} s^{-1}]	35.4 / 25.1	17.3 / 16.4	19.3 / 16.6	29.2 / 22.0

Table 3.3 Global performance parameters of monochromatization IR optics with nonzero horizontal IP dispersion based on the "FCC-ee GHC V22 $t\bar{t}$" optics under the head-on configuration.

Parameter	**[Unit]**	**Standard TES**	**MonochroM TH4IP**	**MonochroM TH2IP**	**MonochroM THS**
# of IPs n_{IP}		4			
Circumference C	[km]	91			
Full crossing angle θ_c	[mrad]	30			
SR power / beam P_{SR}	[MW]	50	50	49	50
Beam energy E_0	[GeV]	62.5			
Energy loss / turn U_0	[GeV]	0.138	0.143	0.141	0.143
Beam current I	[mA]	360	350	350	350
Bunches / beam n_b		12000			
Bunch population N_b	[10^{11}]	0.57	0.55	0.55	0.55
Horizontal emittance (SR / BS) ε_x	[nm]	0.17 / 0.17	1.48 / 6.80	0.84 / 3.99	0.35 / 0.35
Vertical emittance (SR / BS) ε_y	[pm]	0.35 / 0.35	2.96 / 2.96	1.68 / 1.68	0.71 / 0.71
Momentum compaction factor α_{C}	[10^{-6}]	7.31	6.92	7.12	7.06
$\beta^*_{x/y}$	[mm]	1000 / 1.6	90 / 1	90 / 1	1000 / 1.6
$D^*_{x/y}$	[m]	0 / 0	0.105 / 0	0.105 / 0	0 / 0
Relative energy spread (SR / BS) σ_δ	[%]	0.054 / 0.108	0.055 / 0.057	0.054 / 0.057	0.055 / 0.084
Bunch length (SR / BS) σ_z	[mm]	3.86 / 7.71	4.05 / 4.19	3.95 / 4.11	4.09 / 6.23
RF voltage 400/800 MHz V_{RF}	[GV]	0.170 / 0			
RF frequency (400 MHz) f_{RF}	[MHz]	399.994581			
Synchrotron tune Q_s		0.015	0.014	0.014	0.014
Long. damping time τ_E/T_{rev}	[turns]	454	436	445	436
Horizontal beam-beam (SR / BS) ξ_x		1.20 / 1.20	0.0052 / 0.0043	0.0055 / 0.0047	0.57 / 0.57
Vertical beam-beam (SR / BS) ξ_y		1.07 / 1.07	0.063 / 0.057	0.085 / 0.079	0.51 / 0.51
CM energy spread (SR / BS) σ_W	[MeV]	47.46 / 95.03	9.54 / 19.25	7.24 / 15.20	48.81 / 74.4
Luminosity / IP (SR / BS) $\mathcal{L}$	[10^{34} cm^{-2} s^{-1}]	328 / 328	29.9 / 27.2	40.6 / 37.5	152 / 152

Table 3.4 Global performance parameters of monochromatization IR optics with nonzero horizontal IP dispersion based on the "FCC-ee GHC V22 $t\bar{t}$" optics under the crossing-angle configuration.

Parameter	**[Unit]**	**Standard TES**	**MonochroM TH4IP**	**MonochroM TH2IP**	**MonochroM THS**
# of IPs n_{IP}		4			
Circumference C	[km]	91			
Full crossing angle θ_c	[mrad]	30			
SR power / beam P_{SR}	[MW]	50	50	49	50
Beam energy E_0	[GeV]	62.5			
Energy loss / turn U_0	[GeV]	0.138	0.143	0.141	0.143
Beam current I	[mA]	360	350	350	350
Bunches / beam n_b		12000			
Bunch population N_b	[10^{11}]	0.57	0.55	0.55	0.55
Horizontal emittance (SR / BS) ε_x	[nm]	0.17 / 0.17	1.48 / 7.27	0.84 / 4.23	0.35 / 0.35
Vertical emittance (SR / BS) ε_y	[pm]	0.35 / 0.35	2.96 / 2.96	1.68 / 1.68	0.71 / 0.71
Momentum compaction factor α_{C}	[10^{-6}]	7.31	6.92	7.12	7.06
$\beta^*_{x/y}$	[mm]	1000 / 1.6	90 / 1	90 / 1	1000 / 1.6
$D^*_{x/y}$	[m]	0 / 0	0.105 / 0	0.105 / 0	0 / 0
Relative energy spread (SR / BS) σ_δ	[%]	0.054 / 0.076	0.055 / 0.057	0.054 / 0.057	0.055 / 0.068
Bunch length (SR / BS) σ_z	[mm]	3.86 / 5.49	4.05 / 4.20	3.95 / 4.12	4.09 / 5.07
RF voltage 400/800 MHz V_{RF}	[GV]	0.170 / 0			
RF frequency (400 MHz) f_{RF}	[MHz]	399.994581			
Synchrotron tune Q_s		0.015	0.014	0.014	0.014
Long. damping time τ_E/T_{rev}	[turns]	454	436	445	436
Horizontal beam-beam (SR / BS) ξ_x		0.059 / 0.030	0.0025 / 0.0022	0.0027 / 0.0024	0.049 / 0.033
Vertical beam-beam (SR / BS) ξ_y		0.24 / 0.17	0.044 / 0.041	0.060 / 0.056	0.15 / 0.12
CM energy spread (SR / BS) σ_W	[MeV]	47.45 / 67.58	13.41 / 25.75	10.25 / 20.95	48.80 / 60.47
Luminosity / IP (SR / BS) $\mathcal{L}$	[10^{34} cm^{-2} s^{-1}]	72.8 / 51.9	20.9 / 19.5	28.3 / 26.6	44.6 / 36.6

3.3.2 Preliminary dynamic aperture studies

The determination of dynamic aperture (DA) is a critical consideration in modern high-energy accelerators, such as synchrotron light sources, high-luminosity electron-positron colliders, and large hadron colliders. In early circular accelerators, the dynamic aperture was typically larger than the physical aperture, making it less of a concern in their design. However, in modern high-energy circular accelerators, the complex nonlinear forces acting on the beam can lead to unstable motion. These nonlinearities arise from sextupoles used for chromaticity correction and higher-order magnetic field errors in magnets.

Preliminary 6D (x, x', y, y', t, t') DA studies were conducted using the code Xsuite [133], following the transferring and re-matching of the designed monochromatization optics from the MAD-X version to the Xsuite version. With an initial particle motion amplitude

$$\begin{aligned} A_x &= \frac{\Delta x}{\sigma_x} = 40\,\sigma \\ A_y &= \frac{\Delta y}{\sigma_y} = 40\,\sigma \end{aligned} \tag{3.7}$$

at phase $\phi = 0$, and assuming zero momentum deviation ($\delta = 0$), we obtained the stable horizontal amplitude A_x as function of the stable vertical amplitude A_y according to the particle tracking results. The number of tracking turns was chosen to correspond to approximately twice longitudinal damping time (τ_E/T_{rev}). This analysis was performed without optimizing family sextupole settings in the arc. The resulting DA plots for the "MonochroM ZH4IP" and "MonochroM ZH2IP" optics based on the "FCC-ee GHC V22 Z" optics are presented in the left and right of Fig. 3.15, respectively. The results of the same study procedure for the monochromatization optics based on the "FCC-ee GHC V22 $\mathrm{t\bar{t}}$" optics are shown in Fig. 3.16. We can observe that the DAs of the "MonochroM ZH4IP" and "MonochroM TH4IP" optics are extremely limited in the horizontal plane, measuring only $1.5\,\sigma$. This limitation arises because the horizontal chromaticity introduced by the nonzero horizontal IP dispersion is not corrected locally within the IR, and the arc sextupole families have not been optimized to address this issue. In contrast, the DAs of the "MonochroM ZH2IP" and "MonochroM TH2IP" optics are relatively better, as they feature only two IPs with nonzero horizontal dispersion, further supporting the identified cause of the limited DAs.

In conclusion, the limited DAs in the horizontal plane of the monochromatization optics design with nonzero horizontal IP dispersion based on the "FCC-ee GHC V22" optics is primarily due to local correction being applied only for the vertical chromaticity, with no specific optimization performed for the arc sextupole families. Notably, this situation could be improved if a similar monochromatization scheme were implemented in the FCC-ee LCC optics (Sec. 2.2.2), where the chromaticity in both planes is corrected locally.

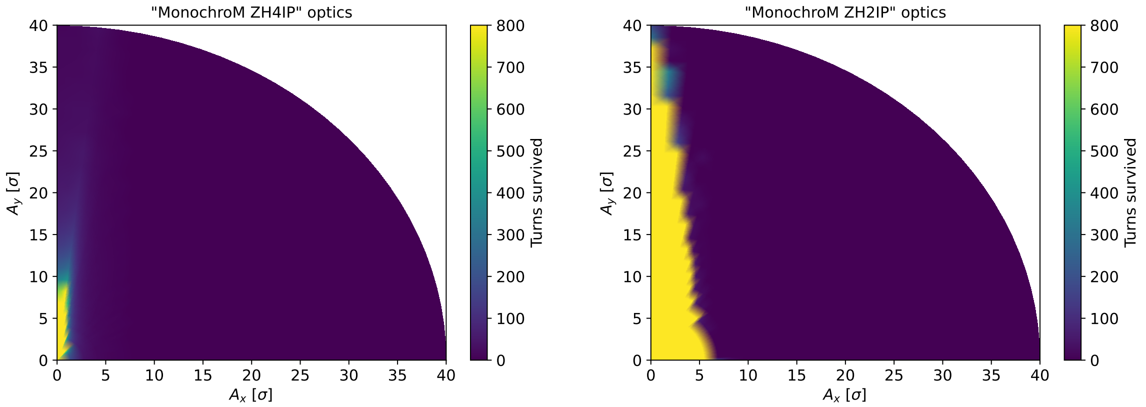

Fig. 3.15 Results of preliminary 6D DA studies for the “MonochroM ZH4IP” (left) and “MonochroM ZH2IP” (right) optics based on the “FCC-ee GHC V22 Z” optics calculated with Xsuite. The varying colors indicate the number of particle surviving turns.

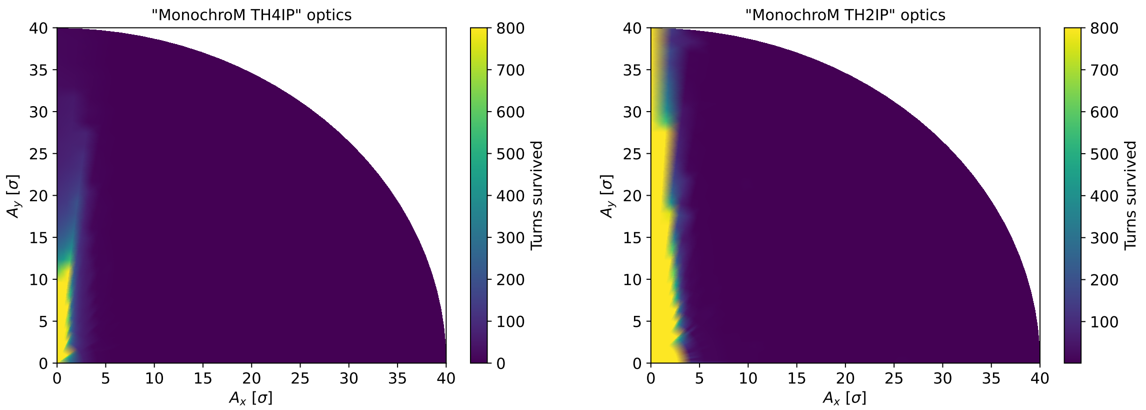

Fig. 3.16 Results of preliminary 6D DA studies for the “MonochroM T4IP” (left) and “MonochroM T2IP” (right) optics based on the “FCC-ee GHC V22 t$\bar{t}$” optics calculated with Xsuite. The varying colors indicate the number of particle surviving turns.

3.3.3 Physics performance

Two critical optical parameters—CM energy spread σ_W and integrated luminosity $\mathcal{L}_{\rm int}$—are key indicators of the physics performance in collider experiments. To accurately assess the performances of the FCC-ee monochromatization IR optics, which features nonzero horizontal dispersion at the IP, we first calculated the σ_W and luminosity per IP $\mathcal{L}$ for various configurations using the simulation tool Guinea-Pig, incorporating a preliminary estimation of the beam-beam effects. In this calculation, the particle distribution at the IP was not a realistic distribution generated by accelerator optics, but modeled as an ideal Gaussian distribution comprising 40000 particles. Each particle are characterized by six parameters: particle energy E in GeV (if it is negative its absolute value is used and the particle is attributed to the opposing bunch on the other side of the IP), horizontal position x in μm when the particle crosses the IP, vertical position y in μm when the particle crosses the IP, longitudinal position z in μm within the bunch (negative values indicate that the particles are under the head of the bunch), horizontal angle x' in μrad and vertical angle y' in μrad. These parameters are represented using a standard normal random variable $Z \sim \mathcal{N}(0,1)$, determined by the beam energy E_0, relative beam energy spread σ_δ, emittance $\varepsilon_{x,y}$, IP betatron function $\beta^*_{x,y}$, IP dispersion function $D^*_{x,y}$, bunch length σ_z and full crossing angle θ_c:

$$
\begin{aligned}
E_\pm &= (Z\sigma_\delta + 1)\, E_0 \\
x_\pm &= \left(Z\sqrt{\varepsilon_x\beta^*_x} + Z\sigma_\delta D^*_{x\pm}\right)\sqrt{1 + \tan\frac{\theta_c}{2}\frac{\sigma_z}{\sqrt{\varepsilon_x\beta^*_x + \sigma_\delta^2 D^{*2}_x}}} \\
y_\pm &= Z\sqrt{\varepsilon_y\beta^*_y} + Z\sigma_\delta D^*_{y\pm} \\
z_\pm &= Z\sigma_z \\
x'_\pm &= Z\sqrt{\frac{\varepsilon_x}{\beta^*_x}} - \frac{\theta_c}{2} \\
y'_\pm &= Z\sqrt{\frac{\varepsilon_y}{\beta^*_y}}\,,
\end{aligned}
\tag{3.8}
$$

where the subscripts "+" and "−" denote the parameters for positrons and electrons, respectively. Additionally, before running the simulation in Guinea-Pig, the particles within each bunch have to be sorted according to their longitudinal position. Fig. 3.17 depicts the inverse correlation between horizontal spatial position x and energy deviation of the positron distribution (left) and the electron distribution (right) at the IP of the "MonochroM ZH4IP" optics, based on the "FCC-ee GHC V22 Z" optics under the crossing-angle collision configuration. The positron beam features a horizontal IP dispersion of 0.105 m, while the electron beam has a dispersion of −0.105 m.

As Guinea-Pig simulates the collision per bunch crossing, it omits the number of bunches per beam n_b, or the revolution frequency f_r [24], when calculating the luminosity per IP. Therefore, when simulating the collision scenario at the IP for each optics design

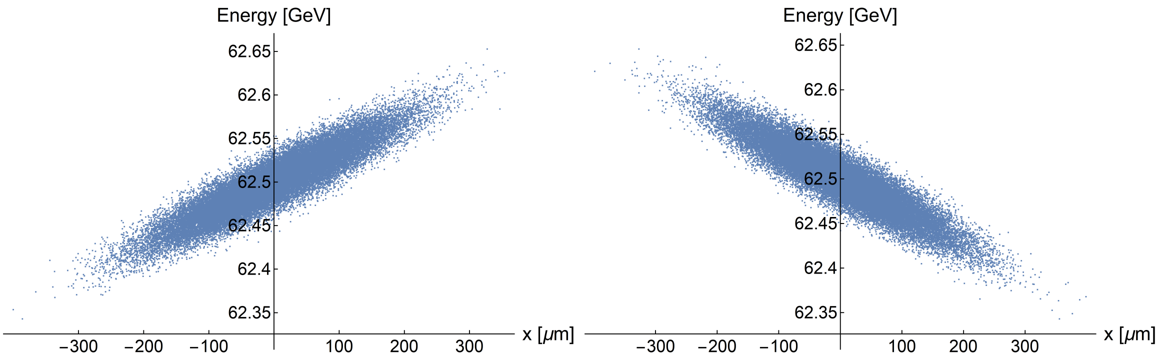

Fig. 3.17 Opposite correlation between horizontal spatial position x and energy deviation of the positron distribution (left) and the electron distribution (right) at the IP of the "MonochroM ZH4IP" optics, based on the "FCC-ee GHC V22 Z" optics under the crossing-angle collision configuration.

using Guinea-Pig, the bunch population N_b needs to be adjusted to an appropriate value so that the luminosity per IP calculated by Guinea-Pig under the head-on collision configuration matches the analytical values of the corresponding optics design listed in Table 3.1 and Table 3.3. Then, the luminosity per IP under the crossing-angle collision configuration should be calculated using the adjusted N_b [134]. Additionally, Guinea-Pig is unable to simulate beamstrahlung effects in the presence of non-zero dispersion at the IP. Therefore, during the simulations, the initial particle distributions were generated using theoretical values of σ_δ, $\varepsilon_{x,y}$, and σ_z that already account for the impact of beamstrahlung. To avoid double-counting the beamstrahlung effects, the corresponding simulation functionality was disabled in Guinea-Pig.

Guinea-Pig simulates and records all the colliding electron-positron pairs along with the following parameters of each pair: energy of the electron, energy of the positron, horizontal collision position, vertical collision position, longitudinal collision position, horizontal angle of the electron, vertical angle of the electron, horizontal angle of the positron, and vertical angle of the positron. The sum of the electron energy and positron energy gives the CM energy of each colliding pair. By analyzing the distribution of the CM energy for all these colliding pairs, we could calculate the CM energy spread. The top of Fig. 3.18 compares the CM energy distribution and correlation between collision energy and longitudinal position of the "Standard ZES" and "MonochroM ZH4IP" optics under the head-on collision configuration. It is evident that the CM energy spread of the monochromatizaiton mode is reduced with opposite correlation between horizontal spatial position x and energy deviation, thanks to the nonzero horizontal dispersion at the IP. The correlation between collision energy and longitudinal position of the "MonochroM ZH4IP" optics under the crossing-angle collision configuration, as depicted at the bottom

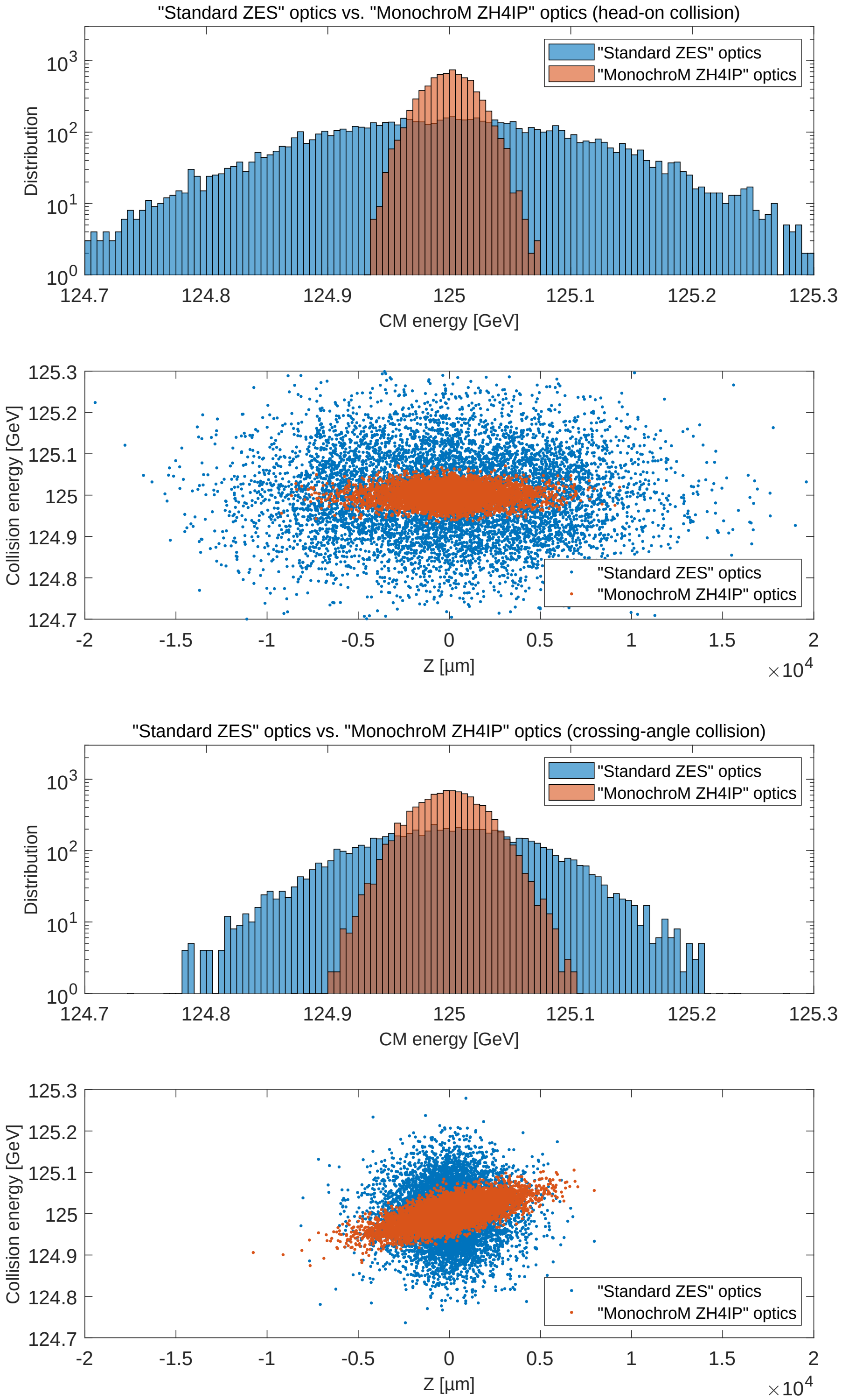

Fig. 3.18 Comparison between the "Standard ZES" and "MonochroM ZH4IP" optics in terms of the CM energy distribution and its correlation with the longitudinal collision position simulated using Guinea-Pig, under the head-on (top) or crossing-angle (bottom) collision configuration.

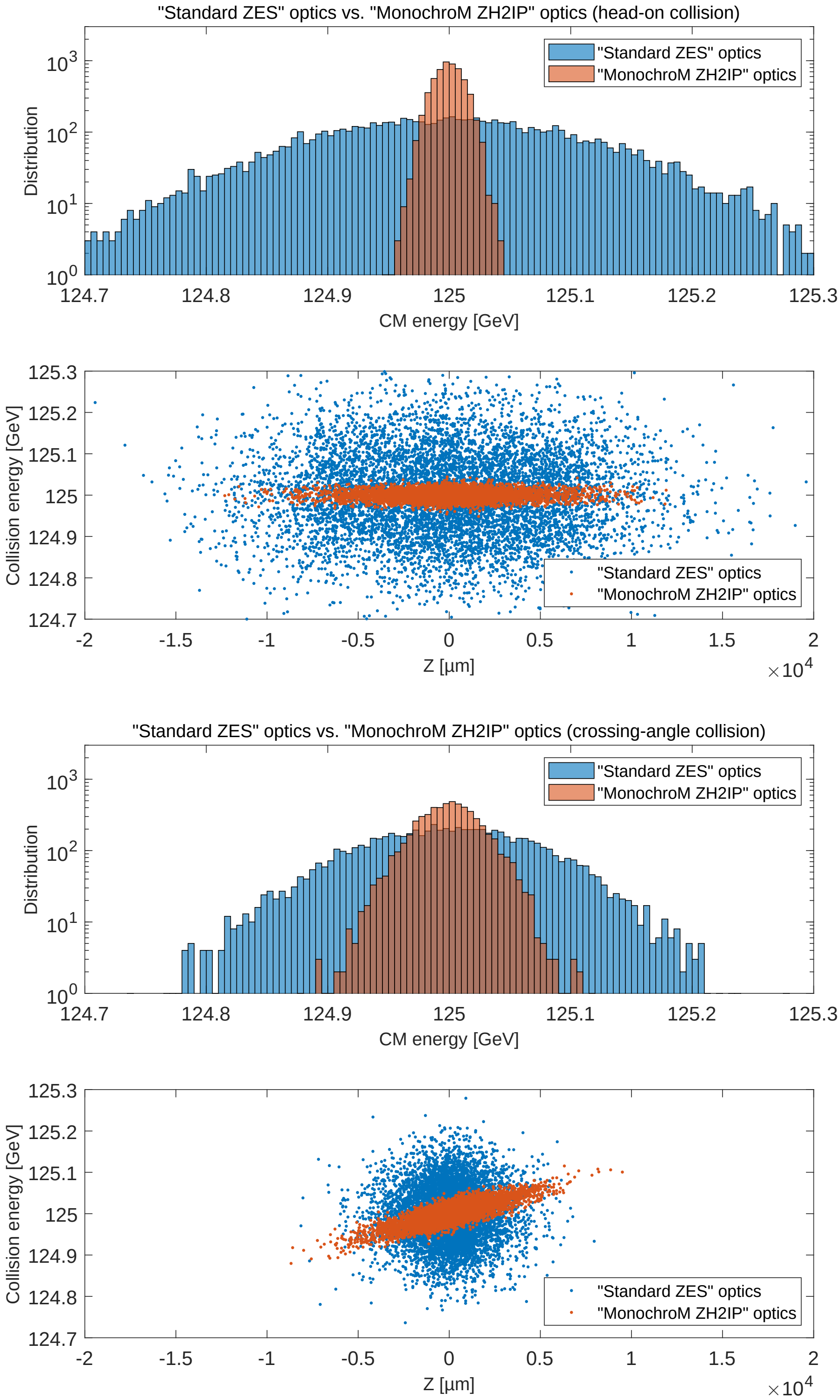

Fig. 3.19 Comparison between the "Standard ZES" and "MonochroM ZH2IP" optics in terms of the CM energy distribution and its correlation with the longitudinal collision position simulated using Guinea-Pig, under the head-on (top) or crossing-angle (bottom) collision configuration.

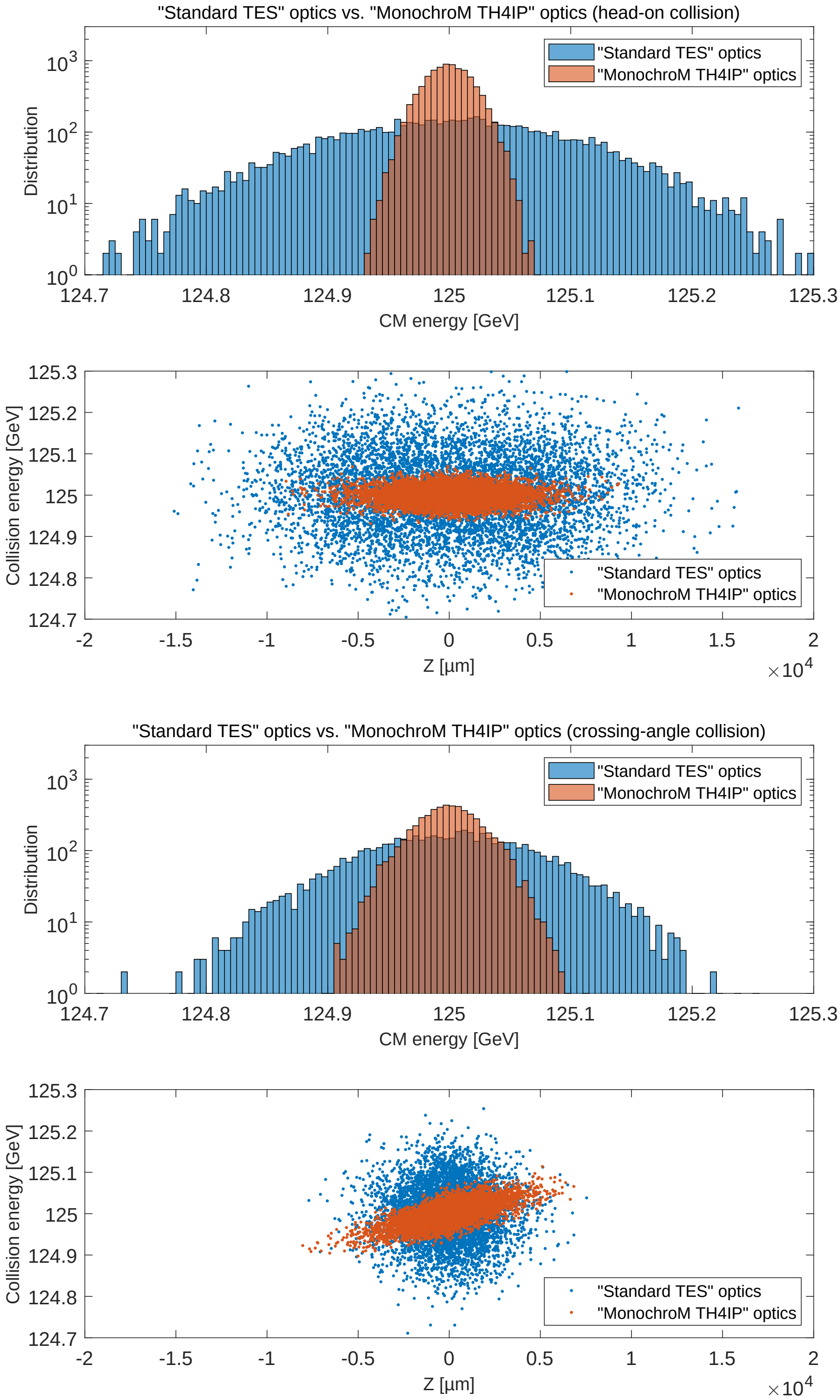

Fig. 3.20 Comparison between the “Standard TES” and “MonochroM TH4IP” optics in terms of the CM energy distribution and its correlation with the longitudinal collision position simulated using Guinea-Pig, under the head-on (top) or crossing-angle (bottom) collision configuration.

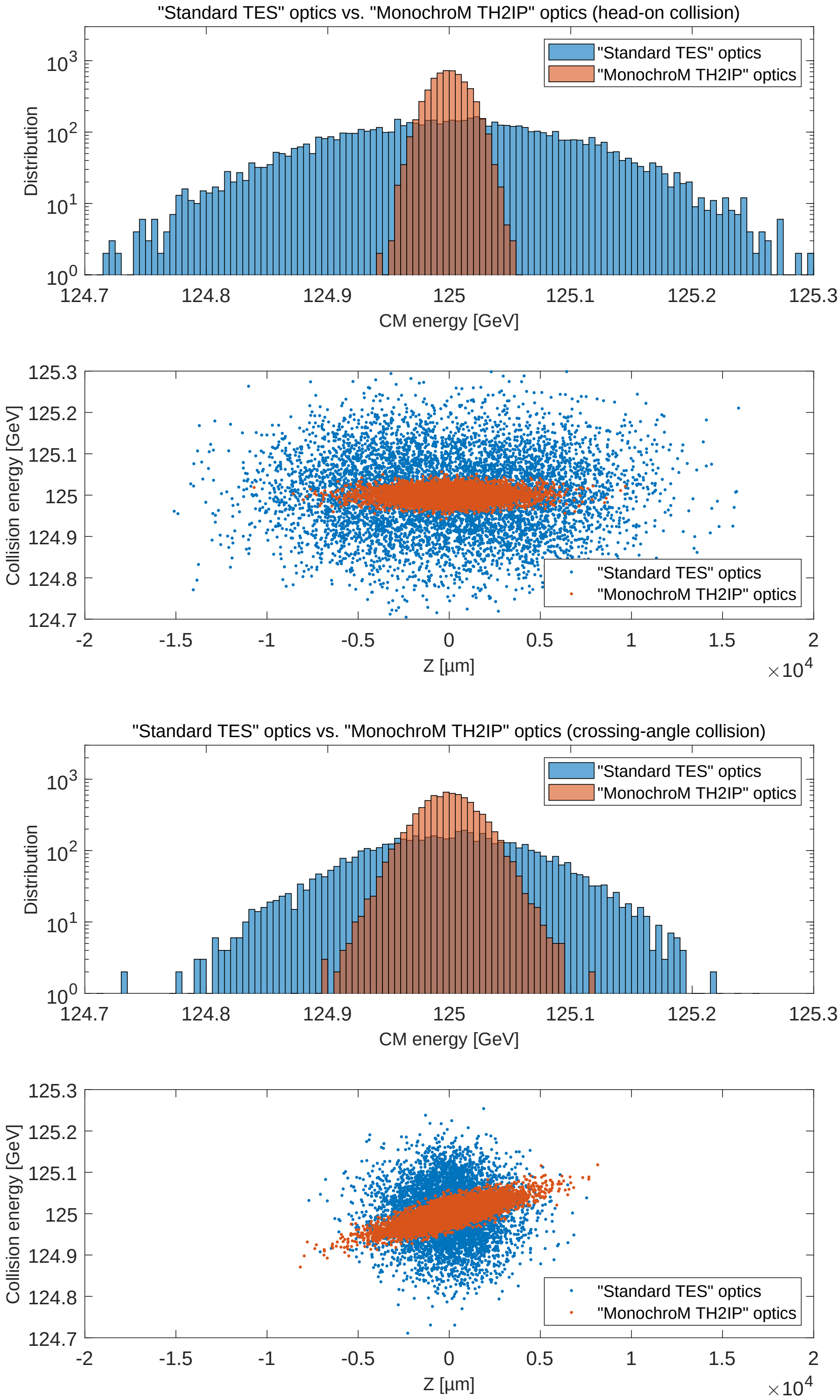

Fig. 3.21 Comparison between the "Standard TES" and "MonochroM TH2IP" optics in terms of the CM energy distribution and its correlation with the longitudinal collision position simulated using Guinea-Pig, under the head-on (top) or crossing-angle (bottom) collision configuration.

Table 3.5 CM energy spread, luminosity per IP, integrated luminosity per IP and year of monochromatization IR optics with nonzero horizontal IP dispersion based on the "FCC-ee GHC V22 Z" optics with or without crab cavities.

Parameter	**[Unit]**	**Standard ZES**	**MonochroM ZH4IP**	**MonochroM ZH2IP**	**MonochroM ZHS**
CM energy spread (with / without crab cavities) σ_W	[MeV]	103.1 / 69.15	20.28 / 27.29	11.99 / 24.12	93.76 / 66.21
Luminosity / IP (with / without crab cavities) $\mathcal{L}$	[10^{34} cm^{-2} s^{-1}]	197 / 44.6	23.1 / 15.0	18.4 / 18.4	148 / 37.6
Integrated luminosity / IP / year (with / without crab cavities) $\mathcal{L}_{\text{int}}$	[ab^{-1}]	23.6 / 5.35	2.77 / 1.80	2.21 / 2.21	17.8 / 4.51

Table 3.6 CM energy spread, luminosity per IP, integrated luminosity per IP and year of monochromatization IR optics with nonzero horizontal IP dispersion based on the "FCC-ee GHC V22 $\mathrm{t\bar{t}}$" optics with or without crab cavities.

Parameter	**[Unit]**	**Standard TES**	**MonochroM TH4IP**	**MonochroM TH2IP**	**MonochroM THS**
CM energy spread (with / without crab cavities) σ_W	[MeV]	93.76 / 67.51	19.39 / 26.32	15.54 / 23.68	74.32 / 59.25
Luminosity / IP (with / without crab cavities) $\mathcal{L}$	[10^{34} cm^{-2} s^{-1}]	336 / 71.2	27.3 / 17.8	37.6 / 24.5	155 / 44.4
Integrated luminosity / IP / year (with / without crab cavities) $\mathcal{L}_{\text{int}}$	[ab^{-1}]	40.3 / 8.54	3.28 / 2.14	4.51 / 2.94	18.6 / 5.33

of Fig. 3.18, demonstrates that the monochromatization efficiency is diminished due to the crossing angle, as illustrated in Fig. 1.6 and in accordance with Eq. 1.59 and Eq. 1.60.

The CM energy spread and luminosity per IP, with or without crab cavities, were calculated using Guinea-Pig for all optics associated with monochromatization optics with nonzero horizontal IP dispersion, as shown in Fig. 3.18, Fig. 3.19, Fig. 3.20 and Fig. 3.21. The results are summarized in two tables: Table 3.5 for those based on the "FCC-ee GHC V22 Z" optics and Table 3.6 for those based on the "FCC-ee GHC V22 $\mathrm{t\bar{t}}$" optics.

Regarding the integrated luminosity $\mathcal{L}_{\mathrm{int}}$, based on the assumptions laid out in the FCC-ee CDR [1], which include 185 physics days per year and a physics efficiency of 75%, an instantaneous luminosity of $10^{35}\,\mathrm{cm^{-2}\,s^{-1}}$ yields $1.2\,\mathrm{ab^{-1}}$ per IP per year. Using this relation, the $\mathcal{L}_{\mathrm{int}}$ values were calculated and are listed in the corresponding tables.

Finally, we assessed the physics performance of the proposed monochromatization optics with nonzero horizontal IP dispersion by establishing their $\delta_{\sqrt{s}}$-$\mathcal{L}_{\mathrm{int}}$ benchmarks on the upper limits contours (95% CL) for y_e coupling, as described in Subsec. 1.2.3. These benchmarks were determined by the σ_W and $\mathcal{L}_{\mathrm{int}}$ of each type of monochromatization optics, as listed in Table 3.5 and Table 3.6. Fig. 3.22 shows these benchmarks, with the top panel comparing the designed monochromatization optics to the FCC-ee monochromatization self-consistent parameters 1.1 with crab cavities (head-on collision configuration), and the bottom panel showing the comparison without crab cavities (crossing-angle collision configuration). The pink star above the $\delta_{\sqrt{s}} = \Gamma_{\mathrm{H}} = 4.1\,\mathrm{MeV}$ dashed line indicates the ideal assumed point [69]. The red stars represent the FCC-ee monochromatization self-consistent parameter [53, 55] working points, corresponding to a CM energy spread of 13 MeV and an integrated luminosity of $3.12\,\mathrm{ab^{-1}}$ with crab cavities, and a CM energy spread of 25 MeV and an integrated luminosity of $2.76\,\mathrm{ab^{-1}}$ without crab cavities. The cyan benchmarks refer to the "MonochroM ZH4IP" and "MonochroM ZH2IP" optics based on the "FCC-ee GHC V22 Z" optics, while the yellow ones are based on the "FCC-ee GHC V22 $\mathrm{t\bar{t}}$" optics. The physics performances of all designed realistic monochromatization optics with nonzero horizontal dispersion at the IP are comparable to or even exceed that of the FCC-ee monochromatization self-consistent parameters. Under the head-on configuration, the "MonochroM TH2IP" optics, based on the "FCC-ee GHC V22 $\mathrm{t\bar{t}}$" optics, achieves the best $\delta_{\sqrt{s}}$-$\mathcal{L}_{\mathrm{int}}$ benchmark, with $\sigma_W = 15.54\,\mathrm{MeV}$ and $\mathcal{L}_{\mathrm{int}} = 4.51\,\mathrm{ab^{-1}}$. This corresponds to an upper limit of $|y_e| < 2.7|y_e^{\mathrm{SM}}|$ in the 95% CL contours for the Higgs-electron coupling per IP and year. Under the crossing-angle configuration, the "MonochroM TH2IP" optics also delivers the best $\delta_{\sqrt{s}}$-$\mathcal{L}_{\mathrm{int}}$ benchmark, with $\sigma_W = 23.68\,\mathrm{MeV}$ and $\mathcal{L}_{\mathrm{int}} = 2.94\,\mathrm{ab^{-1}}$, indicating an upper limit of $|y_e| < 3.2|y_e^{\mathrm{SM}}|$.

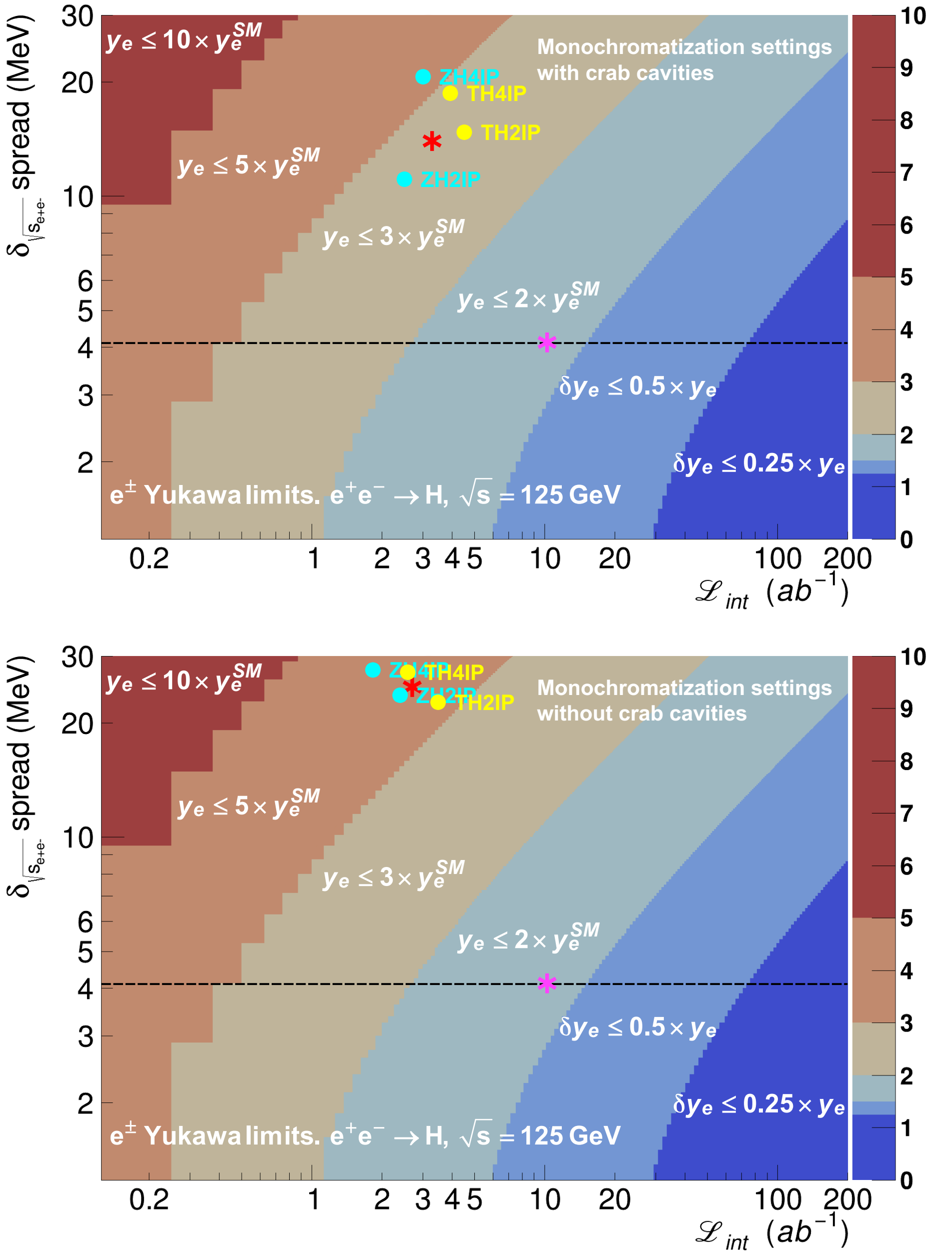

Fig. 3.22 Physics performance evaluation of the proposed monochromatization optics with nonzero horizontal IP dispersion, under the head-on (top) or crossing-angle (bottom) collision configuration, indicated by the $\delta_{\sqrt{s}}$-$\mathcal{L}_{\text{int}}$ benchmarks in the upper limits contours (95% CL) on the y_e. The monochromatization optics base on the "FCC-ee GHC V22 Z" optics and "FCC-ee GHC V22 $t\bar{t}$" optics are marked in cyan and yellow, respectively. The pink star over the $\delta_{\sqrt{s}} = \Gamma_{\text{H}} = 4.1\,\text{MeV}$ dashed line, indicates the baseline point assumed in the original physics simulation analysis [69]. The red stars represent the previously achieved working point with parameterized studies [53, 55].

Chapter 4

FCC-ee GHC monochromatization IR optics design with vertical IP dispersion

The FCC-ee, owing to its extremely low vertical emittance of 1 pm, features a vertical beam size at the IP that is significantly smaller than the horizontal one. Therefore, achieving a sufficient monochromatization factor, as indicated by Eq. 1.28, requires an approximately 100 times smaller vertical IP dispersion of around 1 mm. Introducing this minimal vertical dispersion at the IP can be accomplished simply by implementing skew quadrupoles in the IR [116–128].

In this chapter, we begin by discussing the principle of this monochromatization scenario with nonzero vertical dispersion at the IP, inspired by the detector solenoid compensation of FCC-ee LCC optics. We then detail its application to FCC-ee GHC optics, including the design of monochromatization IR optics, global implementation, and performance evaluations.

4.1 Principle of vertical IP dispersion generation

4.1.1 Principle for FCC-ee LCC optics

Detector solenoid and its compensation

The detector solenoid in particle colliders primarily serves to provide a strong magnetic field within the detector, which is crucial for controlling and guiding particle beams as they pass through the detector [135]. In the design of the FCC-ee Machine-Detector Interface (MDI) region, a detector solenoid with a 2 T magnetic field was proposed in the context of the crab-waist collision scheme, featuring a crossing angle of 30 mrad [136].

When passing though the detector solenoid (magnetic field: B_s) with a crossing angle of θ_c in the horizontal plane, electrons or positrons will experience a vertical Lorentz force F due to the horizontal component of the solenoid magnetic field, $B_x = B_s(\theta_c/2)$, as schematically depicted in Fig. 4.1. In beam optics, this vertical kick can be modeled

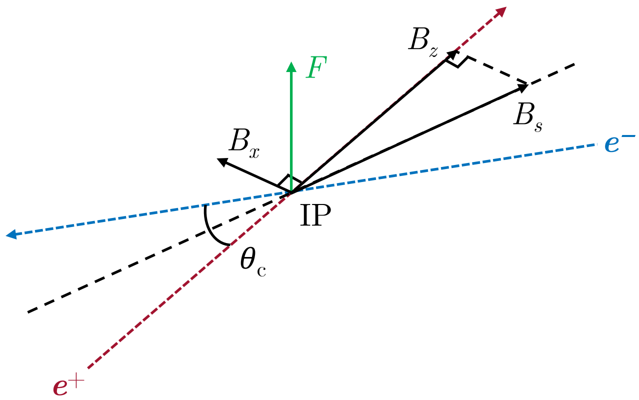

Fig. 4.1 Vertical kick on the beam induced by the detector solenoid in context of crab-waist collision scheme.

as a vertical closed orbit corrector at the IP. Assuming the length of this closed orbit corrector is L, the resulting angle θ is given by:

$$\theta = \frac{B_x e L}{p} = \frac{B_x L}{B\rho} \,, \tag{4.1}$$

where e denotes the elementary charge, p represents the momentum of the electrons or positrons, $B\rho$ is the magnetic rigidity determined by beam energy: $B\rho = E_0/c$. This vertical kick can generate several kilowatts of synchrotron radiation power and induce coupling between horizontal and vertical betatron motions, leading to an increase of vertical emittance [137]. A compensation scheme without inner counter-solenoids for minimizing these effects was proposed when considering the implementation of the detector solenoid in the “FCC-ee LCC V22” optics [138, 139], as illustrated in Fig. 4.2. The elements marked in blue are part of the original lattice and are included here to indicate the locations of the additional elements marked in red, which consist of weak correctors and skew quadrupoles inserted into the original lattice’s drift sections. The compensation is performed through the following steps:

1. Give the horizontal component of the detector solenoid B_x by implementing the vertical closed orbit corrector with a length of 1 m nearby the IP. The corrector’s angle is defined by Eq. 4.1.

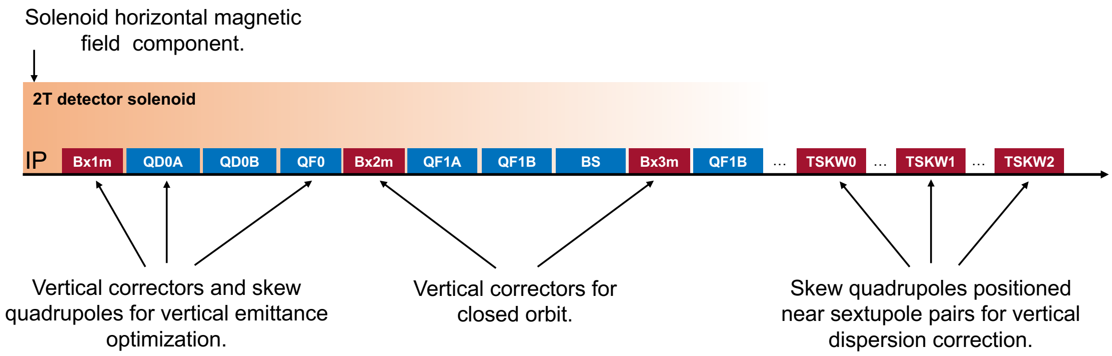

Fig. 4.2 Detector solenoid compensation scheme for the "FCC-ee LCC V22" optics [139].

2. Close the vertical beam orbit y by varying the angle of the two correctors labeled as "Bx2m" and "Bx3m."

3. Correct the vertical dispersion D_y and its slope D'_y by varying the strength of the three skew quadrupoles, labeled as "TSKW0," "TSKW1," and "TSKW2," implemented at the location near the sextupole pairs in the IR. Note that the strength of the "TSKW1" and the "TSKW2" are the same in magnitude but opposite in sign.

4. Minimize the vertical emittance by optimizing the angle of the corrector "Bx1m" and the tilt angle of the two quadrupoles, labeled as "QD0A" and "QF0."

Vertical IP dispersion generation

To generate vertical dispersion at the IP, we first performed all the steps mentioned above without introducing vertical IP dispersion. Following the completion of these steps, with the additional elements in place and their angles or strengths optimized, we introduced a nonzero vertical IP dispersion of 1 mm and resumed the procedure from the second step [139]. Note that the optimization performed in the fourth step was manually conducted as a temporary measure. In the future, a dedicated program will be developed to automate and refine this optimization process.

Fig. 4.3 illustrates the IR lattice and optics of the "FCC-ee LCC V22 Z" optics with the implementation of a 2 T detector solenoid and a 1 mm vertical IP dispersion [116–118]. On each side of the IP, the vertical beam orbit error induced by the detector solenoid is corrected immediately after the "Bx3m" corrector. The introduced 1 mm vertical IP dispersion, along with the vertical dispersion caused by the detector solenoid, is further corrected after the "TSKW2" skew quadrupole. Following its global implementation, the vertical emittance was 13.97 pm without further optimization.

This monochromatization principle with nonzero vertical IP dispersion generation is also worth investigating for the CEPC CDR lattice [43], which features a final focus system design similar to that of the FCC-ee LCC optics. Additionally, existing low-energy circular colliders such as BEPCII [140], SuperKEKB [44], and DAΦNE [141, 142] incorporate detector solenoids along with correctors and skew quadrupoles, providing a unique opportunity for the experimental validation of the monochromatization concept.

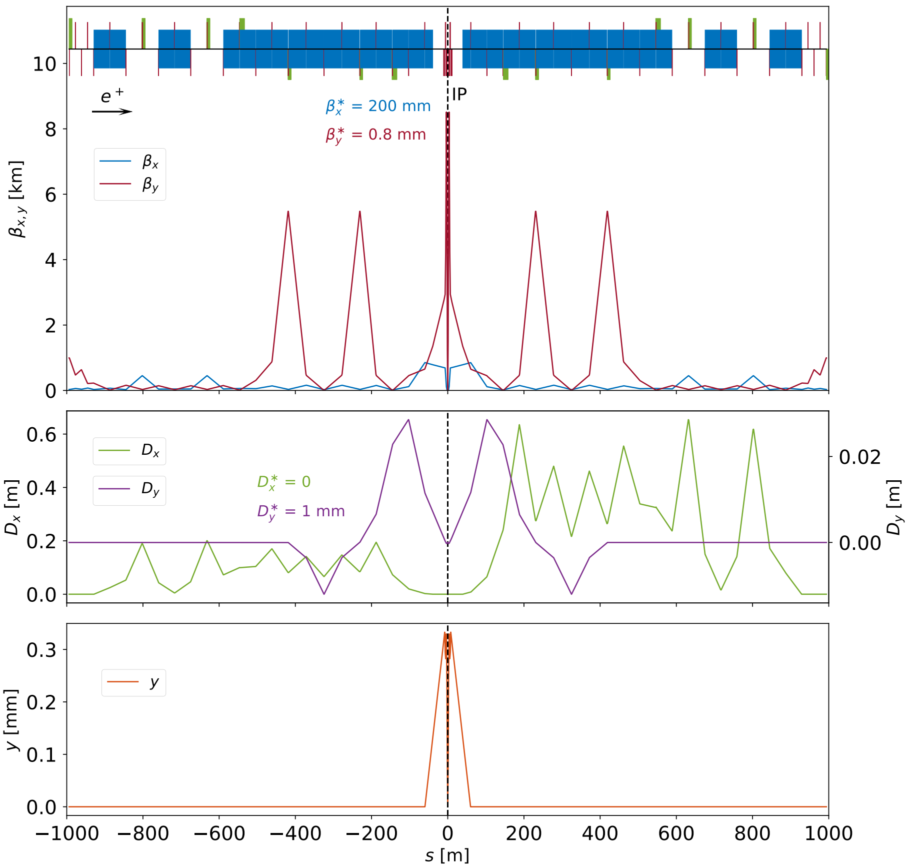

Fig. 4.3 IR lattice and optics of the “FCC-ee LCC V22 Z” optics with the implementation of the 2 T detector solenoid and 1 mm vertical IP dispersion, calculated using MAD-X. The beam direction is from left to right; the dashed line $s = 0$ marks the location of IP. In the lattice, dipoles, quadrupoles, and sextupoles are shown in blue, red, and green, respectively, while focusing and defocusing elements are positioned above and below the orbit. In the optics, horizontal and vertical betatron functions are shown in blue and red, respectively, while horizontal and vertical dispersion function are shown in green and purple, respectively. The vertical beam orbit is shown in orange.

4.1.2 Principle for FCC-ee GHC optics

"Skew quadrupole" scheme

Inspired by the monochromatization scheme for FCC-ee LCC optics, the introduction of nonzero vertical dispersion at the IP was also considered for the FCC-ee GHC optics. In the absence of a detector solenoid in the FCC-ee GHC optics, the generation of the required 1 mm vertical IP dispersion can be simply achieved without altering the IR orbit by adjusting the strength of IR skew quadrupoles, which are already necessary for correcting the skew-quadrupole field caused by quadrupole roll errors [143].

The locations of these skew quadrupoles are illustrated in Fig. 4.4. Following the same approach for correcting vertical dispersion, two skew quadrupoles, labeled (a) and (d), are installed between the crab sextupole pairs, while the other two, labeled (b) and (c), are placed between the chromaticity sextupole pairs. The two skew quadrupoles on the same side of the IP, such as (a) and (b), have identical magnitudes but opposite signs in their strengths [119–128].

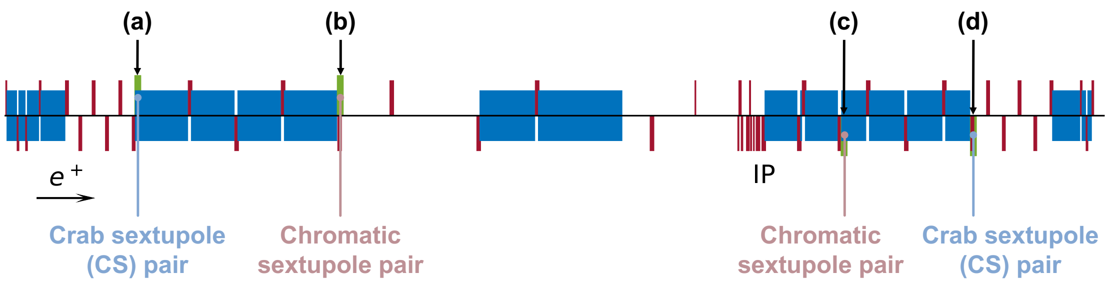

Fig. 4.4 Placement of skew quadrupole implementation for generating nonzero vertical IP dispersion in FCC-ee GHC optics. Dipoles, quadrupoles, and sextupoles are shown in blue, red, and green, respectively, while focusing and defocusing elements are positioned above and below the orbit [119–128].

Using this scheme, the first monochromatization IR optics designs were developed based on the two types of the "FCC-ee GHC V22" optics ("FCC-ee GHC V22 Z" and "FCC-ee GHC V22 $t\bar{t}$" optics) [119–128]. While maintaining zero vertical dispersion at both the entrance and exit of the IR, we matched the IP vertical dispersion to 1 mm and 2 mm, respectively, by varying the strength of the installed skew quadrupoles. The resulting monochromatization IR lattices and optics based on the "FCC-ee GHC V22 Z" optics are depicted in Fig. 4.5. After integrating this setup into the global lattice, following the procedures described in Subsec. 3.2.3, the global performance parameters were calculated in the crossing-angle collision configuration and are listed in Table 4.1.

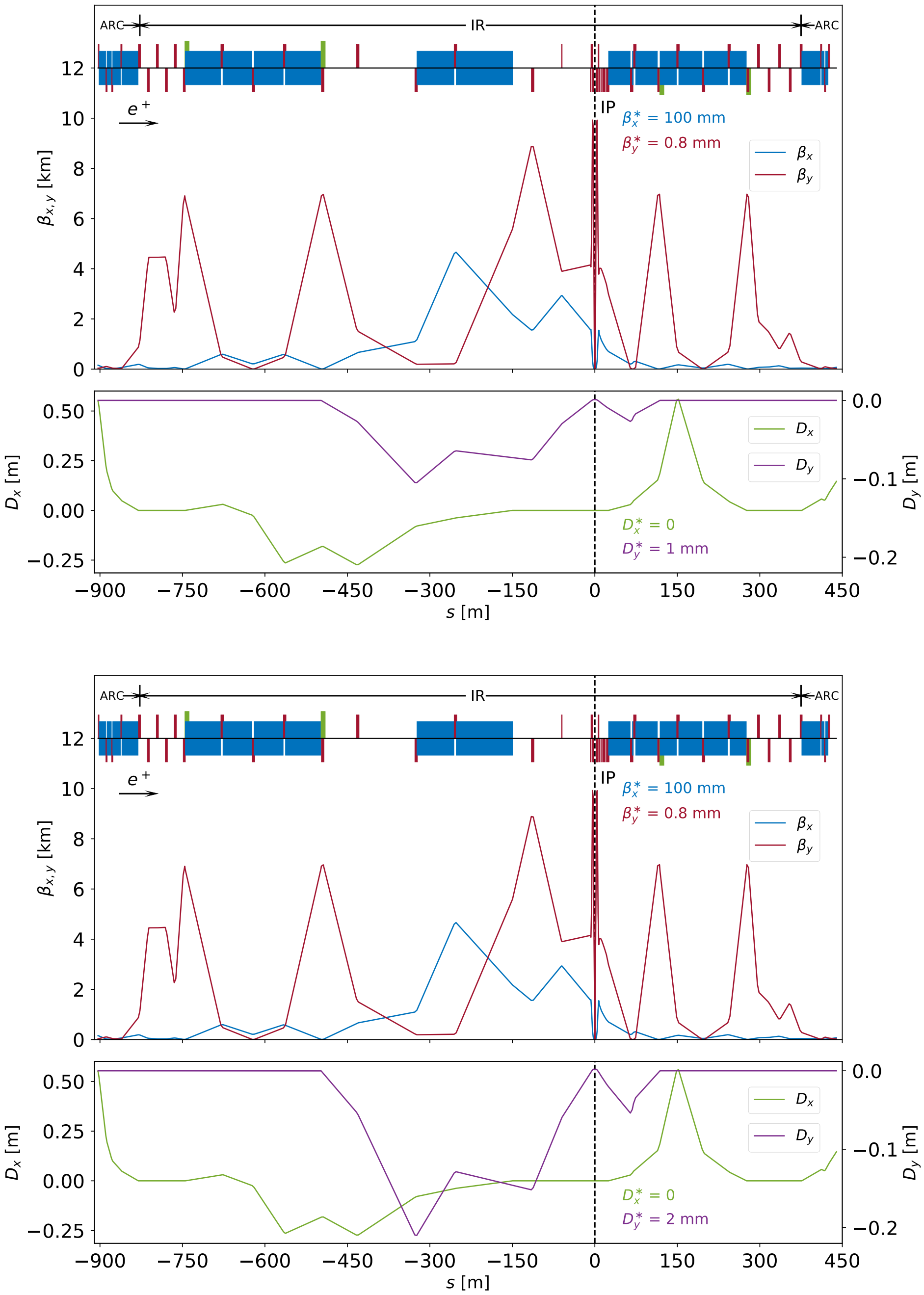

Fig. 4.5 First monochromatization IR optics design with 1 mm (top) and 2 mm (bottom) vertical IP dispersion based on the “FCC-ee GHC V22 Z” optics calculated using MAD-X. The beam direction is from left to right; the dashed line $s = 0$ marks the location of IP. In the lattice, dipoles, quadrupoles, and sextupoles are shown in blue, red, and green, respectively, while focusing and defocusing elements are positioned above and below the orbit. In the optics, horizontal and vertical betatron functions are shown in blue and red, respectively, while horizontal and vertical dispersion functions are shown in green and purple, respectively.

Table 4.1 Global performance parameters of first monochromatization IR optics with nonzero vertical IP dispersion based on the "FCC-ee GHC V22 Z" optics under the crossing-angle configuration.

Parameter	**[Unit]**	**Standard ZES**	**MonochroM ZVF1**	**MonochroM ZVF2**
# of IPs n_{IP}			4	
Circumference C	[km]		91	
Full crossing angle θ_c	[mrad]		30	
SR power / beam P_{SR}	[MW]		50	
Beam energy E_0	[GeV]		62.5	
Energy loss / turn U_0	[GeV]		0.138	
Beam current I	[mA]		360	
Bunches / beam n_b			12000	
Bunch population N_b	[10^{11}]		0.57	
Horizontal emittance (SR / BS) ε_x	[nm]	1.33 / 1.33	1.32 / 1.32	1.32 / 1.32
Vertical emittance (SR / BS) ε_y	[pm]	2.65 / 2.65	5.07 / 808	20.3 / 3244
Momentum compaction factor α_{C}	[10^{-6}]	28.0	27.9	27.9
$\beta^*_{x/y}$	[mm]		100 / 0.8	
$D^*_{x/y}$	[m]	0 / 0	0 / 0.001	0 / 0.002
Relative energy spread (SR / BS) σ_δ	[%]		0.054 / 0.078	
Bunch length (SR / BS) σ_z	[mm]	4.09 / 5.82	4.10 / 5.85	4.10 / 5.85
RF voltage 400/800 MHz V_{RF}	[GV]		0.360 / 0	
RF frequency (400 MHz) f_{RF}	[MHz]		399.994581	
Synchrotron tune Q_s			0.054	
Long. damping time τ_E/T_{rev}	[turns]	453	454	454
Horizontal beam-beam (SR / BS) ξ_x		0.0054 / 0.0027	0.0053 / 0.0026	0.0053 / 0.0026
Vertical beam-beam (SR / BS) ξ_y		0.058 / 0.041	0.0049 / 0.0017	0.0024 / 0.0008
CM energy spread (SR / BS) σ_W	[MeV]	47.47 / 68.78	5.59 / 49.51	5.59 / 49.57
Luminosity / IP (SR / BS) $\mathcal{L}$	[10^{34} cm^{-2} s^{-1}]	35.4 / 25.1	3.01 / 1.03	1.51 / 0.51

The optics labeled "MonochroM ZVF1" features 1 mm vertical dispersion at all four IPs, while "MonochroM ZVF2" features 2 mm vertical dispersion.

Mitigation of vertical emittance blow-up due to beamstrahlung

In Table 4.1, we observe that the CM energy spread σ_W for the "MonochroM ZVF1" optics significantly reduces to 5.59 MeV when beamstrahlung is not considered under the crossing-angle collision configuration. However, the introduction of nonzero vertical IP dispersion D_y^* leads to a substantial vertical emittance ε_y increase from 5.07 pm to 808 pm due to beamstrahlung, as described by Eq. 1.84. This increase results in a reduction of the monochromatization factor λ from 8.49 to 1.39, according to Eq. 1.59, which in turn causes the CM energy spread to rise to 49.51 MeV.

To mitigate the ε_y blow-up due to beamstrahlung, two approaches were considered: reducing the coefficient V or increasing the horizontal IP beam size σ_x^* in Eq. 1.84.

For reducing the coefficient V (Eq. 1.87 for head-on collisions and Eq. 1.88 for crossing-angle collisions), since the bunch population N_b is constrained by the maximum number of bunches per beam n_b as discussed in Subsec. 3.3.1, and the momentum compaction factor α_C is fixed by the lattice, the most straightforward option is to lower the synchrotron tune Q_s by adjusting the RF voltage V_{RF} as indicated by Eq. A.19. Besides, according

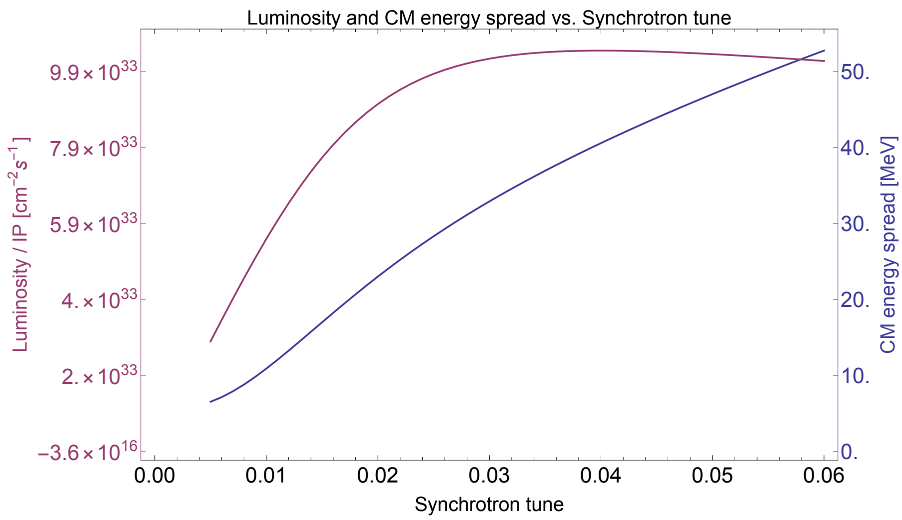

Fig. 4.6 Variation in luminosity per IP (red curve) and CM energy spread (blue curve) of the "MonochroM ZVF1" optics, plotted as a function of synchrotron tune, including the beamstrahlung impact in the crossing-angle collision configuration.

to Eq. A.17, a smaller Q_s contributes to an increased bunch length σ_z, which raises the Piwinski angle (Eq. 1.57) in crossing-angle collision configuration, further decreasing the coefficient V. Fig. 4.6 depicts the variation in luminosity per IP $\mathcal{L}$ and σ_W of the "MonochroM ZVF1" optics, plotted as a function of synchrotron tune, including the beamstrahlung impact in the crossing-angle collision configuration. By reducing the Q_s from ~0.054 to ~0.022, the σ_W of the "MonochroM ZVF1" optics can be reduced to the same level as that of the monochromatization IR optics with nonzero horizontal IP dispersion. However, such a low Q_s (≤ 0.05) makes the use of resonant depolarization, a technique for precise beam energy measurement, impractical [144]. In this case, the only remaining option for reducing the coefficient V is to increase the α_{C} (Eq. A.18) by modifying the arc lattice.

The other mentioned approach to mitigate the ε_y blow up involves increasing the σ_x^*, which can be achieved by raising the horizontal IP betatron function β_x^* through varying the strength of the final focus quadrupoles. The impact of this adjustment on the global optical parameters calculated using MAD-X is negligible. If we plot the variation in $\mathcal{L}$ and σ_W of the "MonochroM ZVF1" optics as a function of β_x^*, including the beamstrahlung impact in the crossing-angle collision configuration, as shown in Fig. 4.7, we observe that

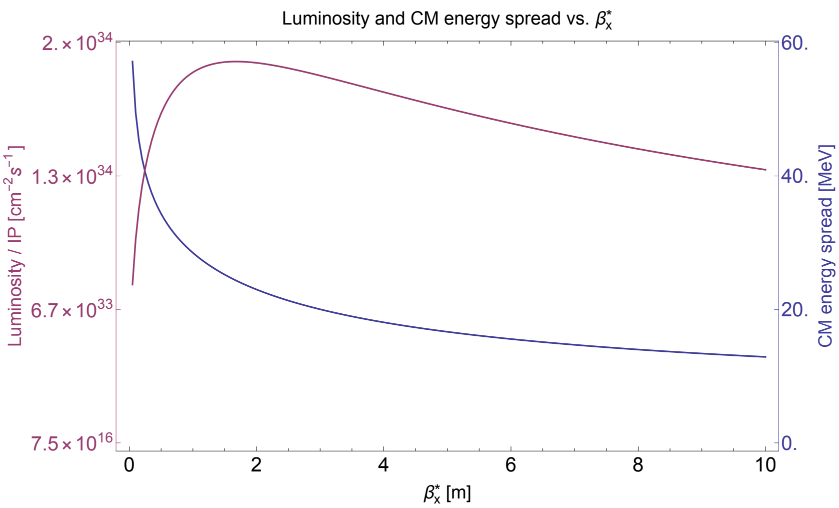

Fig. 4.7 Variation in luminosity per IP (red curve) and CM energy spread (blue curve) of the "MonochroM ZVF1" optics, plotted as a function of horizontal IP betatron function, including the beamstrahlung impact in the crossing-angle collision configuration.

the original setting of $\beta_x^* = 0.1\,\mathrm{m}$ is sub-optimal for monochromatization, with low $\mathcal{L}$ and high σ_W. As β_x^* increases, $\mathcal{L}$ rises to a peak at $\beta_x^* \approx 1.5\,\mathrm{m}$ and then gradually decreases, while the σ_W continues to decrease. The green curve in Fig. 4.8 represents the evaluation of physics performance across different values of β_x^*, with the green star indicating the optimal benchmark at approximately $5\,\mathrm{m}$ for β_x^*. A similar analysis was performed on the first monochromatization IR optics design, featuring a $1\,\mathrm{mm}$ vertical IP dispersion,

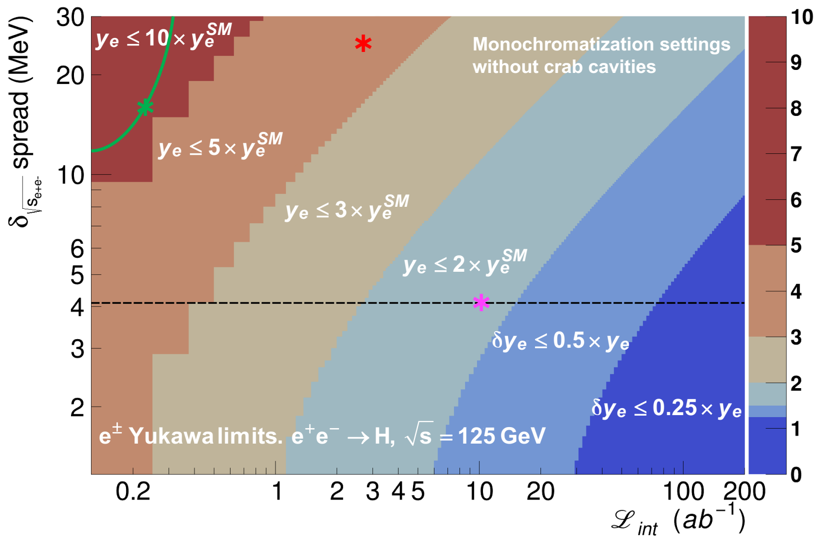

Fig. 4.8 Physics performance evaluation of the "MonochroM ZVF1" optics across different values of β_x^* (green curve) in the upper limits contours (95% CL) for y_e. The green star indicates the optimal benchmark at a β_x^* of 5 m.

based on the "FCC-ee GHC V22 t$\bar{\text{t}}$" optics and labeled as "MonochroM TVF1." Fig. 4.9 and Fig. 4.10 display the variations in $\mathcal{L}$ and σ_W for the "MonochroM TVF1" optics and the corresponding physics performance. From this analysis, it was concluded that the

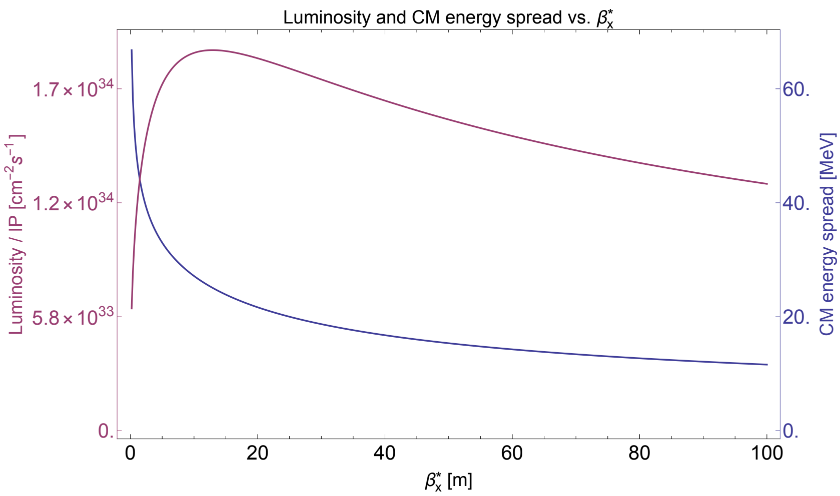

Fig. 4.9 Variation in luminosity per IP (red curve) and CM energy spread (blue curve) of the "MonochroM TVF1" optics, plotted as a function of horizontal IP betatron function, including the beamstrahlung impact in the crossing-angle collision configuration.

β_x^* of the "MonochroM TVF1" optics could be increased to approximately 50 times its original value for optimal physics performance, as indicated by the green star in Fig. 4.10.

Although the adjusted β_x^* values for "MonochroM ZVF1" and "MonochroM TVF1" optics differ, they exhibit similar horizontal beam sizes, around 85 µm, due to their differing horizontal emittances, and thus, they exhibit comparable $\mathcal{L}$.

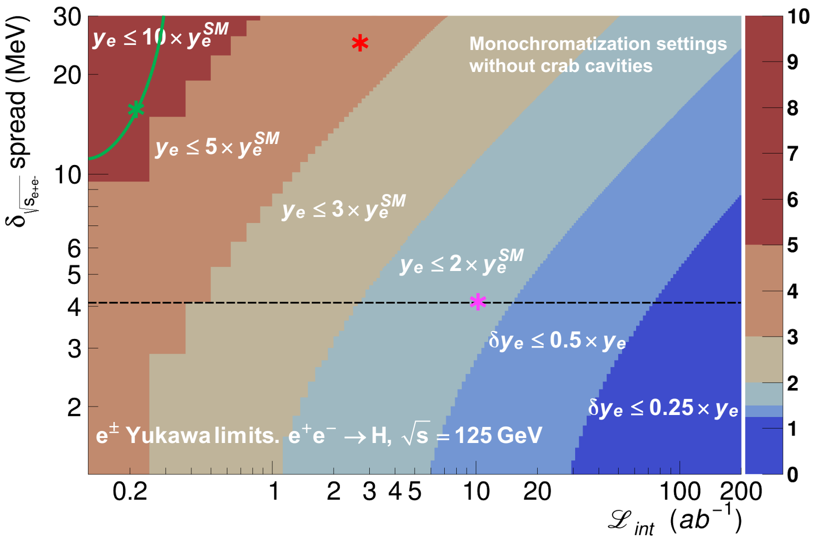

Fig. 4.10 Physics performance evaluation of the "MonochroM TVF1" optics across different values of β_x^* (green curve) in the upper limits contours (95% CL) for y_e. The green star indicates the optimal point at a β_x^* of 50 m.

Selection of the magnitude of vertical IP dispersion

Table 4.1 also shows that, with a larger D_y^*, the σ_W for the "MonochroM ZVF2" optics does not decrease further compared to the "MonochroM ZVF1" optics, while experiencing more luminosity loss. Given that changes in D_y^* only affect the vertical emittance, which is primarily influenced by beamstrahlung, we could plot the variation in $\mathcal{L}$ and σ_δ for the "MonochroM ZVF1" optics as a function of D_y^*, with the optimized β_x^* of 5 m, including the beamstrahlung impact in the crossing-angle collision configuration, as illustrated in Fig. 4.11. The decreasing slope of σ_δ flattens earlier than that of $\mathcal{L}$ after reaching $D_y^* = 1$ mm. At $D_y^* = 1$ mm, σ_δ is 16.65 MeV, while $\mathcal{L}$ is $1.69 \times 10^{34}\,\mathrm{cm^{-2}\,s^{-1}}$. As D_y^* increases to 2 mm, σ_δ slightly decreases to 16.08 MeV, but $\mathcal{L}$ drops significantly to $8.49 \times 10^{33}\,\mathrm{cm^{-2}\,s^{-1}}$. Therefore, considering $D_y^* = 2$ mm is not meaningful. However, it is noteworthy that at $D_y^* = 0.5$ mm, although σ_δ is slightly higher at 18.6 MeV, $\mathcal{L}$ is nearly double, reaching $3.32 \times 10^{34}\,\mathrm{cm^{-2}\,s^{-1}}$, compared to $D_y^* = 1$ mm. Thus, D_y^* values of 0.5 mm and 1 mm were selected for introduction into the "FCC-ee GHC V22 Z" optics for the monochromatization IR optics design and subsequent comparison. The same D_y^*

values were chosen for the "FCC-ee GHC V22 $\mathrm{t\bar{t}}$" optics following a similar analysis, as shown in Fig. 4.12.

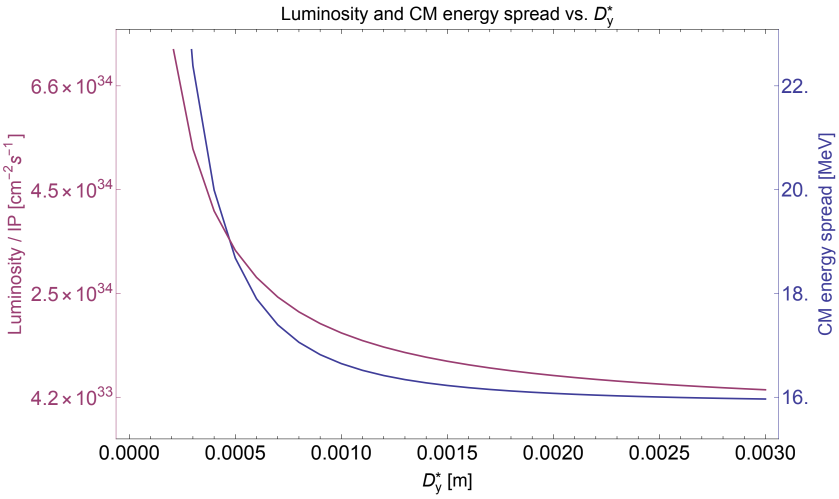

Fig. 4.11 Variation in luminosity per IP (red curve) and CM energy spread (blue curve) of the "MonochroM ZVF1" optics as a function of D_y^*, with the optimized β_x^* of 5 m, including the beamstrahlung impact in the crossing-angle collision configuration.

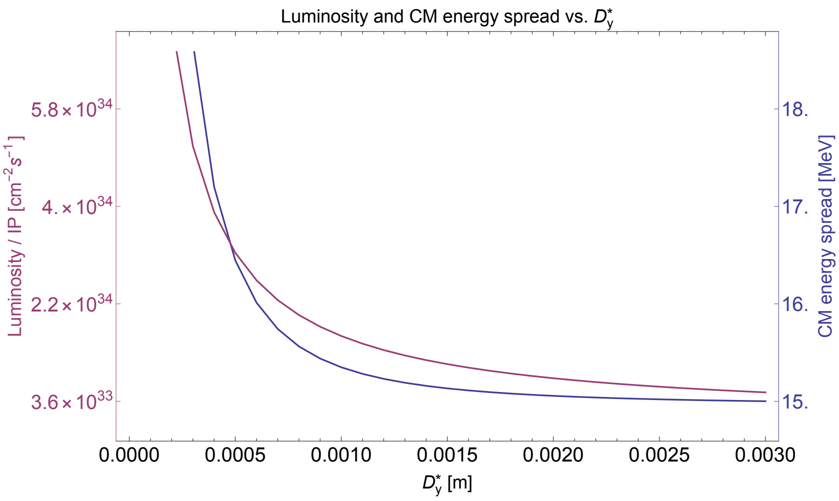

Fig. 4.12 Variation in luminosity per IP (red curve) and CM energy spread (blue curve) of the "MonochroM TVF1" optics as a function of D_y^*, with the optimized β_x^* of 50 m, including the beamstrahlung impact in the crossing-angle collision configuration.

4.2 Application to FCC-ee GHC optics

Following the principle of vertical IP dispersion generation proposed for FCC-ee GHC optics, we first completed the monochromatization IR optics design using MAD-X, based on the "FCC-ee GHC V22 Z" baseline standard optics. The target beam parameters, derived from preliminary parametric studies, were set as $\beta^*_{x,y} = 5\,\mathrm{m}, 0.8\,\mathrm{mm}$, and $D^*_y = 0.5\,\mathrm{mm}$ or $1\,\mathrm{mm}$. The steps and constraints for the IR optics design are detailed below.

Design steps:

1. Switch off the RF cavity in standard optics and calculated the optics function in the whole ring without considering the synchrotron radiation energy loss.

2. Get the Twiss function ($\beta_{x,y}$ and $\alpha_{x,y}$) and dispersion function ($D_{x,y}$) and its slope ($D'_{x,y}$) at the IR entrance, IR exit and IP.

3. Extract the IR from the global ring, for instance, we extracted the IR at the straight section labeled as "PG" in Fig. 2.2, from the marker "FF1.2" to "FG.5."

4. Separate the upstream IR (from "FF1.2" to "IP") and downstream IR (from "IP" to "Fg.5"), then reflect the lattice of upstream IR, as it is easier to match with a starting point that has simple optical functions, especially since the optical functions at the IP are characterized by: $\alpha_{x,y} = 0$, $D'_{x,y} = 0$.

5. Increase the β^*_x slightly for original 0.1 m to 0.2 m first. Vary the strength of all the quadrupoles to match the corresponding constraints that will be discussed later.

6. Use the matched strength of each quadrupole as a new initial condition. Increase the β^*_x to 0.3 m, and match the constraints again. Repeat this step until the required β^*_x is achieved.

7. Implement skew quadrupoles between the sextupole pairs as illustrated in Fig. 4.4.

8. Introduced the required nonzero vertical dispersion at the IP, and match vertical dispersion to zero at both the entrance and exit of the IR by varying the strength of the installed skew quadrupoles.

9. Reflect the designed monochromatization upstream IR back to its normal orientation, and connect it with the designed monochromatization downstream IR.

Matching constraints:

1. The optical functions at the IP match target beam parameters: $\beta^*_{x,y} = 5\,\mathrm{m}, 0.8\,\mathrm{mm}$, and $D^*_y = 0.5\,\mathrm{mm}/1\,\mathrm{mm}$, with all other optical functions maintained at zero.

2. The optical functions at the entrance and exit of the IR match those of the standard IR optics without monochromatization.

3. The dispersion-free region before the arc in either upstream or downstream IR should be restored.

4. The phase advance between the IP and the inner sextupole pairs should be $\mu_{x,y} = \pi, 1.5\pi$. The phase advance between the IP and the outer sextupole pairs should be $\mu_{x,y} = 2\pi, 2.5\pi$.

5. The four peak values of the vertical betatron function at the locations of the sextupole pairs should be identical.

The designed monochromatization IR lattice and optics satisfied all the constraints are shown in Fig. 4.13. A similar approach was also applied to the "FCC-ee GHC V22 $t\bar{t}$" optics. The betatron function at the IP were matched to: $\beta^*_{x,y} = 50\,\mathrm{m}, 0.8\,\mathrm{mm}$. Fig. 4.14 illustrates the monochromatization IR optics with a vertical IP dispersion of 1 mm at the top and 0.5 mm at the bottom.

Compatibility with the standard operation mode without dispersion at the IP, could be achieved by deactivating the installed skew quadrupoles and restoring the quadrupole strengths in the IR to their original values in the standard optics.

The global insertion of the monochromatization IR optics with nonzero vertical IP dispersion was simpler than that of the horizontal one. It only required the installation of four skew quadrupoles between the sextupole pairs in each of the four IRs, with their strengths matched to generate the desired vertical IP dispersion. Subsequently, the strengths of all quadrupoles in the IR were adjusted to their matched values to increase the horizontal betatron function at the IPs.

The local chromaticity correction, global chromaticity correction, and tune corrections were carried out following the same steps as described in Subsec. 3.2.3. The local vertical chromaticity from each outer skew quadrupole to each IP was matched to zero by adjusting the strength of the inner chromaticity sextupoles in the IR. The strength of the crab sextupoles was determined using Eq. 3.3. Global horizontal and vertical chromaticity were matched to a value of 5 by adjusting the strengths of all focusing and defocusing arc sextupoles.

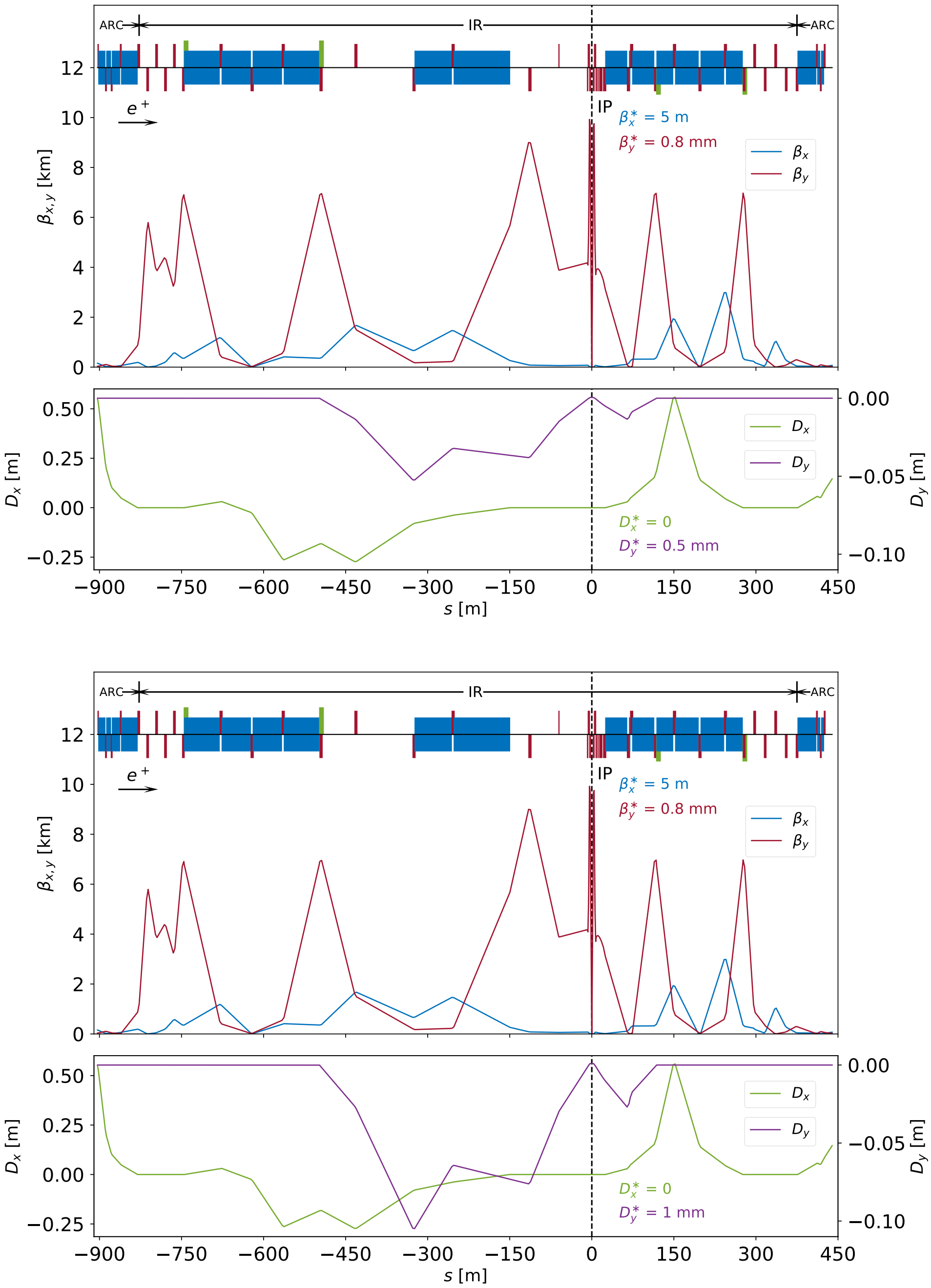

Fig. 4.13 Monochromatization IR lattices and optics with nonzero vertical IP dispersion of 0.5 mm (top) and 1 mm (bottom) based on the "FCC-ee GHC V22 Z" optics calculated using MAD-X. The beam direction is from left to right; the dashed line $s = 0$ marks the location of IP. In the lattice, dipoles, quadrupoles, and sextupoles are shown in blue, red, and green, respectively, while focusing and defocusing elements are positioned above and below the orbit. In the optics, horizontal and vertical betatron functions are shown in blue and red, respectively, while horizontal and vertical dispersion functions are shown in green and purple, respectively.

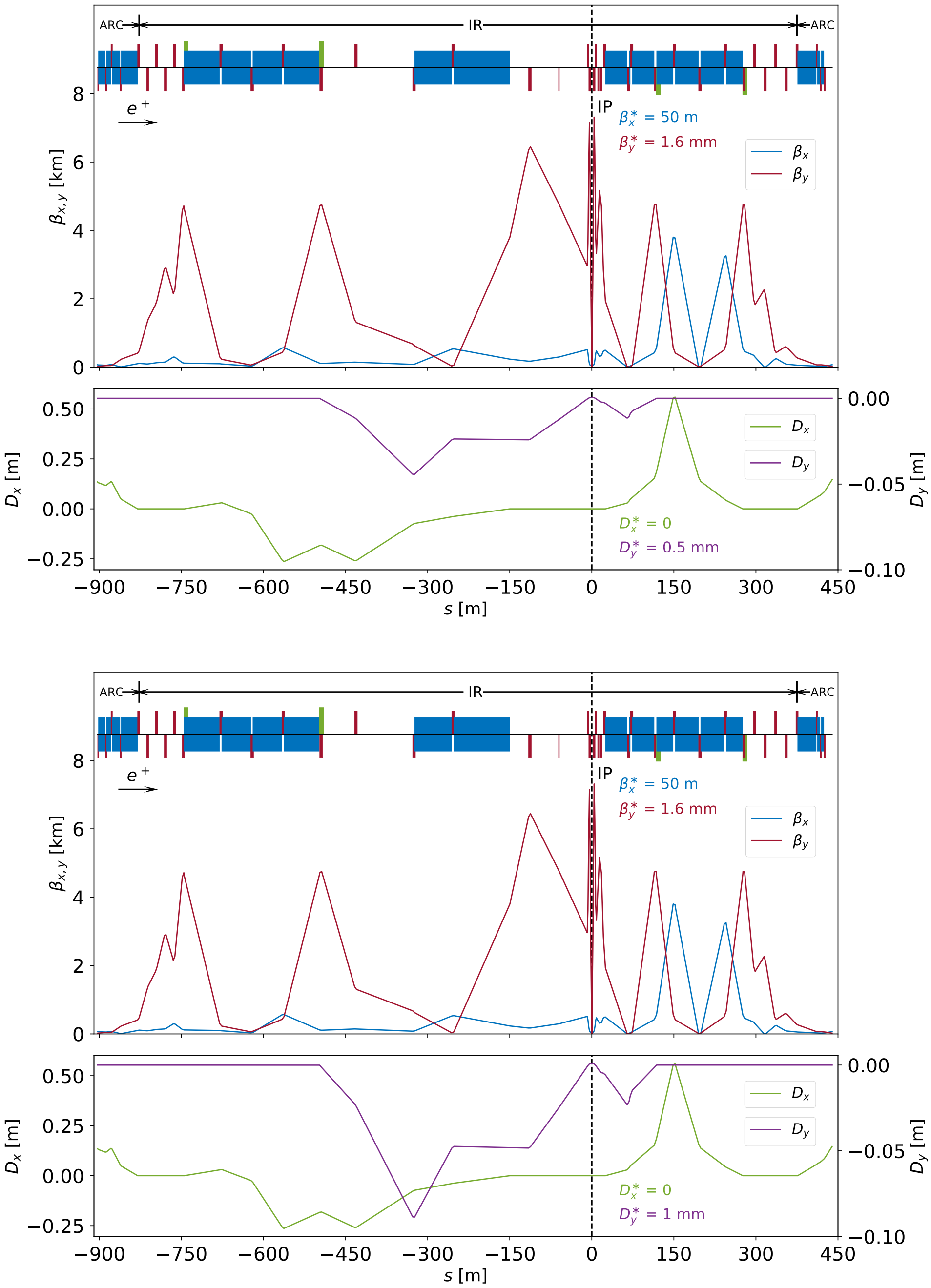

Fig. 4.14 Monochromatization IR lattices and optics with nonzero vertical IP dispersion of 0.5 mm (top) and 1 mm (bottom) based on the "FCC-ee GHC V22 $t\bar{t}$" optics calculated using MAD-X. The beam direction is from left to right; the dashed line $s = 0$ marks the location of IP. In the lattice, dipoles, quadrupoles, and sextupoles are shown in blue, red, and green, respectively, while focusing and defocusing elements are positioned above and below the orbit. In the optics, horizontal and vertical betatron functions are shown in blue and red, respectively, while horizontal and vertical dispersion functions are shown in green and purple, respectively.

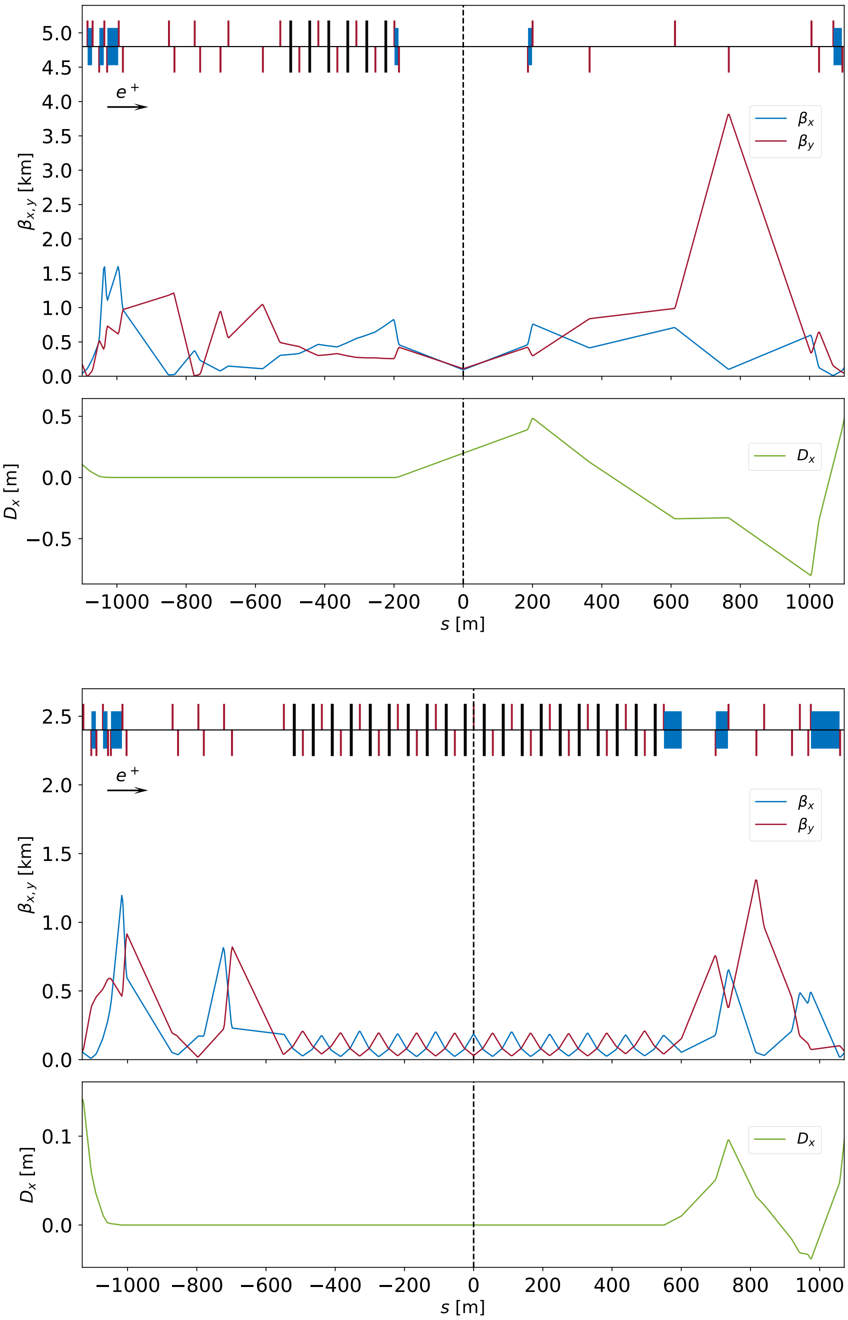

Fig. 4.15 Lattices and optics of the RF insertion after tune correction of the global implementation of monochromatization IR optics with nonzero vertical IP dispersion based on the “FCC-ee GHC V22 Z” (top) and “FCC-ee GHC V22 $t\bar{t}$” (bottom) optics calculated using MAD-X. The beam direction is from left to right, with the dashed line $s = 0$ indicating the center of the RF insertion. In the lattice, dipoles, quadrupoles, and RF cavities are shown in blue, red, and black, respectively, while focusing and defocusing elements are positioned above and below the orbit. In the optics, horizontal and vertical betatron functions are shown in blue and red, respectively, while horizontal dispersion function is shown in green.

Fig. 4.15 illustrates the RF insertion lattice and optics after tune correction, based on the "FCC-ee GHC V22 Z" (top) and "FCC-ee GHC V22 $t\bar{t}$" (bottom) optics. The horizontal and vertical tunes $Q_{x,y}$, were matched to those of the standard mode by adjusting the strength of the quadrupoles in the RF insertion. The Twiss function $\alpha_{x,y}$ at the center of the RF insertion was also matched to zero, while ensuring the beam parameters were maintained at all four IPs. All RF cavities were positioned in the dispersion-free region.

To compensate for the energy loss due to synchrotron radiation, the RF cavities were activated, and their phases were adjusted to match the value of the t' (Eq. 3.4), to zero. The RF cavity voltage was set to the same value used in the global implementation of the monochromatization IR optics with nonzero horizontal IP dispersion.

4.3 Performance evaluation

4.3.1 Global optical performance

The global performance of all designed monochromatization IR optics with nonzero vertical IP dispersion ($D_y^* \neq 0$) was evaluated analytically after their global implementation, taking into account the effects of beamstrahlung. The evaluation included both of the proposed FCC-ee monochromatization collision schemes, as illustrated in Fig. 1.9: the CC scheme which uses crab cavities for head-on collisions, and the IRS scheme which operates without crab cavities and involves a crossing-angle collision.

Table 4.2 and Table 4.3 summarize the global performance of the monochromatization IR optics with nonzero D_y^* based on the "FCC-ee GHC V22 Z" optics under the head-on and crossing-angle collision configurations, respectively. For comparison, the first column lists the performance parameters of the "Standard ZES" optics, as described in Subsec. 3.3.1. The optics labeled "MonochroM ZV0.5" and "MonochroM ZV1" represent the monochromatization optics designs with D_y^* of 0.5 mm and 1 mm at four IPs, respectively. All parameters were calculated using the same method as outlined in Subsec. 3.3.1, where values due to synchrotron radiation alone are marked with "SR," and those including the impact of beamstrahlung are marked with "BS."

It is important to note that the vertical emittance ε_y due solely to synchrotron radiation was also calculated based on the assumed 0.2% coupling ratio (Eq. 2.3) (full current) between horizontal and vertical motions, rather than being computed using MAD-X, as done in Table 4.1. This was necessary because the MAD-X results yielded smaller values compared to those obtained as per the coupling ratio with the increased horizontal IP betatron function.

To determine an appropriate number of bunches per beam n_b, we plotted the trade-off between the luminosity per IP $\mathcal{L}$ and the CM energy spread σ_W for the "MonochroM ZV1" optics, as a function of n_b, incorporating the beamstrahlung effects under the crossing-angle collision configuration, as illustrated in Fig. 4.16. The maximum n_b is constrained to 12000 by the harmonic number h (Eq. A.22) and a minimum bunch spacing of 25 ns. As n_b increases, σ_W drops sharply from over 150 MeV to below 20 MeV, while $\mathcal{L}$ experiences a modest decline from approximately $2.9 \times 10^{34}\,\mathrm{cm^{-2}\,s^{-1}}$ to $1.8 \times 10^{34}\,\mathrm{cm^{-2}\,s^{-1}}$. Based on these results, we selected a maximum n_b of 12000, consistent with the value chosen for the monochromatization optics with nonzero horizontal dispersion at the IP.

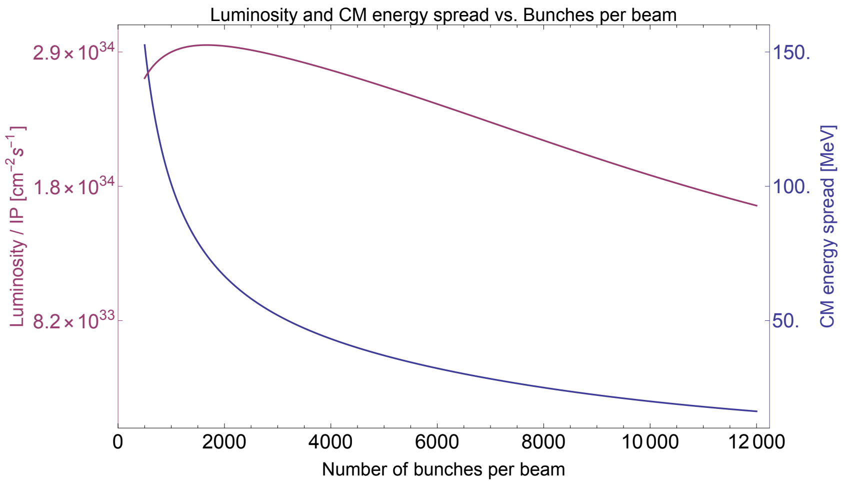

Fig. 4.16 Trade-off between luminosity per IP (red curve) and CM energy spread (blue curve) of the "MonochroM ZV1" optics, plotted as a function of number of bunches per beam, including the beamstrahlung impact under the crossing-angle collision configuration.

Under the head-on collision configuration, the σ_W of the "MonochroM ZV0.5" optics significantly decreases to 8.06 MeV when the impact of beamstrahlung is excluded. However, the presence of nonzero D_y^* causes a ε_y blow-up, from 2.67 pm to 10.7 pm due to beamstrahlung, as described by Eq. 1.84. This increase leads to a reduction in the monochromatization factor λ from 5.89 to 3.13, as calculated from Eq. 1.28. Meanwhile, the σ_δ (Eq. 1.85) with the beamstrahlung impact, remains close to the synchrotron radiation-only value of around 0.055%, owing to the increased horizontal IP betatron function β_x^*, from 0.1 m to 5 m. This reduction, along with the inverse correlation between vertical position and energy deviation, results in a final σ_W of 15.47 MeV. The decreased

Table 4.2 Global performance parameters of monochromatization IR optics with nonzero vertical IP dispersion based on the "FCC-ee GHC V22 Z" optics under the head-on configuration.

Parameter	**[Unit]**	**Standard ZES**	**MonochroM ZV0.5**	**MonochroM ZV1**
# of IPs n_{IP}			4	
Circumference C	[km]		91	
Full crossing angle θ_c	[mrad]		30	
SR power / beam P_{SR}	[MW]		50	
Beam energy E_0	[GeV]		62.5	
Energy loss / turn U_0	[GeV]		0.138	
Beam current I	[mA]		360	
Bunches / beam n_b			12000	
Bunch population N_b	[10^{11}]		0.57	
Horizontal emittance (SR / BS) ε_x	[nm]	1.33 / 1.33	1.34 / 1.34	1.34 / 1.34
Vertical emittance (SR / BS) ε_y	[pm]	2.65 / 2.65	2.67 / 10.7	2.67 / 34.6
Momentum compaction factor α_{C}	[10^{-6}]	28.0	27.9	27.9
$\beta^*_{x/y}$	[mm]	100 / 0.8	5000 / 0.8	5000 / 0.8
$D^*_{x/y}$	[m]	0 / 0	0 / 0.0005	0 / 0.001
Relative energy spread (SR / BS) σ_δ	[%]	0.054 / 0.115	0.054 / 0.055	0.054 / 0.055
Bunch length (SR / BS) σ_z	[mm]	4.09 / 8.61	4.10 / 4.11	4.10 / 4.11
RF voltage 400/800 MHz V_{RF}	[GV]		0.360 / 0	
RF frequency (400 MHz) f_{RF}	[MHz]		399.994581	
Synchrotron tune Q_s			0.054	
Long. damping time τ_E/T_{rev}	[turns]	453	454	454
Horizontal beam-beam (SR / BS) ξ_x			0.16 / 0.16	
Vertical beam-beam (SR / BS) ξ_y		0.31 / 0.31	0.0075 / 0.0070	0.0038 / 0.0035
CM energy spread (SR / BS) σ_W	[MeV]	47.47 / 101.89	8.06 / 15.47	4.07 / 14.08
Luminosity / IP (SR / BS) $\mathcal{L}$	[10^{34} cm^{-2} s^{-1}]	192 / 192	4.57 / 4.30	2.31 / 2.17

Table 4.3 Global performance parameters of monochromatization IR optics with nonzero vertical IP dispersion based on the "FCC-ee GHC V22 Z" optics under the crossing-angle configuration.

Parameter	**[Unit]**	**Standard ZES**	**MonochroM ZV0.5**	**MonochroM ZV1**
# of IPs n_{IP}			4	
Circumference C	[km]		91	
Full crossing angle θ_c	[mrad]		30	
SR power / beam P_{SR}	[MW]		50	
Beam energy E_0	[GeV]		62.5	
Energy loss / turn U_0	[GeV]		0.138	
Beam current I	[mA]		360	
Bunches / beam n_b			12000	
Bunch population N_b	[10^{11}]		0.57	
Horizontal emittance (SR / BS) ε_x	[nm]	1.33 / 1.33	1.34 / 1.34	1.34 / 1.34
Vertical emittance (SR / BS) ε_y	[pm]	2.65 / 2.65	2.67 / 13.84	2.67 / 47.32
Momentum compaction factor α_{C}	[10^{-6}]	28.0	27.9	27.9
$\beta^*_{x/y}$	[mm]	100 / 0.8	5000 / 0.8	5000 / 0.8
$D^*_{x/y}$	[m]	0 / 0	0 / 0.0005	0 / 0.001
Relative energy spread (SR / BS) σ_δ	[%]	0.054 / 0.078	0.054 / 0.055	0.054 / 0.055
Bunch length (SR / BS) σ_z	[mm]	4.09 / 5.82	4.10 / 4.14	4.10 / 4.14
RF voltage 400/800 MHz V_{RF}	[GV]		0.360 / 0	
RF frequency (400 MHz) f_{RF}	[MHz]		399.994581	
Synchrotron tune Q_s			0.054	
Long. damping time τ_E/T_{rev}	[turns]	453	454	454
Horizontal beam-beam (SR / BS) ξ_x		0.0054 / 0.0027	0.10 / 0.099	0.099 / 0.098
Vertical beam-beam (SR / BS) ξ_y		0.058 / 0.041	0.0060 / 0.0055	0.0030 / 0.0028
CM energy spread (SR / BS) σ_W	[MeV]	47.47 / 68.78	8.06 / 17.38	4.07 / 16.22
Luminosity / IP (SR / BS) $\mathcal{L}$	[10^{34} cm^{-2} s^{-1}]	35.4 / 25.1	3.65 / 3.35	1.85 / 1.69

Table 4.4 Global performance parameters of monochromatization IR optics with nonzero vertical IP dispersion based on the "FCC-ee GHC V22 $t\bar{t}$" optics under the head-on configuration.

Parameter	[Unit]	Standard TES	MonochroM TV0.5	MonochroM TV1
# of IPs n_{IP}			4	
Circumference C	[km]		91	
Full crossing angle θ_c	[mrad]		30	
SR power / beam P_{SR}	[MW]		50	
Beam energy E_0	[GeV]		62.5	
Energy loss / turn U_0	[GeV]		0.138	
Beam current I	[mA]		360	
Bunches / beam n_b			12000	
Bunch population N_b	[10^{11}]		0.57	
Horizontal emittance (SR / BS) ε_x	[nm]	0.17 / 0.17	0.19 / 0.19	0.19 / 0.19
Vertical emittance (SR / BS) ε_y	[pm]	0.35 / 0.35	0.37 / 3.05	0.37 / 11.1
Momentum compaction factor α_{C}	[10^{-6}]		7.31	
$\beta^*_{x/y}$	[mm]	1000 / 1.6	50000 / 1.6	50000 / 1.6
$D^*_{x/y}$	[m]	0 / 0	0 / 0.0005	0 / 0.001
Relative energy spread (SR / BS) σ_δ	[%]	0.054 / 0.108	0.054 / 0.054	0.054 / 0.054
Bunch length (SR / BS) σ_z	[mm]	3.86 / 7.71	3.86 / 3.91	3.86 / 3.91
RF voltage 400/800 MHz V_{RF}	[GV]		0.170 / 0	
RF frequency (400 MHz) f_{RF}	[MHz]		399.994581	
Synchrotron tune Q_s			0.015	
Long. damping time τ_E/T_{rev}	[turns]		454	
Horizontal beam-beam (SR / BS) ξ_x		1.20 / 1.20	1.12 / 1.12	1.11 / 1.11
Vertical beam-beam (SR / BS) ξ_y		1.07 / 1.07	0.013 / 0.012	0.0064 / 0.0061
CM energy spread (SR / BS) σ_W	[MeV]	47.46 / 95.03	4.30 / 11.96	2.16 / 11.43
Luminosity / IP (SR / BS) $\mathcal{L}$	[10^{34} cm^{-2} s^{-1}]	328 / 328	3.91 / 3.75	1.96 / 1.88

Table 4.5 Global performance parameters of monochromatization IR optics with nonzero vertical IP dispersion based on the "FCC-ee GHC V22 $t\bar{t}$" optics under the crossing-angle configuration.

Parameter	**[Unit]**	**Standard TES**	**MonochroM TV0.5**	**MonochroM TV1**
# of IPs n_{IP}			4	
Circumference C	[km]		91	
Full crossing angle θ_c	[mrad]		30	
SR power / beam P_{SR}	[MW]		50	
Beam energy E_0	[GeV]		62.5	
Energy loss / turn U_0	[GeV]		0.138	
Beam current I	[mA]		360	
Bunches / beam n_b			12000	
Bunch population N_b	[10^{11}]		0.57	
Horizontal emittance (SR / BS) ε_x	[nm]	0.17 / 0.17	0.19 / 0.19	0.19 / 0.19
Vertical emittance (SR / BS) ε_y	[pm]	0.35 / 0.35	0.37 / 4.99	0.37 / 18.8
Momentum compaction factor α_{C}	[10^{-6}]		7.31	
$\beta^*_{x/y}$	[mm]	1000 / 1.6	50000 / 1.6	50000 / 1.6
$D^*_{x/y}$	[m]	0 / 0	0 / 0.0005	0 / 0.001
Relative energy spread (SR / BS) σ_δ	[%]	0.054 / 0.076	0.054 / 0.055	0.054 / 0.055
Bunch length (SR / BS) σ_z	[mm]	3.86 / 5.49	3.86 / 3.95	3.86 / 3.95
RF voltage 400/800 MHz V_{RF}	[GV]		0.170 / 0	
RF frequency (400 MHz) f_{RF}	[MHz]		399.994581	
Synchrotron tune Q_s			0.015	
Long. damping time τ_E/T_{rev}	[turns]		454	
Horizontal beam-beam (SR / BS) ξ_x		0.059 / 0.030	0.82 / 0.81	0.82 / 0.81
Vertical beam-beam (SR / BS) ξ_y		0.24 / 0.17	0.011 / 0.010	0.0055 / 0.0051
CM energy spread (SR / BS) σ_W	[MeV]	47.45 / 68.58	4.30 / 15.02	2.16 / 14.63
Luminosity / IP (SR / BS) $\mathcal{L}$	[10^{34} cm^{-2} s^{-1}]	72.8 / 51.9	3.36 / 3.11	1.68 / 1.56

$\mathcal{L}$ of $4.30 \times 10^{34}\,\mathrm{cm^{-2}\,s^{-1}}$, is attributed to both the increased horizontal and vertical IP beam sizes, $\sigma^*_{x,y}$. The horizontal size increase results from the larger β^*_x, while the vertical size is due to both the increased ε_y and the nonzero D^*_y. For the "MonochroM ZV1" optics, with a higher D^*_y, the σ_W further decreases to 14.08 MeV, though at the cost of more luminosity loss compared to the "MonochroM ZV0.5" optics. The vertical beam-beam tune shift ξ_y remains within its limitation (Eq. 3.6), aided by the increased $\sigma^*_{x,y}$, demonstrating the feasibility of the CC scheme for FCC-ee monochromatization mode with nonzero D^*_y.

Under the crossing-angle collision configuration, the vertical emittance ε_y of the "MonochroM ZV1" optics is significantly smaller than that of the "MonochroM ZVF1" (Table 4.1), considering the beamstrahlung impact, due to the increased β^*_x from 0.1 m to 5 m. Compared to the head-on collision configuration, both the "MonochroM ZV0.5" and "MonochroM ZV1" optics experience greater ε_y blow-up due to their Piwinski angles being less than 1, which leads to higher CM energy spread σ_W and lower luminosity $\mathcal{L}$.

The same calculations and analyses were carried out for the monochromatization IR optics based on the "FCC-ee GHC V22 $\mathrm{t\bar{t}}$" optics, and the results are presented in two tables: Table 4.4 for the head-on collision configuration and Table 4.5 for the crossing-angle configuration, with the corresponding monochromatization optics labeled as "Standard TES," "MonochroM TV0.5," and "MonochroM TV1." The selection of the n_b is shown in Fig. 4.17. The vertical beam-beam tune shift ξ_y for all these monochromatization designs

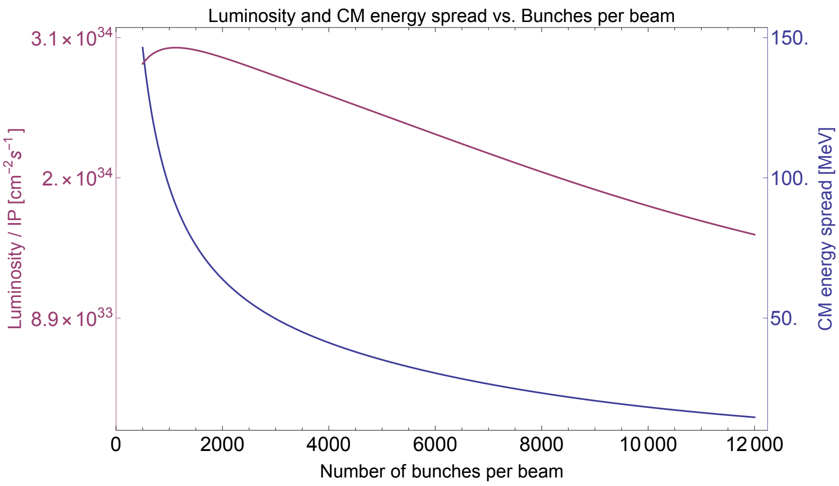

Fig. 4.17 Trade-off between luminosity per IP (red curve) and CM energy spread (blue curve) of the "MonochroM TV1" optics, plotted as a function of number of bunches per beam, including the beamstrahlung impact under the crossing-angle collision configuration.

based on the "FCC-ee GHC V22 $t\bar{t}$" optics remains within the acceptable limit (Eq. 3.6), similar to the designs based on the "FCC-ee GHC V22 Z" optics.

4.3.2 Preliminary dynamic aperture studies

Preliminary 6D DA studies were conducted for the designed monochromatization optics with nonzero vertical IP dispersion using Xsuite, after transferring and re-matching the optics from the MAD-X version to the Xsuite version.

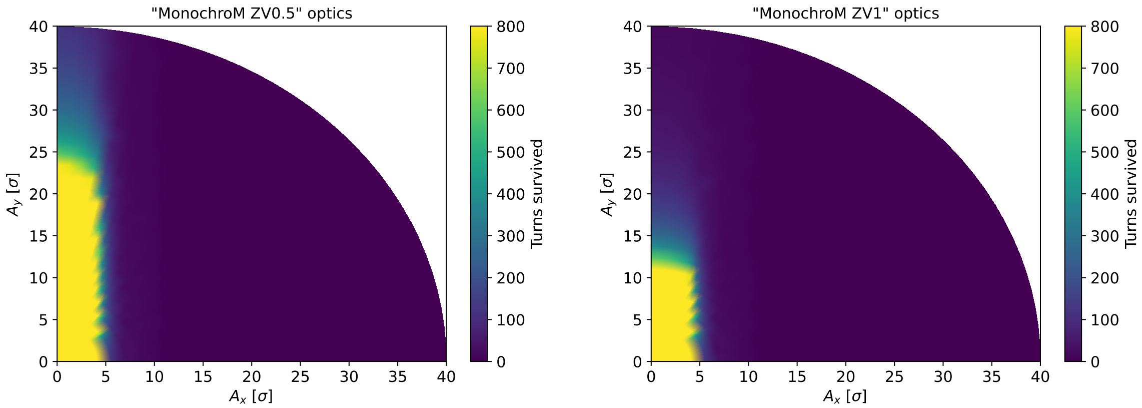

Fig. 4.18 Results of preliminary 6D DA studies for the "MonochroM ZV0.5" (left) and "MonochroM ZV1" (right) optics based on the "FCC-ee GHC V22 Z" optics calculated with Xsuite. The varying colors indicate the number of particle surviving turns.

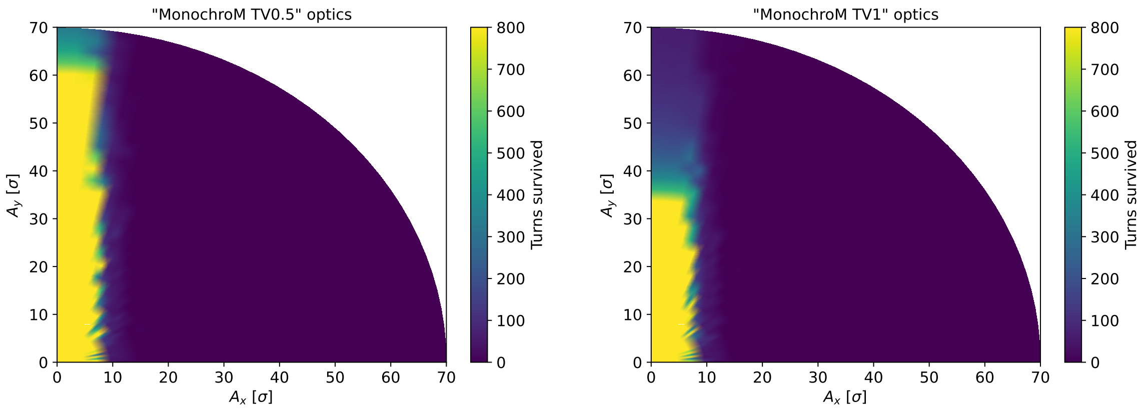

Fig. 4.19 Results of preliminary 6D DA studies for the "MonochroM TV0.5" (left) and "MonochroM TV1" (right) optics based on the "FCC-ee GHC V22 $t\bar{t}$" optics calculated with Xsuite. The varying colors indicate the number of particle surviving turns.

The initial particle motion amplitude $A_{x,y}$ (Eq. 3.7) was set as $70\,\sigma$, with phase $\phi = 0$ and momentum deviation $\delta = 0$. The number of tracking turns was set to twice the longitudinal damping time (τ_E/T_{rev}). The resulting DA plots for the "MonochroM ZV0.5" and "MonochroM ZV1" optics based on the "FCC-ee GHC V22 Z" optics are shown in the left and right of Fig. 4.18, respectively, without conducting the optimization of the arc family sextupoles. Similarly, Fig. 4.19 presents the results of the same study procedure for the monochromatization optics based on the "FCC-ee GHC V22 $\mathrm{t\bar{t}}$" optics.

4.3.3 Physics performance

For the physics performance evaluation of the FCC-ee monochromatization IR optics with nonzero vertical dispersion at the IP, the CM energy spread σ_W and luminosity per IP $\mathcal{L}$ were calculated using Guinea-Pig. The six characteristic parameters for each particle in the ideal Gaussian distribution at the IP—energy E, horizontal position x, vertical position y, longitudinal position z, horizontal angle x', and vertical angle y'—are determined by the optical parameters: beam energy E_0, relative beam energy spread σ_δ, emittance $\varepsilon_{x,y}$, IP betatron function $\beta^*_{x,y}$, IP dispersion function $D^*_{x,y}$, bunch length σ_z, and full crossing angle θ_c, following Eq. 3.8. Fig. 4.20 illustrates the inverse correlation

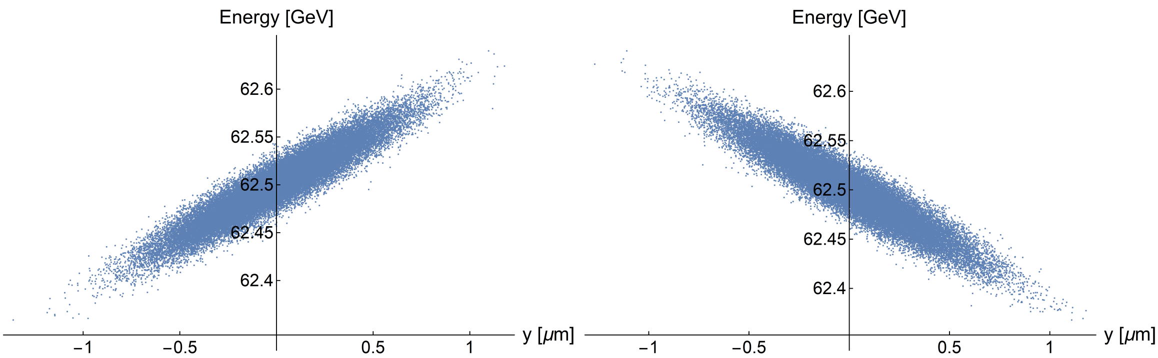

Fig. 4.20 Opposite correlation between vertical spatial position y and energy deviation of the position distribution (left) and the electron distribution (right) at the IP of the "MonochroM ZV0.5" optics, based on the "FCC-ee GHC V22 Z" optics.

between vertical spatial position y and energy deviation for the positron distribution (left) and electron distribution (right) at the IP of the "MonochroM ZV0.5" optics, based on the "FCC-ee GHC V22 Z" optics under the crossing-angle collision configuration. The positron beam exhibits a vertical IP dispersion of 0.5 mm, while the electron beam has a dispersion of −0.5 mm.

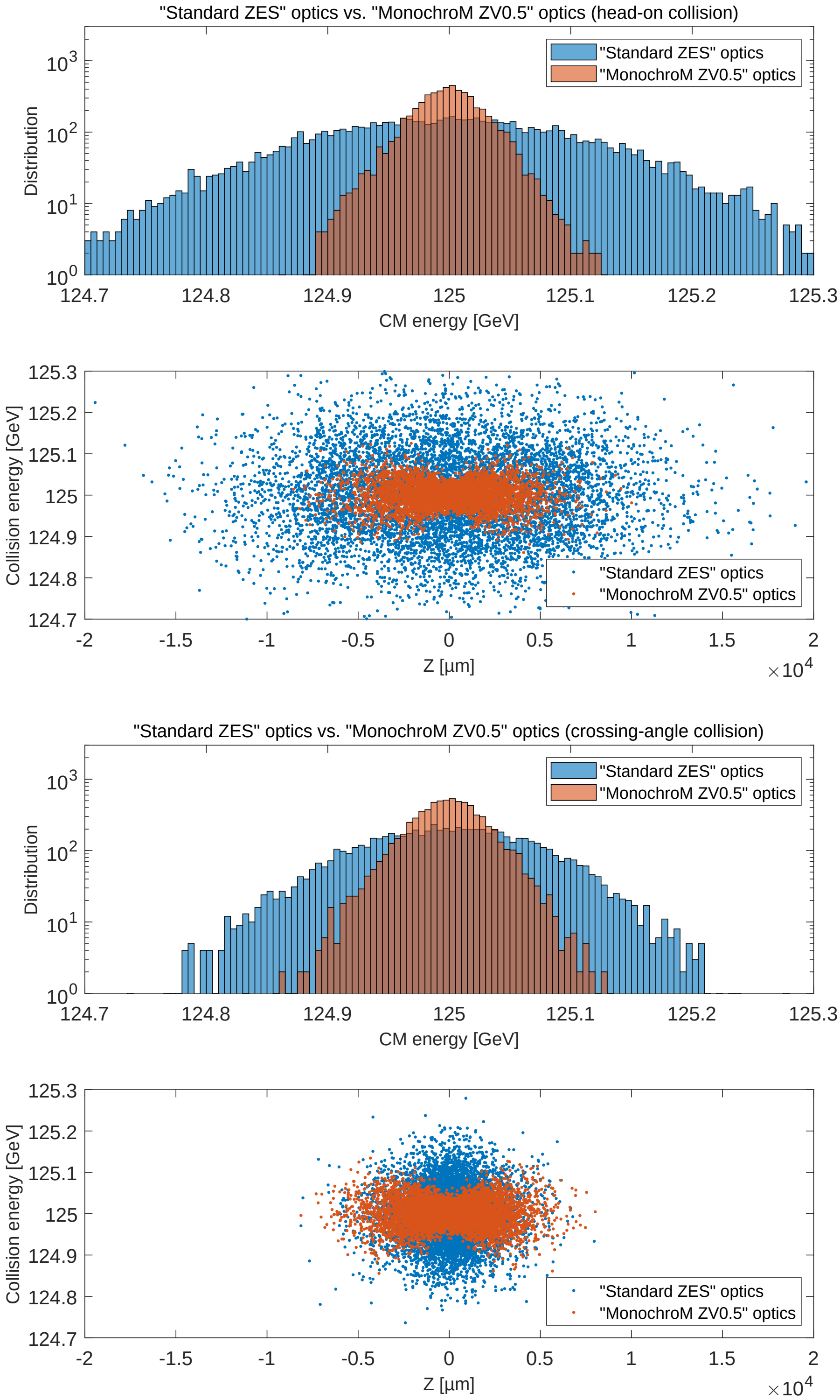

Fig. 4.21 Comparison between the "Standard ZES" and "MonochroM ZV0.5" optics in terms of the CM energy distribution and its correlation with the longitudinal collision position simulated using Guinea-Pig, under the head-on (top) or crossing-angle (bottom) collision configuration.

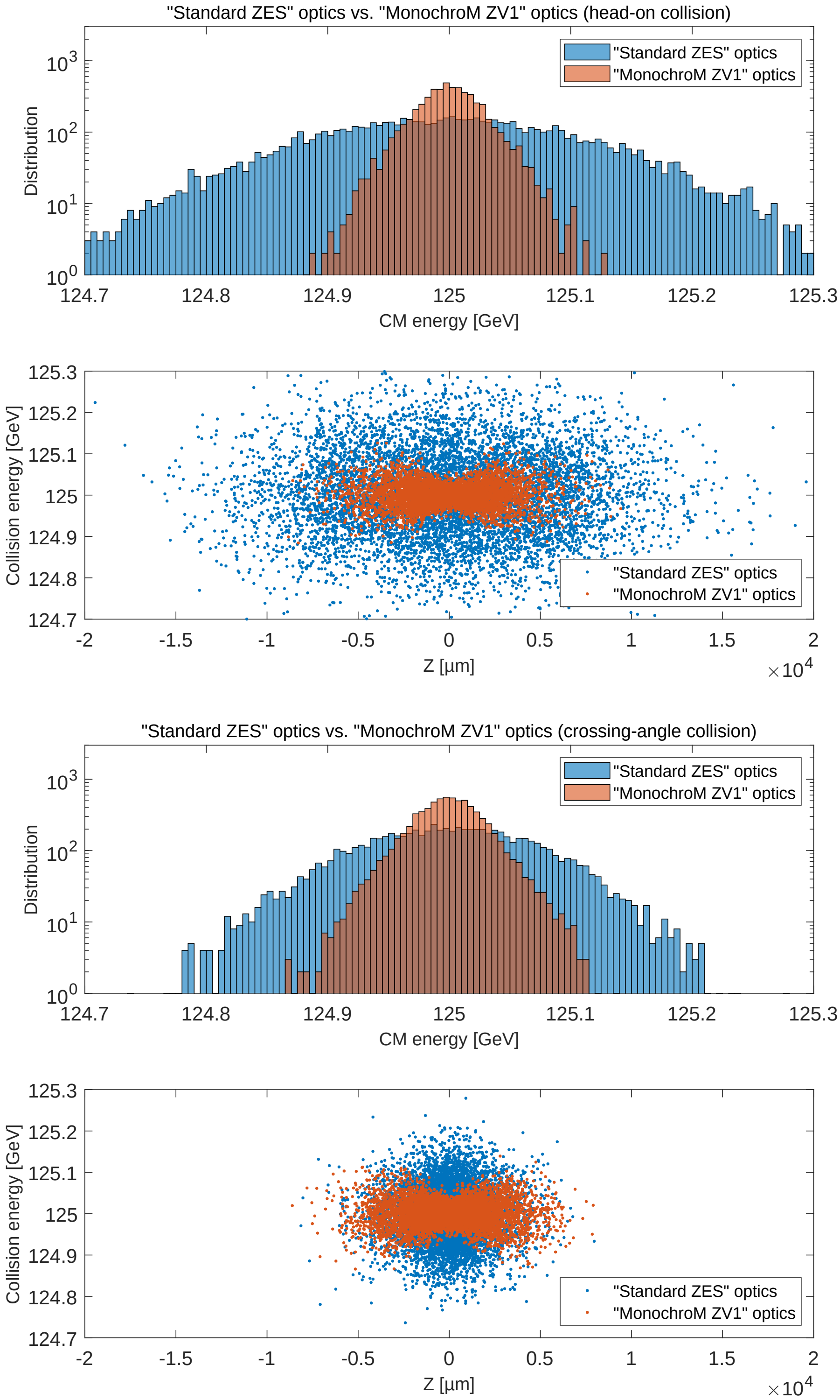

Fig. 4.22 Comparison between the “Standard ZES” and “MonochroM ZV1” optics in terms of the CM energy distribution and its correlation with the longitudinal collision position simulated using Guinea-Pig, under the head-on (top) or crossing-angle (bottom) collision configuration.

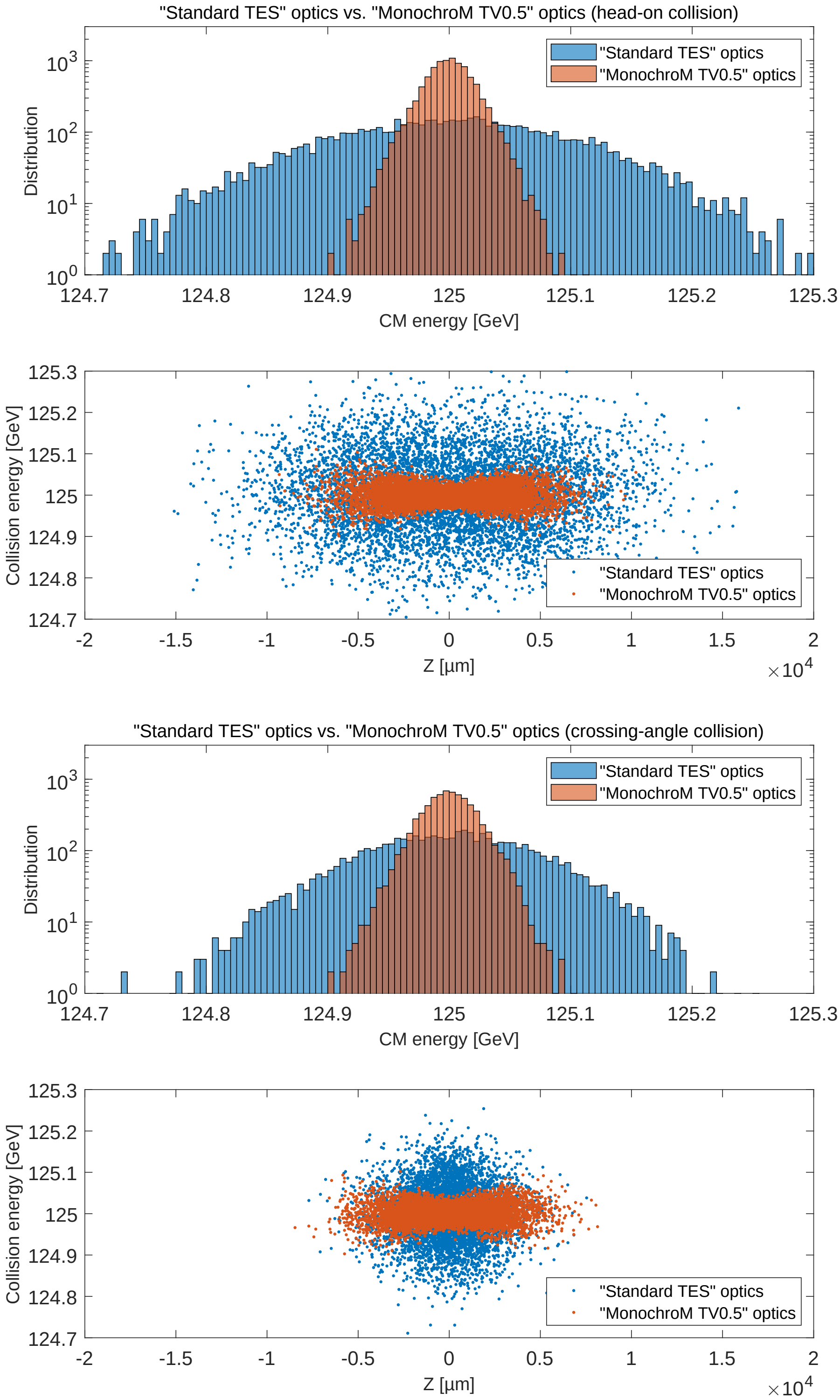

Fig. 4.23 Comparison between the “Standard TES” and “MonochroM TV0.5” optics in terms of the CM energy distribution and its correlation with the longitudinal collision position simulated using Guinea-Pig, under the head-on (top) or crossing-angle (bottom) collision configuration.

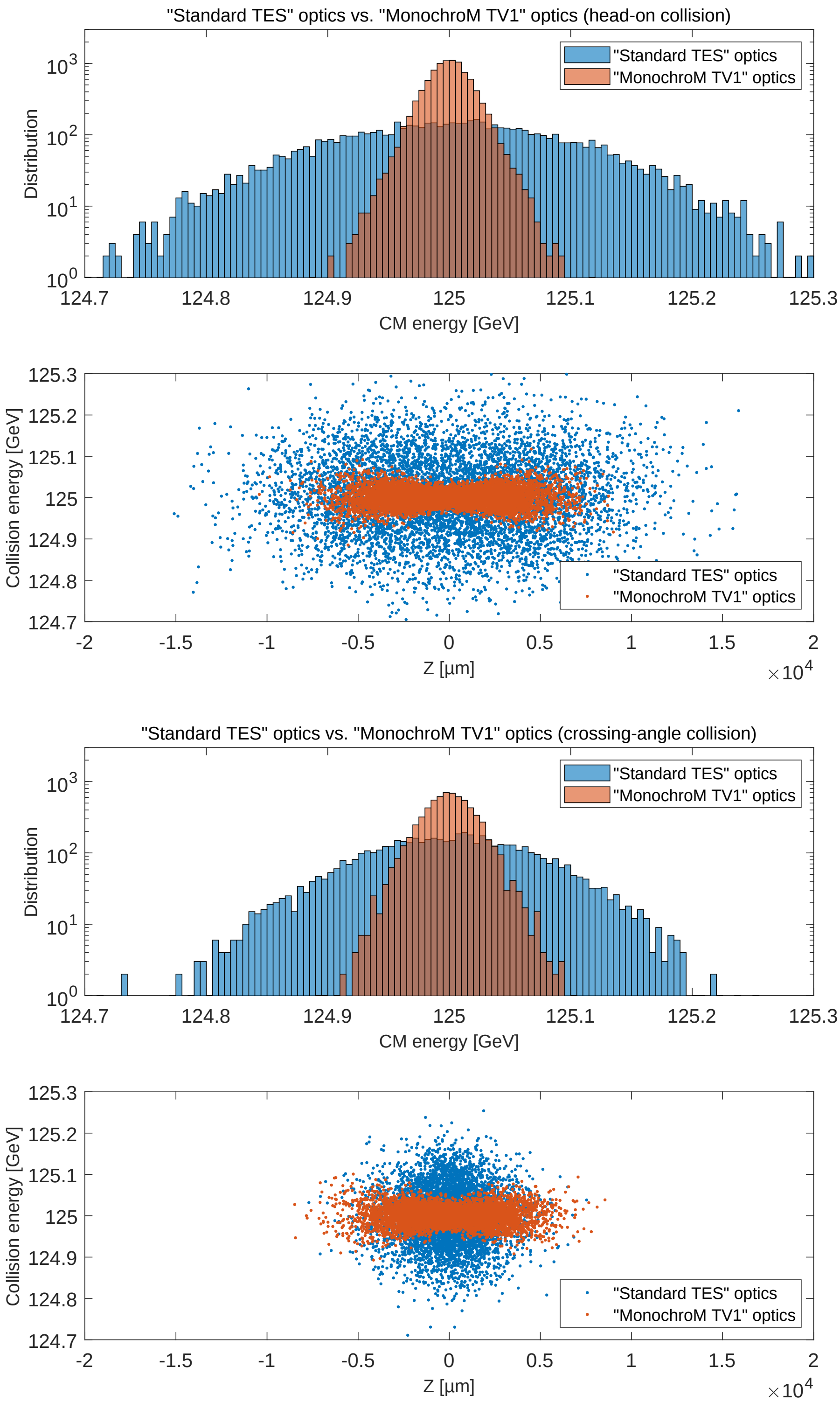

Fig. 4.24 Comparison between the "Standard TES" and "MonochroM TV1" optics in terms of the CM energy distribution and its correlation with the longitudinal collision position simulated using Guinea-Pig, under the head-on (top) or crossing-angle (bottom) collision configuration.

Table 4.6 CM energy spread, luminosity per IP, integrated luminosity per IP and year of monochromatization IR optics with nonzero vertical IP dispersion based on the "FCC-ee GHC V22 Z" optics with or without crab cavities.

Parameter	**[Unit]**	**Standard ZES**	**MonochroM ZV0.5**	**MonochroM ZV1**
CM energy spread (with / without crab cavities) σ_W	[MeV]	103.1 / 69.15	25.50 / 27.12	24.06 / 25.82
Luminosity / IP (with / without crab cavities) $\mathcal{L}$	[10^{34} cm^{-2} s^{-1}]	197 / 44.6	4.31 / 2.91	2.18 / 1.46
Integrated luminosity / IP / year (with / without crab cavities) $\mathcal{L}_{\text{int}}$	[ab^{-1}]	23.6 / 5.35	0.52 / 0.35	0.26 / 0.18

Table 4.7 CM energy spread, luminosity per IP, integrated luminosity per IP and year of monochromatization IR optics with nonzero vertical IP dispersion based on the "FCC-ee GHC V22 $\mathrm{t\bar{t}}$" optics with or without crab cavities.

Parameter	**[Unit]**	**Standard TES**	**MonochroM TV0.5**	**MonochroM TV1**
CM energy spread (with / without crab cavities) σ_W	[MeV]	93.76 / 67.51	17.59 / 20.14	16.55 / 19.52
Luminosity / IP (with / without crab cavities) $\mathcal{L}$	[10^{34} cm^{-2} s^{-1}]	336 / 71.2	3.79 / 2.73	1.88 / 1.37
Integrated luminosity / IP / year (with / without crab cavities) $\mathcal{L}_{\text{int}}$	[ab^{-1}]	40.3 / 8.54	0.45 / 0.33	0.23 / 0.16

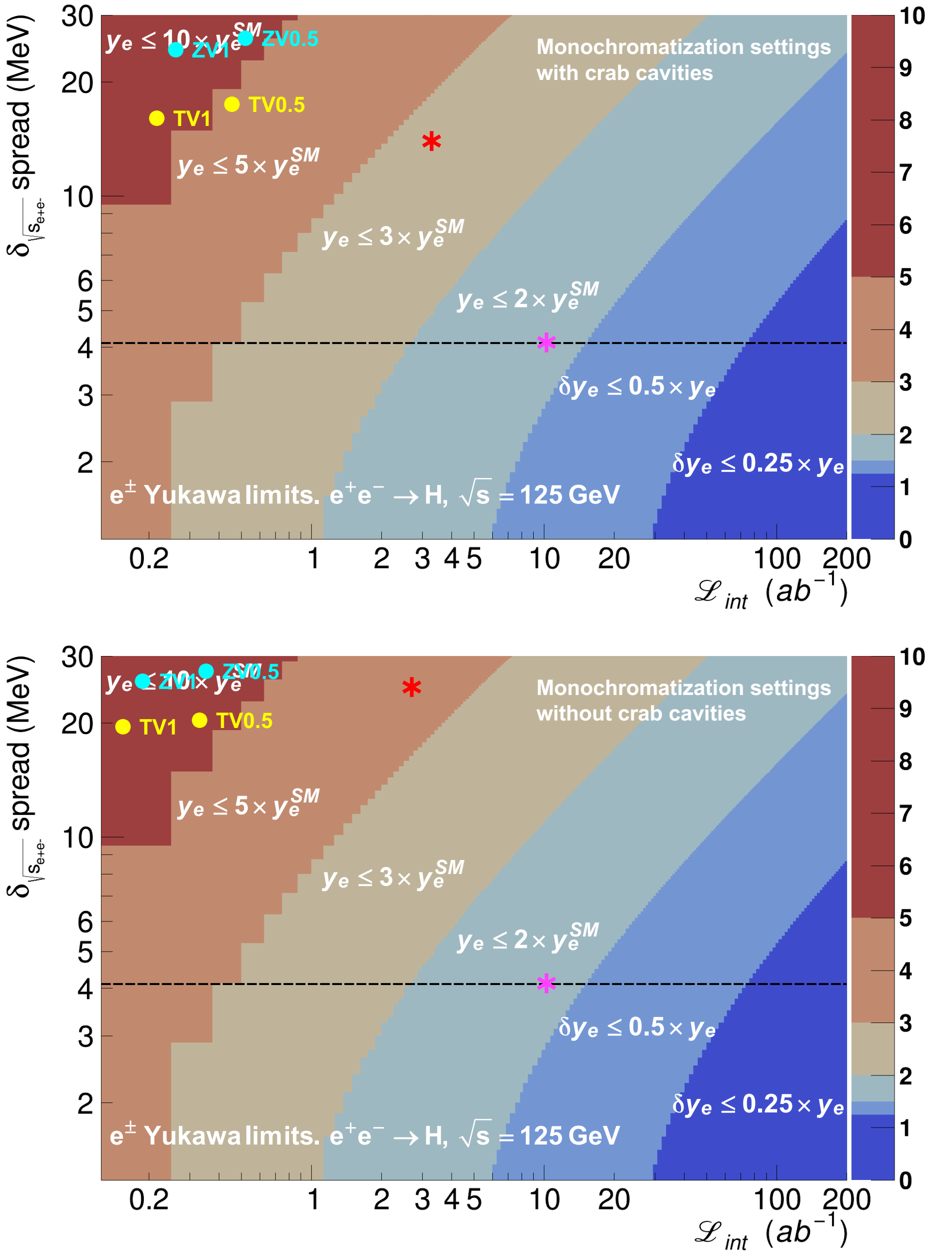

Fig. 4.25 Physics performance evaluation of the proposed monochromatization optics with nonzero vertical IP dispersion, under the head-on (top) or crossing-angle (bottom) collision configuration, indicated by the $\delta_{\sqrt{s}}$-$\mathcal{L}_{\rm int}$ benchmarks in the upper limits contours (95% CL) on the y_e. The monochromatization optics base on the "FCC-ee GHC V22 Z" optics and "FCC-ee GHC V22 $t\bar{t}$" optics are marked in cyan and yellow, respectively. The pink star over the $\delta_{\sqrt{s}} = \Gamma_{\rm H} = 4.1\,$MeV dashed line, indicates the baseline point assumed in the original physics simulation analysis [69]. The red stars represent the previously achieved working point with parameterized studies [53, 55].

Using the particle distribution at the IP, σ_W and $\mathcal{L}$, with or without crab cavities, were calculated for all the designed monochromatization optics, following the procedure outlined in Subsec. 3.3.3. The corresponding results are illustrated in Fig. 4.21, Fig. 4.22, Fig. 4.23, Fig. 4.24, and are summarized in Table 4.6 for optics based on the "FCC-ee GHC V22 Z" optics, and in Table 4.7 for those based on the "FCC-ee GHC V22 $\mathrm{t\bar{t}}$" optics. The integrated luminosity values, $\mathcal{L}_{\text{int}}$, were calculated using the same scaling ratios of $\mathcal{L}$ as those used in Table 3.5 and Table 3.6. The $\delta_{\sqrt{s}}$-$\mathcal{L}_{\text{int}}$ benchmarks of each proposed monochromatization optics with nonzero vertical IP dispersion were established in the plot of upper limits contours (95% CL) for y_e coupling, as depicted in Fig. 4.25. The top figure corresponds to the head-on collision configuration, while the bottom figure shows the crossing-angle collision configuration. The best physics performance benchmark was achieved with the "MonochroM TV0.5" optics, yielding an upper limit of $|y_e| < 4.9|y_e^{\text{SM}}|$ for head-on collisions and $|y_e| < 5.1|y_e^{\text{SM}}|$ for crossing-angle collisions.

Chapter 5

FCC-ee GHC monochromatization IR optic design with combined IP dispersion

Considering the potential benefits of combining the two monochromatization schemes discussed above, an attempt is made to introduce combined horizontal and vertical dispersion at the IP. This is achieved by integrating skew quadrupoles into the monochromatization IR optics, which already have horizontal IP dispersion at the IP [120–128].

In this chapter, a monochromatization IR optics design featuring a combination of nonzero horizontal and vertical IP dispersion ($D_x^* \neq 0$, $D_y^* \neq 0$) is introduced. After integrating this design into the global lattice, its performance is evaluated and compared with the monochromatization optics that have only nonzero horizontal IP dispersion ($D_x^* \neq 0, D_y^* = 0$) and only nonzero vertical IP dispersion ($D_x^* = 0, D_y^* \neq 0$), as described in Chapter 3 and Chapter 4, respectively.

5.1 Principle of combined IP dispersion generation

With only nonzero horizontal IP dispersion ($D_x^* \neq 0, D_y^* = 0$), as described in Chapter 3, the CM energy spread σ_W is minimized to 11.97 MeV in a head-on collision setup. Likewise, with only nonzero vertical IP dispersion ($D_x^* = 0, D_y^* \neq 0$), as discussed in Chapter 4, the σ_W is minimized to 16.65 MeV. However, neither approach brings σ_W down to the target level, which should be comparable to the natural width of the Higgs boson, $\Gamma_{\mathrm{H}} = 4.1$ MeV. Therefore, based on the definition of the monochromatization factor λ (Eq. 1.28), we propose combining nonzero D_x^* and D_y^* to further increase λ

and achieve a greater reduction in σ_W. Additionally, in Chapter 4, we increased the horizontal IP beam size σ_x^* by raising the horizontal IP betatron function β_x^*, in order to mitigate the vertical emittance blow-up ε_y caused by nonzero D_y^* due to beamstrahlung. However, the nonzero D_x^* serves the same purpose as an increased β_x^*, as indicated by Eq. 1.23, meaning that increasing β_x^* is not necessary to counteract the ε_y blow-up in this monochromatization scenario with nonzero combined IP dispersion.

The generation of this combined IP dispersion can be achieved by incorporating skew quadrupoles into the monochromatization IR with nonzero D_x^*, as outlined in Chapter 3. The nonzero D_y^*, being independent of the horizontal dispersion in linear optics, will be corrected by these skew quadrupoles, which are expected to be placed near the sextupole pairs in the LCC system, as shown in Fig. 4.4.

5.2 Application to FCC-ee GHC optics

The principle of combined IP dispersion generation was first applied to the “FCC-ee GHC V22 Z” baseline standard optics. The IR optics design and its global implementation were carried out using MAD-X, following these steps below:

1. Extract the IR of the “MonochroM ZH4IP” optics, for instance, we extracted the IR at the straight section labeled as “PG” in Fig. 2.2, from the marker “FF1.2” to “FG.5.”
2. Separate the upstream IR (from “FF1.2” to “IP”) and downstream IR (from “IP” to “Fg.5”), then reflect the lattice of upstream IR, as it is easier to match with a starting point that has simple optical functions.
3. Implement skew quadrupoles between the sextupole pairs as illustrated in Fig. 4.4.
4. Introduced the vertical IP dispersion of 1 mm, and match vertical dispersion to zero at both the entrance and exit of the IR by varying the strength of the installed skew quadrupoles.
5. Reflect the designed monochromatization upstream IR back to its normal orientation, and connect it with the designed monochromatization downstream IR.
6. Insert the four skew quadrupoles with their matched strength between the sextupole pairs in each of the four IRs of the “MonochroM ZH4IP” optics.
7. Switch off the RF cavities then correct the local chromaticity, global chromaticity, and tune, following the same steps as described in Sucsec. 3.2.3.

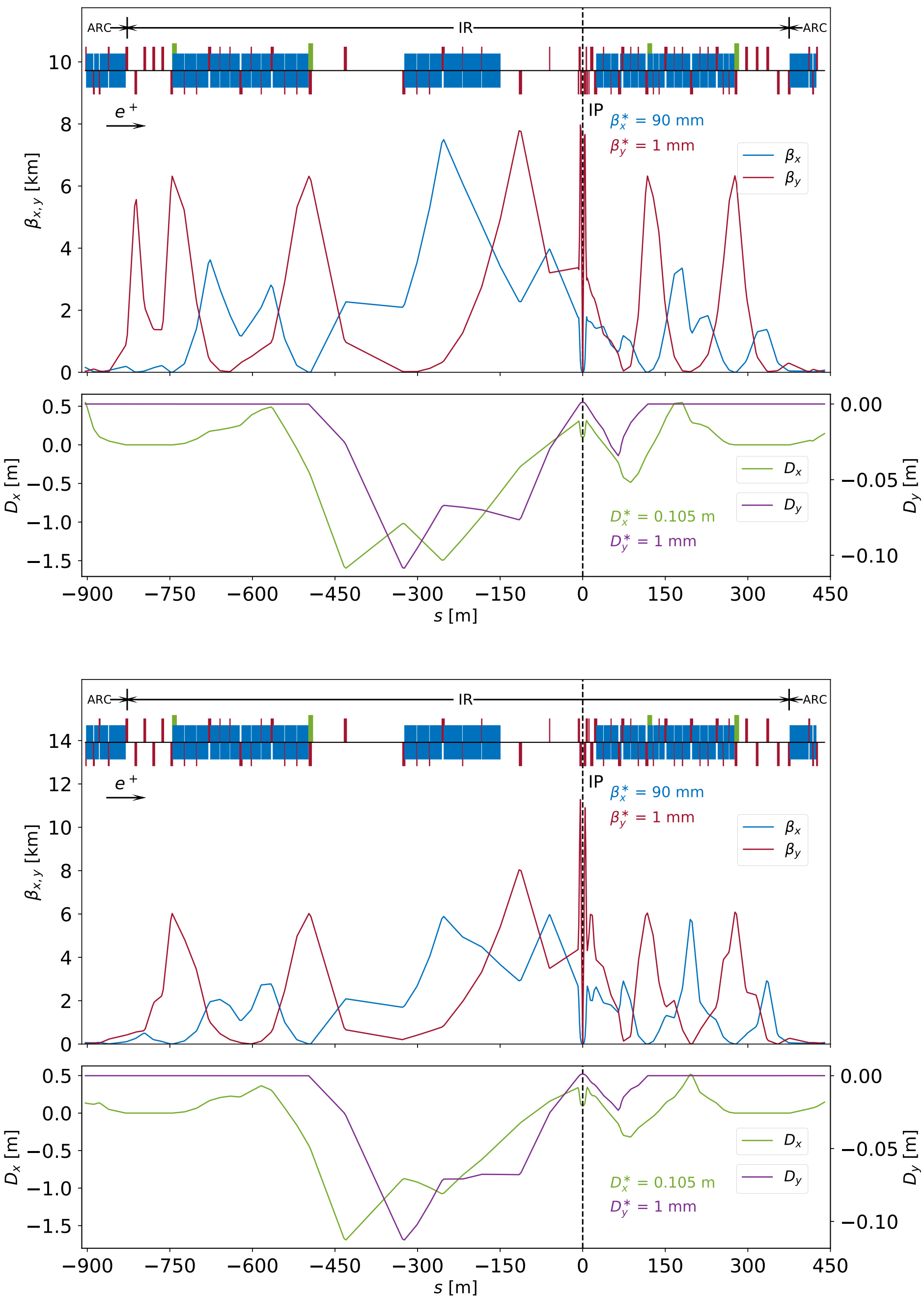

Fig. 5.1 Monochromatization IR lattices and optics with combined IP dispersion (0.105 m horizontal IP dispersion and 1 mm vertical IP dispersion) based on the "FCC-ee GHC V22 Z" (top) and "FCC-ee GHC V22 $\mathrm{t\bar{t}}$" (bottom) optics calculated using MAD-X. The beam direction is from left to right; the dashed line $s = 0$ marks the location of IP. In the lattice, dipoles, quadrupoles, and sextupoles are shown in blue, red, and green, respectively, while focusing and defocusing elements are positioned above and below the orbit. In the optics, horizontal and vertical betatron functions are shown in blue and red, respectively, while horizontal and vertical dispersion functions are shown in green and purple, respectively.

8. Switch on the RF cavities and consider the energy loss due to synchrotron radiation. Match value of the t' (Eq. 3.4) to zero by adjusting the phase of these RF cavities.

The designed monochromatization IR lattice and optics, which satisfied all the necessary constraints, are shown at the top of Fig. 5.1. A similar approach was applied to the "FCC-ee GHC V22 $\mathrm{t\bar{t}}$" optics, with the results displayed at the bottom of Fig. 5.1.

5.3 Performance evaluation

5.3.1 Global optical performance

The global performance of the monochromatization IR optics with nonzero combined IP dispersion ($D_x^* = 0.105\,\mathrm{m}$, $D_y^* = 1\,\mathrm{mm}$), referred to as "MonochroM ZHV" based on the "FCC-ee GHC V22 Z" optics and "MonochroM THV" based on the "FCC-ee GHC V22 $\mathrm{t\bar{t}}$" optics, was calculated analytically following the same procedure outlined in Subsec. 3.3.1.

The optical performance of the "MonochroM ZHV" optics based on the "FCC-ee GHC V22 Z" optics are summarized in Table 5.1 under the head-on collision configuration and Table 5.2 for crossing-angle configuration.

Under the head-on collision configuration, including the impact of beamstrahlung, the CM energy spread σ_W for the "MonochroM ZHV" optics is reduced from 19.87 MeV to 13.78 MeV, compared to the "MonochroM ZH4IP" optics, thanks to the inclusion of the nonzero D_y^*. However, the luminosity per IP $\mathcal{L}$ decreases from $2.30 \times 10^{35}\,\mathrm{cm^{-2}\,s^{-1}}$ to $2.44 \times 10^{34}\,\mathrm{cm^{-2}\,s^{-1}}$ due to the ε_y blow-up caused by the nonzero D_y^*.

Under the crossing-angle collision configuration, the σ_W drops from 26.43 MeV to 15.87 MeV, while the $\mathcal{L}$ decreases from $1.64 \times 10^{35}\,\mathrm{cm^{-2}\,s^{-1}}$ to $1.73 \times 10^{34}\,\mathrm{cm^{-2}\,s^{-1}}$.

The same calculations and analyses were performed for the monochromatization IR optics based on the "FCC-ee GHC V22 $\mathrm{t\bar{t}}$" optics, and the results are presented in two tables: Table 5.3 for the head-on collision configuration and Table 5.4 for the crossing-angle configuration. For both the "MonochroM ZHV" and "MonochroM THV" optics, the vertical beam-beam tune shift ξ_y stays within the acceptable limit (Eq. 3.6), regardless of whether crab cavities are used.

Table 5.1 Global performance parameters of monochromatization IR optics with nonzero combined (horizontal and vertical) IP dispersion based on the "FCC-ee GHC V22 Z" optics under the head-on configuration.

Parameter	**[Unit]**	**Standard ZES**	**MonochroM ZHV**
# of IPs n_{IP}		4	
Circumference C	[km]	91	
Full crossing angle θ_c	[mrad]	30	
SR power / beam P_{SR}	[MW]	50	
Beam energy E_0	[GeV]	62.5	
Energy loss / turn U_0	[GeV]	0.138	0.143
Beam current I	[mA]	360	350
Bunches / beam n_b		12000	
Bunch population N_b	[10^{11}]	0.57	0.55
Horizontal emittance (SR / BS) ε_x	[nm]	1.33 / 1.33	2.03 / 7.29
Vertical emittance (SR / BS) ε_y	[pm]	2.65 / 2.65	4.06 / 47.03
Momentum compaction factor α_{C}	[10^{-6}]	28.0	27.4
$\beta^*_{x/y}$	[mm]	100 / 0.8	90 / 1
$D^*_{x/y}$	[m]	0 / 0	0.105 / 0.001
Relative energy spread (SR / BS) σ_δ	[%]	0.054 / 0.115	0.055 / 0.057
Bunch length (SR / BS) σ_z	[mm]	4.09 / 8.61	4.15 / 4.22
RF voltage 400/800 MHz V_{RF}	[GV]	0.360 / 0	
RF frequency (400 MHz) f_{RF}	[MHz]	399.994581	
Synchrotron tune Q_s		0.054	0.053
Long. damping time τ_E/T_{rev}	[turns]	453	438
Horizontal beam-beam (SR / BS) ξ_x		0.16 / 0.16	0.0052 / 0.0043
Vertical beam-beam (SR / BS) ξ_y		0.31 / 0.31	0.0062 / 0.0051
CM energy spread (SR / BS) σ_W	[MeV]	47.47 / 101.89	5.02 / 13.78
Luminosity / IP (SR / BS) $\mathcal{L}$	[10^{34} cm^{-2} s^{-1}]	192 / 192	2.95 / 2.44

Table 5.2 Global performance parameters of monochromatization IR optics with nonzero combined (horizontal and vertical) IP dispersion based on the "FCC-ee GHC V22 Z" optics under the crossing-angle configuration.

Parameter	**[Unit]**	**Standard ZES**	**MonochroM ZHV**
# of IPs n_{IP}		4	
Circumference C	[km]	91	
Full crossing angle θ_c	[mrad]	30	
SR power / beam P_{SR}	[MW]	50	
Beam energy E_0	[GeV]	62.5	
Energy loss / turn U_0	[GeV]	0.138	0.143
Beam current I	[mA]	360	350
Bunches / beam n_b		12000	
Bunch population N_b	[10^{11}]	0.57	0.55
Horizontal emittance (SR / BS) ε_x	[nm]	1.33 / 1.33	2.03 / 7.72
Vertical emittance (SR / BS) ε_y	[pm]	2.65 / 2.65	4.06 / 50.55
Momentum compaction factor α_{C}	[10^{-6}]	28.0	27.4
$\beta^*_{x/y}$	[mm]	100 / 0.8	90 / 1
$D^*_{x/y}$	[m]	0 / 0	0.105 / 0.001
Relative energy spread (SR / BS) σ_δ	[%]	0.054 / 0.078	0.055 / 0.057
Bunch length (SR / BS) σ_z	[mm]	4.09 / 5.82	4.15 / 4.23
RF voltage 400/800 MHz V_{RF}	[GV]	0.360 / 0	
RF frequency (400 MHz) f_{RF}	[MHz]	399.994581	
Synchrotron tune Q_s		0.054	0.053
Long. damping time τ_E/T_{rev}	[turns]	453	438
Horizontal beam-beam (SR / BS) ξ_x		0.0054 / 0.0027	0.0025 / 0.0022
Vertical beam-beam (SR / BS) ξ_y		0.058 / 0.041	0.0043 / 0.0036
CM energy spread (SR / BS) σ_W	[MeV]	47.47 / 68.78	5.30 / 15.87
Luminosity / IP (SR / BS) $\mathcal{L}$	[10^{34} cm^{-2} s^{-1}]	35.4 / 25.1	2.03 / 1.73

Table 5.3 Global performance parameters of monochromatization IR optics with nonzero combined (horizontal and vertical) IP dispersion based on the "FCC-ee GHC V22 $t\bar{t}$" optics under the head-on configuration.

Parameter	**[Unit]**	**Standard TES**	**MonochroM THV**
# of IPs n_{IP}		4	
Circumference C	[km]	91	
Full crossing angle θ_c	[mrad]	30	
SR power / beam P_{SR}	[MW]	50	
Beam energy E_0	[GeV]	62.5	
Energy loss / turn U_0	[GeV]	0.138	0.143
Beam current I	[mA]	360	350
Bunches / beam n_b		12000	
Bunch population N_b	[10^{11}]	0.57	0.55
Horizontal emittance (SR / BS) ε_x	[nm]	0.17 / 0.17	1.48 / 6.79
Vertical emittance (SR / BS) ε_y	[pm]	0.35 / 0.35	2.96 / 46.34
Momentum compaction factor α_{C}	[10^{-6}]	7.31	6.92
$\beta^*_{x/y}$	[mm]	1000 / 1.6	90 / 1
$D^*_{x/y}$	[m]	0 / 0	0.105 / 0.001
Relative energy spread (SR / BS) σ_δ	[%]	0.054 / 0.108	0.055 / 0.057
Bunch length (SR / BS) σ_z	[mm]	3.86 / 7.71	4.05 / 4.19
RF voltage 400/800 MHz V_{RF}	[GV]	0.170 / 0	
RF frequency (400 MHz) f_{RF}	[MHz]	399.994581	
Synchrotron tune Q_s		0.015	0.014
Long. damping time τ_E/T_{rev}	[turns]	454	436
Horizontal beam-beam (SR / BS) ξ_x		1.20 / 1.20	0.0052 / 0.0043
Vertical beam-beam (SR / BS) ξ_y		1.07 / 1.07	0.0061 / 0.0051
CM energy spread (SR / BS) σ_W	[MeV]	47.46 / 95.03	4.29 / 13.53
Luminosity / IP (SR / BS) $\mathcal{L}$	[10^{34} cm^{-2} s^{-1}]	328 / 328	2.94 / 2.43

Table 5.4 Global performance parameters of monochromatization IR optics with nonzero combined (horizontal and vertical) IP dispersion based on the "FCC-ee GHC V22 $t\bar{t}$" optics under the crossing-angle configuration.

Parameter	**[Unit]**	**Standard TES**	**MonochroM THV**
# of IPs n_{IP}		4	
Circumference C	[km]	91	
Full crossing angle θ_c	[mrad]	30	
SR power / beam P_{SR}	[MW]	50	
Beam energy E_0	[GeV]	62.5	
Energy loss / turn U_0	[GeV]	0.138	0.143
Beam current I	[mA]	360	350
Bunches / beam n_b		12000	
Bunch population N_b	[10^{11}]	0.57	0.55
Horizontal emittance (SR / BS) ε_x	[nm]	0.17 / 0.17	1.48 / 7.26
Vertical emittance (SR / BS) ε_y	[pm]	0.35 / 0.35	2.96 / 50.18
Momentum compaction factor α_{C}	[10^{-6}]	7.31	6.92
$\beta^*_{x/y}$	[mm]	1000 / 1.6	90 / 1
$D^*_{x/y}$	[m]	0 / 0	0.105 / 0.001
Relative energy spread (SR / BS) σ_δ	[%]	0.054 / 0.076	0.055 / 0.057
Bunch length (SR / BS) σ_z	[mm]	3.86 / 5.49	4.05 / 4.20
RF voltage 400/800 MHz V_{RF}	[GV]	0.170 / 0	
RF frequency (400 MHz) f_{RF}	[MHz]	399.994581	
Synchrotron tune Q_s		0.015	0.014
Long. damping time τ_E/T_{rev}	[turns]	454	436
Horizontal beam-beam (SR / BS) ξ_x		0.059 / 0.030	0.0025 / 0.0022
Vertical beam-beam (SR / BS) ξ_y		0.24 / 0.17	0.0043 / 0.0036
CM energy spread (SR / BS) σ_W	[MeV]	47.45 / 67.58	4.52 / 15.69
Luminosity / IP (SR / BS) $\mathcal{L}$	[10^{34} cm^{-2} s^{-1}]	72.8 / 51.9	2.05 / 1.72

5.3.2 Preliminary dynamic aperture studies

Preliminary 6D dynamic aperture (DA) studies were carried out for the monochromatization optics design with nonzero combined IP dispersion using Xsuite, following the transfer and re-matching of the optics from the MAD-X version to the Xsuite version. The initial particle motion amplitude $A_{x,y}$ (Eq. 3.7) was set as $10\,\sigma$, with phase $\phi = 0$ and momentum deviation $\delta = 0$. The number of tracking turns was set to twice the longitudinal damping time ($\tau_E/T_{\rm rev}$). The resulting DA plots for the "MonochroM ZHV" optics, based on the "FCC-ee GHC V22 Z" optics, are shown at the left of Fig. 5.2, without accounting for optimization of the arc family sextupoles. Similarly, the right of Fig. 5.2 displays the results of the same study procedure for the monochromatization optics based on the "FCC-ee GHC V22 $\mathrm{t\bar{t}}$" optics.

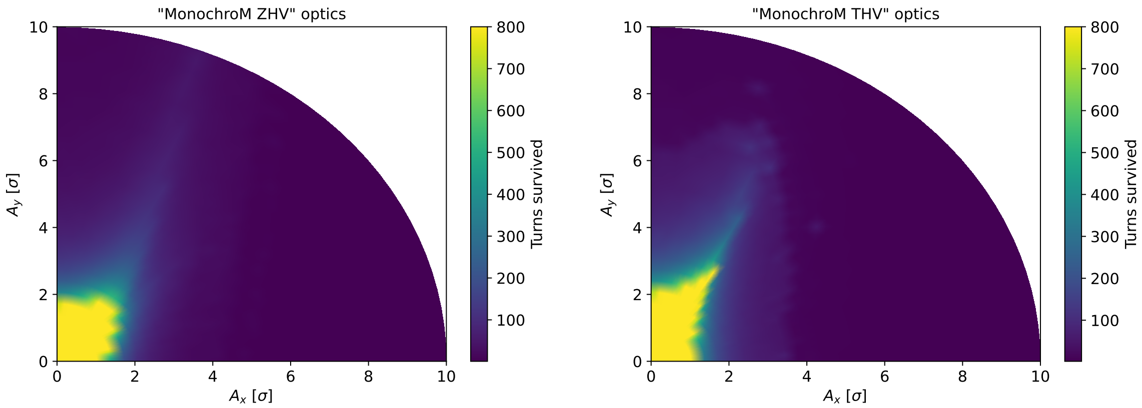

Fig. 5.2 Results of preliminary 6D DA studies for the monochromatization optics with nonzero combined IP dispersion based on the "FCC-ee GHC V22 Z" optics (left) and "FCC-ee GHC V22 $\mathrm{t\bar{t}}$" optics (right) calculated with Xsuite. The varying colors indicate the number of particle surviving turns.

5.3.3 Physics performance

The CM energy spread σ_W and luminosity per IP $\mathcal{L}$ of the monochromatization optics design with nonzero combined IP dispersion were calculated using Guinea-Pig to assess its physics performance. The particle distribution at the IP follows an ideal Gaussian distribution, characterized by the global optical parameters of each optics configuration, as described by Eq. 3.8. The energy deviation of the positron and electron distributions exhibits opposite correlations with the spatial position in both the horizontal and vertical planes, as illustrated in Fig. 3.17 and Fig. 4.20.

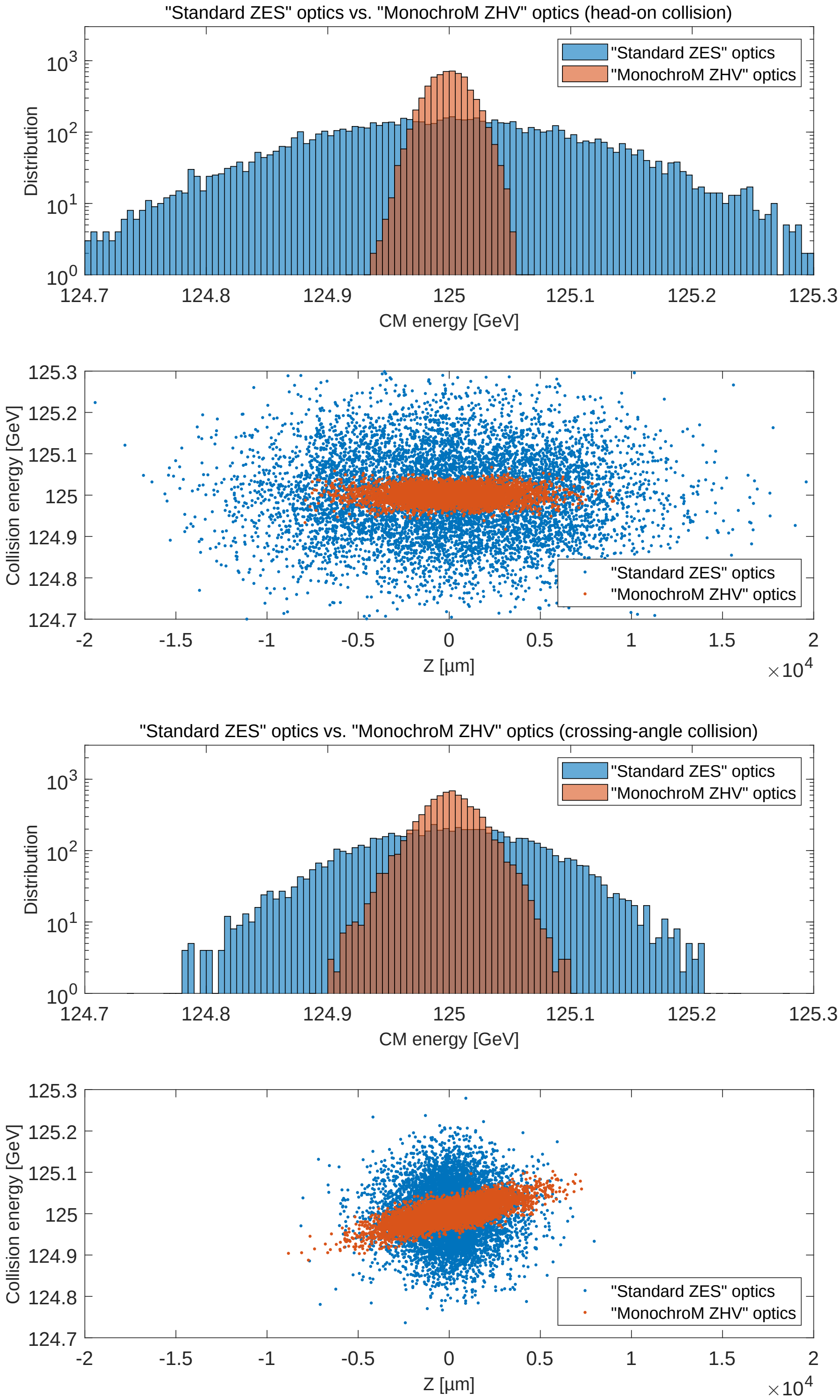

Fig. 5.3 Comparison between the "Standard ZES" and "MonochroM ZHV" optics in terms of the CM energy distribution and its correlation with the longitudinal collision position simulated using Guinea-Pig, under the head-on (top) or crossing-angle (bottom) collision configuration.

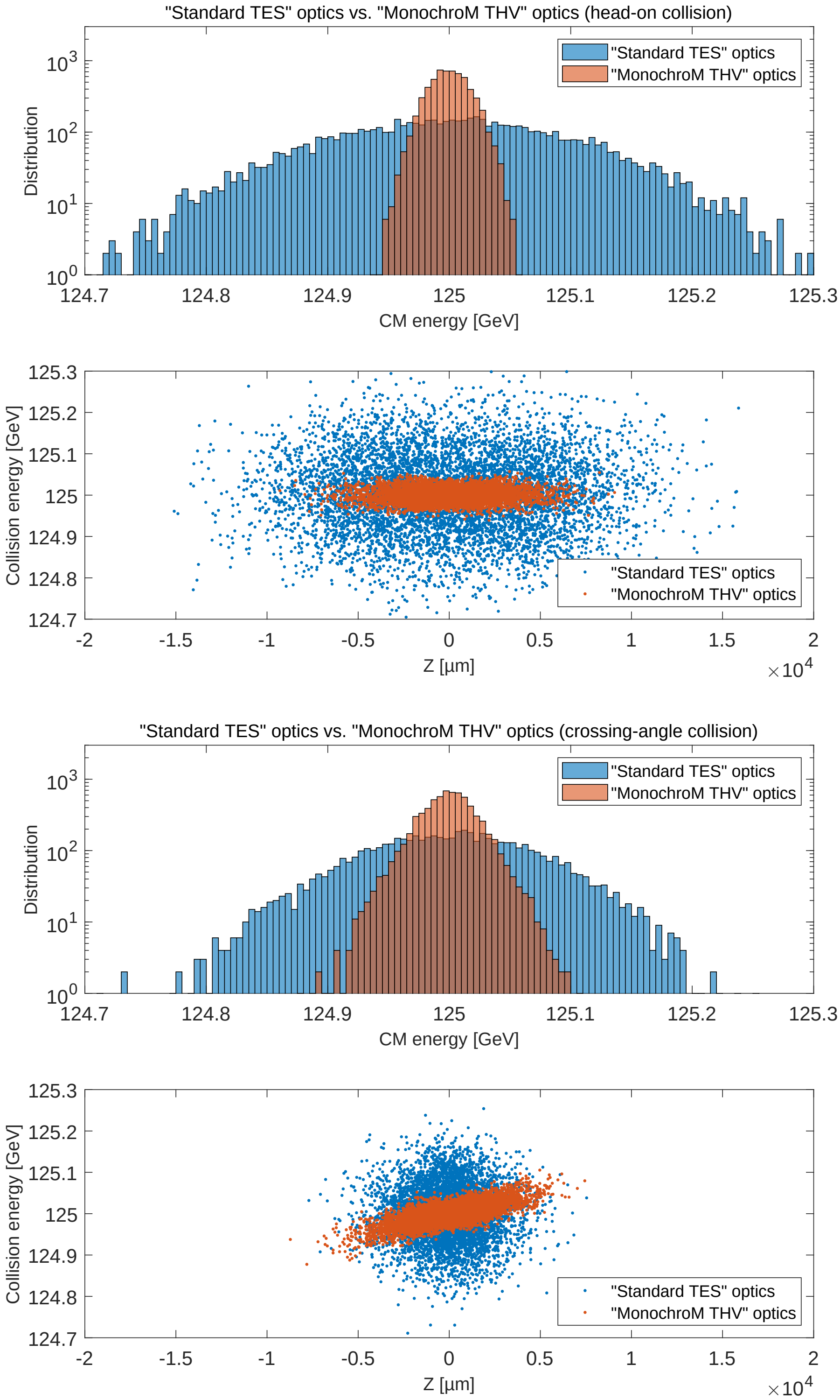

Fig. 5.4 Comparison between the "Standard TES" and "MonochroM THV" optics in terms of the CM energy distribution and its correlation with the longitudinal collision position simulated using Guinea-Pig, under the head-on (top) or crossing-angle (bottom) collision configuration.

Table 5.5 CM energy spread, luminosity per IP, integrated luminosity per IP and year of monochromatization IR optics with nonzero combined (horizontal and vertical) IP dispersion based on the "FCC-ee GHC V22 Z" optics with or without crab cavities.

Parameter	**[Unit]**	**Standard ZES**	**MonochroM ZHV**
CM energy spread (with / without crab cavities) σ_W	[MeV]	103.1 / 69.15	16.82 / 21.52
Luminosity / IP (with / without crab cavities) $\mathcal{L}$	[10^{34} cm^{-2} s^{-1}]	197 / 44.6	2.45 / 1.42
Integrated luminosity / IP / year (with / without crab cavities) $\mathcal{L}_{\text{int}}$	[ab^{-1}]	23.6 / 5.35	0.29 / 0.17

Table 5.6 CM energy spread, luminosity per IP, integrated luminosity per IP and year of monochromatization IR optics with nonzero combined (horizontal and vertical) IP dispersion based on the "FCC-ee GHC V22 $t\bar{t}$" optics with or without crab cavities.

Parameter	**[Unit]**	**Standard TES**	**MonochroM THV**
CM energy spread (with / without crab cavities) σ_W	[MeV]	93.76 / 67.51	16.29 / 20.44
Luminosity / IP (with / without crab cavities) $\mathcal{L}$	[10^{34} cm^{-2} s^{-1}]	336 / 71.2	2.45 / 1.41
Integrated luminosity / IP / year (with / without crab cavities) $\mathcal{L}_{\text{int}}$	[ab^{-1}]	40.3 / 8.54	0.29 / 0.17

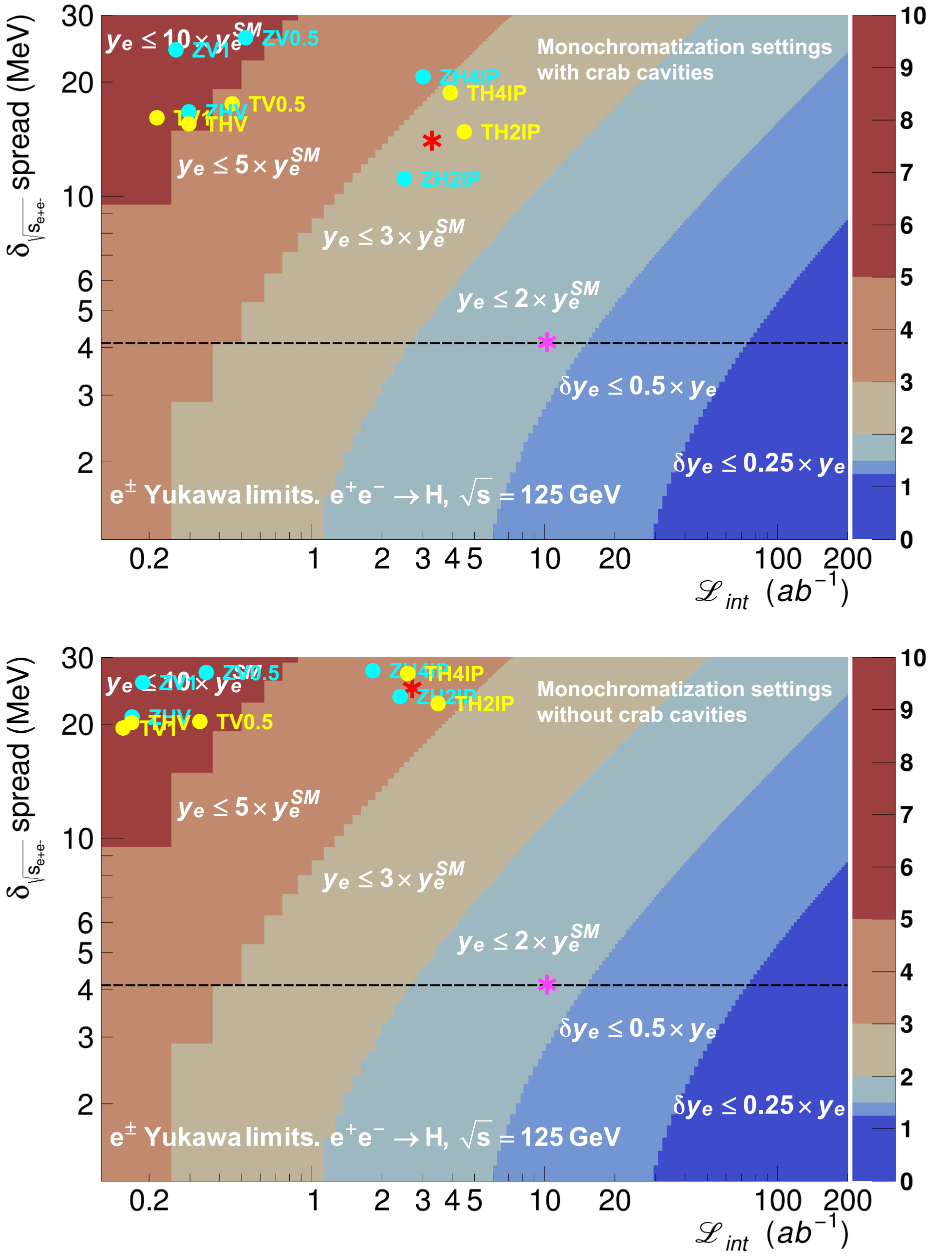

Fig. 5.5 Physics performance evaluation of all proposed monochromatization optics with (top) or without crab cavities (bottom) indicated by the $\delta_{\sqrt{s}}$-$\mathcal{L}_{\rm int}$ benchmarks in the upper limits contours (95% CL) on the y_e. The monochromatization optics base on the "FCC-ee GHC V22 Z" optics and "FCC-ee GHC V22 $t\bar{t}$" optics are marked in cyan and yellow, respectively. The pink star over the $\delta_{\sqrt{s}} = \Gamma_{\rm H} = 4.1\,\rm MeV$ dashed line, indicates the baseline point assumed in the original physics simulation analysis [69]. The red stars represent the previously achieved working point with parameterized studies [53, 55].

Fig. 5.3 presents the CM energy distribution and the correlation between collision energy and longitudinal position for the "MonochroM ZHV" optics based on the "FCC-ee GHC V22 Z" optics, under head-on collision configuration (top) and crossing-angle collision configuration (bottom). The corresponding values for σ_W, $\mathcal{L}$, and integrated luminosity $\mathcal{L}_{\text{int}}$ are summarized in Table 5.5. The results for the "MonochroM THV" optics based on the "FCC-ee GHC V22 $\mathrm{t\bar{t}}$" optics are shown in Fig. 5.4 and summarized in Table 5.6.

The σ_W and $\mathcal{L}_{\text{int}}$ values for all proposed monochromatization optics, as summarized in Table 3.5, Table 3.6, Table 4.6, Table 4.7, Table 5.5 and Table 5.6, have been used to establish their $\delta_{\sqrt{s}}$-$\mathcal{L}_{\text{int}}$ benchmarks in the plot of upper limits contour (95% CL) on the y_e coupling, as shown in Fig. 5.5. The upper panel of the figure corresponds to the head-on collision configuration, while the lower panel illustrates the crossing-angle collision setup. The "MonochroM ZHV" and "MonochroM THV" optics, which incorporate combined IP dispersion, do not provide improved physics performance compared to that of the "MonochroM ZH4IP" and "MonochroM TH4IP" optics with only horizontal dispersion at the IP. This is primarily due to greater luminosity loss caused by vertical emittance blow-up, when accounting for the impact of beamstrahlung. The monochromatization scheme discussed in this chapter achieves optimal physics performance with the "MonochroM THV" optics under both head-on and crossing-angle collision configuration, resulting in $|y_e| < 5.0|y_e^{\text{SM}}|$ and $|y_e| < 7.1|y_e^{\text{SM}}|$, respectively.

Chapter 6

Conclusion and perspectives

In this thesis, we have conducted a comprehensive study on the application of the monochromatization scheme in the FCC-ee, with a focus on the IR optics design, along with its first tentative integration and performance evaluation within the global lattice. The physics motivation is to significantly reduce the CM energy spread of FCC-ee, enabling the precise measurement of the electron Yukawa coupling through direct s-channel Higgs production: $e^+e^- \rightarrow \mathrm{H}$ at a CM energy of about 125 GeV. The proposed monochromatization techniques are based on the introduction of nonzero dispersion at the IP to generate opposite correlations between transverse spatial position and energy deviation within the colliding beams, thereby reducing the CM energy spread to a level comparable to the natural width of the SM Higgs boson, $\Gamma_{\mathrm{H}} = 4.1\,\mathrm{MeV}$.

The thesis begins with a detailed introduction to the concept of monochromatization in Chapter 1, starting with its original formulation for low-energy e^+e^- colliders with head-on collision configurations, followed by the extension of this concept for the application in high-energy colliders with crossing-angle collision configurations, including the consideration of the hourglass and beamstrahlung effect. We then discuss the application of monochromatization in the FCC-ee, including its physics motivation and preliminary parametric studies combined with physics performance evaluation, prior to the optics design.

In Chapter 2, we provide an overview of the FCC-ee project, its motivation, and its potential as a high-precision platform for investigating the SM and exploring new physics beyond it. We then describe the general layout of the FCC-ee accelerator and two kinds of FCC-ee baseline standard optics: the FCC-ee GHC optics and FCC LCC optics, which serve as the starting point for the three distinct FCC-ee GHC monochromatization IR optics design, presented in the subsequent chapters of this thesis.

Chapter 3 explores the monochromatization scenario involving nonzero horizontal dispersion at the IP. Based on the targeted IP parameters derived from the FCC-ee monochromatization self-consistent parameter optimization, with $\beta^*_{x,y} = 90, 1\,\mathrm{mm}$ and $D^*_x = 0.105\,\mathrm{m}$, the design of this monochromatization IR optics was developed using two types of the "FCC-ee GHC V22" optics. The design was achieved by implementing four smooth close-orbit "three-angle" chicane structures, optimized step by step, ensuring the compatibility with standard operation modes and maintaining luminosity in an ideal level by minimizing the horizontal emittance blow-up. After the global implementation, we observed that the CM energy spread was successfully reduced, with the beamstrahlung impact taken into account. The physics performance evaluations demonstrates that this approach could significantly enhance the rate of Higgs bosons though direct s-channel production. Under the head-on configuration, the "MonochroM TH2IP" optics (with monochromatization IR optics integrated only in two IRs), based on the "FCC-ee GHC V22 $\mathrm{t\bar{t}}$" optics, achieves the best $\delta_{\sqrt{s}}$-$\mathcal{L}_{\mathrm{int}}$ benchmark, with $\sigma_W = 15.54\,\mathrm{MeV}$ and $\mathcal{L}_{\mathrm{int}} = 4.51\,\mathrm{ab}^{-1}$. This corresponds to an upper limits of $|y_e| < 2.7|y_e^{\mathrm{SM}}|$ in the 95% CL contours for the Higgs-electron coupling. Under the crossing-angle configuration, the "MonochroM TH2IP" optics also delivers the best benchmark, with $\sigma_W = 23.68\,\mathrm{MeV}$ and $\mathcal{L}_{\mathrm{int}} = 2.94\,\mathrm{ab}^{-1}$, indicating an upper limits of $|y_e| < 3.2|y_e^{\mathrm{SM}}|$. Although this monochromatization scheme provides the best physics performance compared to the others, its complex optics design—where all the IR LCC horizontal dipoles are split into three sets with thin quadrupoles inserted between for compatibility with the standard operation mode—requires further simplification.

In Chapter 4, we investigate a second monochromatization scheme, introducing nonzero vertical dispersion at the IP. Due to the FCC-ee's exceptionally low vertical emittance, a vertical dispersion of only 1 mm is sufficient to achieve the desired monochromatization effect. Inspired by the detector solenoid compensation scheme used in the "FCC LCC V22" optics, this approach was applied to both types of the "FCC-ee GHC V22" optics by incorporating skew quadrupoles into the IR. To mitigate vertical emittance blow-up caused by beamstrahlung with nonzero vertical dispersion at the IP, the horizontal betatron function at the IP was increased. The resulting design was shown to be effective in reducing the CM energy spread. The best physics performance benchmark was achieved with the "MonochroM TV0.5" optics (featuring 0.5 mm vertical dispersion at four IPs), yielding upper limits of $|y_e| < 4.9|y_e^{\mathrm{SM}}|$ for head-on collisions and $|y_e| < 5.1|y_e^{\mathrm{SM}}|$ for crossing-angle collisions. Although the physics performance is not as favorable as the scheme with nonzero horizontal IP dispersion, this approach is easier to implement without altering the IR orbit, making it feasible for existing lower-energy colliders. Without the vertical emittance blow-up from beamstrahlung, this scheme could potentially achieve better performance in such settings.

Chapter 5 combines the two previous approaches by introducing both horizontal and vertical dispersion at the IP. This hybrid scheme was implemented by integrating skew quadrupoles into the IR optics, which already included nonzero horizontal IP dispersion. When evaluated in comparison to the individual horizontal and vertical dispersion schemes, it was found that, although the hybrid scheme results in a lower CM energy spread, its physics performance does not improve as expected due to increased luminosity loss. Additionally, this design may encounter potential challenges related to betatron coupling.

In conclusion, while monochromatization is a straightforward conceptual idea, its practical implementation in a collider is challenging, particularly if it is not integrated into the IR optics design from the beginning as a dedicated operational mode. The research on monochromatization has not yet matured to the point of enabling its full implementation and experimental validation. To address this, a flexible lattice design that accommodates both operational modes—with and without monochromatization—is essential. This thesis has demonstrated that monochromatization is a promising approach for improving CM energy resolution in future high-energy e^+e^- colliders, particularly for precision Higgs boson measurements at the FCC-ee. By exploring various monochromatization schemes and optimizing the IR optics for each scenario, we have laid the groundwork for future experimental implementation and validation. The results indicate that both horizontal and vertical dispersion schemes are viable options, with the potential to significantly reduce the CM energy spread and enhance the physics reach of the FCC-ee. Additionally, it is evident that crab-cavity implementation advances the physics performance of the monochromatization settings.

Several avenues for future research have been identified through this thesis. First, the FCC-ee GHC monochromatization IR optics will be updated to the latest version of the continuously evolving FCC-ee GHC optics, with Version 2024 being the most current. The optical parameters for the monochromatization mode, such as the IP betatron function, IP dispersion, bunch population, synchrotron tune, and momentum compaction factor, will continue to be optimized for enhanced performance. Second, the dynamic aperture optimization for these new types of monochromatization optics will be carried out step-by-step by adjusting the arc sextupole families based on particle tracking results. This will allow for beam-beam simulations with nonzero IP dispersion in Xsuite, incorporating the hourglass and beamstrahlung effects, rather than relying solely on analytical evaluations. Third, further comparisons and implementations of monochromatization in more symmetric IRs, such as those in the FCC-ee LCC optics and CEPC optics, will be explored. Fourth, two novel monochromatization schemes—superconducting RF deflecting (SCRF-D) cavities and residual nonzero local vertical chromaticity (RLC)—will be investigated for feasibility. Finally, experimental validation of the monochromatization concept in existing low-energy e^+e^- colliders, such as BEPC II, DAΦNE, and SuperKEKB, is under study. These future efforts will be essential in realizing the full potential of monochromatization in future collider projects.

References

[1] A. Abada et al. “FCC-ee: The Lepton Collider”. In: *Eur. Phys. J. Spec. Top.* 228 (2019), pp. 261–623. DOI: 10.1140/epjst/e2019-900045-4.

[2] S. Jadach and R. A. Kycia. “Lineshape of the Higgs boson in future lepton colliders”. In: *Phys. Lett. B* 755 (2016), pp. 58–63. DOI: 10.1016/j.physletb.2016.01.065. arXiv: 1509.02406 `[hep-ph]`.

[3] A. Abada et al. “FCC Physics Opportunities: Future Circular Collider Conceptual Design Report Volume 1”. In: *Eur. Phys. J. C* 79.6 (2019), p. 474. DOI: 10.1140/epjc/s10052-019-6904-3.

[4] H. Jiang et al. “Update on the monochromatization studies”. In: *FCC-FS EPOL group and FCCIS WP2.5 meeting 4*. Jan. 2022. URL: https://indico.cern.ch/event/1108961/.

[5] A. Renieri. “Possibility of Achieving Very High-Energy Resolution in electron-Positron Storage Rings”. Rep. LNF-75/6-R. Feb. 1975.

[6] A. Wolski. “Low-emittance Storage Rings”. In: (2014), pp. 245–294. DOI: 10.5170/CERN-2014-009.245. arXiv: 1507.02213.

[7] P. A. Zyla et al. “Review of Particle Physics”. In: *Progress of Theoretical and Experimental Physics* 2020.8 (2020), p. 083C01. DOI: 10.1093/ptep/ptaa104.

[8] S. Lee. *Accelerator Physics*. World Scientific Publishing, 2004.

[9] H. Wiedemann. “Is it possible to improve the eventrate for narrow resonances in SPEAR and PEP”. In: (Oct. 1979). DOI: 10.2172/6401677.

[10] H. Wiedemann. “Wigglers, beam emittance and energy spread”. In: (Oct. 1979). DOI: 10.2172/6401678.

[11] A. Faus-Golfe. “Etude d’un anneau e^+e^- à très haute luminosité, avec et sans monochromatisation des faisceaux (cas particulier d’une usine Tau-Charme)”. PhD thesis. Orsay, LAL, 1994.

[12] A. A. Avdienko et al. “The project of modernization of the VEPP-4 storage ring for monochromatic experiments in the energy range of psi and upsilon mesons”. In: *Conf. Proc. C* 830811 (1983), pp. 186–189.

[13] M. Bassetti et al. “ADONE: Present Status and Experiments.” Rep. LNF-74-22-P. May 1974.

[14] I. Y. Protopopov, A. N. Skrinsky, and A. A. Zholents. “Energy monochromatization of particle interaction in storage rings”. Rep. IYF-79-06. Jan. 1979.

[15] K. Wille and A. W. Chao. “Investigation of a monochromator scheme for SPEAR”. Rep. SLAC/AP-32. Aug. 1984.

[16] J. M. Jowett. “Feasibility of a monochromator scheme in LEP”. Rep. CERN-LEP-Note-544. Sept. 1985.

[17] M. Bassetti and J. M. Jowett. “Improving the Energy Resolution of LEP Experiments”. Rep. CERN-LEP-TH-87-09. Mar. 1987.

[18] J. M. Jowett, J. Wenninger, and J. M. Yamartino. “Influence of Dispersion and Collision Offsets on the Centre-of-Mass Energy at LEP; rev. version”. Tech. rep. Geneva: CERN, 1995. URL: https://cds.cern.ch/record/806265.

[19] A. Dubrovin, A. Vlasov, and A. Zholents. “Interaction Region of 4 × 7-GeV Asymmetric B-Factory”. In: *Annals of the New York Academy of Sciences* 619 (Feb. 1991), pp. 193–201. DOI: 10.1111/j.1749-6632.1991.tb37833.x.

[20] V. G. Veshcherevich, V. A. Lebedev, P. V. Logachev, and V. P. Yakovlev. “Monochromatization as the way to maximum luminosity B-factories”. In: *Nucl. Phys. B Proc. Suppl.* 27 (1992), pp. 12–26. DOI: 10.1016/0920-5632(92)90028-Q.

[21] Y. I. Alexahin, A. N. Dubrovin, and A. A. Zholents. “Proposal on a tau charm factory with monochromatization”. In: *Conf. Proc. C* 900612 (1990), pp. 398–400.

[22] A. A. Zholents. “Polarized J / ψ mesons at a tau charm factory with a monochromator scheme”. Rep. CERN-SL-92-27-AP. June 1992.

[23] A. Faus-Golfe and J. Le Duff. “Versatile DBA and TBA lattices for a tau charm factory with and without beam monochromatization”. In: *Nucl. Instrum. Meth. A* 372 (Mar. 1996), pp. 6–18. DOI: 10.1016/0168-9002(95)01275-3.

[24] D. Schulte. “Study of Electromagnetic and Hadronic Background in the Interaction Region of the TESLA Collider”. PhD thesis. Hamburg U., 1997.

[25] N. Huang, L. Jin, W. Liu, et al. “Study of the lattice design of BTCF storage ring (in Chinese)”. In: *High Energy Physics and Nuclear Physics* 22 (Dec. 1998), pp. 1164–1173.

[26] J. Wang and S. Fang. “Application of the nagetive momentum compaction lattice in a tau-charm factory (in Chinese)”. In: *High Energy Physics and Nuclear Physics* 23 (Apr. 1999), pp. 388–396.

[27] J. Kirkby. “A τ-Charm Factory at CERN”. In: *Spectroscopy of Light and Heavy Quarks*. Boston, MA: Springer US, 1989, pp. 401–421. DOI: 10.1007/978-1-4613-0763-1_18.

[28] *Proceedings, Tau - Charm Factory Workshop: Study of Tau, Charm and J/ψ Physics, Development of High Luminosity e^+e^- Rings, Design of e^+e^- Detectors for Tau Charm Physics.* June 1989.

[29] A. Hutton and M. S. Zisman. “An asymmetric B factory in the PEP tunnel”. In: *AIP Conference Proceedings* 214.1 (Oct. 1990), pp. 594–601. DOI: 10.1063/1.39759.

[30] S. Kurokawa, K. Saton, and F. Takasaki. “Accelerator design of the KEK B-factory”. In: *Conference Record of the 1991 IEEE Particle Accelerator Conference*. Vol. 1. 1991, pp. 138–140. DOI: 10.1109/PAC.1991.164226.

[31] P. Beloshitsky. “A Magnet lattice for a tau charm factory suitable for both standard scheme and monochromatization scheme”. Rep. LAL-RT-92-09. June 1992.

[32] J. Gonichon, J. Le Duff, B. Mouton, and C. Travier. "Preliminary study of a high luminosity e^+e^- storage ring at a CM energy of 5 GeV". Rep. LAL-RT-90-02. Jan. 1990.

[33] A. L. Gerasimov, D. N. Shatilov, and A. A. Zholents. "Beam-beam effects with large dispersion function at the interaction point". In: *Nucl. Instrum. Meth. A* 305.1 (July 1991), pp. 25–29. DOI: https://doi.org/10.1016/0168-9002(91)90515-R.

[34] A. A. Zholents and O. A. Nezhevenko. "RF monochromatization of particle interaction energy in storage rings (in Russian)". In: *13th International Conference on High-energy Accelerators*. 1986, pp. 70–73.

[35] A. A. Zholents. "Sophisticated accelerator techniques for colliding beam experiments". In: *Nucl. Instrum. Meth. A* 265 (1988), pp. 179–185. DOI: 10.1016/0168-9002(88)91070-4.

[36] P. Raimondi. Private communication. 2022.

[37] J. Keintzel. "FCC-ee energy calibration and challenges". In: *Proc. US FCC Workshop* (BNL). Apr. 2023. URL: https://indico.cern.ch/event/1244371/contributions/5312690/.

[38] P. Raimondi et al. "Crab Waist Collisions in DAFNE and Super-B Design". In: *Conf. Proc. C* 0806233 (2008). Ed. by I. Andrian and C. Petit-Jean-Genaz, WEXG02.

[39] M. Zobov et al. "Test of crab-waist collisions at DAFNE Phi factory". In: *Phys. Rev. Lett.* 104 (2010), p. 174801. DOI: 10.1103/PhysRevLett.104.174801.

[40] M. Zobov. "Crab Waist collision scheme: a novel approach for particle colliders". In: *J. Phys. Conf. Ser.* 747.1 (2016), p. 012090. DOI: 10.1088/1742-6596/747/1/012090. arXiv: 1608.06150 [physics.acc-ph].

[41] Y. Ohnishi et al. "Accelerator design at SuperKEKB". In: *PTEP* 2013 (2013), 03A011. DOI: 10.1093/ptep/pts083.

[42] A. E. Bondar et al. "Project of a Super Charm-Tau factory at the Budker Institute of Nuclear Physics in Novosibirsk". In: *Phys. Atom. Nucl.* 76 (2013), pp. 1072–1085. DOI: 10.1134/S1063778813090032.

[43] "CEPC Conceptual Design Report: Volume 1 - Accelerator". In: (Sept. 2018). arXiv: 1809.00285 [physics.acc-ph].

[44] M. Bona et al. "SuperB: A High-Luminosity Asymmetric e^+e^- Super Flavor Factory. Conceptual Design Report". In: (2007). arXiv: 0709.0451 [hep-ex].

[45] M. A. Valdivia García, A. Faus-Golfe, and F. Zimmermann. "Towards a Monochromatization Scheme for Direct Higgs Production at FCC-ee". In: *7th International Particle Accelerator Conference*. 2016, WEPMW009. DOI: 10.18429/JACoW-IPAC2016-WEPMW009.

[46] M. Valdivia García and F. Zimmermann. "Effect of Beamstrahlung on Bunch Length and Emittance in Future Circular e^+e^- Colliders". In: *7th International Particle Accelerator Conference*. 2016, WEPMW010. DOI: 10.18429/JACoW-IPAC2016-WEPMW010.

[47] M. A. Valdivia García and F. Zimmermann. "Towards an Optimized Monochromatization for direct Higgs Production in Future Circular e^+e^- Colliders". In: *CERN-BINP Workshop for Young Scientists in* e^+e^- *Colliders*. 2017, pp. 1–12. DOI: 10.23727/CERN-Proceedings-2017-001.1.

[48] A. Bogomyagkov and E. Levichev. "Collision monochromatization in e^+e^- colliders". In: *Phys. Rev. Accel. Beams* 20.5 (2017). [Erratum: Phys.Rev.Accel.Beams 21, 029902 (2018)], p. 051001. DOI: 10.1103/PhysRevAccelBeams.20.051001. arXiv: 1702.03634 [physics.acc-ph].

[49] M. A. Valdivia García and F. Zimmermann. "Optimized Monochromatization for Direct Higgs Production in Future Circular e^+e^- Colliders". In: *8th International Particle Accelerator Conference*. May 2017. DOI: 10.18429/JACoW-IPAC2017-WEPIK015.

[50] M. Valdivia García, D. El Khechen, K. Oide, and F. Zimmermann. "Quantum Excitation due to Classical Beamstrahlung in Circular Colliders". In: *9th International Particle Accelerator Conference*. 2018, MOPMF068. DOI: 10.18429/JACoW-IPAC2018-MOPMF068.

[51] M. A. Valdivia García and F. Zimmermann. "Effect of emittance constraints on monochromatization at the Future Circular e^+e^- Collider". In: *10th International Particle Accelerator Conference*. 2019, MOPMP035. DOI: 10.18429/JACoW-IPAC2019-MOPMP035.

[52] M. A. Valdivia García and F. Zimmermann. "Beam blow up due to Beamstrahlung in circular e^+e^- colliders". In: *Eur. Phys. J. Plus* 136.5 (2021), p. 501. DOI: 10.1140/epjp/s13360-021-01485-x. arXiv: 1911.03420 [physics.acc-ph].

[53] M. A. Valdivia Garcia. "Optimized Monochromatization under Beamstrahlung for Direct Higgs Production". PhD thesis. Guanajuato U., 2022.

[54] V. I. Telnov. "Monochromatization of e^+e^- colliders with a large crossing angle". In: (2020). arXiv: 2008.13668 [physics.acc-ph].

[55] A. Faus-Golfe, M. A. Valdivia García, and F. Zimmermann. "The challenge of monochromatization: direct *s*-channel Higgs production: $e^+e^- \to H$". In: *Eur. Phys. J. Plus* 137.1 (2022), p. 31. DOI: 10.1140/epjp/s13360-021-02151-y.

[56] Y. Peng and Y. Zhang. "The Luminosity Reduction with Hourglass Effect and Crossing Angle in an e-p Collider". In: *6th International Particle Accelerator Conference*. 2015, TUPTY010. DOI: 10.18429/JACoW-IPAC2015-TUPTY010.

[57] T. Sen. "Luminosity and beam-beam tune shifts with crossing angle and hourglass effects in e^+e^- colliders". In: (2022). arXiv: 2208.08615 [physics.acc-ph].

[58] F. Ruggiero and F. Zimmermann. "Luminosity optimization near the beam-beam limit by increasing bunch length or crossing angle". In: *Phys. Rev. ST Accel. Beams* 5 (6 June 2002), p. 061001. DOI: 10.1103/PhysRevSTAB.5.061001.

[59] P. Raimondi, D. N. Shatilov, and M. Zobov. "Beam-Beam Issues for Colliding Schemes with Large Piwinski Angle and Crabbed Waist". In: (Feb. 2007). arXiv: physics/0702033.

[60] K. Yokoya and P. Chen. "Beam-beam phenomena in linear colliders". In: *Lect. Notes Phys.* 400 (1992). Ed. by M. Dienes, M. Month, and S. Turner, pp. 415–445. DOI: 10.1007/3-540-55250-2_37.

[61] M. Sands. "The Physics of Electron Storage Rings: An Introduction". In: *Conf. Proc. C* 6906161 (1969), pp. 257–411.

[62] G. Aad et al. "Observation of a new particle in the search for the Standard Model Higgs boson with the ATLAS detector at the LHC". In: *Phys. Lett. B* 716 (2012), pp. 1–29. DOI: 10.1016/j.physletb.2012.08.020. arXiv: 1207.7214 [hep-ex].

[63] S. Chatrchyan et al. "Observation of a New Boson at a Mass of 125 GeV with the CMS Experiment at the LHC". In: *Phys. Lett. B* 716 (2012), pp. 30–61. DOI: 10.1016/j.physletb.2012.08.021. arXiv: 1207.7235 [hep-ex].

[64] T. Han and Z.-g. Wang. "Precision Higgsstrahlung as a Probe of New Physics". In: *Phys. Rev. D* 89 (2014), p. 075006. DOI: 10.1103/PhysRevD.89.075006.

[65] V. Barger, M. Berger, J. Gunion, and T. Han. "Higgs boson physics in the s-channel at $\mu^+\mu^-$ colliders". In: *Physics Reports* 286.1 (1997), pp. 1–51. DOI: 10.1016/S0370-1573(96)00041-5.

[66] M. Bicer et al. "First Look at the Physics Case of TLEP". In: *JHEP* 01 (2014). Ed. by N. A. Graf, M. E. Peskin, and J. L. Rosner, p. 164. DOI: 10.1007/JHEP01(2014)164. arXiv: 1308.6176 [hep-ex].

[67] D. d'Enterria. "Resonant s-channel Higgs boson production". In: *Proc. FCC-ee (TLEP) Physics Workshop* (Paris, France). Oct. 2014. URL: https://indico.cern.ch/event/337673/contributions/1728502/.

[68] D. d'Enterria. "Higgs physics at the Future Circular Collider". In: *PoS* ICHEP2016 (2017), p. 434. DOI: 10.22323/1.282.0434. arXiv: 1701.02663 [hep-ex].

[69] D. d'Enterria, A. Poldaru, and G. Wojcik. "Measuring the electron Yukawa coupling via resonant s-channel Higgs production at FCC-ee". In: *Eur. Phys. J. Plus* 137.2 (2022), p. 201. DOI: 10.1140/epjp/s13360-021-02204-2. arXiv: 2107.02686 [hep-ex].

[70] W. Altmannshofer, J. Brod, and M. Schmaltz. "Experimental constraints on the coupling of the Higgs boson to electrons". In: *JHEP* 05 (2015), p. 125. DOI: 10.1007/JHEP05(2015)125. arXiv: 1503.04830 [hep-ph].

[71] M. Greco, T. Han, and Z. Liu. "ISR effects for resonant Higgs production at future lepton colliders". In: *Physics Letters B* 763 (2016), pp. 409–415. DOI: 10.1016/j.physletb.2016.10.078.

[72] A. Dery, C. Frugiuele, and Y. Nir. "Large Higgs-electron Yukawa coupling in 2HDM". In: *JHEP* 04 (2018), p. 044. DOI: 10.1007/JHEP04(2018)044. arXiv: 1712.04514 [hep-ph].

[73] K. Oide et al. "Design of beam optics for the Future Circular Collider e^+e^- collider rings". In: *Phys. Rev. Accel. Beams* 19.11 (2016). [Addendum: Phys.Rev.Accel.Beams 20, 049901 (2017)], p. 111005. DOI: 10.1103/PhysRevAccelBeams.19.111005. arXiv: 1610.07170 [physics.acc-ph].

[74] F. Zimmermann. "Parameter Space Beyond 1034". Rep. EuCARD-CON-2010-041. 2010. URL: https://cds.cern.ch/record/1304238.

[75] R. Calaga. "Crab Cavities for the High-luminosity LHC". In: *18th International Conference on RF Superconductivity*. 2018, THXA03. DOI: 10.18429/JACoW-SRF2017-THXA03.

[76] A. Blonel. Private communication.

[77] T. Sjöstrand, S. Mrenna, and P. Skands. "A brief introduction to PYTHIA 8.1". In: *Computer Physics Communications* 178.11 (2008), pp. 852–867. DOI: 10.1016/j.cpc.2008.01.036.

[78] L. Evans and P. Bryant. "LHC Machine". In: *JINST* 3 (2008), S08001. DOI: 10.1088/1748-0221/3/08/S08001.

[79] O. S. Brüning et al. *LHC Design Report*. CERN Yellow Reports: Monographs. Geneva: CERN, 2004. DOI: 10.5170/CERN-2004-003-V-1. URL: https://cds.cern.ch/record/782076.

[80] M. Benedikt, A. Blondel, P. Janot, M. Mangano, and F. Zimmermann. "Future Circular Colliders succeeding the LHC". In: *Nature Phys.* 16.4 (2020), pp. 402–407. DOI: 10.1038/s41567-020-0856-2.

[81] M. K. Gaillard, P. D. Grannis, and F. J. Sciulli. "The standard model of particle physics". In: *Reviews of Modern Physics* 71.2 (Mar. 1999), S96–S111. DOI: 10.1103/revmodphys.71.s96.

[82] "The European Strategy for Particle Physics Update". In: (2013). URL: https://cds.cern.ch/record/1567258.

[83] T. Behnke et al. "The International Linear Collider Technical Design Report - Volume 1: Executive Summary". In: (2013). arXiv: 1306.6327 `[physics.acc-ph]`.

[84] K. Fujii et al. Physics Case for the 250 GeV Stage of the International Linear Collider. 2018. arXiv: 1710.07621 `[hep-ex]`.

[85] M. Aicheler et al. *A Multi-TeV Linear Collider Based on CLIC Technology: CLIC Conceptual Design Report*. CERN Yellow Reports: Monographs. Geneva: CERN, 2012. DOI: 10.5170/CERN-2012-007. URL: https://cds.cern.ch/record/1500095.

[86] M. J. Boland et al. "Updated baseline for a staged Compact Linear Collider". In: (Aug. 2016). DOI: 10.5170/CERN-2016-004. arXiv: 1608.07537 `[physics.acc-ph]`.

[87] W. Abdallah et al. "CEPC Technical Design Report: Accelerator". In: *Radiat. Detect. Technol. Methods* 8.1 (2024), pp. 1–1105. DOI: 10.1007/s41605-024-00463-y. arXiv: 2312.14363 `[physics.acc-ph]`.

[88] D. Treille and T. Taylor. "The Large Electron-Positron Collider". In: *Rep. Prog. Phys.* 61 (1998), pp. 177–234. DOI: 10.1088/0034-4885/61/2/002.

[89] A. Abada, T. Sjöstrand, P. Skands, and K. Furukawa. "Future Circular Collider: Vol. 3 The Hadron Collider (FCC-hh)". In: *Eur. Phys. J. ST* (2019). DOI: 10.1140/epjst/e2019-900087-0.

[90] F. Gianotti. "The Future Circular Collider: CERN plans". In: *Proc. FCC Week 2024* (San Francisco, CA). June 2024. URL: https://indico.cern.ch/event/1298458/contributions/5975648/.

[91] B. Richter. "Very High-Energy electron-Positron Colliding Beams for the Study of the Weak Interactions". In: *Nucl. Instrum. Meth.* 136 (1976), pp. 47–60. DOI: 10.1016/0029-554X(76)90396-7.

[92] J. Keintzel et al. "FCC-ee Lattice Design". In: *JACoW* eeFACT2022 (2023), pp. 52–60. DOI: 10.18429/JACoW-eeFACT2022-TUYAT0102.

[93] L. van Riesen-Haupt et al. "The status of the FCC-ee optics tuning". In: *JACoW* IPAC2024 (2024), WEPR02. DOI: 10.18429/JACoW-IPAC2024-WEPR02.

[94] P. Ramondi. “Final Focus design with local compensation of geometric and chromatic aberrations”. In: *Proc. FCCIS 2022 Workshop* (CERN). Dec. 2022. URL: https://indico.cern.ch/event/1203316/contributions/5156515/.

[95] P. Ramondi. “Alternative optics and variants”. In: *Proc. FCCIS 2023 WP2 Workshop* (Roma, Italy). Nov. 2023. URL: https://indico.cern.ch/event/1326738/contributions/5654524/.

[96] SAD — Strategic Accelerator Design. http://acc-physics.kek.jp/SAD/.

[97] A. Blondel et al. “Polarization and Centre-of-mass Energy Calibration at FCC-ee”. In: (Sept. 2019). arXiv: 1909.12245 [physics.acc-ph].

[98] MAD-X — Methodical Accelerator Design. http://madx.web.cern.ch/madx/.

[99] CERN optics repository. https://acc-models.web.cern.ch/acc-models/fcc/.

[100] K. Oide. “IR optics for FCC-ee”. In: *Proc. FCC-EIC Jonit & MDI Workshop* (Geneva, Switzerland). Oct. 2022. URL: https://indico.cern.ch/event/1186798/contributions/5062582/.

[101] M. Koratzinos. “Status Update of the FCC-ee IR Magnet Design”. In: *Proc. the 65th ICFA Advanced Beam Dynamics Workshop on High Luminosity Circular* e^+e^- *Colliders (eeFACT22)* (Frascati (RM), Italy). Sept. 2022. URL: https://agenda.infn.it/event/21199/contributions/173695/.

[102] R. L. Ramjiawan. “FCCee e+/e- injection and RCS booster”. In: *Proc. the 65th ICFA Advanced Beam Dynamics Workshop on High Luminosity Circular* e^+e^- *Colliders (eeFACT22)* (Frascati (RM), Italy). Sept. 2022. URL: https://agenda.infn.it/event/21199/contributions/173254/.

[103] P. Hunchak et al. “Studies on Top-Up Injection into the FCC-ee Collider Ring”. In: *JACoW* IPAC2022 (2022), pp. 1699–1702. DOI: 10.18429/JACoW-IPAC2022-WEPOST011.

[104] M. Aiba et al. “Top-up injection schemes for future circular lepton collider”. In: *Nucl. Instrum. Meth. A* 880 (2018), pp. 98–106. DOI: 10.1016/j.nima.2017.10.075.

[105] J. Keintzel. “Energy sawtooth due to SR and CM energy”. In: *Proc. 2nd EPOL Workshop* (Frascati (RM), Italy). Sept. 2022. URL: https://indico.cern.ch/event/1181966/contributions/5047163/.

[106] F. Peauger. “Baseline & Cavity options for FCC-ee”. In: *Proc. the 65th ICFA Advanced Beam Dynamics Workshop on High Luminosity Circular* e^+e^- *Colliders (eeFACT22)* (Frascati (RM), Italy). Sept. 2022. URL: https://agenda.infn.it/event/21199/contributions/174260/.

[107] J. Keintzel, A. Blondel, D. Shatilov, R. Tomás García, and F. Zimmermann. “Centre-of-Mass Energy in FCC-ee”. In: *JACoW* IPAC2022 (2022), pp. 1683–1686. DOI: 10.18429/JACoW-IPAC2022-WEPOST007.

[108] P. Raimondi and S. M. Liuzzo. “Toward a diffraction limited light source”. In: *Phys. Rev. Accel. Beams* 26.2 (2023), p. 021601. DOI: 10.1103/PhysRevAccelBeams.26.021601.

[109] D. Einfeld, J. Schaper, and M. Plesko. “Design of a diffraction limited light source (DIFL)”. In: *Proceedings Particle Accelerator Conference*. Vol. 1. 1995, 177–179 vol.1. DOI: 10.1109/PAC.1995.504602.

[110] A. Faus-Golfe. "Progress on monochromatization". In: *Proc. FCC Week 2022* (Paris, France). June 2022. URL: https://indico.cern.ch/event/1064327/contributions/4893337/.

[111] H. Jiang, A. Faus-Golfe, K. Oide, Z. Zhang, and F. Zimmermann. "First optics design for a transverse monochromatic scheme for the direct s-channel Higgs production at FCC-ee collider". In: *JACoW* IPAC2022 (2022), pp. 1878–1880. DOI: 10.18429/JACoW-IPAC2022-WEPOPT017.

[112] H. Jiang. "First optics design for a transverse monochromatic scheme for the direct s-channel Higgs production at FCC-ee collider". In: *Proc. 65th ICFA Advanced Beam Dynamics Workshop on High Luminosity Circular* $\mathrm{e^+e^-}$ *Colliders (eeFACT2022)* (Rome, Italy). Sept. 2022. URL: https://agenda.infn.it/event/21199/contributions/173268/.

[113] H. Jiang. "Progress on monochromatization". In: *Proc. CEPC Workshop 2022* (Beijing, China). Oct. 2022. URL: https://indico.ihep.ac.cn/event/17020/contributions/118195/.

[114] Z. Zhang. "IR monocromatization studies". In: *Proc. Joint FCC-France & Italy workshop on Higgs, Top, EW, HF and SM physics* (Lyon, France). Nov. 2022. URL: https://indico.in2p3.fr/event/27968/contributions/115475/.

[115] Z. Zhang et al. "Monochromatization Interaction Region Optics Design for Direct s-channel production at FCC-ee". In: *JACoW* IPAC2023 (2023), MOPL079. DOI: 10.18429/JACoW-IPAC2023-MOPL079.

[116] Z. Zhang. "Monochromatization optics for FCC-ee lattices". In: *Proc. FCC Week 2023* (London, UK). June 2023. URL: https://indico.cern.ch/event/1202105/contributions/5396871/.

[117] Z. Zhang. "Monochromatization optics for FCC-ee lattices". In: *Proc. CEPC Workshop 2023* (Nanjing, China). Oct. 2023. URL: https://indico.ihep.ac.cn/event/19316/contributions/142896/.

[118] Z. Zhang. "Recent advance in the monochrom scheme for the FCC-ee". In: *Proc. 14th Workshop of France China Particle Physics Laboratory (FCPPL2023)* (Zhuhai, China). Nov. 2023. URL: https://indico.ihep.ac.cn/event/20622/contributions/143813/.

[119] Z. Zhang. "Monochromatization studies". In: *Proc. FCC-FS EPOL group and FCCIS WP2.5 meeting #25* (CERN). Dec. 2023. URL: https://indico.cern.ch/event/1355703/.

[120] A. Faus-Golfe. "Monochromatisation scheme study status for FCCee". In: *Proc. IAS Program on High Energy Physics (HEP 2024)* (Hongkong, China). Jan. 2024. URL: https://indico.cern.ch/event/1335278/contributions/5723850/.

[121] A. Faus-Golfe. "Progress on monochromatization studies". In: *Proc. 7th FCC Physics Workshop* (Annecy, France). Feb. 2024. URL: https://indico.cern.ch/event/1307378/contributions/5724239/.

[122] Z. Zhang. "Monochromatization optics design for FCC-ee". In: *Proc. CEPC Workshop 2024 EU-Edition* (Marseille, France). Apr. 2024. URL: https://indico.in2p3.fr/event/20053/contributions/137761/.

[123] Z. Zhang et al. "Update in the optics design of monochromatization interaction region for direct Higgs s-channel production at FCC-ee". In: *JACoW* IPAC2024 (2024), WEPR21. DOI: 10.18429/JACoW-IPAC2024-WEPR21.

[124] A. Faus-Golfe. "Monochromatization a new operation mode for e^+e^- circular colliders". In: *Proc. IPAC'24* (Nashville, TN). May 2024. URL: https://indico.jacow.org/event/63/contributions/3067/.

[125] A. Faus-Golfe. "Monochromatization optics for FCC-ee". In: *Proc. FCC Week 2024* (San Francisco, CA). June 2024. URL: https://indico.cern.ch/event/1298458/contributions/5977864/.

[126] Z. Zhang. "Monochromatization: a new operation mode of FCC-ee". In: *Proc. 15th France China Particle Physics Network/Laboratory workshop (FCPPN/L2024)* (Bordeaux, France). June 2024. URL: https://indico.in2p3.fr/event/20434/contributions/140623/.

[127] Z. Zhang et al. "Monochromatization interaction region optics design for direct s-channel Higgs production at FCC-ee". In: *Preprint submitted to Nucl. Instrum. Meth. A* (Nov. 2024). arXiv: 2411.04210 `[physics.acc-ph]`.

[128] Z. Zhang. "FCC-ee monochromatization issues". In: *Proc. 6th International Workshop on Future Tau Charm Facilities* (Guangzhou, China). Nov. 2024. URL: https://indico.pnp.ustc.edu.cn/event/1948/contributions/18080/.

[129] M. Hofer. Private communication. June 2023.

[130] A. S. Muller and J. Wenninger. "Synchrotron tune and beam energy at LEP-2". In: *7th European Particle Accelerator Conference (EPAC 2000)*. June 2000, pp. 427–429.

[131] K. Oide. Private communication. Nov. 2024.

[132] K. Oide. "Polarimeter and wigglers integration status". In: *Proc. FCC Week 2022* (Paris, France). June 2022. URL: https://indico.cern.ch/event/1064327/contributions/4893299/.

[133] G. Iadarola et al. "Xsuite: An Integrated Beam Physics Simulation Framework". In: *JACoW* HB2023 (2024), TUA2I1. DOI: 10.18429/JACoW-HB2023-TUA2I1. arXiv: 2310.00317 `[physics.acc-ph]`.

[134] X. Buffat. Private communication. Apr. 2024.

[135] Y. Nosochkov and A. Seryi. "Compensation of detector solenoid effects on the beam size in a linear collider". In: *Phys. Rev. ST Accel. Beams* 8 (2 Feb. 2005), p. 021001. DOI: 10.1103/PhysRevSTAB.8.021001.

[136] M. Boscolo et al. "Progress in the design of the future circular collider FCC-ee interaction region". In: *JACoW* IPAC2024 (2024), TUPC67. DOI: 10.18429/JACoW-IPAC2024-TUPC67.

[137] A. Ciarma, H. Burkhardt, M. Boscolo, and P. Raimondi. "Alternative solenoid compensation scheme for the FCC-ee interaction region". In: *JACoW* IPAC2024 (2024), TUPC68. DOI: 10.18429/JACoW-IPAC2024-TUPC68.

[138] P. Ramondi. "Possible study on the detector solenoid compensation scheme". In: *Proc. FCC-ee MDI meeting #44 and FCCIS WP2.3 meeting #15* (CERN). Feb. 2023. URL: https://indico.cern.ch/event/1251507/.

[139] P. Raimondi. Private communication. Mar. 2023.

[140] Institute of High Energy Physics, Beijing. “BEPCII Design Report”. Beijing, China: Institute of High Energy Physics, 2009.

[141] C. Milardi, M. Preger, and P. Raimondi. “The DAFNE interaction region for the KLOE-2 run”. Rep. DAFNE-TECHNICAL-NOTE-IR-14. Mar. 2010.

[142] M. Bassetti, M. E. Biagini, and C. Biscari. “Solenoidal field compensation”. In: *Frascati Phys. Ser.* 10 (1998). Ed. by L. Palumbo and G. Vignola, pp. 209–214.

[143] T. K. Charles, B. Holzer, R. Tomas, K. Oide, L. van Riesen-Haupt, and F. Zimmermann. “Alignment & stability challenges for FCC-ee”. In: *EPJ Tech. Instrum.* 10.1 (2023), p. 8. DOI: 10.1140/epjti/s40485-023-00096-3.

[144] I. Koop. “Resonant Depolarization at Z and W at FCC-ee”. In: *62nd ICFA Advanced Beam Dynamics Workshop on High Luminosity Circular* e^+e^- *Colliders*. 2019, TUPBB04. DOI: 10.18429/JACoW-eeFACT2018-TUPBB04.

Appendix A

Overview of synchrotron radiation

Synchrotron radiation is a type of electromagnetic radiation emitted when a charged ultra-relativistic particle passes through the accelerator bending magnets (rings). Due to relativistic kinematics, an ultra-relativistic particle can only radiate within an angle $1/\gamma$ with γ the relativistic Lorentz factor, approximately equal to the ratio of particle energy and its rest mass energy. Then the pulse length of the radiation observed at a location far from the ring can be estimated by the time difference between the particle and the light:

$$\Delta t \approx \frac{\rho/\gamma}{v} - \frac{\rho \sin(1/\gamma)}{c} \approx \frac{2\rho}{3\gamma^3 c}\,, \tag{A.1}$$

where ρ denotes the bending radius of the ring, v the spreed of the particles, and c the speed of light. For electron (or positron), the energy of the photon should be characterized by critical energy using the uncertainty principle:

$$u_c = \frac{\hbar}{\Delta t} = \frac{3}{2}\gamma^3 \frac{\hbar c}{\rho} = \frac{3}{2}\gamma^3 m_e c^2 \left(\frac{r_e}{\alpha \rho}\right)\,, \tag{A.2}$$

where $\hbar$ denotes the Planck constant [7], m_e the electron rest mass [7], r_e the classical electron radius [7], and α the fine structure constant [7]. This could be concluded that the strength of the synchrotron radiation is mainly determined by γ, m, and ρ.

In the absence of radiation, particle motion is symplectic, and the beam emittances are conserved. The inclusion of radiation effects in a classical approximation leads to emittance damping.

The effects of synchrotron radiation on particle motion are crucial for initial performance evaluation especially for e^+e^- rings. To quantitatively describe the impact of synchrotron radiation, five synchrotron radiation integrals are introduced associated with

ρ:

$$I_1 \equiv \oint \left(\frac{D_x}{\rho_x} + \frac{D_y}{\rho_y} \right) ds \;, \tag{A.3}$$

$$I_2 \equiv \oint \frac{1}{\rho^2} ds \;, \tag{A.4}$$

$$I_3 \equiv \oint \frac{1}{|\rho|^3} ds \;, \tag{A.5}$$

$$\begin{aligned} I_{4x} &\equiv \oint D_x \left(\frac{1}{\rho_x} + 2\frac{B_y}{B^2}\frac{\partial B_y}{\partial x} \right) ds \\ I_{4y} &\equiv \oint D_y \left(\frac{1}{\rho_y} + 2\frac{B_x}{B^2}\frac{\partial B_x}{\partial y} \right) ds \;, \end{aligned} \tag{A.6}$$

$$I_{5x,y} \equiv \oint \frac{\mathcal{H}_{x,y}}{|\rho|^3} ds \;, \tag{A.7}$$

where the $D_{x,y}$ denote the dispersion, $B_{x,y}$ the dipole field, and $\mathcal{H}_{x,y}$ the dispersion invariant defined as

$$\mathcal{H}_{x,y} = \frac{\left(\beta_{x,y} D'_{x,y} + \alpha_{x,y} D_{x,y}\right)^2 + \left(D_{x,y}\right)^2}{\beta_{x,y}} \;. \tag{A.8}$$

The horizontal, vertical and longitudinal radiation damping times caused by synchrotron radiation are given by:

$$J_x \tau_x = J_y \tau_y = J_z \tau_E = 2\frac{E_0}{U_0} T_{\text{rev}} \;. \tag{A.9}$$

E_0 denotes the beam energy. U_0 is the energy loss per turn given by:

$$U_0 = \frac{C_\gamma}{2\pi} E_0^4 I_2 \;, \tag{A.10}$$

where for electron (or positron) C_γ is defined as:

$$C_\gamma = \frac{4\pi}{3} \frac{r_e}{(m_e c^2)^3} \approx 8.846 \times 10^{-5}\,\mathrm{m\,GeV^{-3}} \tag{A.11}$$

T_{rev} is the revolution period, which equals to the ratio of collider circumference C and the speed of light c:

$$T_{\text{rev}} = \frac{C}{c} \tag{A.12}$$

The corresponding damping partition number are given by:

$$
\begin{aligned}
J_x &= 1 - \frac{I_{4x} + I_{4y}}{I_2} \\
J_y &= 1 \\
J_z &= 2 + \frac{I_{4x} + I_{4y}}{I_2} \,.
\end{aligned}
\tag{A.13}
$$

The natural emittance is:

$$\varepsilon_{x,y} = C_q \gamma^2 \frac{I_{5x,y}}{J_{x,y} I_2} \,, \tag{A.14}$$

where for electron (or positron) C_q is defined as:

$$C_q = \frac{55}{32\sqrt{3}} \frac{\hbar}{m_e c} \approx 3.832 \times 10^{-13}\,\mathrm{m} \,. \tag{A.15}$$

The natural relative beam energy spread σ_δ and bunch length σ_z are respectively given by:

$$\sigma_\delta^2 = C_q \gamma^2 \frac{I_3}{J_z I_2} \tag{A.16}$$

and

$$\sigma_z = \frac{\alpha_\mathrm{C} C}{2\pi Q_s} \sigma_\delta \,, \tag{A.17}$$

where α_C denotes the momentum compaction factor defined as:

$$\alpha_\mathrm{C} = \frac{I_1}{C} \,, \tag{A.18}$$

and Q_s the synchrotron tune defined as

$$Q_s^2 = \frac{\alpha_\mathrm{C} h}{2\pi E_0} \sqrt{e^2 V_\mathrm{RF}^2 - U_0^2} \,. \tag{A.19}$$

In Eq. A.19, e is the elementary charge. V_RF is the voltage of the RF cavity for compensating the synchrotron power loss P_SR given by:

$$P_\mathrm{SR} = U_0 I \tag{A.20}$$

with I the beam current defined by

$$I = e n_b f_r N_b \,, \tag{A.21}$$

where n_b denotes the number of bunches, N_b the bunch population, and f_r the revolution frequency ($f_r = 1/T_{\text{rev}}$). h the harmonic number equal to the ratio of RF frequency f_{RF} and f_r:

$$h = \frac{f_{\text{RF}}}{f_r} \,. \tag{A.22}$$

In summary, this appendix provides a detailed introduction to the key formulas related to synchrotron radiation and its effects on particle motion. These formulas enable the quantitative analysis and evaluation of the impact of synchrotron radiation in high-energy accelerators, including energy loss per turn, radiation damping times, natural emittance, energy spread, and bunch length. Understanding these effects is crucial for the design and performance evaluation of electron-positron colliders, offering essential theoretical support for this work.

Appendix B

Different accelerator simulation programs

MAD-X

MAD-X (Methodical Accelerator Design) [98] is a comprehensive software tool developed at CERN for computational simulating and designing particle accelerators. It is widely used in the field of accelerator physics for the modeling, optimization, and analysis of beam dynamics in complex accelerator structures. MAD-X provides a versatile platform for simulating various aspects of accelerator behavior, including beam optics, orbit correction, and particle tracking. It supports the study of both linear and non-linear beam dynamics, allowing users to design and optimize accelerators for a wide range of applications, from Synchrotron Radiation light source to colliders. MAD-X is particularly renowned for its robust scripting capabilities, which enable users to define and manipulate complex accelerator lattices with high precision. The software's flexibility and powerful features make it an essential tool for accelerator physicists and engineers working on the design and operation of modern particle accelerators.

In this PhD work, we primarily use MAD-X for the optics design. Given the application of various types of magnets, including dipoles, quadrupoles, and sextupoles, across multiple electron beam lines, MAD-X facilitates the efficient computation of transport matrices, whether they are first-order or second-order, making the process significantly more straightforward.

Xsuite

Xsuite [133] is a cutting-edge Python-based software package developed by CERN for advanced accelerator physics simulations. Designed with a modular architecture, Xsuite allows researchers and engineers to model, optimize, and analyze the behavior of particle beams in complex accelerator systems. Its integration with Python makes it particularly powerful, as it enables seamless interaction with a wide range of Python libraries, making it easier to incorporate optimization techniques, data analysis, and machine learning into accelerator design and simulation workflows.

Xsuite is designed to handle high-intensity beams and advanced accelerator configurations, and its Python foundation facilitates rapid prototyping and flexible development. The package supports high-precision simulations, including beam tracking, collective effects, and optics design, leveraging Python's capabilities to provide an intuitive and efficient user experience. One of Xsuite's key advantages is its ability to perform more accurate simulations for high-energy accelerators like the FCC-ee compared to traditional tools like MAD-X, particularly in accounting for effects such as beamstrahlung.

Due to its superior accuracy in these scenarios, we used MAD-X for the initial design work and then converted the MAD-X version to Xsuite for detailed dynamic aperture particle tracking. This transition also positions us well for future simulations involving beam-beam interactions. As a result, Xsuite is becoming increasingly popular among the accelerator physics community for both research and operational purposes.

Guinea-Pig

Guinea-Pig (Generator of Unwanted Interactions for Numerical Experiment Analysis Program Interfaced to GEANT) is a specialized simulation software originally developed by D. Schulte as part of his PhD thesis [24], and it is maintained and updated by SLAC National Accelerator Laboratory (SLAC). Guinea-Pig is designed to simulate the interactions of particle beams in colliders, including complex phenomena such as beam-beam interactions and the generation of secondary particles. Its capability to simulate the effect of beamstrahlung makes Guinea-Pig particularly valuable for analyzing luminosity in e^+e^- colliders, especially those planned for future high-energy physics experiments.

In practical applications, Guinea-Pig is typically employed after the initial design phase has been completed using general accelerator physics software like MAD-X. Once the baseline design is established, the design parameters, including beam sizes, emittances, and energy spreads are transferred to Guinea-Pig to perform detailed simulations during the beam collisions. It is notable that Guinea-Pig calculates all the parameters per bunch crossing, without considering revolution frequency or bunches per beam. Therefore, for luminosity calculations, the luminosity without a crossing angle is required to be first determined in Guinea-Pig, and the bunch population needs to be adjusted to match the analytical result. Then we calculated the luminosity with the crossing angle using the adjusted bunch population.

In this work, after completing the optics design in MAD-X, we used the resulting beam parameters at the interaction point to generate a Gaussian distribution of particles as input for Guinea-Pig. This allowed us to simulate the beam-beam interactions and obtain the luminosity and the centre-of-mass energy spread, both of which account for the effects of beamstrahlung. This approach ensures that our simulations accurately reflect the physical conditions expected in the collider, providing valuable insights into its performance.